UNICA

UNIVERSITÀ
DEGLI STUDI
DI CAGLIARI

Ph.D. DEGREE IN

In Physics

Cycle XXXV

TITLE OF THE Ph.D. THESIS

Studies of Ξ_c^+ production in pPb collisions

Scientific Disciplinary Sector(s)

02/A1

Ph.D. Student: Roman Litvinov

Supervisor Rudolf Oldeman

Final exam. Academic Year 2021/2022
Thesis defence: February 2023 Session

Declaration of Authorship

I, Roman Litvinov, declare that this doctoral thesis titled, "Studies of Ξ_c^+ production in pPb collisions" and the work presented in it are my own. I confirm that:

- Where I have consulted the published work of others, this is always clearly attributed.
- Where I have quoted from the work of others, the source is always given. With the exception of such quotations, this thesis is entirely my own work.
- I have acknowledged all main sources of help.
- Where the thesis is based on work done by myself jointly with others, I have made clear exactly what was done by others and what I have contributed myself.

Signed: 

Date: 31/10/2022

Abstract

Università degli studi di Cagliari
Dipartimento di Fisica

Doctor of Physics

Studies of Ξ_c^+ production in pPb collisions

by Roman Litvinov

In this thesis I report the studies of production of Ξ_c^+, a baryon made of usc quarks produced in proton-lead collisions at a centre-of-mass energy $\sqrt{s} = 8.16$ TeV measured with the LHCb detector at CERN. The studies are based on samples of proton-lead and lead-proton collision data, corresponding to an integrated luminosity of 12.5 and 17.4 nb^{-1}, respectively, collected by the LHCb detector in 2016. The Ξ_c^+ events are reconstructed in the detector through the decay of the Ξ_c^+ baryon in a proton, a kaon and a pion. The analysis is performed over the transverse momentum range $2.0 < p_{\rm T} < 12.0$ GeV/c in the regions of rapidity from 1.5 to 4.0 and from -5.0 to -2.5. I present the measurements of the Ξ_c^+ cross-section, production ratios of Ξ_c^+/Λ_c^+ and Ξ_c^+/D^0, and forward-backward asymmetry. The results are compared to the latest theoretical predictions. These measurements can provide important information on the hadronisation of charm hadrons, as well as on the hadron structure. Since the Ξ_c^+ contains an s quark, the enhancement in the production ratios can be an indication of Quark Gluon Plasma formation.

Acknowledgements

Firstly, I want to thank first my supervisor Giulia Manca for her great support and help with every obstacle during three years of PhD, especially during the pandemic period. She always managed to keep me motivated and efficient. I want to thank my unofficial supervisors, Jiayin Sun and Samuel Belin, who were helping and giving me advises at every step of this analysis. This work wouldn't be possible without them. I also want to thank different Ph.D. students from our department, especially Alex Chauvin, for all the help with living in a new city, which was a big challenge for me.

My gratitude to all people of the Ion and Fixed Target group of LHCb, with particular thought to Benjamin Audurier that helped me a lot when I was working on performance of the reconstruction, and Matt Durham for his ideas on the analysis and help with writing a paper. I'm also very grateful to Barbara Sciascia and all the Muon group, who welcomed me at CERN for my period abroad and introduced me the hardware side of our experiment. In a more general notice, I want to thank the university, the INFN, and the LHCb group of Cagliari for providing a good working environment. Thank you!

Contents

Chapter 1

Introduction

It is believed that 13.8 billion years ago our Universe was contained in a single point of high density and temperature which then began to rapidly expand. The evolution of the Universe expansion is described by the model called the Big Bang. Eventually, the Universe cooled sufficiently to allow the formation of confined subatomic particles, and later atoms, as we observe them today. The model which characterizes fundamental particles and their interactions is called Standard Model (SM). In particular, the strong interaction between quarks and gluons and how they are confined into composite particles (hadrons) is described by the Quantum Chromodynamics (QCD) domain. However, if the energy density of a system is large enough, quarks and gluons will be free to move, just as it was a few instants after the Big Bang. Such a state of matter is known as Quark Gluon Plasma (QGP). The characterization of this type of matter is subject of broad investigations at past and current experiments.

In a laboratory, QGP can be created at particle colliders by colliding two heavy nuclei, such as lead (Pb), with ultra-relativistic energy [1]. Right after the collision a lot of particles will be produced and go through the collision media carrying some information about it. These particles can be studied with particle detectors. One method to investigate the colliding media is to study certain particle production rates and cross sections. Theoretical predictions based on perturbative QCD describe the differential charm production cross sections in proton-proton (pp) collisions at different energies with high precision, where no QGP is present.

It is predicted that the behaviour of particles passing through the medium will change if QGP is present [2], and the change will be different for the different particles depending among others on the binding energy. In this sense, quarkonium states (mesons whose constituents are a quark and its own antiquark) are expecting to dissociate more than c- and b-mesons, formed by strong forces. If the state does not live long enough in a medium, this will effectively result in a suppression of the state in collisions of heavy nuclei as lead-lead, where QGP is expected to be formed. This is because, depending on the binding energy, the $q\bar{q}$ state will dissociate in the QGP medium and will not have the time to recombine before freezeout. This will result in a suppression of the state in heavy nuclei collisions, where QGP is expected to be formed. In proton-lead (pPb) collisions the situation is still not entirely defined, as QGP should not be present, but theories predict the formation of "QGP droplets" [3]

which could partially induce the same behaviour as in lead-lead (PbPb) collisions. In addition, in pPb collisions the so called "Cold Nuclear Matter" (CNM) effects are also present, which can mimic the effects due to QGP but with different mechanisms. The main CNM effects, visible in charm and beauty production, include shadowing [4], energy loss [5] and nuclear break-up [6]. The nuclear shadowing is the suppression of the production rate due to multiple scattering of partons in heavy-ion collisions, while the energy loss is related to the gluon radiation of the heavy quark passing through the medium. The nuclear break-up is an inelastic interaction where the nucleons of the colliding nuclei break the newly formed bound state of heavy quarks, such as c and b quarks, that subsequently hadronise into two open heavy-flavour hadrons. While the first two effects are common to all the particles, the break-up affects only quarkonium particles and not open heavy flavour, since the interaction of open heavy-flavour hadrons will give another open heavy flavour hadron, and the net effect is null. For this reason, the study of production and hadronisation of quarkonia and charm and beauty hadrons is important to disentangle all possible effects. In addition, it is predicted by the models that the strange quark production would be enhanced in heavy-ion collisions, as first mentioned by J. Rafelski [7]. For example, strangeness enhancement and strange antibaryons are discussed as a signature for QGP formation [8, 9, 10], mainly due to the predominance of the gluonic $s\bar{s}$ production mechanism $gg \rightarrow s\bar{s}$. This feature allows the strange production to reach equilibrium on a timescale comparable with the QGP lifetime, due to the high gluon density in the QGP. In addition, the expected temperature for the QCD phase transition is very similar to the mass of the strange quark, *i.e.* for $m_s \sim$ 100-200 MeV/c^2 the strangeness formation time is similar to the expected lifetime of the QGP and the strangeness chemical equilibration in QGP is possible, forming a QGP made of u, d, s quarks and gluons. This would lead to abundant strange quark density in the QGP. The particles whose productions are supposed to be enhanced are the anti-hyperons, such as Ξ baryons (ucs), but all strange particles are expected to experience production enhancement in QGP compared to hadron gas. Such enhancement, if observed, could be a strong indication of the formation of the deconfined plasma state.

An interesting way to look for strangeness enhancement at accelerators is to study the ratio of production rates of particles with a strange quark to those without it. Ratios of Λ/π and Ξ/π yields as a function of multiplicity have been measured by ALICE in pp, pPb and PbPb collisions [11], showing an enhancement of strangeness also in pp and pPb collisions for the same multiplicity densities as the ones reached in PbPb collisions, with a hierarchy determined by the strangeness content. This result would confirm the presence of the strangeness enhancement and could hint very strongly to the mechanism responsible for it. One of the possible candidates is the formation of QGP droplets in pp and pPb systems, in the same way as it happens in PbPb, where it has already been established [12].

The main subject of this thesis is the study of Ξ_c^+ production. In this analysis the ratio of Ξ_c^+/Λ_c^+ yields is studied as a function of particle multiplicity, p_T and y of the

particles in pPb collisions collected by LHCb in 2016 at $\sqrt{s} = 8.16\,\text{TeV}$. Given that the Ξ_c^+ is a usc state and the Λ_c^+ is a udc state, if strangeness is enhanced in pPb collisions it should become evident in this ratio. This measurement has the potential of being very precise, since the Ξ_c^+ and Λ_c^+ are reconstructed in the same final state, $pK\pi$, significantly reducing the systematic uncertainties of many factors, as the trigger and particle identification efficiencies of the final state particles, which are expected to cancel in the ratio. The thesis is organised as follows.

Chapter 1 is the introduction. Chapter 2 is devoted to the description of the theory, from the basics of the Standard Model and QCD to the Ξ_c^+ and Λ_c^+ production mechanisms in proton-proton and proton-lead collisions. Chapter 3 presents the experimental layout, starting with a technical presentation of the Large Hadron Collider and LHCb itself, with emphasis on the important subdetectors for the analysis and in the scope of heavy-ion physics. Finally, Chapters 4 - 10 are the core of the thesis as they describe the methodology used in the analysis with the different elements. They are organised as follows; a precise description of the samples used in Chapter 4; a brief introduction of the analysis strategy in Chapter 5; a summary of the different selection criteria in Chapter 6; the description of the methods used to estimate the performance of the detector in Chapter 7; a list of the systematic uncertainties in Chapter 8 and a discussion of the results in Chapter 9. Finally, the conclusions are drawn in Chapter 10.

Chapter 2

Theory

Everything in the Universe is made of a few fundamental particles, managed by four fundamental forces. Today, these particles and interactions are best understood within the Standard Model (SM) of particle physics. The SM is the theory that describes the role of these fundamental particles and interactions between them and assigns them quantum numbers, such as the mass, the electric charge, the spin etc. Many scientific facilities around the world are dedicated to test the validity of the SM theory on a subatomic scale, and in recent years they have become larger and more complex. Despite getting many experimental confirmations, some fundamental questions of the SM are still under investigation. In particular, this is true for Quantum Chromo Dynamics (QCD), the branch of the SM that describes the strong interaction between the quarks mediated by gluons. The particularity of quarks and gluons is that, thanks to the properties of QCD, they are confined to form composite particles called hadrons. However, if the energy density of a system is large enough, the quarks and gluons are free to move in a medium called "Quark Gluon Plasma" (QGP), a state of matter with deconfined quarks and gluons as fundamental constituents. One of the essential goals of heavy-ion physics is to investigate QGP and its properties.

In this chapter we will briefly introduce Standard Model, with particular attention to Quantum Chromodynamics, Quark Gluon Plasma and the different effects studied in heavy-ion physics.

2.1 An overview of the Standard Model

The Standard Model is a quantum field theory that describes the interactions between fundamental particles. It has provided a number of predictions later proven true experimentally. Since the early 20^{th} century, a broad spectrum of particles have been observed. The fundamental particles in the SM are six quarks, six leptons, four gauge bosons, one Higgs boson and their anti-particles. All these particles are represented in Fig. 2.1. Each fundamental particle has a set of quantum numbers like the mass (m), the charge (q) as well as the spin (s), the colour charge, the electric charge, the hypercharge, the baryonic number or the leptonic number. Quark and leptons hold half-integer spins, and thus are characterised by Fermi-Dirac statistics (fermions)

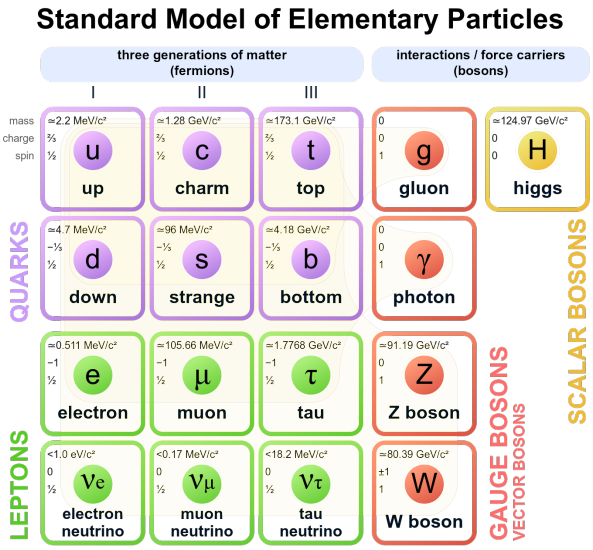

FIGURE 2.1: Fundamental particles of the Standard Model.

following the Pauli exclusion principle, unlike particles with integer spins (bosons), that obey Bose-Einstein statistics.

Fermions are classified in three families or generations

$$\begin{pmatrix} \nu_e \\ e^- \end{pmatrix} \begin{pmatrix} \nu_\mu \\ \mu^- \end{pmatrix} \begin{pmatrix} \nu_\tau \\ \tau^- \end{pmatrix}$$
$$\begin{pmatrix} u \\ d \end{pmatrix} \quad \begin{pmatrix} c \\ s \end{pmatrix} \quad \begin{pmatrix} t \\ b \end{pmatrix}.$$

Here u stands for quark up, d for quark down, s for quark strange, c for quark charm, t for quark top and b for quark bottom. The leptons also come in three generations, where e is the electron and ν_e is the electron neutrino, μ is the muon with, ν_μ, the muon neutrino and τ is a tau-lepton with, ν_τ, the tau neutrino. This classification derives from the fact that at first order the weak interaction couples only quarks within the same family, and from the lepton number conservation. The SM accounts for this with a gauge symmetry that acts on doublets. The fermions and bosons all have their corresponding anti-particles of same mass but with an opposite charge.

To date, four fundamental forces are known:

- Electromagnetic;
- Strong;
- Weak;
- Gravitational.

The electromagnetic force acts between all objects with an electric charge by exchanging massless and electrically neutral photons (γ). Its interaction is described by a relativistic quantum field theory called quantum electrodynamics (QED).

The strong force can be observed in the interaction between nucleons in a nucleus (large scale) or in the interaction between quarks inside a nucleon (small scale). It exists only among particles which carry the colour charge, quarks and gluons, where a gluon (g) is a mediator of the strong interaction. The interaction and behaviour between them are described by Quantum Chromodynamics.

The weak interaction is the interaction between subatomic particles that, among others, is responsible for the radioactive decay of atoms. One can distinguish two types of weak interactions, through neutral current, with the mediation of the Z^0 boson, and through charged current, with the $W^{\pm}$ boson. The theory describing the behaviour and effects of the weak force is called electroweak theory (EWT).

Gravitational forces are negligible at the scale of particle physics due to the negligible mass of elementary particles. The basic features of the fundamental forces, as their strengths and ranges, are summarised in Table 2.1.

TABLE 2.1: The known fundamental interactions, force carriers, their typical charges, relative strengths and interaction ranges.

Interaction	Force carrier	Relative strength	Interaction range
Strong	g	1	10^{-15}
Electromagnetic	γ	$\frac{1}{137}$	∞
Weak	Z^0, $W^{\pm}$	10^{-6}	10^{-18}
Gravitational	-	6×10^{-39}	∞

The Higgs bosons (H) provide a mass to all the fermions as well as to the bosons that interact with the Higgs fields.

The SM is a quantum field theory based on the gauge symmetry group $SU(3)_C \times SU(2)_L \times U(1)_Y$. The group $SU(3)_C$ represents the strong interaction, where C denotes colour, the basic charge of strong interaction, and $SU(2)_L \times U(1)_Y$ the electroweak interactions, since the weak and electromagnetic interactions are unified at energies of the order of 100 GeV.

2.2 Quantum Chromodynamics

2.2.1 QCD Lagrangian

As explained before, the QCD theory describes the underlying dynamics of the strong interaction between coloured quarks and gluons. QCD is a non-abelian gauge theory ($SU(3)$) described by the following lagrangian

$$\mathcal{L}_{QCD} = \bar{\psi}_q^i (i\gamma_\mu)(D^\mu)_{ij}\psi_q^j - m_q \bar{\psi}_q^i \ \psi_q^i - \frac{1}{4} F_{\mu\nu}^A F^{A\mu\nu}, \tag{2.1}$$

where γ_μ is the Dirac matrix, ψ_q^i is a Dirac spinor field of a quark with colour i and flavour q, m_q is the mass of the considered quark. The covariant derivation D_μ connects the quark field to the gluon field, which is defined as

$$(D_\mu)_{ij} = \delta_{ij}\partial_\mu - ig_s\lambda_{ij}^a\mathcal{A}_\mu^A, \tag{2.2}$$

with g_s denoting the colour coupling, $\mathcal{A}_\mu^A$ is the gluon field, λ_{ij}^A are the Gell-Mann matrices. $F_{\mu\nu}^A$ ($A = 1, 2...8$) is the gluon field strength tensor which is defined as

$$F_{\mu\nu}^A = \partial_\mu\mathcal{A}_\nu^A - \partial_\nu\mathcal{A}_\mu^A + g_s f_{ABC}\mathcal{A}_\mu^B\mathcal{A}_\nu^C, \tag{2.3}$$

where f_{ABC} is the structural constant of the $SU(3)$ group. The non-Abelian nature of QCD is reflected in the gluon field $F_{\mu\nu}^A$. Gluons, as the mediators of strong interactions, carry colour charges, hence interact strongly with each other.

2.2.2 Colour confinement and asymptotic freedom

In the QCD description, the vacuum is filled with quantum fluctuations of virtual quarks and gluons. At lowest order, colour confinement (screening) comes from virtual quark/anti-quark pairs, as shown on Fig. 2.2 (a), just like charge screening comes from electron/positron pairs in QCD. The effect is also referred to as "vacuum polarization". In addition, quark–quark scattering might involve a gluon–gluon pair produced in a gluon self-interaction of the type shown Fig. 2.2 (b). Each gluon carries both a colour charge and an anti-colour magnetic moment. The net effect of polarisation of virtual gluons in the vacuum is not to screen the field but to increase it and change its colour.

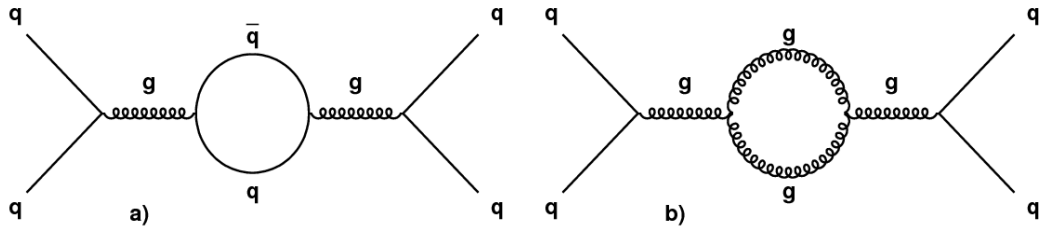

FIGURE 2.2: Example of Feynman diagram at leading order for (a) QCD screening effect, (b) QCD anti-screening effect.

Due to the competition of these two effects the interactions between particles becomes weaker at higher energy scale. The "running coupling constant" of the strong interaction (α_s), that defines the strength of this force, at leading order is defined as

$$\alpha_s = \frac{4\pi}{(11 - \frac{2}{3}n_f)ln(\frac{Q^2}{\lambda_{QCD}})}, \tag{2.4}$$

where n_f is the number of flavours of the quarks, Q is the momentum transfer of the interaction and λ_{QCD} ($\sim 200\ MeV$ [13]) is the energy scale of QCD. As we can observe in Eq. 2.4, α_s depends strongly on Q. The smaller Q the higher α_s will be (soft process), forcing the quarks to be confined inside hadrons at low energy. On the

contrary, the larger Q leads to smaller α_s (hard process), which means that at the limit of $\alpha_s = 0$ the quarks and gluons should be allowed to move freely. Hard processes at large energy scales can be calculated using perturbative QCD (pQCD). However, the soft processes at small energy scales can only be solved by non-perturbative methods such as lattice QCD (lQCD). In Fig. 2.3 a collection of measurements of the $\alpha_s(Q^2)$ are plotted as a function of Q along with the corresponding order of the perturbation calculation used. This phenomenon is called “asymptotic freedom".

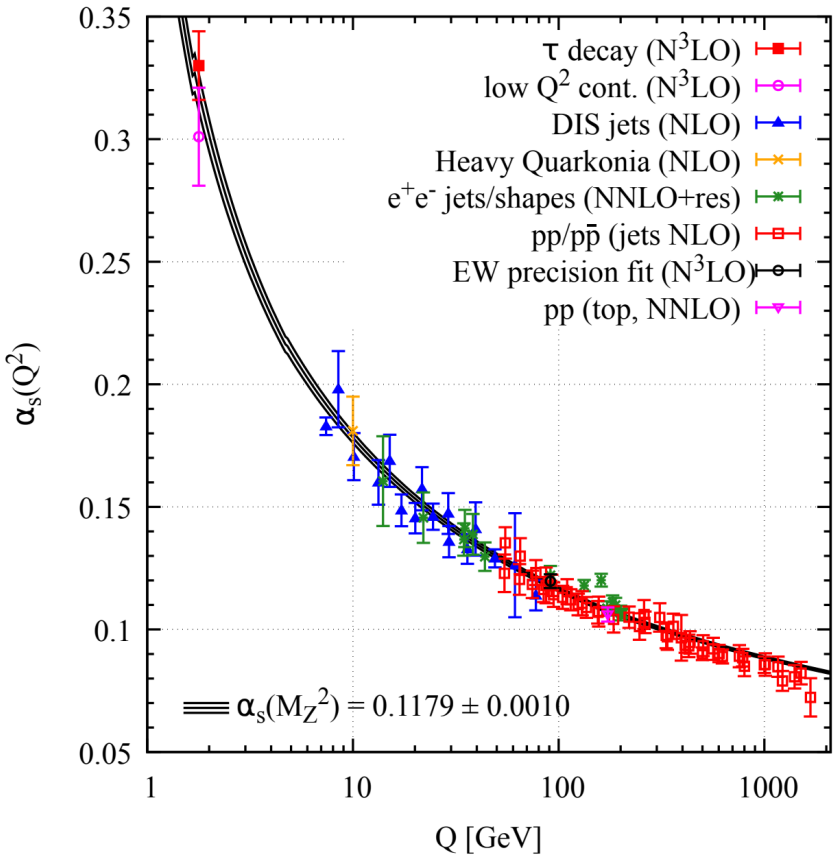

FIGURE 2.3: Summary of the different measurement of the running coupling constant of the strong interaction for different value of the energy scale Q[14].

These characteristics of the theory explain why it is impossible to observe isolated quarks and gluons at a low-energy density. In other words, quarks and gluons are bounded together into hadrons. Such behaviour is often called “colour confinement”.

To study deconfined quarks and gluons is possible in the asymptotic freedom regime at high energy scale where they can be considered as quasi-free particles. As discussed later, in Sec. 2.3.1, this regime could be obtained in high-energy heavy-ion collisions, alongside with the creation of a new state of matter called Quark Gluon Plasma.

2.2.3 Chiral symmetry

The QCD lagrangian has another major property. Massless particles are eigenstates of helicity [1] and as such, entirely left-handed or right-handed. Thus, if we assume the masses of the light quarks (u, d, s) to be zero ($m_q = 0$) [2], the QCD Lagrangian would be invariant under any helicity transformation. This symmetry is described for two quark fields, Ψ and Φ, and their respective left, L, and right, R, field by

$$< \Psi\overline{\Phi} >=< \Psi_R\overline{\Phi}_L + \Psi_L\overline{\Phi}_R >= 0 \ . \tag{2.5}$$

This symmetry indicates that the quark condensate vanishes ($< \Psi\overline{\Phi} >= 0$). However, due to the effects of the vacuum, a spontaneous symmetry break-up occurs ($< \Psi\overline{\Phi} >\neq 0$). One of the direct effects of this breaking of the symmetry is the creation of the Goldstone's bosons (π^0, $\pi^{\pm}$, K^0, $K^{\pm}$, $\overline{K^0}$, η_s) of the Standard Model. Several models predict a restoration of the symmetry at high density, which would be a signature of a hadronic phase transition into a QGP state with the quark condensate as a parameter. The restoration of the symmetry is only partial, as quarks do have masses, but it is often considered as fully restored for the quarks u, d and s, as their mass is relatively small compared to the QCD scale.

2.3 Heavy-ion physics

2.3.1 The Quark Gluon Plasma and the hadronic phase diagram

As mentioned previously, all the matter we observe around us is baryonic - the quarks and gluons are confined together in colourless state. However, it is possible to create systems with high energy density, where hadrons will start to overlap with each other and their constituents will be free to move. If the interaction between quarks and gluons will become sufficiently weak, the QGP will form.

Analogously to the phase diagram for transitions of water, we can reconstruct the phase diagram of the hadronic matter with respect to the Temperature (T) and the Net Baryon Density (μ_B) [3] as seen in Fig. 2.4. The lower left quadrant shown in white represents the region where confinement still applies and hadronic matter exists. Along the x-axis, "Nuclei" corresponds to $\mu_B \approx 940\ MeV$, which represents normal nuclear densities. The orange area represents QGP.

Therefore, the deconfinement of matter can be achieved by either increasing the Net Baryon density and/or by increasing the temperature. At low temperatures and high baryon density, the matter will begin to form a degenerate neutron gas, as it is predicted in neutron stars. As the net baryon density further increases, it begins

[1] The helicity of a particle is the projection of the spin on the direction of the particles's momentum. A particle with a positive helicity is called right-handed, a particle with a negative helicity is called left-handed.

[2] An acceptable approximation as the masses are smaller than the QCD scale ($\sim 218\ MeV$).

[3] The Net baryon density is defined as the number of baryons minus the number of anti-baryons divided by the volume of the system considered.

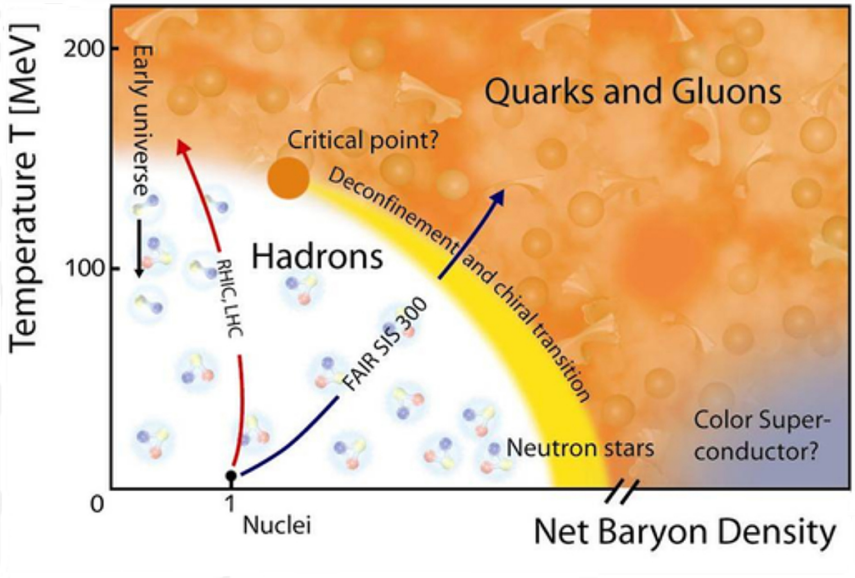

FIGURE 2.4: Phase diagram of the hadronic matter [15].

to overcome the repulsive force between the degenerate neutrons, with the distance between the neutrons becoming so small that a QGP is formed. Conversely, when $\mu_B = 0$, the lQCD result predicts a phase transition between the confined matter and the QGP around the critical temperature $150 \lesssim T_c \lesssim 200$ MeV.

Experimentally, the phase transition of cold hadronic matter to QGP is possible to study in ultra-relativistic heavy-ions collisions (such as PbPb). Since the nuclei travel at the speed of light in the vacuum, one must properly understand the phenomenology of such collisions in order to extract the physical properties of the created medium.

2.3.2 Probing the QGP

Heavy-ion collisions allow us to study the effects of extreme temperatures and densities of nuclear matter in a laboratory. As it involves a series of complex processes, a description of the time-space evolution of a collision is needed. The Bjorken model [16] provides the space-time evolution of an heavy-ion collision at high energy from the beginning of the collision. The basic understanding of the stages of a heavy nuclei collisions is represented in Fig. 2.5. Here, the left and right sides of the plot depict a collision with and without the creation of a QGP.

In the set-up of this model, two nuclei (typically Pb-Pb) are accelerated to velocities close to the speed of light and, due to the Lorentz contraction, are compressed along the direction of travel appearing as thin discs (Fig. 2.6 (a)). Then they travel across each other, where the partons undergo hard scattering processes (b). This phase will depend greatly on the initial state of the two colliding nuclei. Next, a volume of high temperature and energy density is generated (c). If at this stage T_c was reached, QGP is formed. This part is often described within the framework of relativistic hydrodynamics, where the QGP is assumed to be an ideal fluid with a very low viscosity. The system then rapidly expands into the vacuum and, as a result,

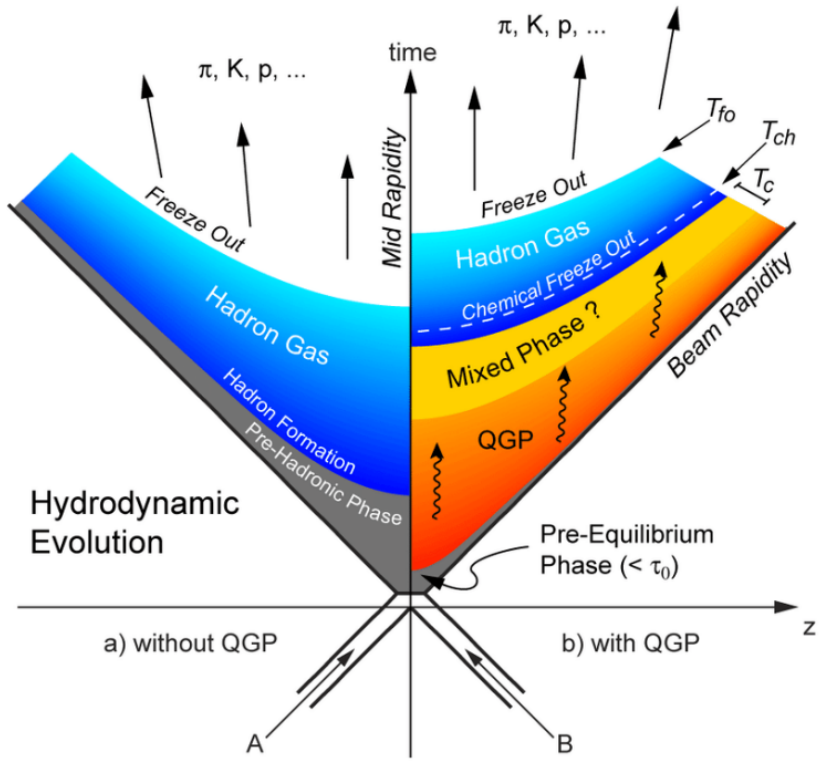

FIGURE 2.5: Space time evolution of a heavy-ion collision with QGP formation as described by the Bjorken model [17].

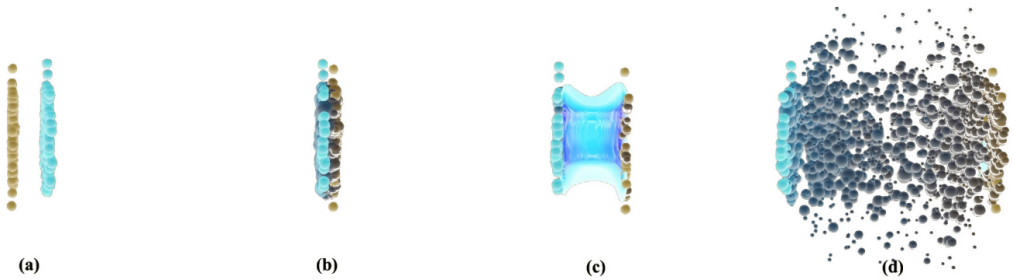

FIGURE 2.6: Four stages of a heavy-ion collision and its evolution. (a) Shows the two Lorentz contracted heavy nuclei moving towards each other in the CM frame, then (b) shows the overlapping nuclei at the collision stage. (c) Just after the collision the heavy-ions travel across each other and generate a volume of high temperature and energy density and finally in (d), the system expands and cools down, eventually fragmenting into hadrons that travel to the detector. [18]

begins to cool down (d). Once the system has cooled down back to T_c, hadronisation occurs with the quarks and gluons fragmenting into hadrons. The system continues to expand until the chemical freeze-out temperature is reached, where inelastic collisions among the hadrons stop. Then, the system continues to expand until it reaches the kinematic freeze-out temperature.

In order to study processes in heavy-ion collisions, first, it is important to derive

the geometrical characteristics of the system. As can be seen in Fig. 2.7, the ions may collide head-on or may only partially overlap at the collision stage, depending on the impact parameter, b. In the overlap region there are conditions that facilitate the QGP formation. The impact parameter defines the overlap region between the two incoming nuclei and thus, it is linked with the number of participating nucleons (N_{part}) and the number of inelastic nucleon-nucleon collisions (N_{coll}). As N_{part} and

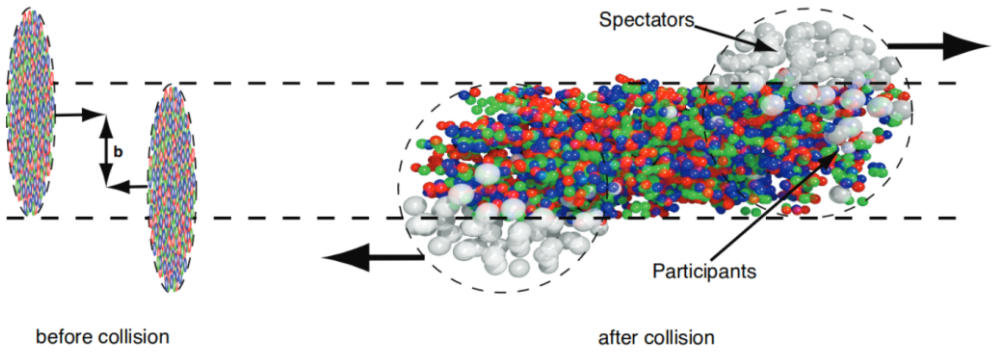

FIGURE 2.7: The scheme of two colliding nuclei in a relativistic heavy-ion collision. [19]

N_{coll} are not observable directly, it is possible to link the centrality[4] of the resulting collision with the charged particle multiplicity (N_{ch}), which is assumed to be increasing monotonically with b. Another model which is often used to characterise the heavy-ion collision geometry is refered as "Glauber Models", which is based on MC Glauber modelling [20]. This model allows to link the centrality of the collision to the produced number of particles. For example, one measures the charged particle multiplicity (dN_{evt}/dN_{ch}) for an ensemble of events; then, after obtaining the total integral of the multiplicity distribution, centrality classes are defined by binning the distribution based upon the fraction of the total integral of the multiplicity distribution. The dashed vertical lines in Fig. 2.8 show a typical binning. The same procedure is applied to a calculated distribution derived from a large number of Monte Carlo samples. For each centrality class, the mean value of Glauber quantities (e.g., N_{part}) is calculated. The mapping of data and simulation allows then to get the correlation between N_{ch} and centrality. This provides us with a potential mechanism for determining the presence and properties of the QGP.

2.3.3 Initial stage

The short life-time of the Quark Gluon Plasma (around 10 fm/c) makes its detection challenging, as it is much shorter than the typical acquisition time of the detectors.

[4]The centrality of a collision is a quantity ranging from 0% to 100% linked to the impact parameter. The more central (peripheral) the collision is, the lower (higher) is the impact parameter, the higher (lower) is the charged particles' multiplicity, with 0% representing the highest multiplicity.

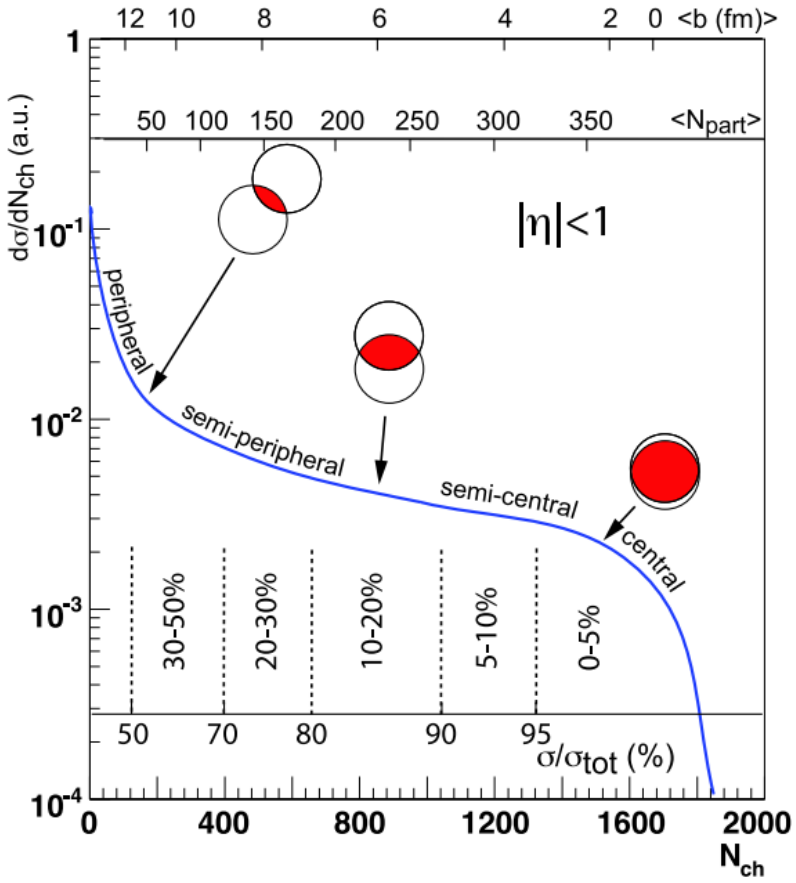

FIGURE 2.8: A cartoon example of the correlation of the final state observable N_{ch} with Glauber calculated quantities (b, N_{part}). [21]

This means that the particles are detectable only after the freeze-out, making impossible to know precisely in which phase they are produced. However, there are two ways to probe the initial processes in heavy-ion collisions. First is to focus on observables related to the early stage of the collision only, produced during the initial hard scattering, which are not affected by rescattering process and system expansion. Second is to study low transverse momentum hadrons, which are produced in "soft processes" and experience the whole evolution of the heavy-ion collision. Produced hadrons carry the information about the final state of a collision and can be used as a base for extrapolation to the early stage. Hadrons composed of the light quarks (u and d) belong to the late signature group (soft probes), while observables such as heavy flavour hadrons and quarkonia represents the early stage group (hard probes).

Many experimental measurements of potential QGP signatures in heavy-ion collisions have been reported and have led to several consents of the key QGP signatures:

- Strangeness enhancement: The study of the properties of QGP can be undertaken using the quarks not present in matter seen around us. Unlike the up and down quarks, strange quarks are not brought into the reaction by the colliding

nuclei. Therefore, they must be created during the collision process. Conveniently, the mass of a strange quark pair is just above T_c. Strangeness enhancement as a function of collision energy was predicted to indicate the presence of a QGP. This has been reported by many different experiments which have studied the enhanced strange baryon production [22, 23, 24].

- Quarkonium suppression: The bound states of a heavy quark and anti-quark, so-called heavy quarkonia, have become a high precision tool in heavy-ion collisions. Due to the heavy quarks' large masses, the pair of quarks has a formation time shorter than the formation time of the QGP and it is produced at hard scattering processes. The formation of a $q\bar{q}$ bound state is suppressed by the neighbouring colour charge in the deconfined medium, and it will lead to the suppression of quarkonia production rate if QGP is present. This effect has been observed by many different experiments [25, 26, 27].

- Jet quenching: in hadronic collisions partons with high p_{T} (jets) are produced in hard scattering process. For instance, in pp collisions two collinear jets are produced and then propagate and evolve in vacuum until they produce showers of particles in the detector. On the contrary, in heavy-ion collisions, jets are produced in relatively rare hard collisions and propagate within the QGP that is created by the rest of the system (Fig. 2.9).

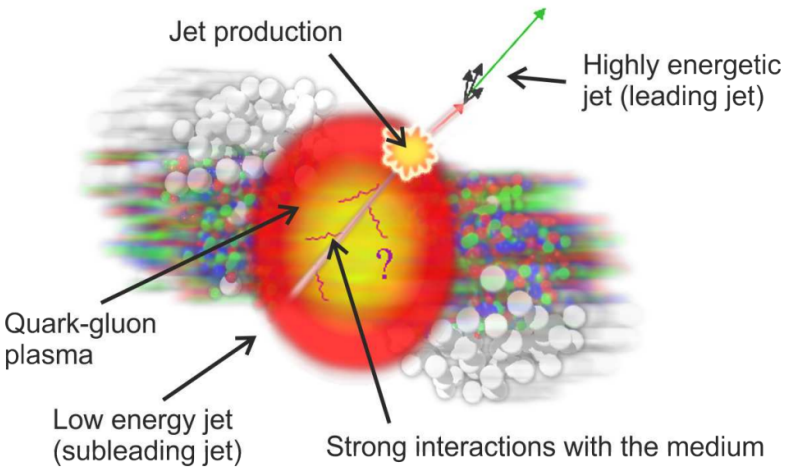

FIGURE 2.9: Sketch of the jet quenching mechanism during heavy-ion collision. [28]

One way to study this effect is to measure the difference between the outcome of production in hadronic collisions and between in heavy-ion collisions. The simplest consequence of having a dense medium is the energy-loss of the propagating parton, that is, "jet-quenching". This effect has been broadly studied by many experiments [29, 30].

In this analysis we are focused on Ξ_c^+ and Λ_c^+ baryons. As both of them contain a c-quark, we discuss charm production in different systems with more details. Unlike light quarks, the mass of the c quark is substantially larger than the temperature of the medium created in a heavy-ion collision. Furthermore, its mass is significantly larger than the QCD energy scale ($m_c \approx 1.275\,\text{GeV} \gg \Lambda_{QCD} \approx 200\,\text{MeV}$), thus, the production of c quarks can be well calculated within pQCD. Being produced at a very early stage of the collision, the c quark can experience the entire evolution of QGP, and it will loose energy due to the interaction with the medium. Hadrons with c quarks are broadly studied in heavy-ion collisions by many experiments.

2.4 Cold Nuclear Matter effects

In order to be able to study QGP properties with charm-quark production it is essential to understand the same processes in pp and pA collisions. QGP is not expected to be created in pp collisions, as the size of the system is too small. Thus, in heavy-ion physics studies, the results in pp collisions serve as baseline measurements. In proton-lead (pPb) collisions the situation is still not entirely defined, but so called "Cold Nuclear Matter" (CNM) effects are present [31], which can mimic the suppression due to QGP but with different mechanisms. In addition, theories predict the formation of "QGP droplets" [3] which could partially induce the same behaviour as in lead-lead (PbPb) collisions, but less dramatic. Studies in pPb are important for understanding QGP, as they allow the evaluation of the contribution of CNM effects in PbPb collisions. A schematic classification of nuclear matter effects taking place in different collision systems is shown in Fig. 2.10. In this chapter we discuss the processes which take place in pp and pPb collisions.

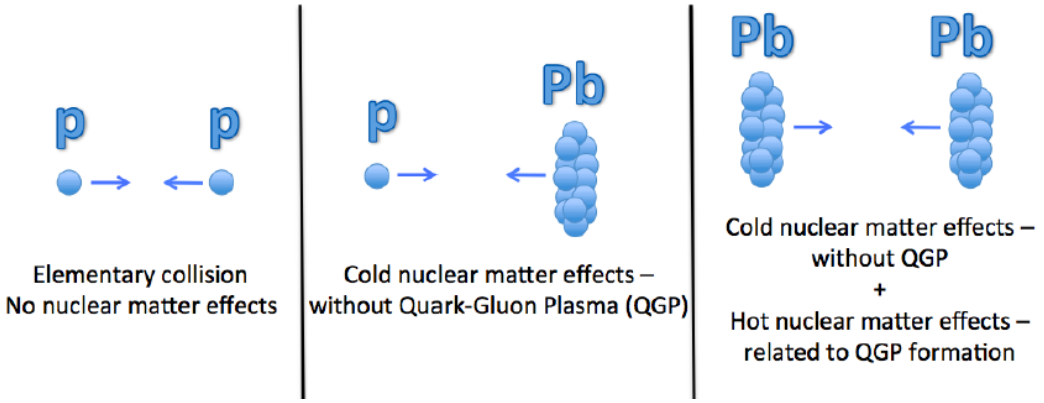

FIGURE 2.10: Schematic classification of nuclear matter effects taking place in different collision systems.

2.4.1 Charm production in pp collisions

In pp collisions charm quark is produced via (see Fig. 2.11) the fusion of two gluons (a), the annihilation of two quarks (b), pair creation with gluon emission (c), flavor

excitation (d), gluon splitting (e), simultaneous gluon splitting and flavor excitation (f).

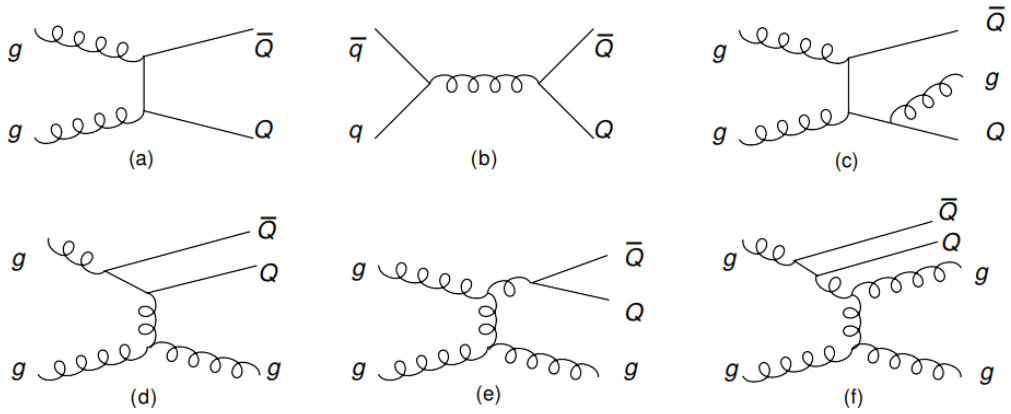

FIGURE 2.11: Heavy quark production diagrams: (a) gluon fusion, (b) quark - anti-quark annihilation, (c) pair creation with gluon emission, (d) flavor excitation, (e) gluon splitting, (f) together gluon splitting and flavor excitation. [32]

The mass of the charm quark allows one to perform the calculation of charm production in the context of pQCD down to very low transverse momenta (p_{T}) with pQCD. However, interactions with the nucleus can affect heavy flavour production rates. Consequently, the measured production rate will be modified. To describe charm production in pp collisions, QCD factorisation approaches, including k_T and collinear [33] factorisation, are introduced.

The overview of the pQCD factorisation approach in hadronic collisions is shown on Fig. 2.12. The single inclusive charm production can be written as a three-term

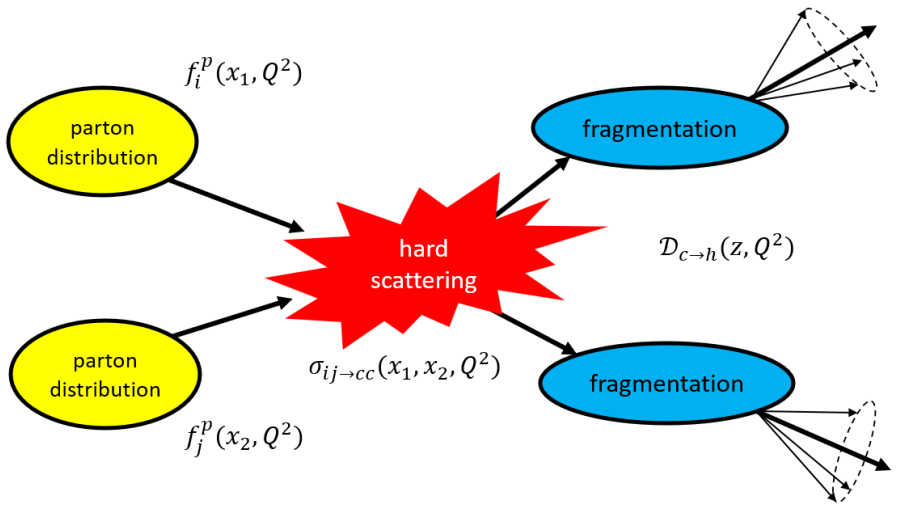

FIGURE 2.12: The schematic of the pQCD factorisation approach in hadronic collisions.

convolution with the pQCD factorisation method as:

$$d\sigma_{pp\to h} = f_i^p(x_1, Q^2) \otimes f_j^p(x_2, Q^2) \otimes d\sigma_{ij\to cc}(x_1, x_2, Q^2, \alpha_s) \otimes \mathcal{D}_{c\to h}(z, Q^2), \quad (2.6)$$

where:

- $f_i^p(f_j^p)$ is the parton distribution function (PDF) of nucleon $i(j)$, which is defined within the framework of collinear factorisation. Here, protons are assumed to be composed of many point-like objects and this function delivers a probability for finding a parton within a free proton with a given momentum fraction x, also known as Bjorken-x, at a given resolution or energy scale (Q) (Fig. 2.13). Thanks to the universal nature of the PDFs (process-independent) they can be obtained Deep Inelastic Scattering (DIS) experiments and Drell-Yan (DY) processes. The precise determination of PDFs of protons is an extremely active area of research where several groups perform global analyses of a wide variety of experimental hard-process data.

- $d\sigma_{ij\to cc}(x_1, x_2, Q^2, \alpha_s)$ is the parton-parton hard scattering cross section into a pair of quarks. It can be calculated using pQCD with a pertubative expansion of α_s at Leading Order (LO) precision, which includes the following processes: $g+g \to Q+\bar{Q}$ and $q+\bar{q} \to Q+\bar{Q}$ or at Next Leading Order (NLO), with these additional processes: $g+g \to Q+\bar{Q}+g$, $g+q \to q+Q+\bar{Q}$ and $g+\bar{q} \to \bar{q}+Q+\bar{Q}$.

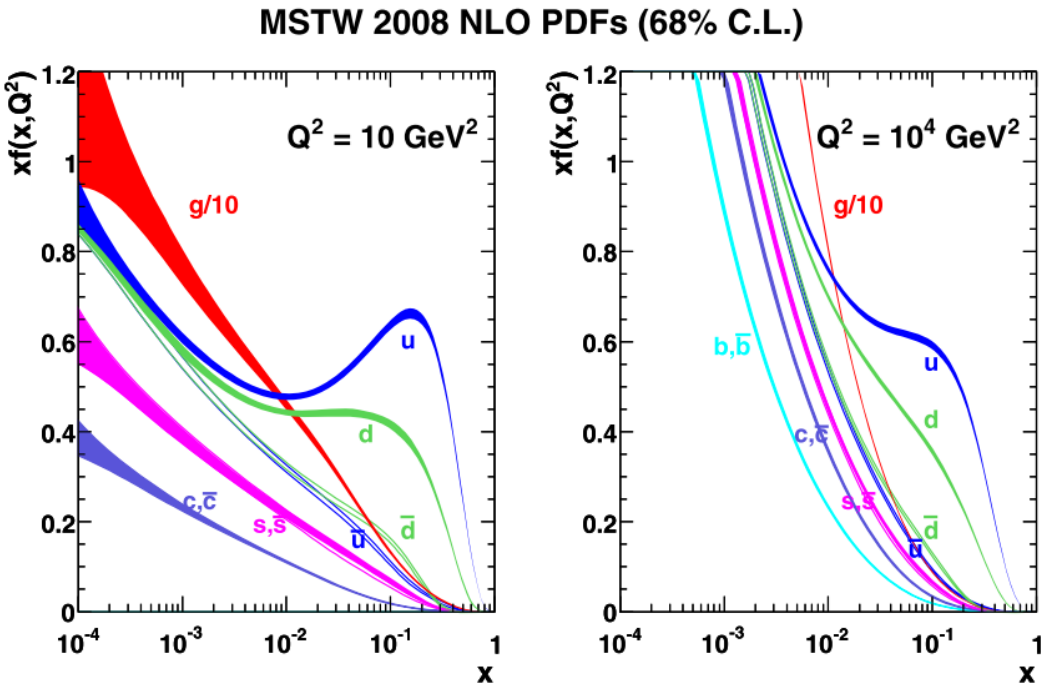

FIGURE 2.13: MSTW 2008 NLO PDFs at $Q^2 = 10$ GeV^2 and $Q^2 = 10^4$ GeV^2 [34].

- $\mathcal{D}_{c\to h}(z, Q^2)$ is the fragmentation function. This final element denotes the hadronisation of a charm quark with momentum (p_c) into a charm flavoured hadron with momentum $p_h = zp_c$.

The factorisation approach describes well charm flavoured hadron production in pp collisions, as observed by many experiments [35].

2.4.2 Charm production in pA

The situation with charm production in pA and AA collisions is more challenging, but not less interesting. Since the early 1980s it is known that nuclei are not a simple collection of free nucleons, and therefore, nuclear PDFs (nPDFs) are not equal to the sum of nucleon PDFs. In fact, the analyses on nPDFs rather employ Nuclear Modification Factors (NMF). One can define NMFs as

$$R_i^A(x, Q^2) = \frac{f_i^A}{Z f_i^p + N f_i^n}, \tag{2.7}$$

with $f_i^A = Z f_i^{p/A} + N f_i^{n/A}$. Here f_i^p and f_i^n are PDFs of proton and neutron, Z and N are the number of protons and neutrons in nucleus with atomic weight A. Fig. 2.14 illustrates different x-regimes represented by the NMF. Past studies showed that, for the quarks:

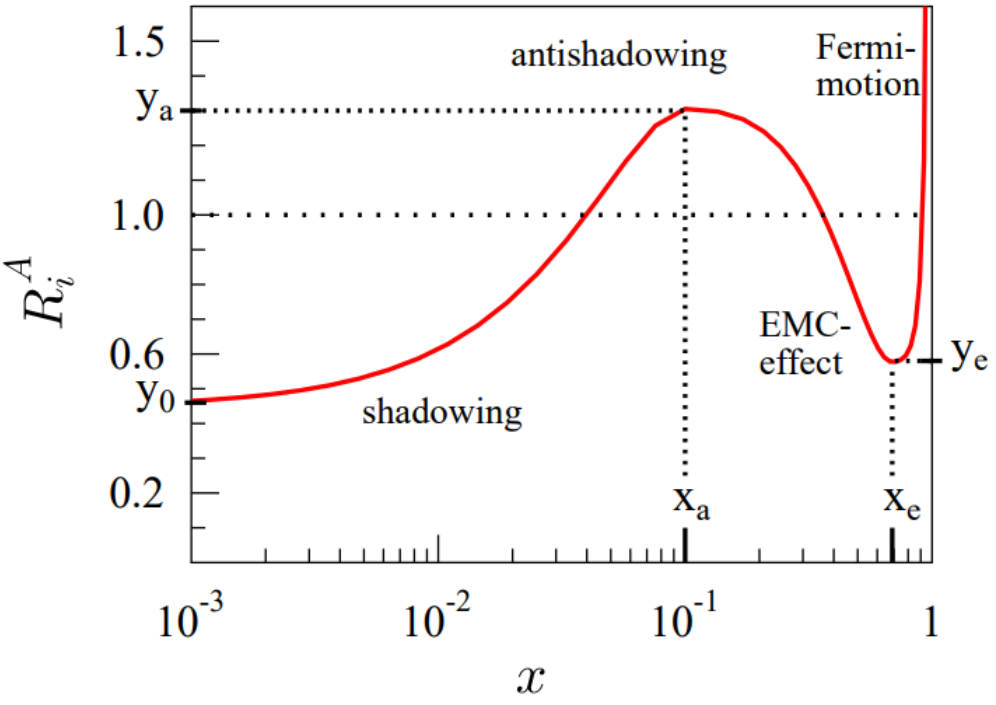

FIGURE 2.14: An illustration of the fit function $R_i^A(x, Q^2)$ [36].

- $x \gtrsim 0.8$ is the Fermi-motion region. This effect describes the modification of the nuclear structure-function at large x taking into account the nucleon momentum distribution in a nucleus [37].
- $0.25 \lesssim x \lesssim 0.8$ is the EMC region, the effect discovered by the European Muon Collaboration (EMC). Unexpectedly, $R_i^A(x, Q^2) < 1$ in this region. Different hypotheses have been offered for the cause of the EMC effect [38].
- $0.1 \lesssim x \lesssim 0.25$ is the antishadowing region. Here $R_i^A(x, Q^2) > 1$, due to multiple-scattering between partons[39].
- $x \lesssim 0.1$ is the shadowing region, and $R_i^A(x, Q^2) < 1$. The shadowing effect results from quantum mechanical interactions between partons and numerous nucleons, supposedly due to the spatial superposition of the low-x partons from different nucleons.

These modification effects are often referred as Cold Nuclear Matter effects. Normally, QGP is not supposed to be created in pA collisions, but it is important to study CNM effects in order to know their contribution to the effects observed in charm production. A common way to study them it is to measure the NMF, defined as the ratio of production in pA collisions to pp collisions scaled by the number of nucleons

$$R_{pA}(p_{\mathrm{T}}, y) = \frac{d^2\sigma_{pA}/dp_{\mathrm{T}}dy}{A \times d^2\sigma_{pp}/dp_{\mathrm{T}}dy}, \tag{2.8}$$

where A is the number of nucleons in a nucleus, $\sigma_{pA(pp)}$ is the cross-section in the pA (pp) collision system, y and p_{T} are the rapidity in the nucleon-nucleon centre-of-mass system and the transverse momentum of the resulting charm flavoured hadron. If $R_{pA}(p_{\mathrm{T}}, y)$ is not equal to unity, CNM effects can be revealed.

In a similar manner the NMF can be measured in AA collisions

$$R_{AA}(p_{\mathrm{T}}, y) = \frac{d^2\sigma_{AA}/dp_{\mathrm{T}}dy}{A^2 \times d^2\sigma_{pp}/dp_{\mathrm{T}}dy}. \tag{2.9}$$

Another peculiarity of pA collisions is that they are asymmetric in rapidities, i.e., the production in forward and backward rapidities does not behave in the same way. For this reason it becomes interesting to measure the forward-backward asymmetry

$$R_{FB}(p_{\mathrm{T}}, y) = \frac{d^2\sigma_{pA}(p_{\mathrm{T}}, +|y|)/dp_{\mathrm{T}}dy}{d^2\sigma_{Ap}(p_{\mathrm{T}}, -|y|)/dp_{\mathrm{T}}dy}. \tag{2.10}$$

Here "Forward" (pA) represents the direction of the proton travelling towards the nucleus, and the rapidity y is defined to be positive; "Backward" (Ap) denotes the opposite direction, and the rapidity is negative. The measurement of R_{FB} is easier to perform, as compared to R_{pA}, it does not require to measure the production in pp collisions and some uncertainties, related to σ_{pA} and σ_{Ap}, will cancel in the ratio.

CNM effects, such as nuclear shadowing [40], gluon saturation [41], Cronin effect [42], could occur in the initial state of the collision, as well as in the final state of

the collision, like hadronic rescatterings [43]. The coherent energy loss is neither an initial nor a final state effect. We briefly describe the effects, which are common in the open charm production:

- Nuclear shadowing. The explanation of this effect varies from model to model. The usual explanation for the origin of shadowing is multiple scattering. At small x the coherence length of the interaction between partons and nucleons $l_c \sim (2m_N x)^{-1}$, where m_N is the nucleons mass, becomes large as compared to the nuclear size ($l_c \gg R_A$) and the interference between partons and multiple nucleons takes place and some nucleons are effectively hidden (shadowed).

  Many theoretical models describe $R_i^A(x, Q^2)$, e.g. EPS09 [36], EKS [44], DSSZ [45], nCTEQ15 [46], EPPS16 [47]. In Fig 2.15 the calculation of $R_i^A(x, Q^2)$ nuclear modifications for Pb nuclei in EPPS16, EPS09 and DSSZ are shown.

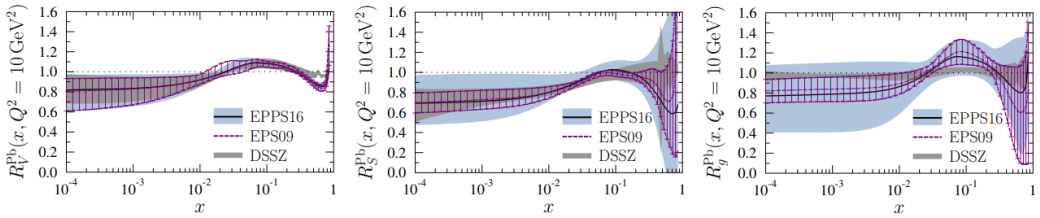

FIGURE 2.15: $R_i^A(x, Q^2)$ nuclear modifications for Pb nuclei calculated with the EPPS16 (black central curve with light-blue uncertainty bands), EPS09 (purple curves with hatching) and DSSZ (grey bands) analyses at $Q^2 = 10$ GeV. The left and middle panels correspond to the average valence and sea-quark modifications, the bottom panel is for gluons [47].

  Recently, it was investigated how experimental data on the inclusive production of heavy-flavor (HF) mesons [$D^0, J/\psi, B \to J/\psi$ and $\Upsilon(1S)$] in proton-lead collisions at the LHC could advance the knowledge of the PDF distribution inside heavy nuclei [48]. The data from LHC experiments was used to reweight the theoretical predictions on $R_i^{pPb}(x, Q^2)$ and allowed to drastically reduce uncertainties. However, due to the absence of data on gluon densities at $x \lesssim 10^{-3}$, the nuclear gluon content remained completely undetermined at small x. Thus, the gluon nPDFs in this region are extrapolated from the region of larger x and essentially follow their x-dependent parameterisations at the extrapolation scale, μ_F. It is varied about the default scale, μ_0, where $\mu_F = \xi\mu_0$ with $\xi = 0.5, 1.0, 2.0$. The central factorisation scale choice, μ_0^2, is different for each meson production: $M^2_{(J/\psi,\Upsilon)} + P^2_{T,(J/\psi,\Upsilon)}$ for J/ψ and $\Upsilon(1S)$, $4M_D^2 + P^2_{T,D}$ for D^0, and $4M_B^2 + (M_B/M_{J/\psi})^2 \times P^2_{T,J/\psi}$ for $B \to J/\psi$ (Fig 2.16).

- Gluon saturation. This phenomenon is also called Colour Glass Condensate (CGC), and constitutes the best candidate to approximate QCD in the saturation regime. Gluon saturation is usually not defined as a strict CNM effect as it can also occur in pp collisions. As you might see from Fig. 2.13 there is

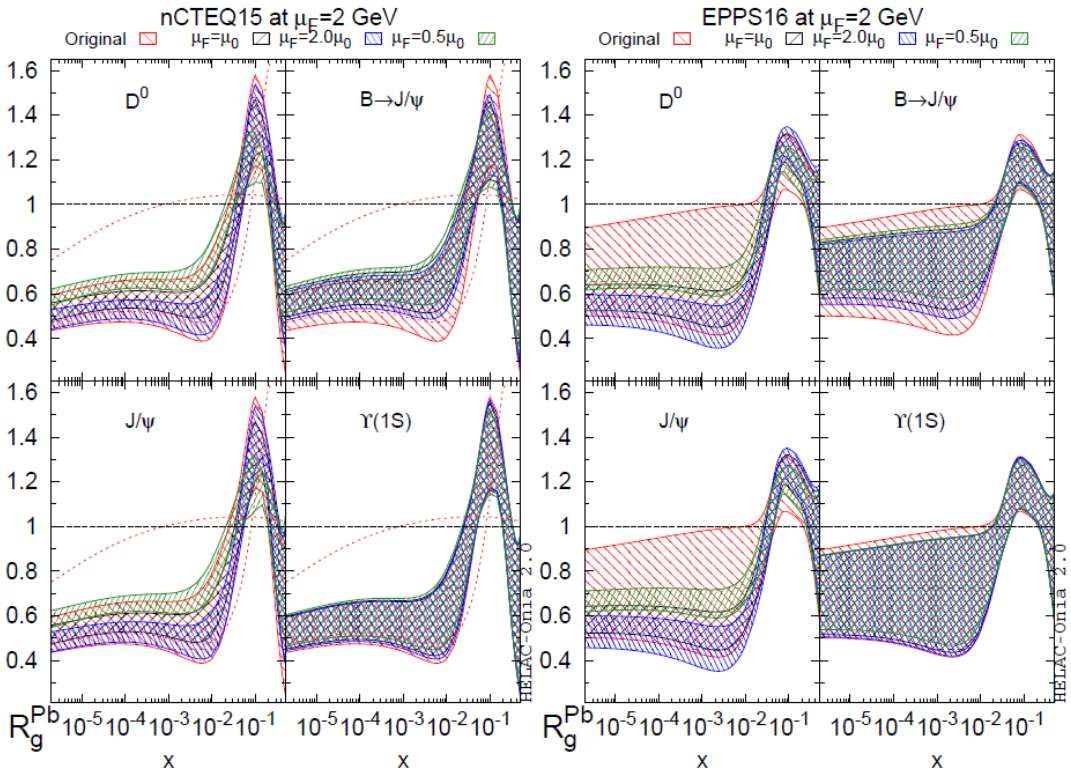

FIGURE 2.16: Selected $R_g^{Pb}(x, Q^2)$ results before and after reweighting with different data. The error bands due to nPDF uncertainty are given at 68% C.L. [48].

a large number of small-x gluons (and quarks) in a proton. At high energy the Pb nucleus is disc shaped due to the relativistic effect. Many gluons populate the transverse extend of nucleus, leading to a very dense saturated wave function. In such state gluons only split into more gluons, but also overlap and recombine reducing their number in the wave function. On Fig. 2.17 (left) one can find the picturing of different regimes of the hadron wave function. Here, the saturation line separates the dilute (DGLAP) regime from the dense (saturation) regime at relatively high x. When x decreases, the quantity of partons in hadrons increases quickly due to effects like bremsstrahlung [49]. This evolution can be described by the Balitsky-Fadin-Kuraev-Lipatov (BFKL) evolution equation [50]. At small x the recombination mechanism (*e.g.* $g + g \to g$) will take place to slow down the growth of gluons until gluons reach saturation. Balitsky-Kovchegov (BK) and Jalilian-Marian-Iancu-McLerran-Weigert-Leonidov-Kovner (JIMWLK) equations describe this non-linear evolution of the process. On Fig. 2.17 (right) the gluon distribution in a phase-space as a function of momentum transverse to the beam (k_T) is shown. Most gluons are near the saturation scale, Q_s. The non-linear BK/JIMWLK equations lead to a large internal momentum scale, Q_s, which grows with both energy (s) and nuclear

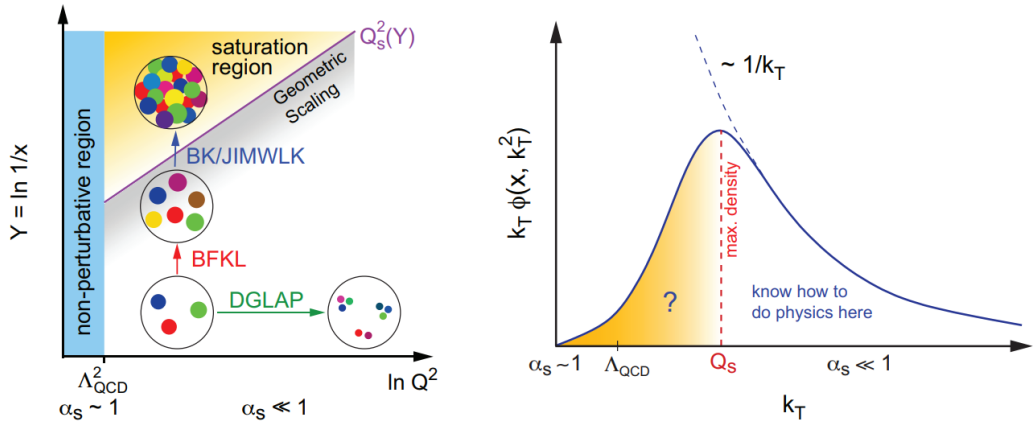

FIGURE 2.17: Left: diagram picturing the different regimes of the hadron wave function, the saturation line separates the dilute (DGLAP) regime from the dense (saturation) regime. Right: the k_T dependence of the gluon distribution at a given x. Most gluons carry $k_T \sim Q_s$. With decreasing x, Q_s increases and the gluon content shifts from the unknown non-perturbative region into a regime theoretically under control ($Q_s \gg \Lambda_{QCD}$) [51].

atomic number (A) according to the law

$$Q_s^2 \sim A^{1/3} s^{\lambda}, \tag{2.11}$$

where $\lambda \sim 0.3$. And so, at large momentum scale $\alpha_s \ll 1$, and we can calculate total cross sections, particle multiplicities, etc, from first principles. Therefore, the measurement of open charm cross-sections in pPb collisions is more appropriate than the one in pp to investigate the CGC theory.

- Coherent energy loss. This effect, also known as fully coherent energy loss (FCEL) [52], is calculated in hadron and jet production in pA collisions and is expected to affect all hadron species in proton-nucleus collisions. As seen in Fig. 2.18, the partons involved in the hadron production can lose energy through gluon radiation before or after passing through the medium. Here, an incoming

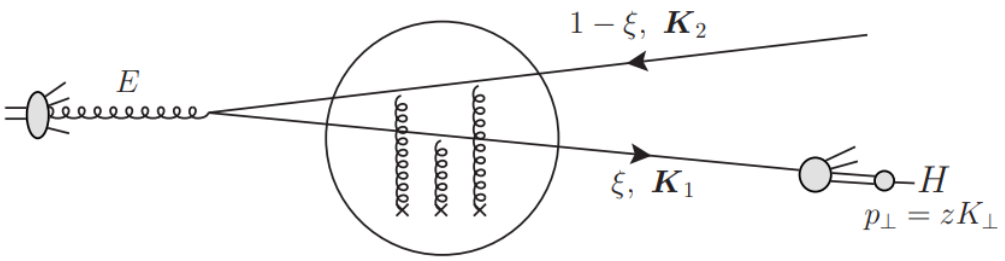

FIGURE 2.18: Contribution to the production of a heavy meson H in pA collisions from the LO process $gg \to Q\bar{Q}$, followed by quark fragmentation $Q \to H$ (represented here). [52].

parton with energy E is splitting on two quarks ($g \to Q\bar{Q}$) with energy fractions ξ and $1-\xi$ and transverse momenta K_1 and K_2, respectively. The fragmented heavy meson, H, inherits the transverse momentum fraction, $p_\perp = zK_\perp$, where z is the fragmentation variable. The average FCEL can be roughly estimated as

$$\Delta E_{FCEL} \propto \alpha_s \frac{l_{\perp A} - l_{\perp p}}{m_\perp} E, \tag{2.12}$$

where $l_{\perp A}(l_{\perp p})$ is the transverse momentum broadening, a parameter related to the average path length of the nucleus (proton), and $m_\perp$ is the quark transverse mass ($m_\perp^2 \equiv K_\perp^2 + m^2$). After studies on quarkonium and light hadron production, this confirms that hadron production in pA collisions cannot be described within the collinear factorisation approach using only nPDFs, calling for a change of paradigm.

2.4.3 Heavy-ion collisions results overview

A major discovery in heavy-ion physics was made by PHENIX at RHIC [53]. It revealed that hadrons with $p_T > 3$ GeV/c are suppressed in central Au+Au collisions by roughly a factor of 5 compared to point-like scaling from pp collisions. In order to verify that the suppression was due to the medium produced in Au+Au collisions and not an effect in the cold matter of an individual nucleus, measurements in d+Au collisions were performed in 2003. Fig. 2.19 shows the NNMFs for non-identified hadrons ($h^\pm$) and for π^0-mesons in d+Au and Au+Au collisions at $\sqrt{s} = 200$ GeV. Fig. 2.20 shows the collection of NMFs measurements in Au+Au data at RICH as a function of p_T. These results show an interesting pattern: most particles with $p_T > 2$ GeV/c are suppressed, but the protons are enhanced. This is called the baryon

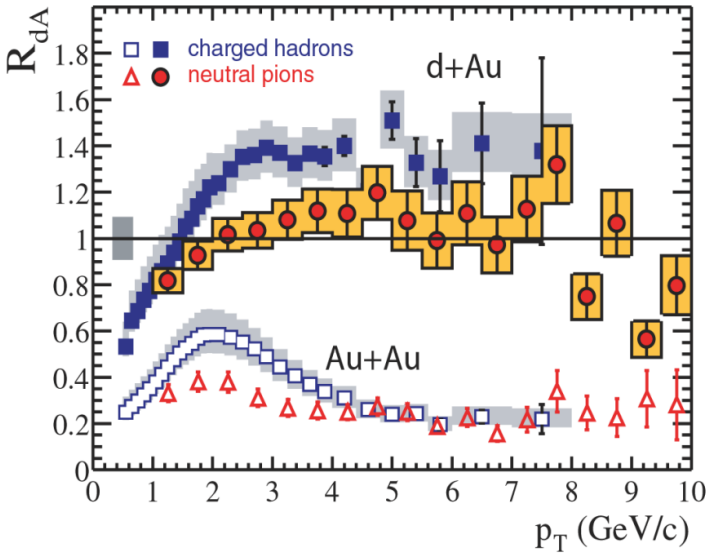

FIGURE 2.19: PHENIX measurements of NMFs for d+Au and Au+Au collisions at $\sqrt{s} = 200$ GeV [53].

anomaly [54]. The non-suppression of the direct-γ ($g + q \rightarrow \gamma + q$) shows that the suppression is an effect of the QGP medium, as photon does not interact with a colourful environment. On contrary, hadrons production is exposed to the loss of energy by their parent quark or gluon with open colour charge.

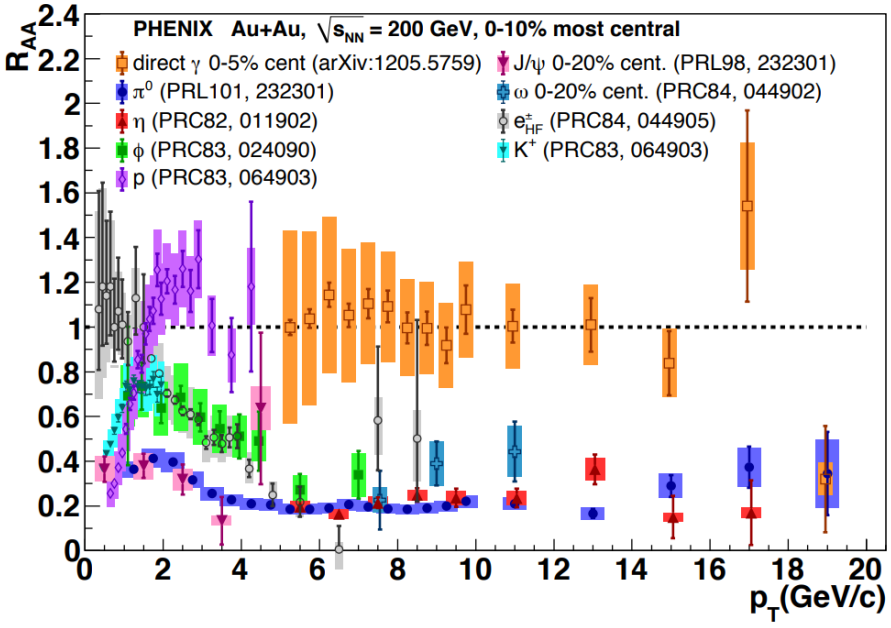

FIGURE 2.20: PHENIX measurements of R_{AA} as a function of p_{T} of many identified particles in central Au+Au collisions at $\sqrt{s} = 200$ GeV, with citations indicated Au+Au. [55]

Fig. 2.21 shows one of the recent results on the measurement of NMF of prompt charged particle production in pPb collisions at $\sqrt{s} = 5$ TeV from the LHCb experiment [56]. Here, different theoretical predictions are compared to data: the green

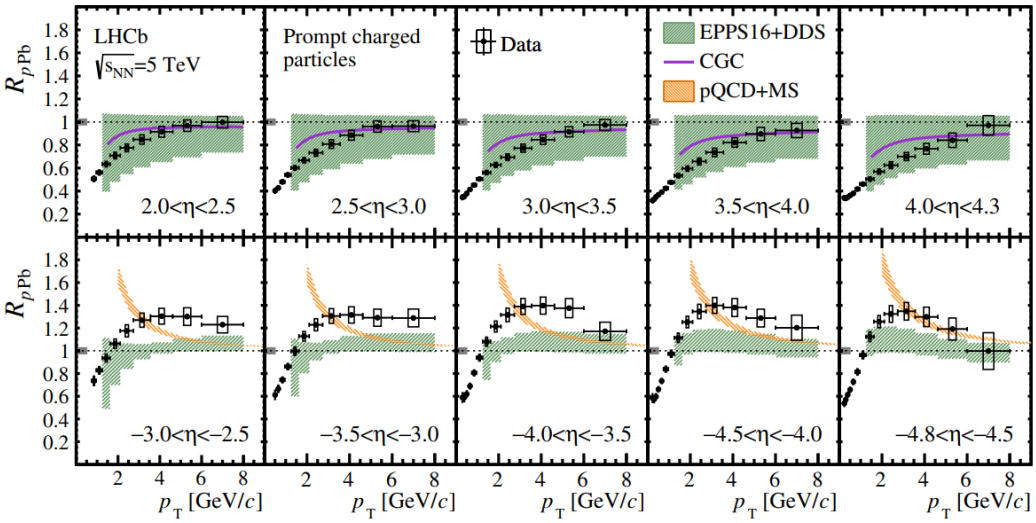

FIGURE 2.21: Nuclear modification factor as a function of p_{T} in different η intervals for the (top) forward and (bottom) backward regions, compared with the theoretical predictions [56].

area is the model based on the nPDF set EPPS16 for the lead nucleus and the PDF set CT14 [57] for the proton with the parton-to-hadron fragmentation functions set DSS [58], the purple line is the CGC effective field theory [59] and the orange area is a pQCD calculation within the high-twist factorisation formalism in the backward region [60].

Recent measurements of R_{FB} as a function of p_{T} by the LHCb experiment in pPb collisions are shown on Fig. 2.22 (a) for D_0 meson [61], (b) prompt J/ψ at $\sqrt{s} = 8.16$ and 5.02 TeV [62], (c) for Λ_c^+ baryon at $\sqrt{s} = 5.02$ TeV [63] and (d) for $\Upsilon(1S)$ at $\sqrt{s} = 8.16$ TeV [64]. The results are compared with different theoretical predictions, such as nPDFs calculations nCTEQ15, EPPS16, EPS09 at LO and NLO. The R_{FB} measurement of D_0 also includes FCEL model [65].

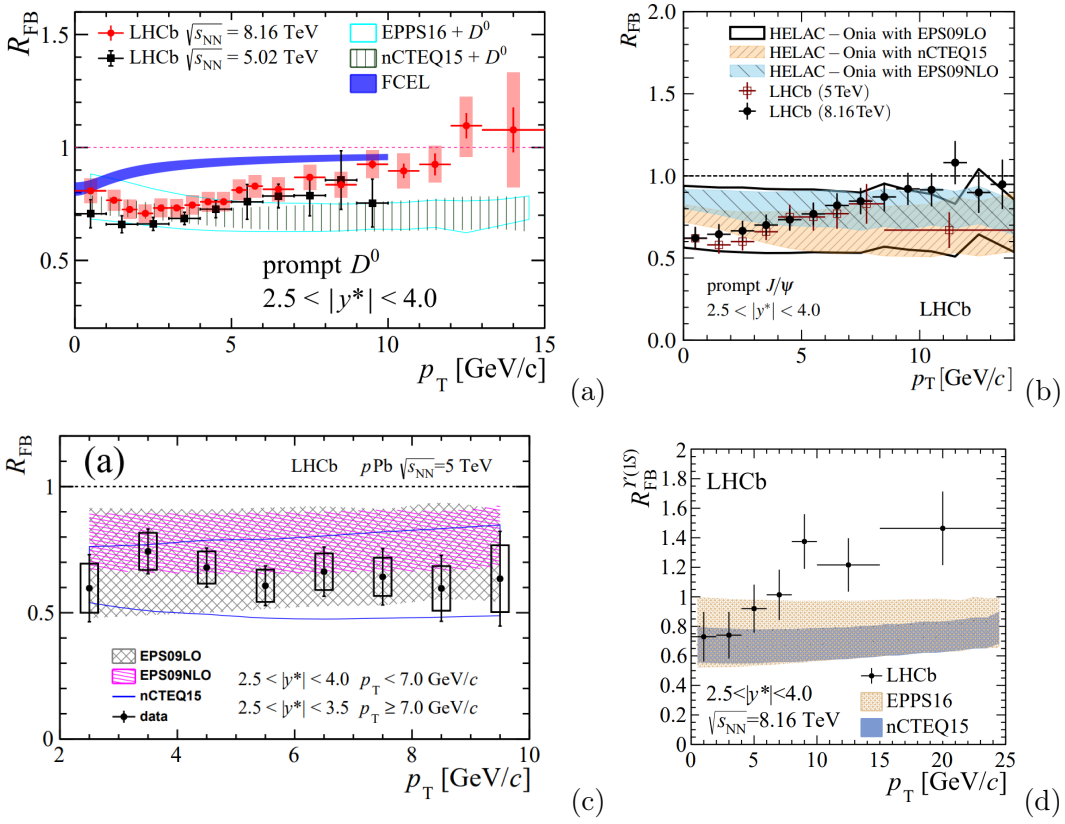

FIGURE 2.22: Measurements of R_{FB} as a function of p_{T} by LHCb experiment. (a) for D_0 meson [61], (b) prompt J/ψ at $\sqrt{s} = 8.16$ and 5.02 TeV [62], (c) for Λ_c^+ baryon at $\sqrt{s} = 5.02$ TeV [63] and (d) for $\Upsilon(1S)$ at $\sqrt{s} = 8.16$ TeV [64]. The results are compared with different theoretical predictions: nPDFs calculations nCTEQ15, EPPS16, EPS09 at LO and NLO and FCEL model.

2.5 The Ξ_c^+ and Λ_c^+ baryons

In the standard quark model, Ξ_c^+ is a *csu* quark combination. It has a short lifetime ($\tau_{\Xi_c^+} = 456.8 \pm 5.5$ fs [66]) and decays via the weak interaction. It was observed for the first time in 1983 by the WA62 collaboration at CERN [67]. The present value for the mass, taken from an average of six experiments, is $M_{\Xi_c^+} = 2467.9 \pm 0.4\,\mathrm{MeV}/c^2$ [68]. The preferred mode to study Ξ_c^+ production is a decay into a proton, a kaon and a pion, which is relatively easy to detect. The first measurement of the Ξ_c^+ production branching ratio (BR) was made in 2019 by the Belle collaboration via its decay into a proton, a kaon and a pion measuring the value of $\mathcal{B}(\Xi_c^+ \to p^+K^-\pi^+) = [0.45 \pm 0.21 \pm 0.07]\%$ [69]. Another measurement of the BR was made in LHCb in 2021, finding the value of $\mathcal{B}(\Xi_c^+ \to p^+K^-\pi^+) = [1.135 \pm 0.002 \pm 0.387]\%$ [70]. In this analysis we are using the branching fraction value taken from the PDG $B(\Xi_c^+ \to p^+K^-\pi^+) = [0.62 \pm 0.30]\%$ [68], which is a combination of the two measurements.

The charm baryon Λ_c^+ consists of *cdu* quarks. Its lifetime is shorter ($\tau_{\Lambda_c^+} = 203.5 \pm 2.2$ fs [66]) than that of the Ξ_c^+, and it also decays via the weak interaction. Since 1975 it was studied by many experiments [71, 72, 73] and as of today the Λ_c^+ measured mass value is $M_{\Lambda_c^+} = 2286.46 \pm 0.14\,\mathrm{MeV}/c^2$ and the BR is $\mathcal{B}(\Lambda_c^+ \to p^+K^-\pi^+) = 6.28 \pm 0.32\%$ [66].

Ξ_c^+ and Λ_c^+ belong to $SU(4)$ multiplets of baryons made from u, d, s and c quarks. The multiplet numerology is $4 \otimes 4 \otimes 4 = 20_S \bigoplus 20_M \bigoplus 20_M \bigoplus 4_A$ (where the subscripts are S=Symmetric, A=Antisymmetric and M=Mixed). Fig. 2.23 shows the 20-plet (symmetric) for $J^P = 3/2^+$ with an $SU(3)$ decuplet on the lowest level and the 20-plet (mixed) for $J^P = 1/2^+$ with an $SU(3)$ octet on the lowest level. All the baryons in a given multiplet have the same spin and parity. At present, 26 decay modes have been measured or seen for Ξ_c^+ and 86 for Λ_c^+ [66]. Fig. 2.24 shows the Feynman diagrams for Ξ_c (left) and Λ_c^+ (right) weak decays. Both baryons decay with W emission and their decay rates are proportional to elements in the Cabibbo–Kobayashi–Maskawa matrix (CKM matrix), which is defined as:

$$\begin{pmatrix} V_{ud} & V_{us} & V_{ub} \\ V_{cd} & V_{cs} & V_{ub} \\ V_{td} & V_{ts} & V_{tb} \end{pmatrix}.$$

The square of the magnitude of the matrix element $|V_{qq'}|^2$ is proportional to the probability for a transition from a quark q to a quark q', therefore is also proportional to the decay rate. Transitions between quarks from one family to another, such as V_{cd} in Ξ_c^+ decays, are called Cabibbo-suppressed decays, while transitions from one family to another, as V_{cs} in Λ_c^+ decays, are called Cabibbo-favoured decays.

2.5.1 Ratio Ξ_c^+ to Λ_c^+ (D^0)

The study of charmed flavoured baryons production is an important tool to test predictions obtained from pQCD calculations for pp collisions. As it was discussed in

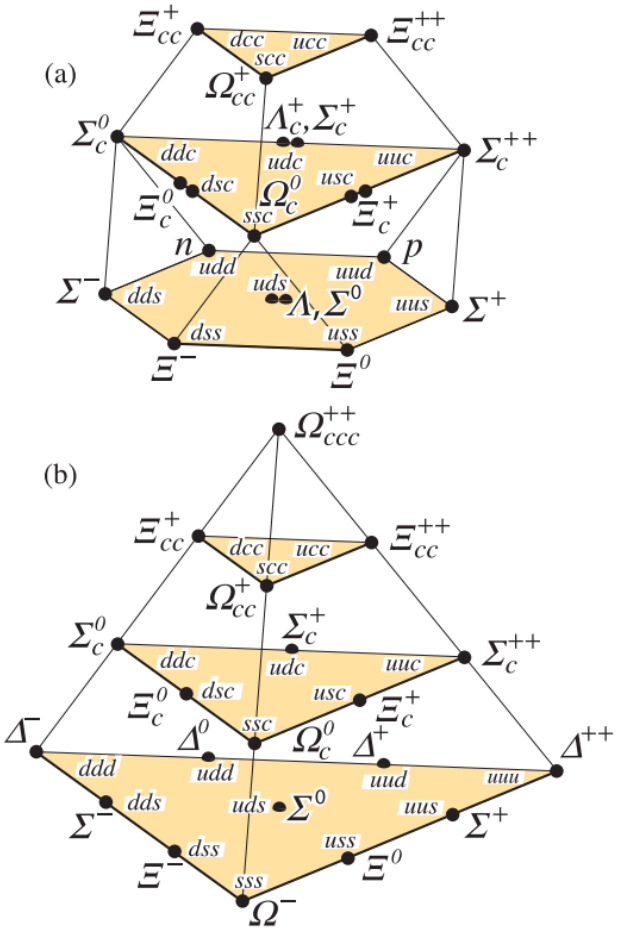

FIGURE 2.23: $SU(4)$ multiplets of baryons made from u, d, s and c quarks, with $J^P = 1/2^+$ (a) and $J^P = 3/2^+$ (b) [66].

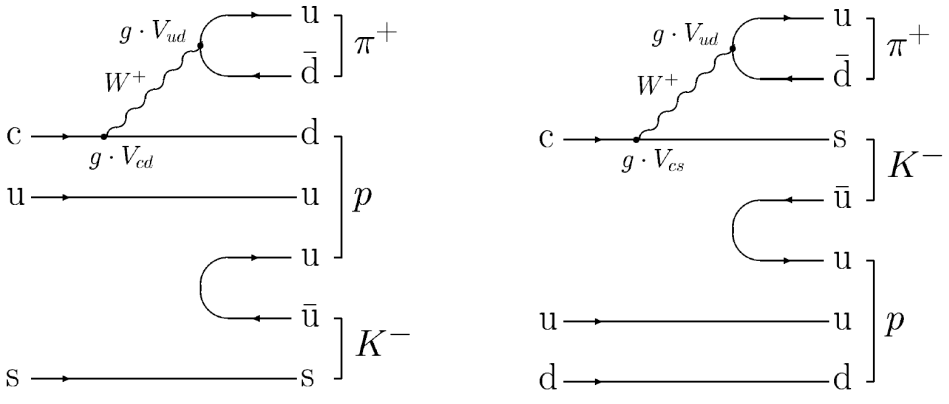

FIGURE 2.24: Ξ_c (left) and Λ_c^+ (right) decays to proton, kaon and pion.

Sec. 2.4.1, these calculations are based on the factorisation approach (eq. 2.6) that describes heavy-flavour production as a convolution of PDFs, the parton hard-scattering cross section and the fragmentation function (FF). However, no predictions are available for baryons due to lack of knowledge of the fragmentation function of charm

quarks into baryons. The hadronisation process is modeled via FF, which parametrises the fraction of the quark energy transferred to the produced hadron and accounts for the probability of a heavy quark to hadronise into a given species of heavy-flavour hadrons. A good way to determine FFs is to study the ratio productions in various collision systems and centre-of-mass energies, such as baryon-to-meson and baryon-to-baryon ratios. In such ratios we cancel out the PDFs and parton hard-scattering cross section contributions, focusing on charm hadronisation instead.

In Monte Carlo generators, FFs are tuned on electron–positron data under the assumption that they are universal. Similarly, the fragmentation fractions were assumed to be the same in different collision systems. However, the evidence of non-universality of FFs was reported by LHCb in a study of the Λ_b^0 baryon to B^- and $\bar{B}^0$ meson production ratio in pp collisions [74]. Fig. 2.25 shows the dependence of the ratio as a function of the transverse momentum, which was interpreted as evidence of non-universality of the FFs in the beauty sector. Measurements of the Λ_c^+/D^0 production ratio were reported by ALICE and CMS experiments at $\sqrt{s} = 5.02$ TeV and 13 TeV [75, 76, 77] in pp collisions, where Λ_c^+/D^0 ratio showed a clear decreasing trend with increasing p_{T}. Likewise, similar indications were obtained from the measurements of $\Xi_c^{0,+}$ baryon and $\Sigma_c^{0,+,++}$ baryon production in pp collisions [78]. Some of these results are shown in Fig. 2.26. Besides, the ratio is measured to be significantly larger than previous measurements at lower centre-of-mass energies in positron-electron (e^+e^-) [79] and electron-proton (e^-p) [80] collisions.

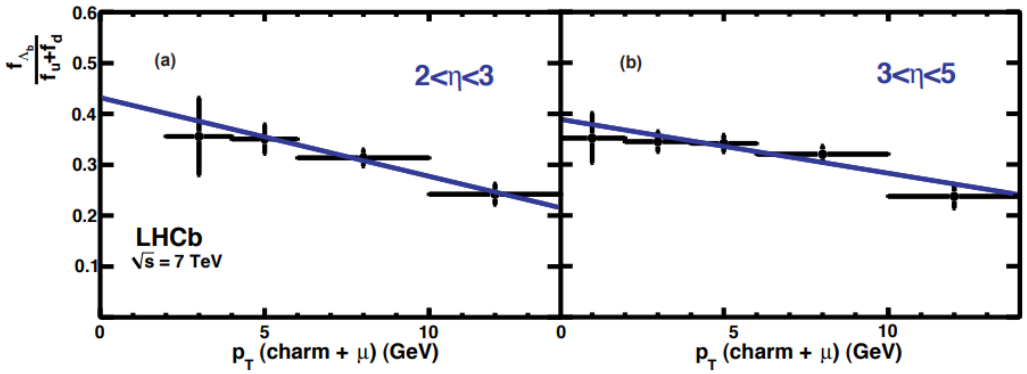

FIGURE 2.25: Fragmentation ratio $f_{\Lambda_b}/(f_u + f_d)$ dependence upon $p_{\mathrm{T}}(\Lambda_c^+\mu^-)$ [74].

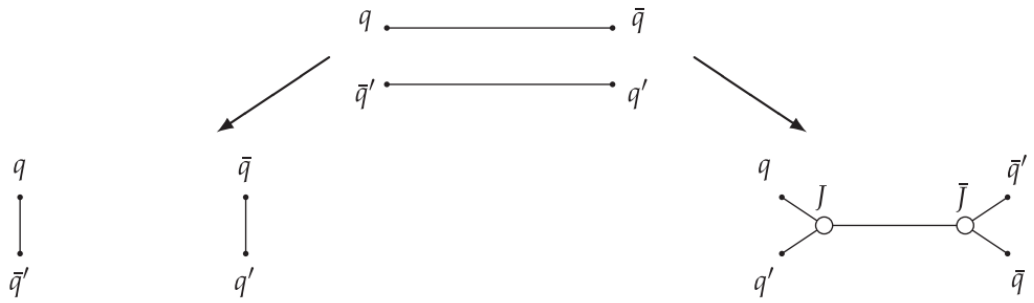

FIGURE 2.27: Sketch of how two $q\bar{q}$ dipoles (top) can be reconnected to different colour topologies (left and right). The right connection gives rise to a double junction, which in turn will produce baryons. [82]

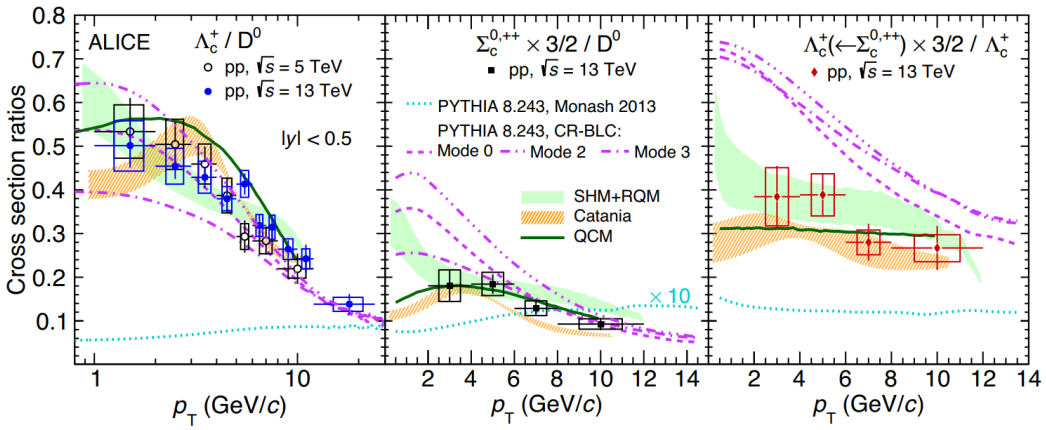

FIGURE 2.26: Prompt-charm-hadron cross-section ratios:Λ_c^+/D^0 (left), $\Sigma_c^{0,+,++}/D^0$ (middle) and $\Lambda_c^+ \leftarrow \Sigma_c^{0,+,++}/\Lambda_c^+$ (right) [78].

In ultra-relativistic hadron-nucleus collisions, multi-parton interactions and coherence effects between multiple partonic interactions may affect the hadronisation processes. These are some effects that might affect hadronisation in nucleus-nucleus collisions, listed below;

- Colour reconnection (CR). It is a mechanism that describes the interaction between colour fields [81]. The final partons are connected by string-like colour fields in a way as to reduce the total strings length to the minimum. One string that connects two partons follows their endpoint movements, resulting in a common boost of string fragmentation. Baryons can, in addition, be created around string junctions, which can arise as a consequence of colour reconnection (Fig. 2.27). In Fig. 2.28 integrated yields, $\mathrm{d}N/\mathrm{d}y$, of various hadrons, $K^0_S, K^{*0}, \phi, \Lambda, \Xi$, and Ω, as functions of $\langle \mathrm{d}N_{ch}/\mathrm{d}\eta \rangle_{|\eta|<0.5}$ with CR theory are shown.

- Coalescence (recombination). Initially, coalescence was proposed as a hadronisation mechanism in high energy heavy-ion collisions [84], where, in densely populated systems, quarks can directly recombine into hadrons. The momentum

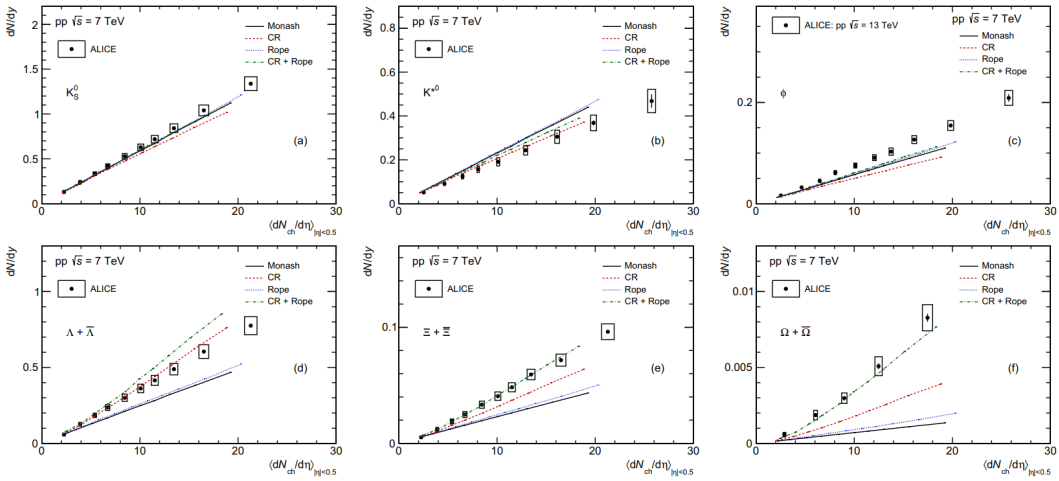

FIGURE 2.28: Integrated yields $\mathrm{d}N/\mathrm{d}y$ of various hadrons, $K^0_S, K^{*0}, \phi, \Lambda, \Xi$, and Ω, as functions of $\langle \mathrm{d}N_{ch}/\mathrm{d}\eta \rangle_{|\eta|<0.5}$. The meson yields are shown in the top plots, and the baryon yields are shown in the bottom plots [83].

spectrum of hadrons formed by coalescence of quarks can be written as

$$\begin{aligned}\frac{\mathrm{d}^2 N_H}{\mathrm{d}y \mathrm{d}p_\mathrm{T}} =& g_H \int \prod_{i=1}^{N_q} \frac{\mathrm{d}^3 p_i}{(2\pi)^3 E_i} p_i \times \mathrm{d}\sigma_i f_{q_i}(x_i, p_i) \\ & \times f_H(x_1 ... x_{N_q}, p_1 ... p_{N_q}) \delta^{(2)} \left(p_\mathrm{T} - \sum_{i=1}^{N_q} p_{T,i} \right),\end{aligned} \tag{2.13}$$

where f_H is the statistical factor to form a colourless hadron, f_{q_i} is the phase-space distribution function i-th quark (anti-quark), f_H is the Wigner function, which describes the spatial and momentum distribution of quarks in a hadron, and N_q is the number of quarks in the formed hadron ($N_q = 3$ for baryons). The Wigner distribution function can be adapted into Gaussian shape in space and momentum:

$$f_H(x_1, x_2; p_1, p_2) = A_W \exp\left(- \frac{x_{r1}^2}{\sigma_r^2} - p_{r1}^2 \sigma_r^2 \right). \tag{2.14}$$

Here, the 4-vectors for the relative coordinates in space and momentum, x_{r1} and p_{r1} are related to the quark coordinate by the Jacobian transformations

$$x_{r1} = x_1 - x_2; \quad p_{r1} = \frac{m_2 p_1 - m_1 p_2}{m_1 + m_2}, \tag{2.15}$$

A_W is a normalisation constant fixed to guarantee that in the limit $p \to 0$ we have all the quarks hadronising $\lim_{p\to 0} P_{coal}^{tot} = 1$. The σ_r are the covariant widths, which can be related to the oscillator frequency ω by $\sigma_r = 1/\sqrt{\mu\omega}$, where μ are the reduced masses of hadrons. The multi-dimensional integrals in the coalescence formula are evaluated by using a Monte-Carlo method [85]. Fig. 2.29

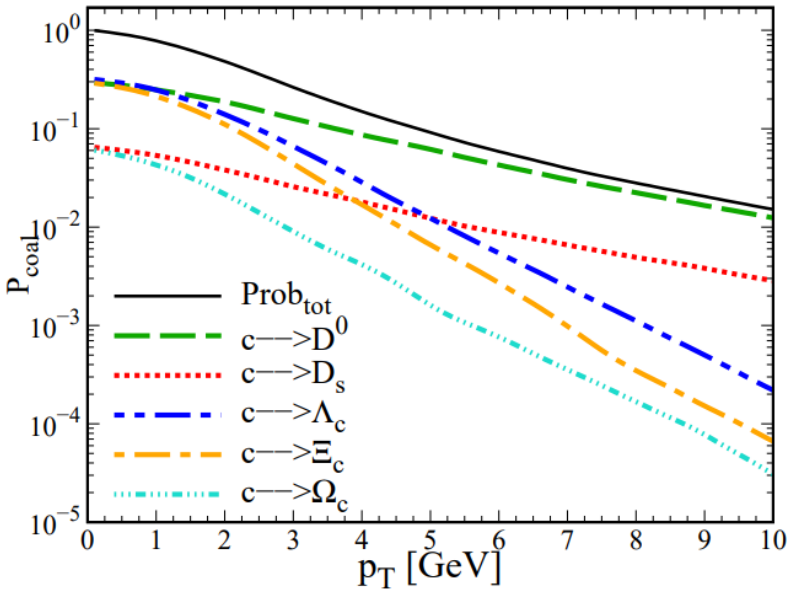

FIGURE 2.29: The charm quark coalescence probability P_{coal} as a function of the charm quark p_T for pp collisions at LHC. The different lines are the coalescence probabilities to produce the different hadron species. Black solid line is the total coalescence probability [84].

shows the coalescence probabilities, P_{coal}, for charm quarks to hadronise via coalescence into a specific hadron. Hadronisation via fragmentation assumes that the part of the momentum of a hadronising quark that is needed to create quarks from a vacuum is $p_h = zp_q$, where z is the fraction of momentum for hadronisation, while in coalescence the momenta of combining quarks will end up in a resulting hadron. As so, coalescence should be dominant at low p_T. In Fig. 2.30 the theoretical calculations of Λ_c^+/D^0 and D_s^+/D^0 ratios in comparison with the LHC experimental data for pp collisions at $\sqrt{s} = 5.02$ TeV are shown. The hybrid approach of coalescence plus fragmentation (solid lines) gives a quite good description of the experimental data from ALICE. The dashed lines show the ratios that come only from fragmentation. the LHCb data for $2.0 < y < 4.5$ rapidity region shows good agreement with the theory, where fragmentation contribution is dominant, as expected.

- Strangeness enhancement. It was originally proposed as a signature of QGP formation in heavy-ions collisions. Although it is assumed that there is no QGP in pPb collisions, theories predict the formation of "QGP droplets" [3] which could partially behave the same as media in PbPb collisions. The effects, typical of heavy-ion phenomenology, have been observed in high-multiplicity pp collisions [86].

The study of Ξ_c^+ production and its ratio to the production of other hadrons as Λ_c^+ and D^0, which are the subject of this thesis, have the potential to disentangle these different effects.

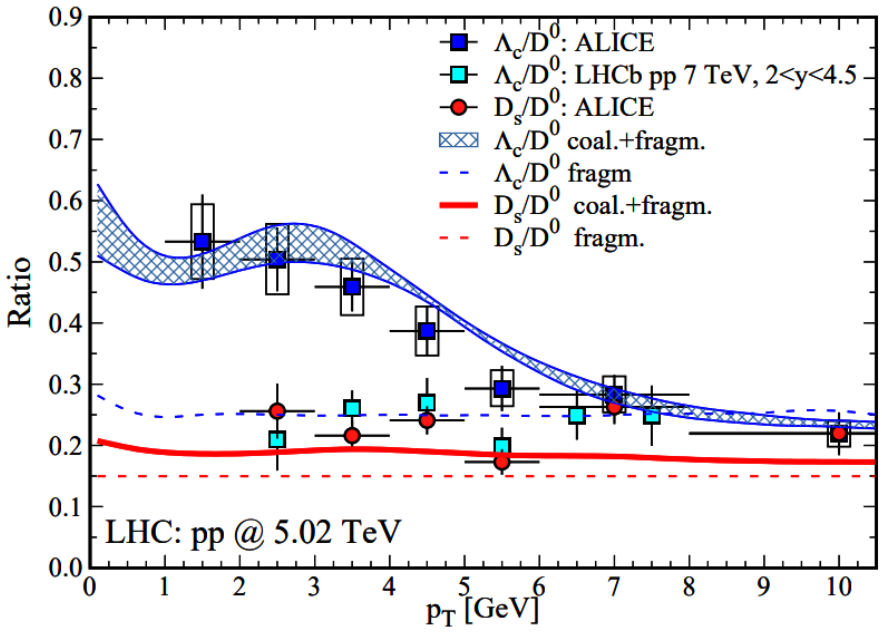

FIGURE 2.30: The theoretical results for the Λ_c^+/D^0 and D_s^+/D^0 ratios in comparison with the LHC experimental data for pp collisions at $\sqrt{s} = 5.02\,\text{TeV}$ [84].

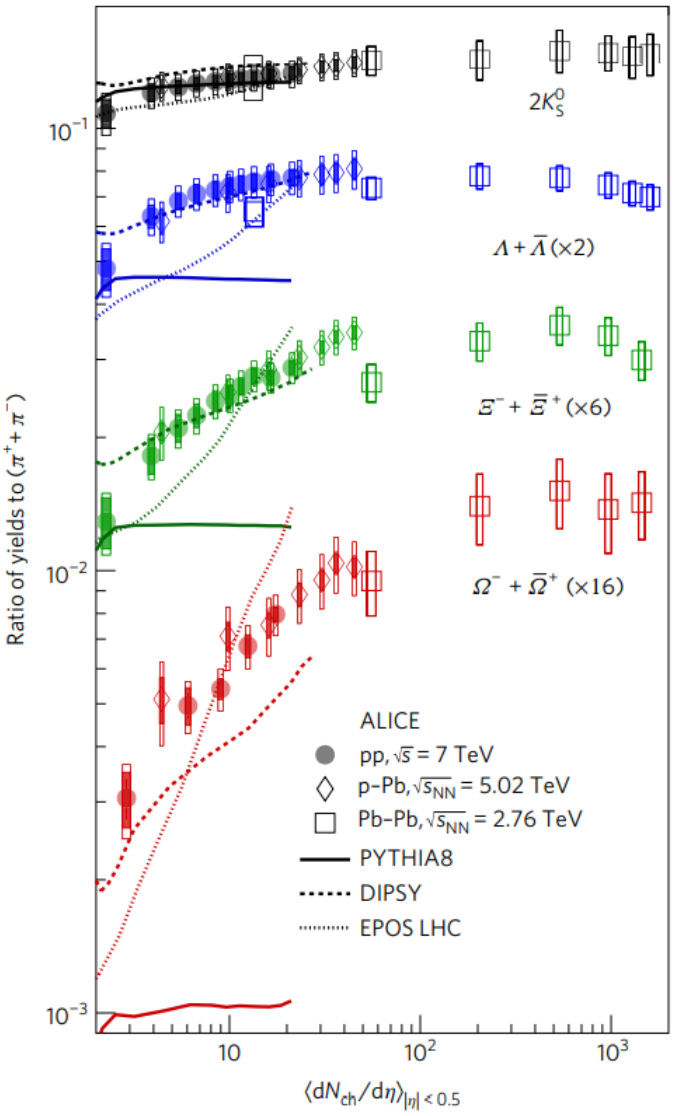

FIGURE 2.31: p_T-integrated yield ratios to pions ($\pi^+ + \pi^-$) as a function of multiplicity ($\langle N_{ch}/d\eta \rangle$) measured in $|y|<0.5$ [86].

Chapter 3

The LHCb experiment

The Large Hadron Collider beauty (LHCb) is one of the main four experiments installed at the Large Hadron Collider (LHC) at the European Organization for Nuclear Research (CERN) in Geneva, Switzerland, along with ALICE, ATLAS and CMS. Its primary scientific goal is to look for indirect evidence of New Physics in Charge-Parity (CP) violation and rare decays of beauty and charm hadrons. It has excellent performances in terms of vertex and momentum resolution, which are key to test SM predictions with very high precision. The LHCb collaboration has also an ambitious heavy-ion physics program with proton-lead and lead-lead collisions, which was expanded in 2015 by creating a new Fixed Target program through the SMOG system [87].

In the following text, we will describe the LHC accelerator complex and the LHCb detector, with particular attention to its performance in heavy-ion collisions.

3.1 The Large Hadron Collider

LHC is a two ring-shaped particle collider (Fig. 3.1) constructed at CERN in the late 90s to replace the Large Electron-Positron Collider (LEP). It started operation in 2009. To date, it is the most powerful collider in the world. The accelerator is located in a circular tunnel of approximately 27 km of circumference at a depth that goes between 80 and 175 meters underground on the French-Swiss border.

Particles are focused in two beams controlled by 1232 dipole and 392 quadrupole magnets. The dipole magnets are kept at a temperature of 1.7 K using a cryogenic system of superfluid helium; the large magnetic field obtained is used to bend the beams on their circular path. Inside the tunnel, which contains two adjacent parallel beamlines, the two beams travel in opposite directions. The quadrupole magnets keep the beams focused. The beams are bent to cross at four points where the main detectors are located.

The four main LHC experiments have all a different design for specific purposes. ATLAS and CMS were designed mainly to search and to study the properties of the Higgs boson and to search for New Physics. The ALICE experiment focuses on the physics of strongly interacting matter at extreme energy densities, testing the

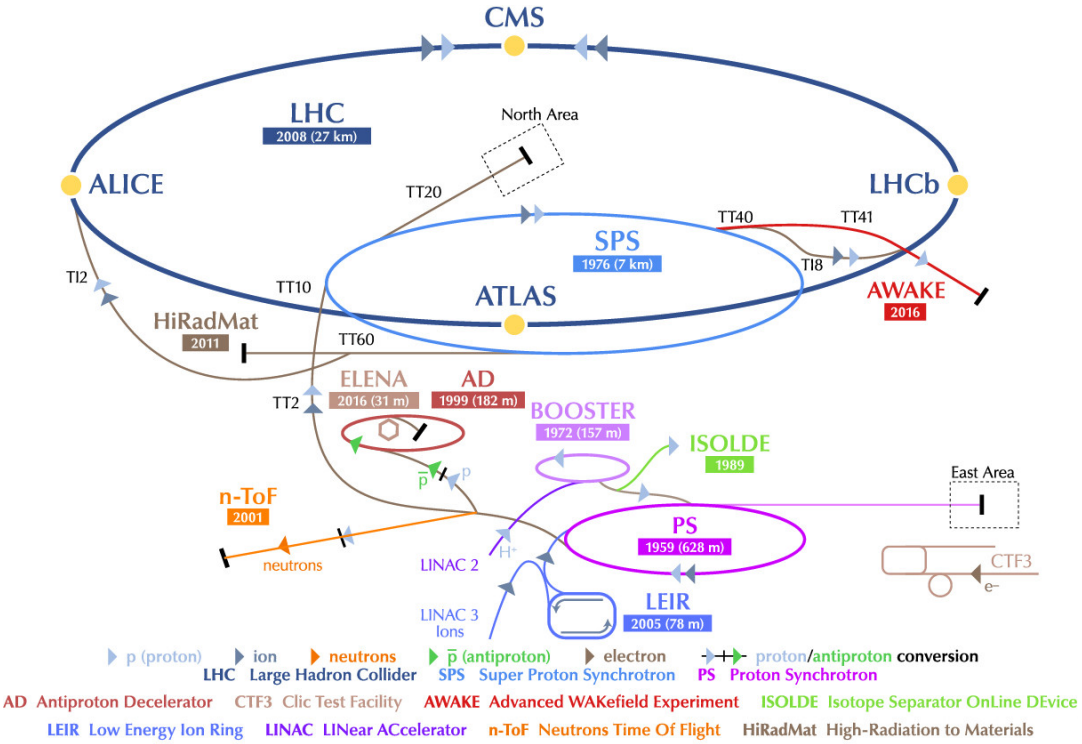

FIGURE 3.1: The scheme of the CERN accelerator complex [88].

existence and properties of the QGP. LHCb is mainly dedicated to the study of CP violation and rare decays in the bottom and charm sectors.

The main LHC operation mode is to collide protons head-on, but for 3 weeks a year the LHC operates in "Heavy Ion mode" by injecting lead beams in the machine. The beams are divided in bunches of protons or lead nuclei [89], each separated by 25, 50 or 75 ns. The number of a certain type of events produced per second at LHC is estimated as

$$N_{event} = \sigma_{event} \times \mathcal{L}_i, \tag{3.1}$$

where σ_{event} is the cross-section of the studied event and $\mathcal{L}_i$ is the instantaneous luminosity, which represents the number of colliding projectiles per surface unit. The instantaneous luminosity can be computed using the following equation

$$\mathcal{L}_i = f_{coll} \frac{n_1 n_2}{4\pi\sigma_x\sigma_y}\ , \tag{3.2}$$

with f_{coll} being the collision frequency, n_1 and n_2 are the number of projectiles in bunch 1 and 2, σ_x and σ_y represent the beam size in transverse directions (assuming Gaussian distribution of particles in the beam). The designed instantaneous luminosity of LHC is 10^{34} cm^{-2}s^{-1}. The high occupancy in LHCb makes the track reconstruction difficult. Therefore, LHCb runs at a reduced luminosity of typically 2×10^{32} cm^{-2}s^{-1} for pp and around 10^{27} cm^{-2}s^{-1} for pPb and PbPb collisions. The integrated luminosities collected by LHCb in pPb and PbPb collisions are shown in Fig. 3.2. During the Run 1, in 2013, LHCb collected around 1.5 nb^{-1} at $\sqrt{s_{\rm NN}}$ =

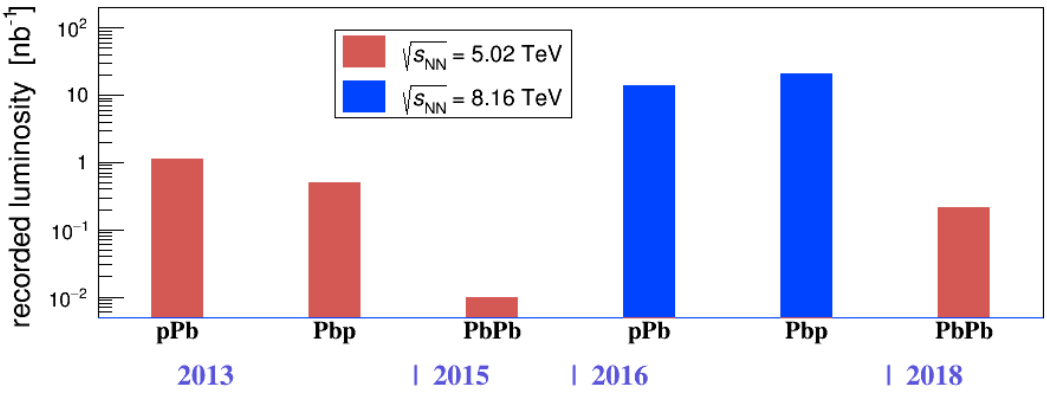

FIGURE 3.2: Integrated luminosities of pPb and PbPb collisions collected by LHCb during the Run 1 and Run 2.

5.02 TeV of pPb collisions. During Run 2 total of 30 nb^{-1} of pPb collision data was recorded at $\sqrt{s_{\text{NN}}} = 8.16$ TeV in 2016 and almost 230 μb^{-1} of PbPb collision data at $\sqrt{s_{\text{NN}}} = 5.02$ in 2015 and 2018.

As can be seen in Fig. 3.3, ATLAS and CMS are general purpose detectors with broad physics programmes, both covering large rapidity region. ALICE detector is dedicated to heavy-ion physics in central rapidity region. Contrary to the other three experiments, LHCb is instrumented in the full rapidity coverage $2.0 - 4.5$, meaning all subdetectors are fully covering this rapidity range allowing a large variety of precise physics studies.

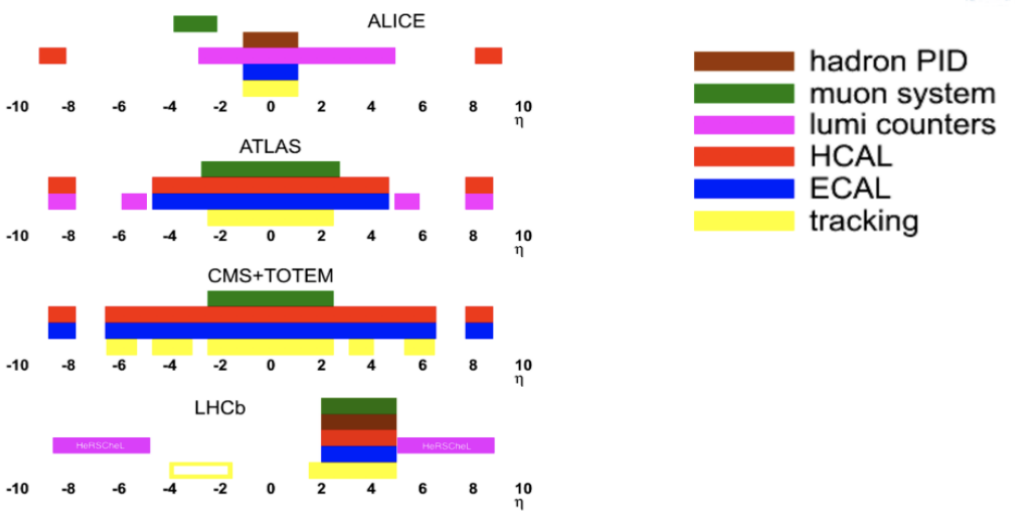

FIGURE 3.3: Acceptance as a function of the pseudorapidity of the four main experiments at the LHC.

The LHCb detector is described in the next section.

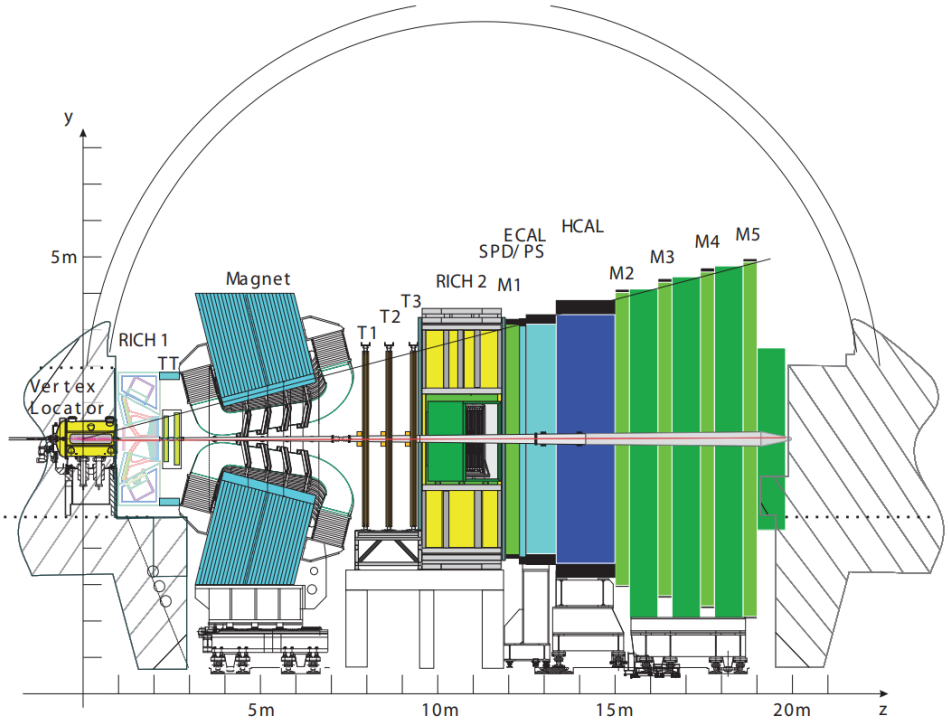

FIGURE 3.4: The LHCb detector: side view [91].

3.2 LHCb detector

The LHCb[1] is a single-arm forward detector, designed to detect particles that contain beauty and charm quarks. This design is based around the fact that the $b\bar{b}$ and $c\bar{c}$ cross-sections are higher in the large rapidity region, thus maximizing the size of the data sample. The LHCb angular acceptance covers 10 to 300 mrad horizontally and 10 to 250 mrad vertically, which, according to the Pythia simulation [90], allows to detect 27% of b and c hadrons. The acceptance equivalence in pseudorapidity is $2 < \eta < 5$, where the pseudorapidity is defined as $\eta = -\ln(tan(\theta/2))$, θ being the angle between the particle and the trajectory of the colliding protons, as shown in Fig. 3.5. The LHCb collaboration performed numerous precision tests of the SM in heavy-flavour physics and continues to study mainly the asymmetry between matter and anti-matter, CP violation, amplitude and angular properties of beauty and charm decays and searches for possible New Physics [91].

The vertical section of the LHCb detector is represented in Fig. 3.4. The z axis is placed along the beam direction with the origin set at the collision vertex and pointing towards the opposite side of the detector. The y axis is vertical and points upward. The coordinate system of the LHCb detector is shown on Fig. 3.5. The various sub-detectors are shown in Fig. 3.4. They are stacked one after the other along the z axis, progressively away from the interaction point (IP).

[1]The LHCb detector has undergone a major upgrade in 2019-2021 has started data taking in 2022 with a brand new detector

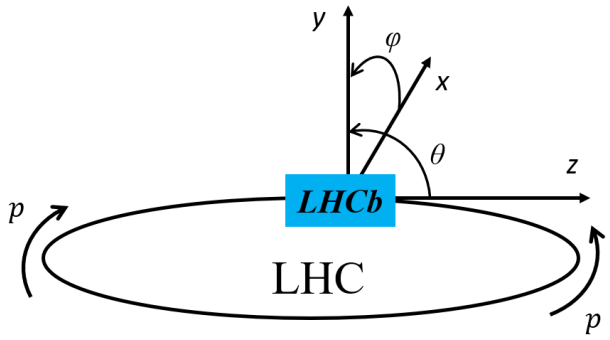

FIGURE 3.5: Coordinate system used in the LHCb detector.

The trajectories of the charged particles are first detected by the VErtex LOcator (VELO) that surrounds the interaction point and provides precise information on the origin of the particles. The produced particles go through the first RInging CHerenkov detector (RICH1), which provides particle identification and enables separation of pions and kaons, and the first pair of tracking stations, called Tracking Turicensis (TT). Their trajectories are then bent by the dipole magnet, that provides a 4 T integrated magnetic field, pass through the second RInging CHerenkov detector (RICH2) and their momenta and charge are measured by the T1, T2 and T3 tracking stations. Then, the electromagnetic and hadronic calorimeters, ECAL and HCAL, respectively, follow, used to measure the energies of the neutral and charged particles as the electrons. Finally, the muons are identified by the dedicated muon stations (M1-M5). In the following, a brief description of the different subdetectors will be given.

3.2.1 Dipole magnet

A powerful magnet is located between the upstream and downstream tracking stations, which allows to deflect the trajectories of charged particles in order to determine their charge and momentum. The LHCb magnet is a warm dipole magnet. Its opening angle with respect to the interaction point is ±250 mrad vertically and ±300 mrad horizontally. The dipole magnet generates a magnetic field oriented along the y-axis in the LHCb detector reference system, and the orientation of the field can be inverted to account for systematic effects. The coils of the magnet are made of superconducting aluminium cables with a total weight of 54 tons and placed 45 degrees with respect to the z-axis symmetrically in a pheasant-shaped magnet yoke. The trapezoidal coils are fed with a nominal current of 5.85 kA and have a total resistance of 130 mΩ. As mentioned previously, the integrated value of the magnetic field is 3.6 T with a maximum of the field at 1.1 T. The technical drawing of the LHCb magnet and the magnet field profile along the z-axis are shown in Fig 3.6.

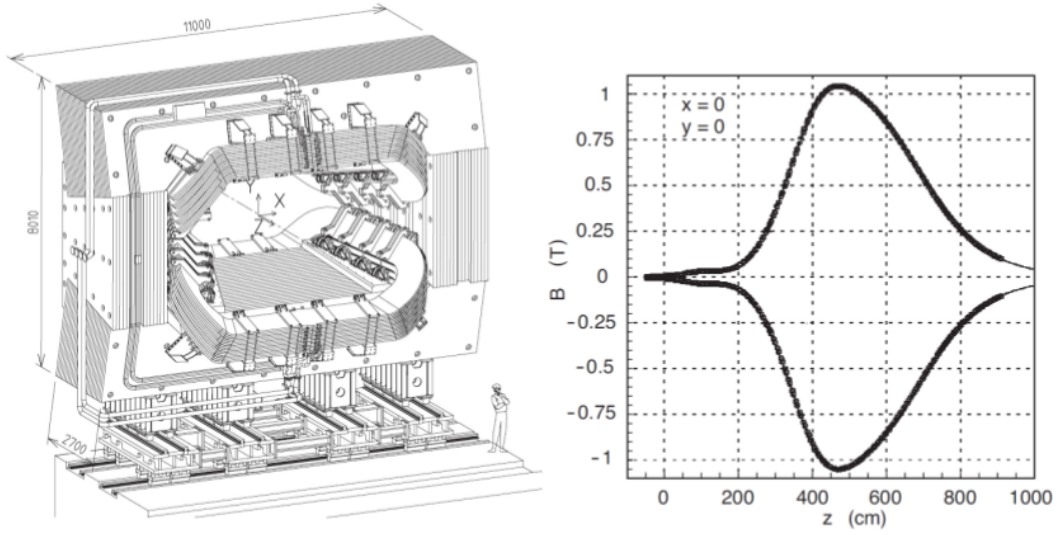

FIGURE 3.6: Illustration of the LHCb magnet (left) and the magnetic field profile versus the z-axis (right).

3.2.2 Tracking system

The tracking system is one of the most important detector system as its high precision is crucial for the studies performed by the LHCb collaboration. The LHCb reconstruction software takes into account information from a VELO detector and four tracking stations (TT, T1-T3) and the map of the magnetic field to determine the charged particle tracks and their momentum. This task is performed by an algorithm which pairs hits in different tracking detectors to reconstruct the track. Each element of the tracking system will be briefly described in the following.

3.2.2.1 VELO

The VErtex LOcator (VELO) is a silicon microstrip detector surrounding the beam pipe region where the collisions occur. The active area of the detector can be seen as a cylinder, with two rows of half-moon shaped silicon sensors, each formed by 42 modules. Each module composed of 2,048 silicon sensors 0.3 mm thick, perpendicular to the beam pipe. One set of sensors is composed of circular strips (ϕ sensors) and the other composed of radial strips (R sensors), so that the combination provides the polar coordinates of the point where the particle hits the station. The inner radius of the active area is 8 mm and the outer 42 mm. Thus, the detector is placed very close to the collision point. During the ramp-up period, before the beams circulating in the LHC stabilise, the two independent parts of the VELO are moved away from the beam to reduce damage from radiations. The VELO can be in two position modes; "OPEN" with the two halves separated by a distance of 6 cm, "CLOSED" with the two halves separated by only 7 mm which is the position used in data taking. These two configurations are represented in Fig 3.7. The proximity of the VELO to the interaction point ensures an spatial resolution of about 4 μm.

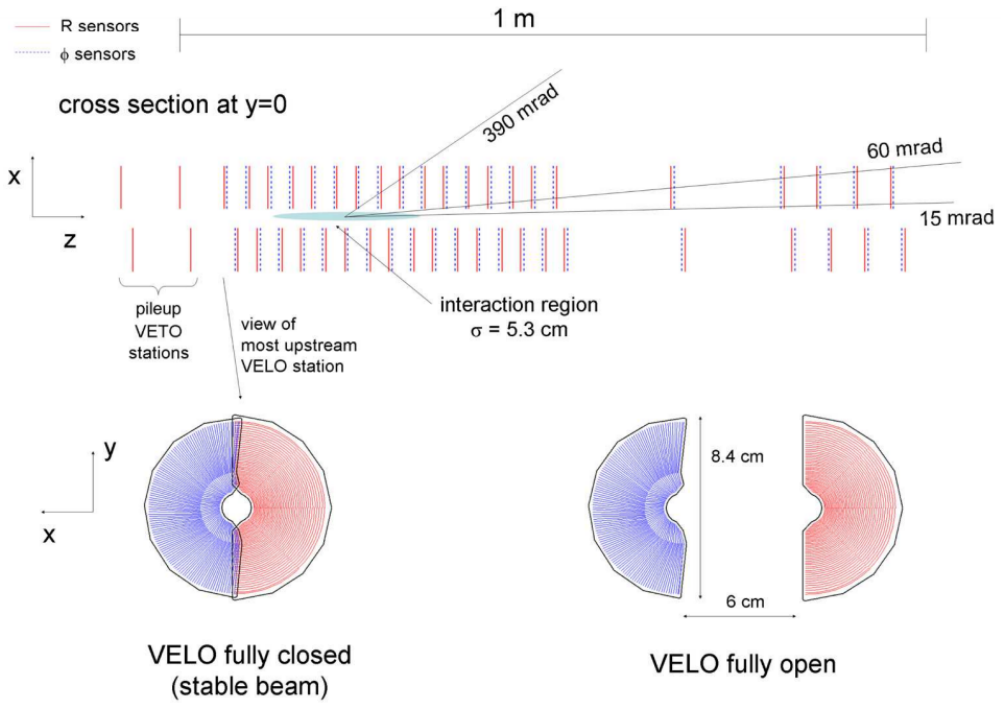

FIGURE 3.7: Scheme of the cross section in the (x, z) plane of the VELO (top) and an illustration of the two configurations of the VELO (bottom). The R sensors are represented in red and the ϕ sensors are represented in blue.

The VELO allows a precise distinction between two different types of vertices:

- The primary vertex (PV), where the initial collision takes place;
- The secondary vertex (SV), where hadrons containing b or c quarks (long lived) decay.

The vertices are determined from the coordinates of the hits in the detector, along with first tracks reconstruction. The VELO allows the determination of flight distances, lifetimes and impact parameters. Apart from being used to find PVs and SVs, tracks reconstructed in the VELO are used as seeds for the rest of the tracking system in track reconstruction. The system is also used to measure the backward charged track multiplicity and to detect multiple interaction events. While VELO's characteristics make it an excellent detector for pp physics, its performance is limited in heavy-ion collisions.

3.2.2.2 Tracking Turicensis

The Tracking Turicensis (TT) tracker is placed between the RICH1 and the magnet at 232 cm from the interaction point in the z direction. The layout of the TT layers is illustrated in Fig 3.8. It is composed of two stations TTa and TTb, each made of two silicon microstrips layers. The layers cover a rectangular surface 150 cm $\times$ 120 cm. The two central layers (named u and v) are tilted by $+5°$ and $-5°$ and the external

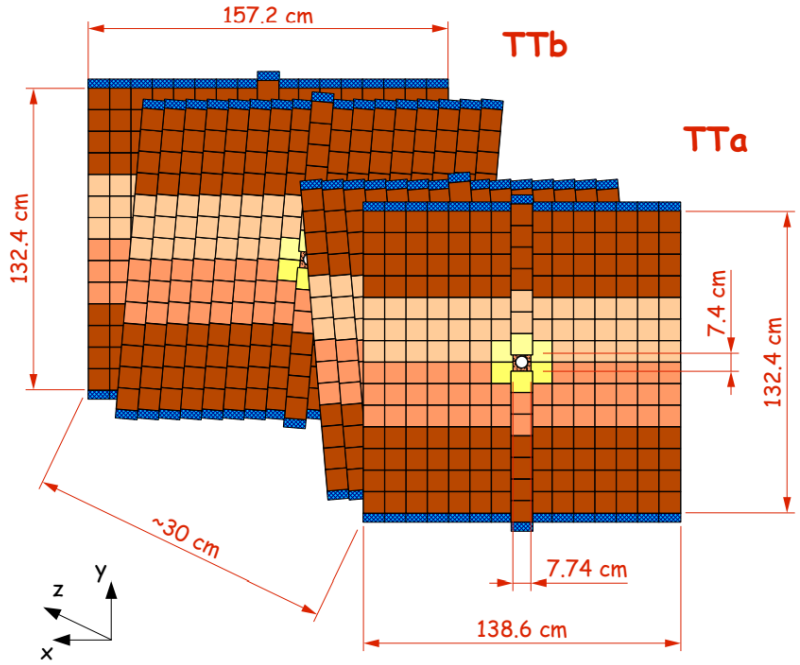

FIGURE 3.8: Layout of the four TT layers.

layers are named x. The particular configuration called $x-u-v-x$ allows a 3D reconstruction of the tracks.

The goal of the TT tracker is to reconstruct tracks produced by low-momentum particles and link them to the VELO tracks. The magnetic field in the TT allows quick measurement of particle momentum for trigger decisions.

3.2.2.3 T1-T3 stations

The T1-T3 stations (see Fig. 3.9) are placed between the magnet and the RICH2, at a distance of around 8 m from the interaction point. Their purpose is to detect the charged particles with momentum greater than 5 GeV/c. They consist of an Inner Tracker (IT) and a Outer Tracker (OT).

The IT is placed closer to the beam pipe in y. It consists of three stations consisting of four individual detector boxes 120 cm in width and 40 cm in height arranged around the beam pipe. Each box is composed of four silicon sensors layers placed in a $x-u-v-y$ configuration. The silicon sensors of the IT have a high granularity as the occupancy around the beam pipe is larger. The spatial resolution is about 50 μm, precise enough to handle the high occupancy around the beam pipe.

The OT covers the largest fraction of sensitive area in T1-T3 stations. It is made up of straw-tube drift chambers, which are arranged in a array of straw-tube modules with two staggered layers of drift-tubes with inner diameters of 4.9 mm. As the region covered by the OT has lower occupancy than around the beam pipe, the technology

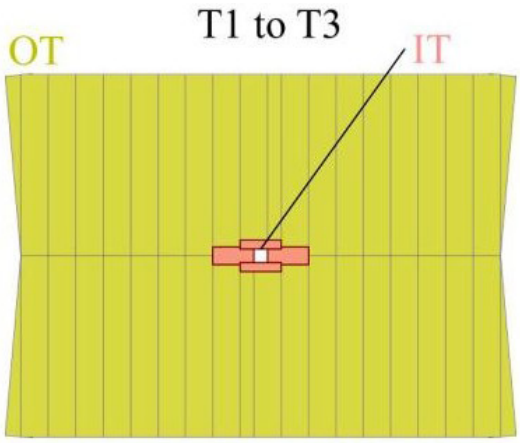

FIGURE 3.9: Layout of a T station in the x-y plane.

used has lower granularity than the IT. The drift time across the tube is less than 50 ns and the spatial resolution is about 200 μm.

3.2.3 Particle identification system

The particle identification (PID) system allows to identify the particle species of the reconstructed tracks. The light hadrons can be identified using the two Ring Imaging Cherenkov (RICH) detectors, the electrons and photons are identified using hadronic calorimeter (HCAL) and electromagnetic calorimeter (ECAL), and the muons are identified using the muon stations (M1-M5). In the following, the three PID systems are briefly discussed.

3.2.3.1 The ring imaging cherenkov detectors

The RICH detectors uses the Cherenkov effect to identify the different charged hadrons (protons, kaons and pions). The LHCb RICH system consists of two different detectors: RICH1, located between the VELO and TT, and RICH2, between T3 and the first muon station. The layout of the two detectors is presented in Fig. 3.10. A particle passing faster than the light in a medium produces a cone of Cherenkov light with an opening angle θ_{Ch} that can be expressed in term of the refractive index of the medium n and the velocity of the particle v by the following equation

$$cos(\theta_{Ch}) = \frac{1}{nv/c} \ . \tag{3.3}$$

The tracking system provides the measured momentum of the particle, it is therefore possible to estimate the mass, m, of the particle of momentum, p, as

$$cos(\theta_{Ch}) = \frac{1}{n}\sqrt{\left(\frac{m}{p}\right)^2 + 1}. \tag{3.4}$$

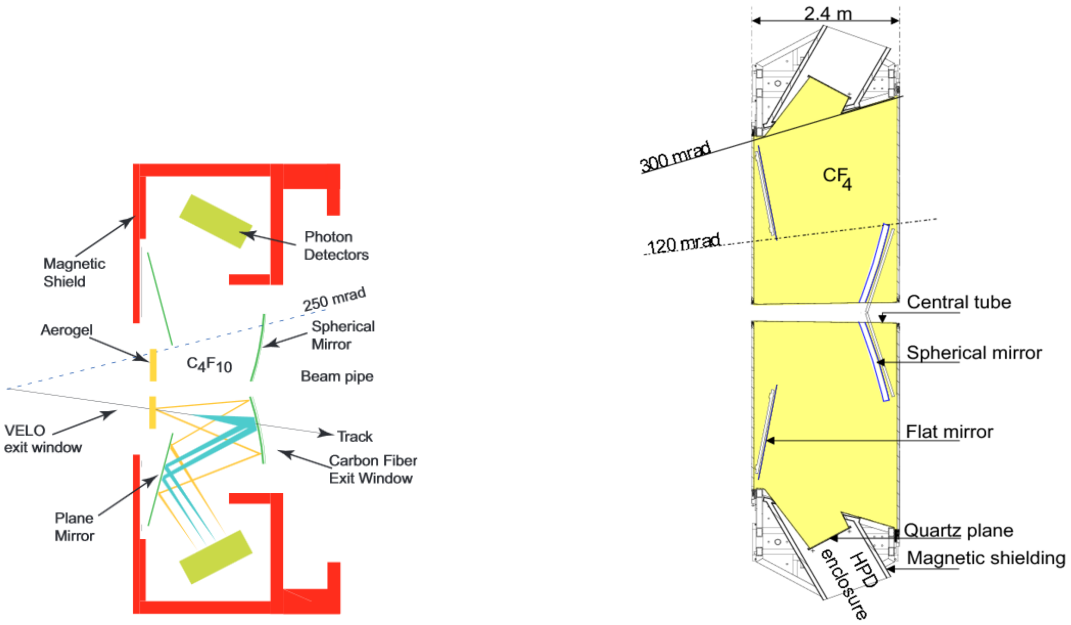

FIGURE 3.10: Layout of the RICH1 (left) and RICH2 (right).

The different hadrons can be separated as shown in Fig. 3.11. The probability to correctly identify charged hadron is consistently above 90% for a 5% misidentification probability.

The Cherenkov photons, emitted by the medium traversing the RICH radiators, are focused into ring images on the photon detector planes, situated outside the spectrometer acceptance. Due to the correlation between the polar angle of the particle and its momentum, two RICH detectors are used to cover two ranges of momentum. The RICH1 covers a range of momentum between 1 and 60 GeV/c and an angular acceptance of 25-300 mrad and 25-250 mrad in the x and y direction, respectively. The RICH2, which is filled with CF_4 (n=1.0005), covers larger momenta, from 10 to 100 GeV/c, and has an angular coverage of 120 mrad in the vertical plane and about 100 mrad in the horizontal plane.

3.2.3.2 The calorimeter system

The calorimeter system is located 12.5 m away from the interaction point in the z direction and it is composed of four sub systems (see Fig. 3.12) starting with a Scintillator Pad Detector (SPD) followed by a PreShower detector (PS), the ECAL and the HCAL. The purpose of the calorimetric system is to identify electrons, photons and hadrons, as well as measure their momentum, position and transverse energy.

All the LHCb calorimeter subdetectors adopt the same principle of operation. They consist of sampling devices with scintillating material separated by absorber materials. The scintillating light produced is transmitted to photomultipliers (PMT) by wavelenght shifting (WLS) fibres.

The SPD and PS consist of a matrix of cells which are composed of a 15 mm thick scintillators and separated by a 12 mm-thick layer of lead.

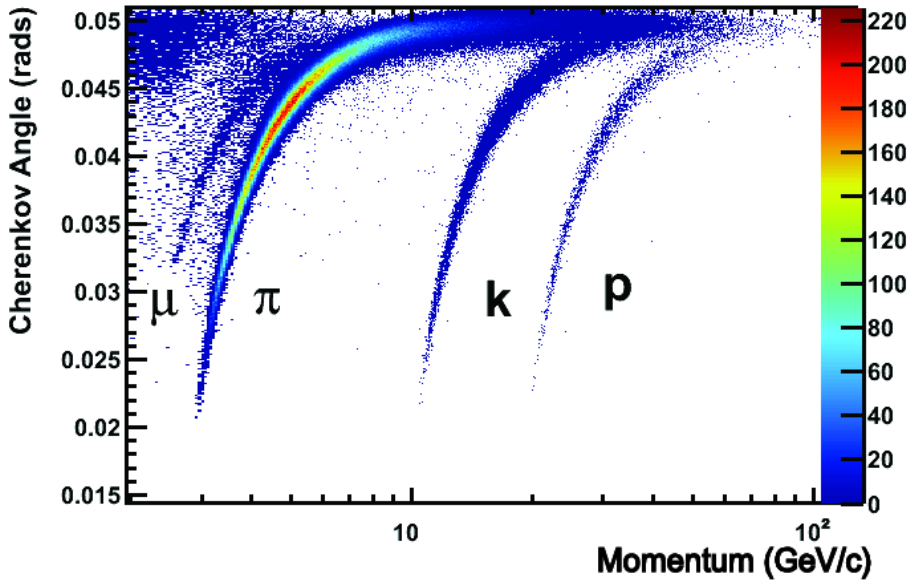

FIGURE 3.11: Reconstructed Cherenkov angle as a function of track momentum from data recorded from pp collisions at LHCb [92].

The ECAL is composed of 4 mm thick scintillator tiles and 2 mm thick lead plates. It detects electrons and photons by measuring the energy of the electromagnetic showers generated by them. The energy resolution was determined at test beams [93] and can be expressed as a function of the energy E (GeV) as

$$\frac{\sigma(E)}{E} = \frac{9.0 \pm 0.5\%}{\sqrt{E}} \bigoplus 0.8\% \ . \tag{3.5}$$

The first term of this equation, depending on the energy, is coming from the statistical uncertainty on the energy deposit, while the second term is a constant detector specific contribution.

HCAL is a sampling calorimeter composed of iron-scintillator tiles oriented parallel to the beam axis. It is composed of 16 mm thick iron tiles and 4 mm thick scintillator layers. In a similar fashion as for ECAL, the resolution as a function of the energy E (GeV) can be written as

$$\frac{\sigma(E)}{E} = \frac{69 \pm 5\%}{\sqrt{E}} \bigoplus (9 \pm 2)\% \ . \tag{3.6}$$

The association of the four sub detectors allows to distinguish between the electrons, photons and hadrons, as shown in Fig. 3.12, in the following way:

- Photons do not leave hits in the SPD station but react with the lead converter creating an electromagnetic shower in the PS and ECAL.
- Electrons leave energy in the SPD, react with the lead converter creating a deposit energy in the PS and ECAL.
- Hadrons can leave energy in the four sub detector but mostly in the HCAL.

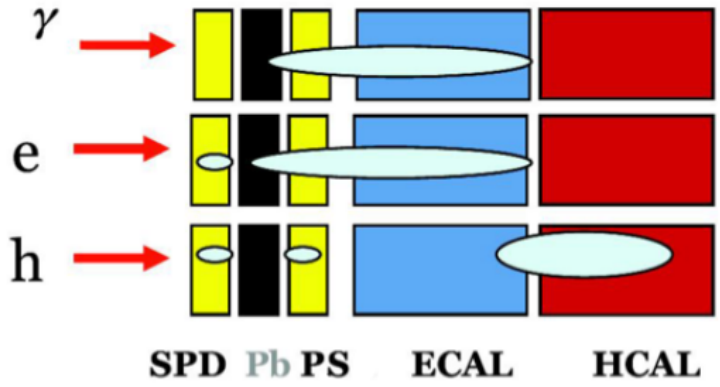

FIGURE 3.12: Disposition of the four sub detectors of the calorimeter system and the typical energy deposit.

The ECAL is a crucial detector for heavy-ion studies as the energy deposit in the calorimeter can be related to the centrality of the collision through the Glauber model, as we saw in Sec. 2.3.2.

3.2.3.3 Muon system

The muon detector is composed of five stations, indicated as M1-M5. The M1 station is placed between the RICH2 and the SPD, while the other 4 stations are placed after the calorimeter systems. Each station is made of wire chambers separated by iron absorbers 70 cm thick, to stop particles other than muons. Since the muons are the only charged particles that can pass through all the calorimeter system without being absorbed, their detection can be achieved by the muon system with a very high efficiency.

The layout of the muon system is presented in Fig. 3.13. Each muon chamber has an increasing height with respect to the z axis to follow the LHCb geometry. The stations are divided in four concentric regions, named R1-R4, with R1 being the closest to the beam pipe as shown in Fig. 3.13. The whole detector is composed of 1368 Multi-Wire Proportional Chambers (MWPCs) and 12 triple GEM detectors (Gas Electron Multiplier). Each station is equipped with 276 MWPCs 12 in R1, 24 in R2, 48 in R3 and 192 in R4, with the exception of the R1 region in M1 that is built with the 12 GEMs to obtain a higher granularity in a zone where the particle occupancy is higher. The minimum momentum required for a muon to cross all the stations is about 6 GeV/c.

Due to the different size of the station and the different rate requirements, there are 20 types of muon chambers, but the geometry is almost the same for all MWPCs.

3.2.4 SMOG

Originally designed for precise luminosity measurement, the System for Measuring Overlap with Gas (SMOG) [94] has been used to perform physics studies, acting as

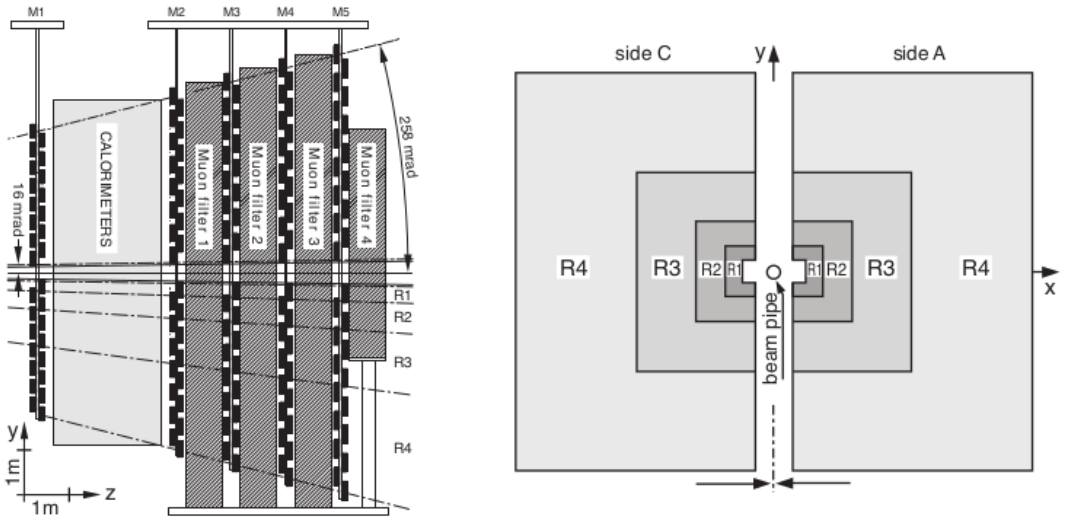

FIGURE 3.13: Side (left) and front (right) view of the LHCb Muon System.

a fixed target experiment. The system injects gas, inside the LHC vacuum, in the beam pipe with nominal pressure of 2×10^{-7} mbar. Noble gases, such as Argon or Helium, can be injected in the tank so that protons or lead from the LHC beams can collide with the gas, producing particles that are recorded by the LHCb detector. The gas injection can happen simultaneously with the *pp*, *p*Pb or PbPb data taking (Sec. 3.1). The SMOG system represents the only fixed-target experiment for heavy ion at the LHC. It allows to study a new region of the phase diagram of the hadronic matter. By varying the gas composition, we can change the size of the system as well as the colliding energy. Thanks to this set up, LHCb is the only detector capable of providing results from proton-proton, proton-lead, lead-lead and fixed target collisions at the LHC, at a unique centre of mass energy.

3.2.5 The trigger system

The trigger is necessary to isolate events that may contain the physical process of interest among many collisions happening at the LHC. The bunch-crossing rate at LHC for proton-proton collisions corresponds to 40 MHz, a rate too high to allow for each collision to be efficiently stored. The LHCb trigger system is designed to reduce the rate from 40 MHz to 12.5 kHz. The trigger system is organized in three levels, the first one, named Level 0 (L0), is a hardware trigger, while the High Level Trigger 1 (HLT1) and the High Level Trigger 2 (HLT2) are software triggers. A summary of the trigger system is shown in Fig. 3.14.

3.2.5.1 L0 trigger

The first stage of the LHCb trigger, L0, is designed to reduce the rate from 40 MHz to 1 MHz which is the maximum the detector can read out. The L0 trigger exploits

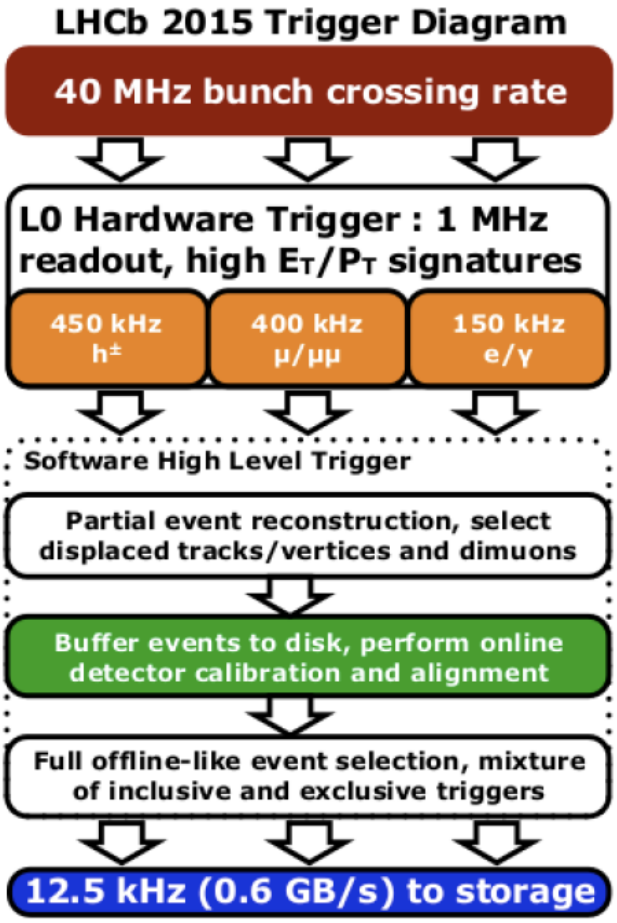

FIGURE 3.14: LHCb trigger scheme for Run II [95].

fast detectors able to provide useful information without relying on complicated algorithms.

The first stage is the calorimeter trigger, which relies on information provided by ECAL, HCAL, SPD and PS detectors. It uses the transverse energy in 2×2 cell blocks in ECAL and HCAL, defined as

$$E_T = \sum_{c=1}^{4} E_c \sin\theta_c \ , \tag{3.7}$$

where c is the cell index, E_c the deposit in each cell and θ_c the angle between the z axis and the line joining the cell to the nominal detector interaction region. According to this information and some information coming from the PS and SPD, it is possible to tag the triggered object as "photon" (L0Photon), "hadron" (L0Hadron) or "electron" (L0Electron).

The second L0 trigger comes from the muon stations. The muon system allows to measure at high rate the transverse momentum of particles traversing it using a rough estimation. Some triggers are then defined for a muon with a transverse momentum greater than a given threshold. The search algorithm starts from the logical pads fired in M3, which define the starting point to search for other hits in the adjacent stations

and compute a first estimation of the muon p_T.

3.2.5.2 High Level Trigger

The HLT1 trigger takes as input events that fired the L0 trigger. The reduced rate allows algorithms to perform simple reconstruction and selection. First, the PV and VELO tracks are reconstructed. The latter are then matched to the hits in the tracking station to obtain a more precise transverse momentum measurement, as well as a first estimate of the particle charge. The tracks are then fitted with a bi-directional Kalman filter, in order to account for effects like multiple scattering and energy loss. In addition, the impact parameter of the tracks with respect to the PV, the secondary vertices positions, invariant masses and flight directions can be used to perform a first selection. In the case of a muon, a first matching is made between the VELO and T-stations tracks with the hits in the muon chambers which allow to perform a simple selection on the transverse momentum of the muon candidates. If the event is selected by an HLT1 trigger, it is later processed by the HLT2 trigger.

The output given by the HLT1 trigger has a rate low enough to perform a complete event reconstruction, including information from the RICH detectors and the calorimeters. After the HLT2 stage, the event rate is reduced to 12.5 kHz in Run 2.

Different HLT1 and HLT2 lines are set where the selections are implemented. Those lines are written before the data taking depending on the physical processes studied by the LHCb collaboration. The trigger lines used in the analysis are presented in Sec. 6.2.

3.2.6 Event processing

3.2.6.1 Track reconstruction

After the event is accepted by the trigger, all the information from the detector is stored and the full event reconstruction can be performed. The reconstructed event is composed by the track trajectories, the vertex information and particle identification. The trajectories of the particle, also called tracks, are estimated using the hits in all the tracking sub-detectors (VELO, TT, IT, OT). The track reconstruction can be divided in two steps; the pattern recognition and the clone removal. The pattern recognition algorithm associates hits in one or more detector to a single track and the clone removal. The tracks are classified in different types, depending on their trajectories in the LHCb tracking system and the clone removal algorithm identifies clones by comparing the shared hit contents of tracks. The different types of tracks are illustrated in Fig. 3.15 and are defined as follows:

- **VELO track** only traverse the VELO. They are used to measure precisely the primary vertex as they are usually emitted at larger polar angles than the other tracks;
- **T tracks** only traverse the T stations;

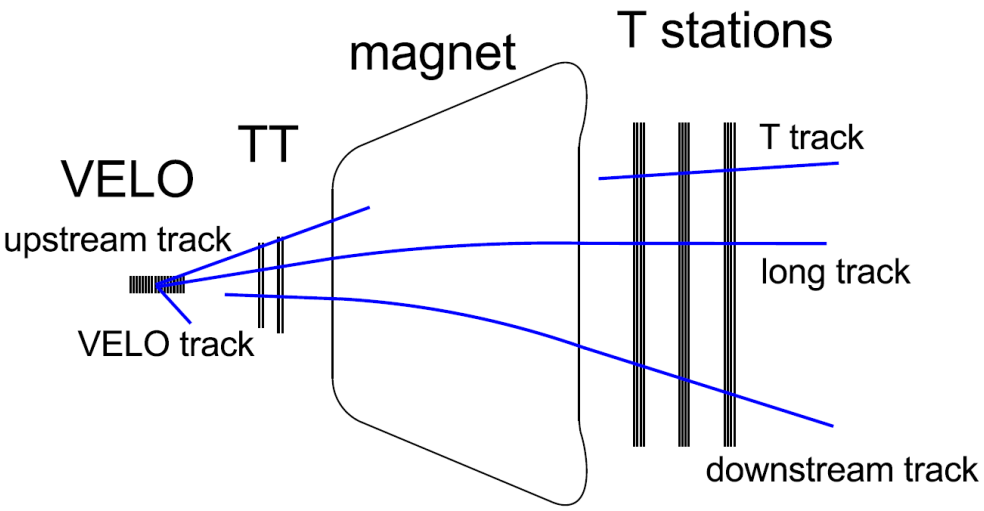

FIGURE 3.15: Scheme of the five different track types in the LHCb tracking system.

- **Upstream tracks** traverse both the VELO and TT stations;
- **Downstream tracks** traverse both the TT stations and the T stations;
- **Long tracks** traverse the full tracking system, they have the most precise momentum measurement and are, consequently, used for physics.

The track finding uses a series of individual algorithms described in the following:

- **VELO seeding:** The magnetic field in the VELO is low enough that the tracks are going in a straight line. The algorithm starts by making three dimensional space points by using the r and ϕ clusters and creating segments with them. Those tracks will be used as seeds by the other track finding algorithms;
- **Forward tracking:** This algorithm uses the segments reconstructed by the VELO and extrapolates them towards the TT and T stations. A first trajectory is determined using a seed from the VELO and a single hit from the T stations, this trajectory is then parametrised by a set of second and third order polynomial. Trajectories with the most compatible hits are kept. To remove possible tracks, which were reconstructed due to the mismatch of hits (ghost tracks), a final likelihood fit is used to confirm the correct tracks. Most of the long tracks are determined using this method;
- **T seeding:** Tracks coming from the T stations can also be used as seeds to determine long tracks. Here the magnetic field is considered low enough to have straight line for the particles trajectories. Some segments are defined using the hits in the TT stations;

- **Track matching:** This algorithm matches the previous discussed T seeds with VELO seeds that were not used in the forward tracking to determine longer tracks;
- **Upstream tracks:** The VELO seeds that are not used by the forward tracking or the track matching algorithm are extrapolated to the hits in the TT stations to determine upstream tracks;
- **Downstream tracking:** This algorithm uses the T seeds and extrapolate them to the TT stations.

The VELO or T seeds that were not used in any of these algorithms are simply named VELO tracks and T tracks.

3.2.6.2 Particle identification

Each type of particle induces a specific response in the detector as shown in Fig. 3.16; the combination of those responses enables us to formulate an hypothesis on the particle type.

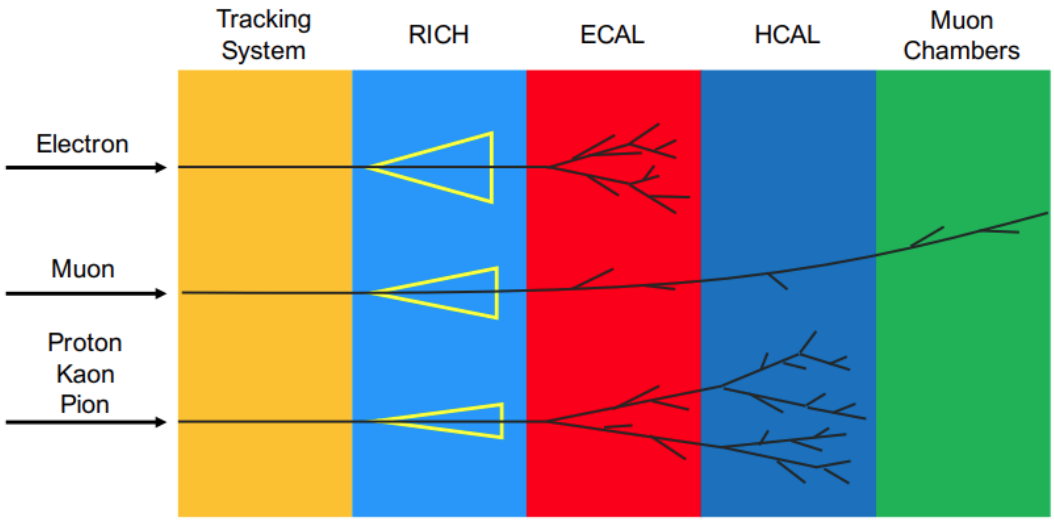

FIGURE 3.16: Illustration of the different particle response in LHCb [96].

We will now focus on the proton, kaon and pion particles identification as it will be used and discussed frequently in this thesis.

To determine the RICH particle identification performance on data, large samples of proton, kaon and pion tracks are required. Such control samples are selected independently on RICH information, which would otherwise bias the results. The decays containing the particles mentioned above are reconstructed exclusively from kinematic selections. Only decay modes with large branching fractions, for which large samples can be easily collected, are used to allow for precise calibration over a range of track kinematics. The following decays, and their charge conjugates, are

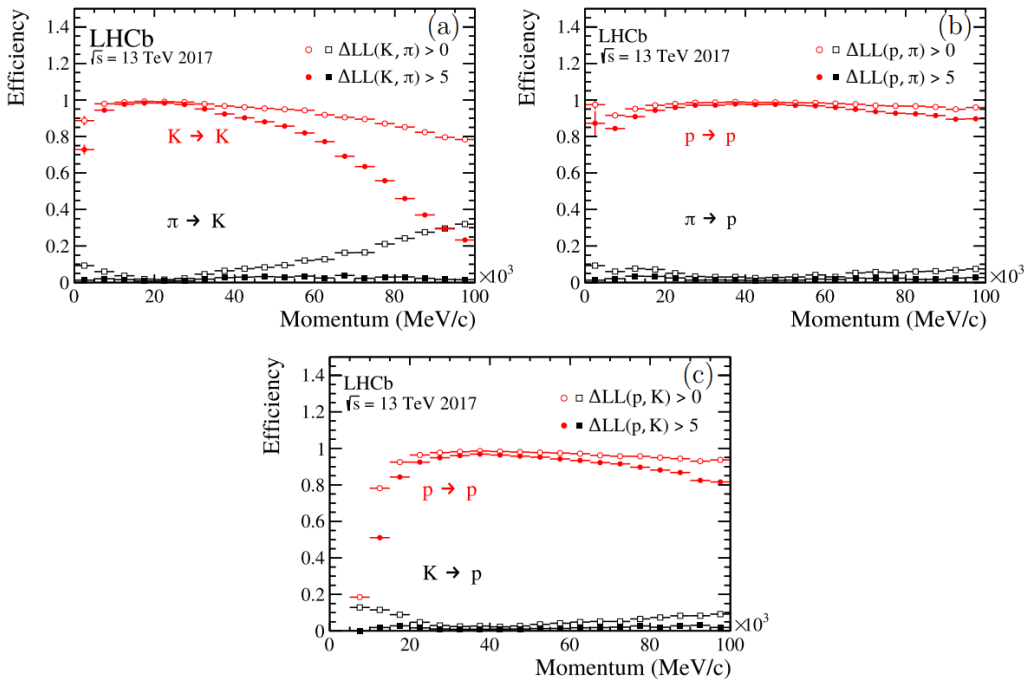

FIGURE 3.17: The efficiency of selecting kaons (a), protons (b and c), with the associate leakage from misidentifying pions (a and b) and kaons (c) as a function of momentum. Two selections are made, a loose selection (hollow circles) and a tight selection (solid circles) [97].

used for PID hadrons calibration: $K^0_S \to \pi^+\pi^-$, $\Lambda \to p\pi^-$ and $D^{*+} \to D^0(K^-\pi^+)\pi^+$. This group of final states provides a complete set of charged particles data to study PID hadrons performance. The efficiency of selecting kaons and protons is shown on Fig. 3.17.

The different tracks can be selected as particular hadrons using two methods that rely on all the subdetectors:

- ΔLL: selection based on the logarithm of the ratio between the likelihoods for the hadron and non-hadron hypotheses;
- $ProbNN$: selection based on a multiclassification algorithm [98]. Information from the LHCb tracking system, RICH and calorimeters are used to compute a single variable to estimate the nature of the track. This multivariate technique uses simulated events to train a Neural Network to identify particles.

The latter variable was introduced during the Run 2 of the LHC operation and has been found to be more efficient as it uses the whole detector to differentiate particles.

3.2.7 Data processing framework

The different applications of the LHCb data processing are part of a bigger project called Gaudi [99]. This framework was specifically developed for LHCb and has been

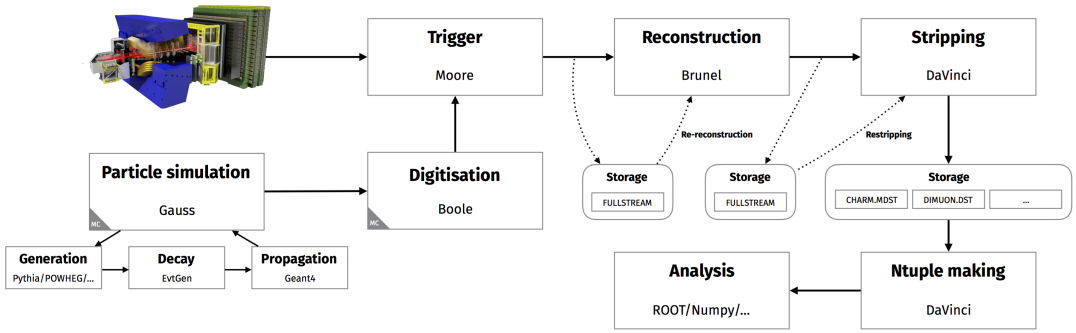

FIGURE 3.18: Scheme of the data processing flow in LHCb [104].

designed to share a common interface between the different applications. The main ones are listed below:

- GAUSS [100] is LHCb's simulation framework that interfaces various generators to decay engines and then simulate the response of our detector. The different aspects of GAUSS will be discussed in Sec. 3.2.9.
- BOOLE [101] is the program that finalises the simulation phase by reproducing the digital detector response. The output given by BOOLE can be then processed by BRUNEL in the same exact way as data.
- MOORE [101] is the application used to define and apply the software trigger algorithm.
- BRUNEL [102] is the LHCb event reconstruction application.
- DA VINCI [103] is the application that allows to perform the data analysis, it uses the information given at reconstruction level to select and build a decay chain.

The whole data processing flow including the simulation applications is illustrated in Fig. 3.18.

The full information from the readout system of LHCb is stored in raw files. Those data can be read by the BRUNEL application to reconstruct the events and stored them in Data Summary Tape (DST) files, the latter include both the raw information of the events as well as the information from the reconstruction step. To further facilitate the accessibility to the data and a faster processing by the user, the data go through a last step called "stripping". The "stripping" performs very loose selections, similar to the ones from HLT2, and arranges the data into different "stripping lines" according to the physical process. The stripping lines are also divided in "streams" depending on the type of study it will be used for. For a study based on the detection on one specific particle like the Ξ_c^+ or Λ_c^+, the corresponding stripping line will automatically link the reconstructed mother particle to the children ones. The stripping data are stored in DST (or micro-DST) files without the raw information, making it lighter and faster to study.

3.2.8 Trigger decision

Once the events are stored and processed in the “stripping" step, the trigger information is compared to the offline output. For each object present in the stripping data base, one can know if a specific trigger was fired by this same object or by another signal in the event. Thus, every signal can be tagged from these categories:

- Trigger On Signal (TOS); the signal fired the trigger regardless of the rest of the event;
- Trigger Independent On Signal (TIS); the signal didn't fire the trigger line, but another object from the same event fired it independently from the signal;
- Trigger Decision (Dec); the event passed the trigger requirements regardless of the TIS or TOS category.

An important feature of these categories is that they are not exclusive, a signal can be tagged both TIS and TOS.

3.2.9 Simulation

Simulated events are used to model signal decays of the Ξ_c^+ (Λ_c^+) of the pPb collisions and all the particles produced in such environment. It is crucial to model the full pPb collisions to virtually reproduce the multiplicity of particles in the LHCb detector, which will help estimate the efficiency of the detector performances.

The Gauss package uses the Pythia8 software [105] to generate the process that leads to the signal event and uses the EPOS generator [106] to simulate pPb collisions. The kinematic of the Ξ_c^+ (Λ_c^+) decay into a proton, a kaon and a pion is then modelled using the EvtGen [107] generator. Next, the GEANT4 [108] package simulates interactions between the particles and the LHCb detector. And, finally, Boole [101] reproduces the digital detector response and the simulation can be further reconstructed, just as data recorded by the detector.

Chapter 4

Data and Monte Carlo samples

In this chapter the information about the data and simulation samples used in the analysis is presented. The study is performed with data collected in 2016 of proton-lead collisions. The description of the proton-lead data is given in Sec. 4.3. The simulation samples, used to measure the efficiency, are described in Sec. 4.4.

4.1 Proton-lead configuration

In this analysis we use data from pPb collisions acquired in 2016 at $\sqrt{s} = 8.16$ TeV, with the energy per nucleon of the lead beam and the proton beam of 2.56 TeV and 6.50 TeV, respectively. The asymmetry in the beam energies produces a boost in rapidity of $y_{boost} \approx 0.4645$ in the direction of the proton beam. Due to the boost, the LHCb kinematic acceptance in the nucleon-nucleon centre-of-mass system is different in the forward and backward configurations. In order to access both the proton and the lead fragmentation regions, LHC provides two different beam configurations. The convention used in the note is that forward (backward) data correspond to the collisions where the proton (lead) beam traverses the LHCb detector from the VELO to the MUON station. A coordinate system is defined such that the z-axis is aligned with the proton beam, so the LHCb detector collects particles in the positive (negative) rapidity for forward (backward) configuration, covering the rapidity range $1.5 < y^* < 4.0$ ($-5.0 < y^* < -2.5$). Here y^* is the rapidity in the nucleon-nucleon centre-of-mass system, which is related to the rapidity in the laboratory frame, y_{lab}, by the relation $y^* = y_{lab} \pm y_{boost}$. The schematic of the two beam configurations is shown in Fig. 4.1.

4.2 Luminosity determination

The luminosity of the forward and backward data sample was determined using the same procedure as for the 2013 pPb run [109]. The luminosity determination relies on two direct methods: the "van der Meer scan" method (VDM) [110] and the "beam-gas imaging" method (BGI) [111]. The VDM method exploits the ability to move the beams in both transverse coordinates with high precision and thus to scan the overlap integral of the colliding beams at different relative beam positions while measuring a relative rate. This method is also being used by the other LHC experiments [112,

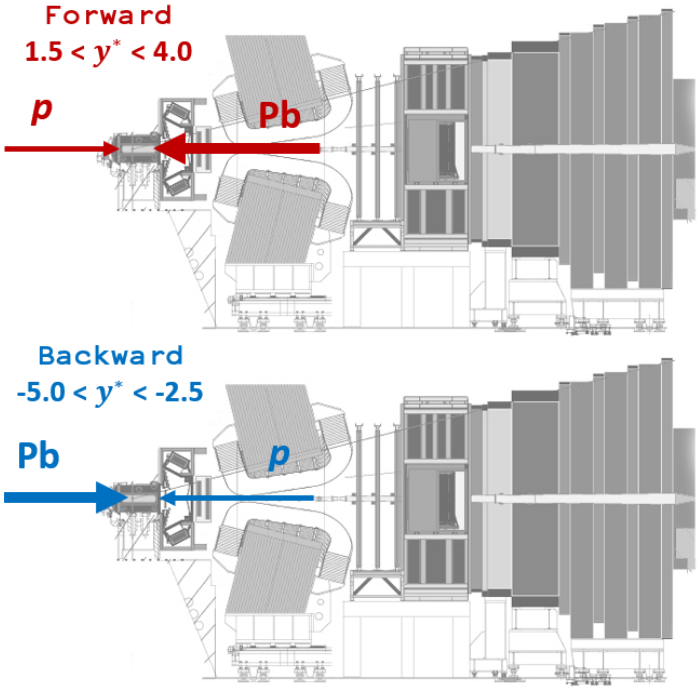

FIGURE 4.1: Forward and backward beam configurations.

113, 114] and was first applied at the CERN ISR [115]. The BGI method is based on reconstructing vertices of interactions between beam particles and gas nuclei in the beam vacuum to measure the angles, positions and shapes of the individual beams without displacing them. The shapes obtained with these data are constrained by the distribution of vertices measured with beam-beam interactions. In both methods, data taken with the LHCb detector located at the interaction point (IP) are used in conjunction with data from the LHC beam instrumentation. The usage of two methods provides an important cross check of the results. The calibration measurements obtained with the VDM and BGI methods are found to be consistent and are averaged for the final result.

4.3 Data samples

The data samples of proton-lead and lead-proton collisions at $\sqrt{s_{NN}} = 8.16$ TeV recorded in 2016 correspond to an integrated luminosity of 12.5 and 17.4 pb^{-1}, respectively. The list of runs used in the analysis is given in Appendix A.

The data are processed through Turbo [116] in the data streaming TURBO++. The idea behind the Turbo stream is to provide a framework by which a physics analysis can be performed using the candidates from trigger reconstruction directly. The events which are sent to the Turbo stream will keep only the candidates identified by the trigger reconstruction, discarding the rest of the event. The schematic data flow of the Turbo stream compared to the traditional data flow (denoted the Full

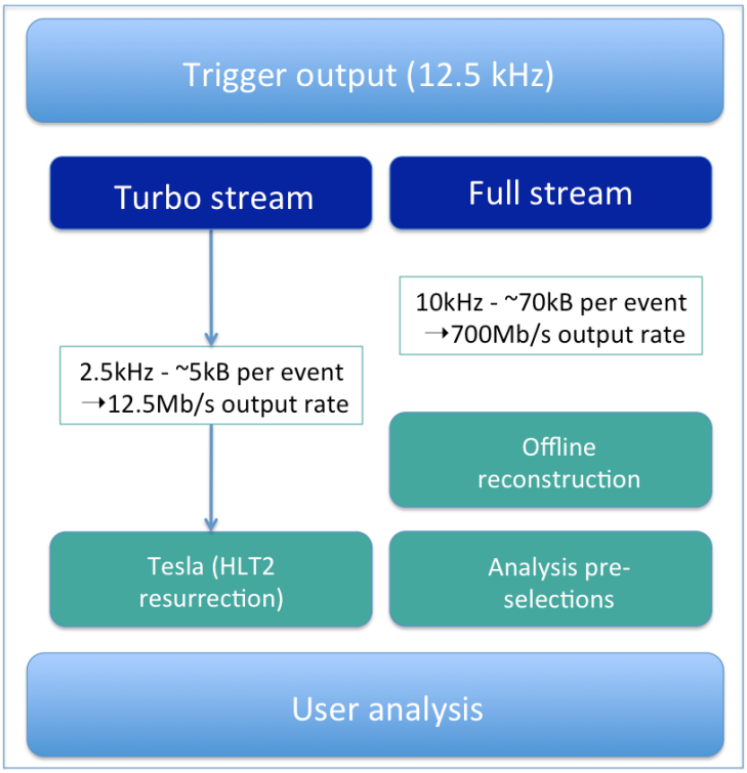

FIGURE 4.2: Turbo stream and Full stream processing stages [116].

stream) is shown in Fig. 4.2. The advantage of the Turbo stream is that the raw event size is an order of magnitude smaller than the event size in the Full stream.

The detailed description of the Turbo line used in this analysis is given in the Sec. 6.2.1.

4.4 Monte Carlo samples

The samples used for this analysis are summarised in Table 4.1. They are crucial to understand detector-induced biases and other experimental effects. Charmed baryons are generated with the official LHCb tune in pp collisions at $\sqrt{s} = 8.16$ TeV using PYTHIA [90] and are embedded into EPOS [117]. Unfortunately, EPOS does not reproduce the particle multiplicities observed in pPb collisions. Thus, a "multiplicity-fixed" simulation is introduced, where the number of EPOS events is corrected to match the multiplicities, which are observed in data. Particle decays are described by EvtGen [118], while the interaction of particles with the detector, and its response in simulation, are implemented using the GEANT4 toolkit [119]. Generated samples are digitised in Boole and the output has the same format of the data collected by the LHCb detector, and goes through the same reconstruction. The comparison of the primary vertex position distributions for data and simulation samples is shown on Fig. 4.3.

Only the simulation samples produced by the PYTHIA generator are used for the acceptance measurement, while the samples produced by PYTHIA and EPOS are used for the determination of the selection efficiency.

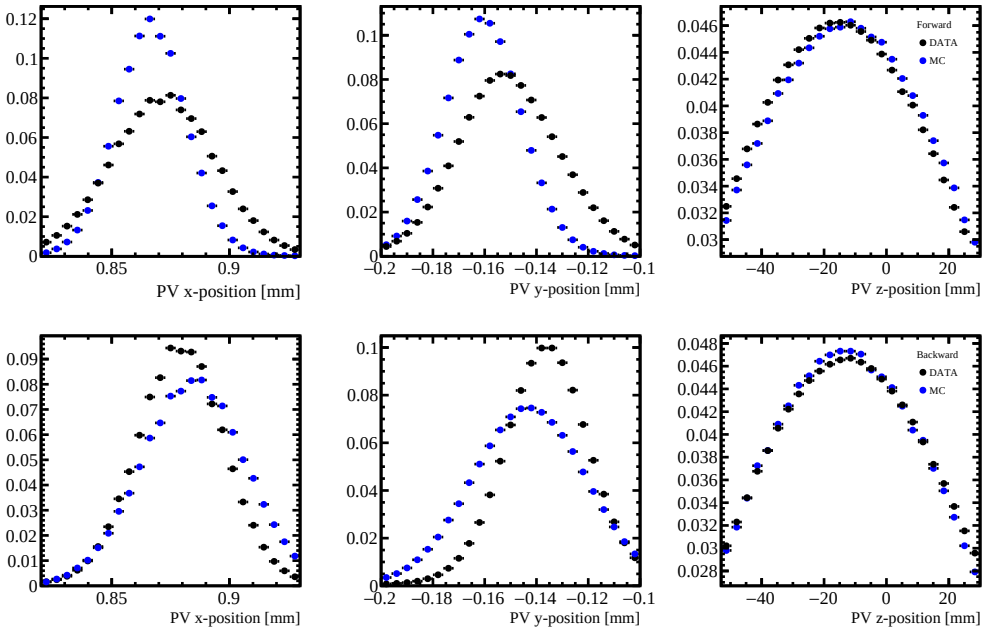

FIGURE 4.3: Comparison of the primary vertex position distributions for data (black) and simulation samples (blue). The vertical axis represents normalised entries of the primary vertex position.

TABLE 4.1: Monte Carlo samples used in the analysis.

Generator	Decay	Number of events
Pythia 8.1	$\Xi_c^+ \to p^+K^-\pi^+$	360000
Pythia 8.1	$\Lambda_c^+ \to p^+K^-\pi^+$	900000
Pythia 8.1+EPOS	$\Xi_c^+ \to p^+K^-\pi^+$	9M
Pythia 8.1+EPOS	$\Lambda_c^+ \to p^+K^-\pi^+$	36M

Chapter 5

Analysis strategy

Based on the pPb data collected at LHCb, the double differential cross-sections, the cross-section ratios and the forward-backward asymmetry for open charmed baryons (Ξ_c^+, Λ_c^+) are measured, as well as the Ξ_c^+/D^0 production ratio. In the following text we give definitions of the quantities we want to measure.

5.1 Cross-section measurement strategy

The differential cross-section for prompt Ξ_c^+ (Λ_c^+) production is defined as

$$\frac{\mathrm{d}^2\sigma_{\Xi_c^+(\Lambda_c^+)}(p_\mathrm{T}, y^*)}{\mathrm{d}p_\mathrm{T}\mathrm{d}y^*} = \frac{N^{\Xi_c^+(\Lambda_c^+)}(p_\mathrm{T}, y^*)}{\mathcal{L} \cdot \mathrm{BR}^{\Xi_c^+(\Lambda_c^+)} \cdot \epsilon_{tot}(p_\mathrm{T}, y^*) \cdot \Delta p_\mathrm{T} \Delta y^*}, \tag{5.1}$$

where:

- $N^{\Xi_c^+(\Lambda_c^+)}(p_\mathrm{T}, y^*)$ is the number of detected prompt Ξ_c^+ (Λ_c^+) produced in a given interval of p_T and y^*, Δp_T and Δy^*, respectively;
- $\mathcal{L}$ is the integrated luminosity;
- $\epsilon_{tot}(p_\mathrm{T}, y^*)$ is the total efficiency determined in a Δp_T and Δy^* interval consisting of four components: acceptance efficiency, reconstruction and selection efficiency, PID efficiency and trigger efficiency;
- $\mathrm{BR}^{\Xi_c^+(\Lambda_c^+)}$ is the branching ratio of Ξ_c^+ (Λ_c^+) decaying to $p^+K^-\pi^+$.

The double differential cross section is measured as a function of p_T, integrated over rapidity in the regions $1.5 < y^* < 4.0$ (forward) and $-5.0 < y^* < -2.5$ (backward), with

- Δp_T [GeV/c] : [2.0, 3.0, 4.0, 5.0, 6.0, 8.0, 12.0],[1]

and as a function of y^*, integrated over transverse momentum in the region $2.0 < p_\mathrm{T} < 12.0$ GeV/c, with

- Δy^* (forward) : [1.5, 2.0, 2.5, 3.0, 3.5, 4.0],
- Δy^* (backward) : [-5.0, -4.5, -4.0, -3.5, -3.0, -2.5].

[1] The range is chosen to make sure there is enough signal in each bin.

5.2 Ratio measurement strategy

The production ratios between different charm hadrons are sensitive probes to the charm hadronisation mechanism. The ratio of Ξ_c^+ to Λ_c^+ production is calculated through the formula

$$R_{\Xi_c^+/\Lambda_c^+}(p_T, y^*) = \frac{N^{\Xi_c^+}(p_T, y^*)}{N^{\Lambda_c^+}(p_T, y^*)} \cdot \frac{\epsilon_{tot}^{\Lambda_c^+}(p_T, y^*)}{\epsilon_{tot}^{\Xi_c^+}(p_T, y^*)} \cdot \frac{\mathcal{B}(\Lambda_c^+ \to p^+K^-\pi^+)}{\mathcal{B}(\Xi_c^+ \to p^+K^-\pi^+)}, \tag{5.2}$$

where:

- $N^{\Xi_c^+}(p_T, y^*)$ and $N^{\Lambda_c^+}(p_T, y^*)$ are the number of promptly produced Ξ_c^+ and Λ_c^+ events, respectively, in a given interval of p_T and y^*;
- $\epsilon_{tot}^{\Xi_c^+}(p_T, y^*)$ and $\epsilon_{tot}^{\Lambda_c^+}(p_T, y^*)$ are the total efficiencies for Ξ_c^+ and Λ_c^+ in a given interval of p_T and y^*;
- $B(\Xi_c^+ \to p^+K^-\pi^+) = [0.62 \pm 0.30]\%$ is the branching fraction of the Ξ_c^+ decay. The value is taken from the PDG [68], which is a combination of two measurements made by Belle [120] and LHCb [121].
- $B(\Lambda_c^+ \to p^+K^-\pi^+) = [6.28 \pm 0.32]\%$ is the branching fraction of the Λ_c^+ decay [66].

Since LHCb has already measured the D^0 cross-section in pPb collisions at $\sqrt{s} = 8.16\,\text{TeV}$ [122], we are able to calculate the cross section ratio of Ξ_c^+ to D^0, using the formula

$$R_{\Xi_c^+/D^0} = \frac{\mathrm{d}^2\sigma_{\Xi_c^+}(p_T, y^*)}{\mathrm{d}p_T\mathrm{d}y^*} \Big/ \frac{\mathrm{d}\sigma_{D^0}^2(p_T, y^*)}{\mathrm{d}p_T\mathrm{d}y^*}. \tag{5.3}$$

The ratio of Ξ_c^+ to Λ_c^+ (D^0) production is measured as a function of p_T, integrated over rapidity in the regions $1.5 < y^* < 4.0$ (forward) and $-5.0 < y^* < -2.5$, with

- Δp_T [GeV/c] : [2.0, 3.0, 4.0, 5.0, 6.0, 8.0, 12.0],

and as a function of y^*, integrated over transverse momentum in the region $2.0 < p_T < 12.0$ GeV/c, with

- Δy^* (forward) : [1.5, 2.0, 2.5, 3.0, 3.5, 4.0],
- Δy^* (backward) : [−5.0, −4.5, −4.0, −3.5, −3.0, −2.5].

5.3 Forward-backward asymmetry measurement strategy.

The measurement of the forward-backward ratio, R_{FB}, allows to study the CNM effects and it is defined by the formula

$$R_{FB} = \frac{\mathrm{d}^2\sigma_{\text{Fwd}}(p_T, |\quad y^*|)/\mathrm{d}p_T\mathrm{d}y^*}{\mathrm{d}^2\sigma_{\text{Bwd}}(p_T, |-y^*|)/\mathrm{d}p_T\mathrm{d}y^*}, \tag{5.4}$$

where $\mathrm{d}\sigma_{\mathrm{Fwd\ (Bwd)}}$ is the double differential cross-section (Eq. 5.1) measured in the forward (backward) data sample. The R_{FB} is measured as a function of p_{T}, integrated over rapidity in the regions $2.5 < |y^*| < 4.0$, with

- Δp_{T} [GeV/c] : [2.0, 3.0, 4.0, 5.0, 6.0, 8.0, 12.0]

and as a function of $|y^*|$, integrated over transverse momentum in the region $2.0 < p_{\mathrm{T}} < 12.0$ GeV/c, with

- $\Delta|y^*|$: [2.50, 2.75, 3.00, 3.25, 3.50, 4.00].

Chapter 6

Event selection

In this chapter the event selection is described. The underlying variables are described in Sec 6.1. The Ξ_c^+ and Λ_c^+ baryons are reconstructed via the decay into a proton, a kaon and a pion, selecting events which fire a specific trigger, as described in Sec. 6.2, based on information from muon systems and the calorimeter, followed by a software stage (Turbo line), which applies a full event reconstruction. Then, in order to improve the signal over background ratio, offline selections are applied. This procedure is described in Sec. 6.3 and the cross-check of the procedure is described in Sec. 6.4. The separation of the events with prompt Ξ_c^+ (Λ_c^+) production from the contribution of b-hadron decays is described in Sec. 6.5. The efficiency determination is described in Chap. 7. The last step will be to estimate the accuracy of our result with systematic uncertainties studies, given in details in Chap. 8.

6.1 Selection variables

The following variables are used in the event selection:

- $\chi^2_{\rm IP}$: The impact parameter (IP), with respect to the primary vertex (PV), is the distance of closest approach of the track, extrapolated to the PV. The prompt stable particles produced directly from the collision point will have a lower impact parameter than particles produced in long-lived decays. The χ^2 parameter is computed as the absolute difference of a vertex fit with and without the particle in question;

- PID: The particle identification systems, discussed in Sec. 3.2.6.2, provide the information on the type of detected particle. In this analysis the ΔLL set of PID variables is used, since it is found to be more efficient in pPb data;

- χ^2_{track}: This variable denotes the quality of the track reconstruction and it is computed as the χ^2 of a track fit;

- χ^2_{VD}: The vertex displacement is the flight distance of composite particles with respect to the related PV;

- χ^2_{vertex}: This variable denotes the quality of the reconstruction of the decay vertex position for the composite particles. It allows to select events with tracks originating from the same vertex;
- τ: The reconstructed decay time is the lifetime of the composite particle estimated from the flight distance;
- cos(DIRA): The parent direction angle is the cosine of the angle between the momentum and displacement vectors. For a correctly reconstructed signal decay the cos(DIRA) should be close to 1.0;
- ProbNN$_{ghost}$: This variable denotes the probability of track to be reconstructed due to the mismatch of hits from separate particles or from detector noise or spill-over.

When the notation h is used, it means that the cuts are applied to all baryon's decay products.

6.2 Triggers

The data are processed and selected with the Turbo stream through the trigger based on SPD station at L0 level and two Multivariate Analysis Triggers (MVA) at HLT1 level.

6.2.1 TURBO

In the Turbo stream line used at least one candidate in each event is reconstructed at the HLT2 software trigger level and is saved for the online analysis [123]. The selections performed by this line are summarised in Table 6.1. Both, Ξ_c^+ (2468) and Λ_c^+ (2286) are selected with the same Turbo line. The data are reconstructed using `Brunel` and are analysed using `DaVinci`. The signal selection criteria are summarised in Table 6.3.

TABLE 6.1: Turbo selection of signal candidates.

Quantity	Selection
p_{T} of all the h tracks	p_{T} >200 MeV/c
IP significance	χ^2_{IP} >4.0
p of the h tracks	p >1000.0 MeV/c
p of the proton tracks	p >10000.0 MeV/c
PID	PID$_p(p^+)$ >5, PID$_K(K^-)$ >5, PID$_K(\pi^+)$ <5
$M_{inv}(p^+K^-\pi^+)$	2201< $M_{inv}(p^+K^-\pi^+)$ <2543 MeV/c^2
At least one h track	p_{T} (h max)>1000 MeV/c, χ^2_{IP} (h max)>50
At least two h track	p_{T} ($h1$,$h2$)>400 MeV/c, χ^2_{IP} ($h1$,$h2$)>10
Ξ_c^+, Λ_c^+	χ^2_{vertex} <25.0
Ξ_c^+, Λ_c^+	χ^2_{VD} >4.0
Ξ_c^+, Λ_c^+	τ >0.075 ps
Ξ_c^+, Λ_c^+	cos(DIRA) > 0.9994

6.2.2 L0 and HLT1 triggers

At the L0 level we use the trigger, which requires at least one hit in the SPD detector. At the HTL1 level two MVA trigger lines `Hlt1TrackMVA, Hlt1TwoTrackMVA` are used with the `OR` logic. The trigger threshold was relaxed for these two HLT1 trigger lines for pPb data collection so that the efficiency is close to 100% except in extreme small transverse momentum regions, where the efficiency is dropping down to around 97%. The selection criteria for the L0 and HLT1 trigger lines we used are reported in Table 6.2.

TABLE 6.2: HLT1 trigger selections of signal candidates.

Quantity	Selection
L0	
	SPD multiplicity > 0
HLT1TrackMVA	
	Tracks:
	$\chi^2_{track}/\text{ndf} < 4.0$
	$\text{ProbNN}_{ghost} < 0.3$
	$\chi^2_{\text{IP}} > 6.0$ for $p_{\text{T}} > 10.0\,\text{GeV}/c$
	$log(\chi^2_{\text{IP}}) > (\frac{0.3}{p^2_{\text{T}}} + \frac{0.2}{10} \cdot (10.0 - p_{\text{T}})+\log(6.0)$ for $p_{\text{T}} \in [0.5,\, 10]\,\text{GeV}/c$
HLT1TwoTrackMVA	
	Tracks:
	$p_{\text{T}} > 0.3\,\text{GeV}/c$; $p > 2\,\text{GeV}/c$
	$\chi^2_{track}/\text{ndf} < 4.0$; $\chi^2_{\text{IP}} > 4.0$
	$\text{ProbNN}_{ghost} < 0.5$
	Vertex:
	χ^2_{vertex} <10.0 for $\eta \in [2.0,\, 5.0]$
	cos(DIRA)>0.0 for $M_{corr} > 0.5$ GeV/c

6.3 Offline selections

The offline selections focus on increasing the signal-to-background ratio, which is is especially necessary for the three-body decays where a large combinatorial background remains after the trigger. All of the children are required to have large transverse momentum $p_T > 400$ MeV/c. The requirement on impact parameter significance $\chi^2_{\text{IP}} > 4.0$ removes all the tracks which come from primary vertices (PV). The tracks are also asked to be in the LHCb acceptance $2.0 < \eta < 5.0$ and in the kinematic range $3.2 < p < 100$ GeV/c. All three child particles are required to have a good quality of reconstruction with $\chi^2_{track}/\text{ndf} < 3.0$. For the further selections all the tracks are required to have RICH PID information. In order to suppress the tracks reconstructed due to the mismatch of hits, the probability of track to be ghost, ProbNN_{ghost}, should be less than 0.3. The proton track has to be more proton-like by requiring $\Delta LL_p >$

15.0, the kaon is required to be more kaon-like by $\Delta LL_K > 5.0$ and pion track more pion-like by requiring $\Delta LL_K < 0.0$. The PID variable distributions are shown on 6.1. The Ξ_c^+ (Λ_c^+) candidate is asked be in the kinematic range 2.0< p <160.0 GeV/c, to have a decay vertex quality parameter $\chi^2_{vertex} < 10.0$ and reconstructed decay time τ between 0.1 and 10 ps. The alignment angle is required to be such that cos(DIRA)>0.99990 (0.99985) We use tighter cut for Ξ_c^+ candidates to improve the lower signal-to-background ratio..

TABLE 6.3: Offline selections of Ξ_c^+ and Λ_c^+ candidates and their children ($h^\pm$).

	Variable name	Selection criteria
$h^\pm$	p_T	> 0.4 GeV/c
	p	$\in$ [3.2, 100.0] GeV/c
	χ^2_{track}/ndf	< 3.0
	η	$\in$ [2.0, 5.0]
	ProbNN$_{ghost}$	< 0.3
	hasRICH	true
p^+	PID$_p$	> 15.0
	PID$_p$-PID$_K$	> 5.0
K^-	PID$_K$	> 5.0
π^+	PID$_K$	< 0.0
$\Xi_c^+(\Lambda_c^+)$	p_T	$\in$ [2.0, 12.0] GeV/c
	η	$\in$ [2.0, 4.5]
	χ^2_{vertex}	< 10.0
	τ	$\in$ [0.1, 10.0] ps
	cos(DIRA)	> 0.99990 (0.99985)

The signal events were estimated through a fit on the invariant mass distribution of the $p^+K^-\pi^+$ particles using a Crystal Ball (CB) function with a Gaussian, while the background is fitted using a first degree polynomial. The CB function contains a Gaussian core with a tail at lower mass to take into account radiative energy loss. It is defined as

$$f(M_{inv}) = \begin{cases} \exp(-\frac{(M_{inv}-\mu)^2}{2\sigma^2}) & \text{for } \frac{M_{inv}-\mu}{\sigma} > -a \\ A \cdot (B - \frac{M_{inv}-\mu}{\sigma})^{-n} & \text{for } \frac{M_{inv}-\mu}{\sigma} \leqslant -a \end{cases}, \tag{6.1}$$

in which

$$A = \left(\frac{n}{|a|}\right)^n \cdot \exp\left(-\frac{|a|^2}{2}\right) \tag{6.2}$$

$$B = \frac{n}{|a|} - |a|\,. \tag{6.3}$$

Here μ is the mean value and σ is the width. These parameters are initially set to a value close to what is observed in simulation. The obtained parameters are then used as a starting value for the fit on the data. Once the selection is applied, the

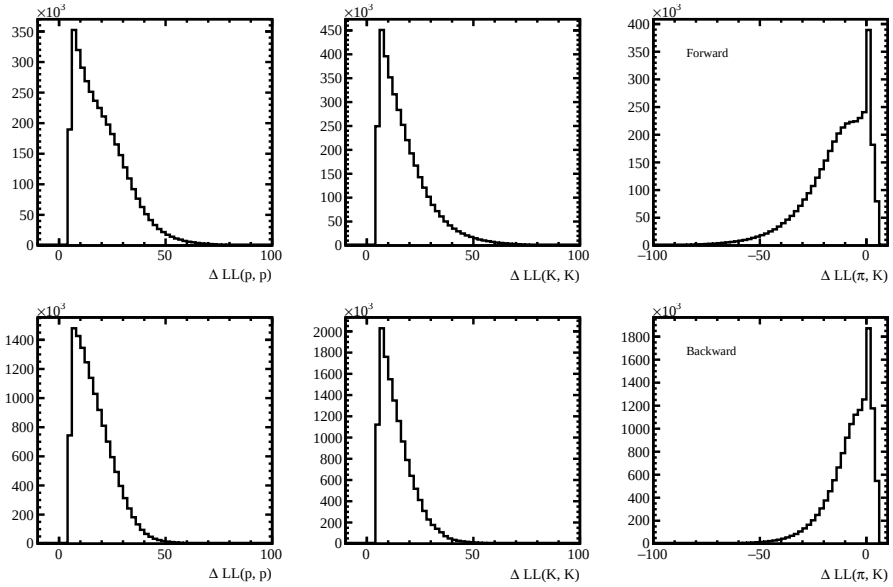

FIGURE 6.1: The ΔLL variable distributions for a proton, a kaon and a pion in forward (top) and backward (bottom) data.

resonance peak is clearly visible in the invariant mass spectrum of a proton, a kaon and a pion, as shown in Fig. 6.2.

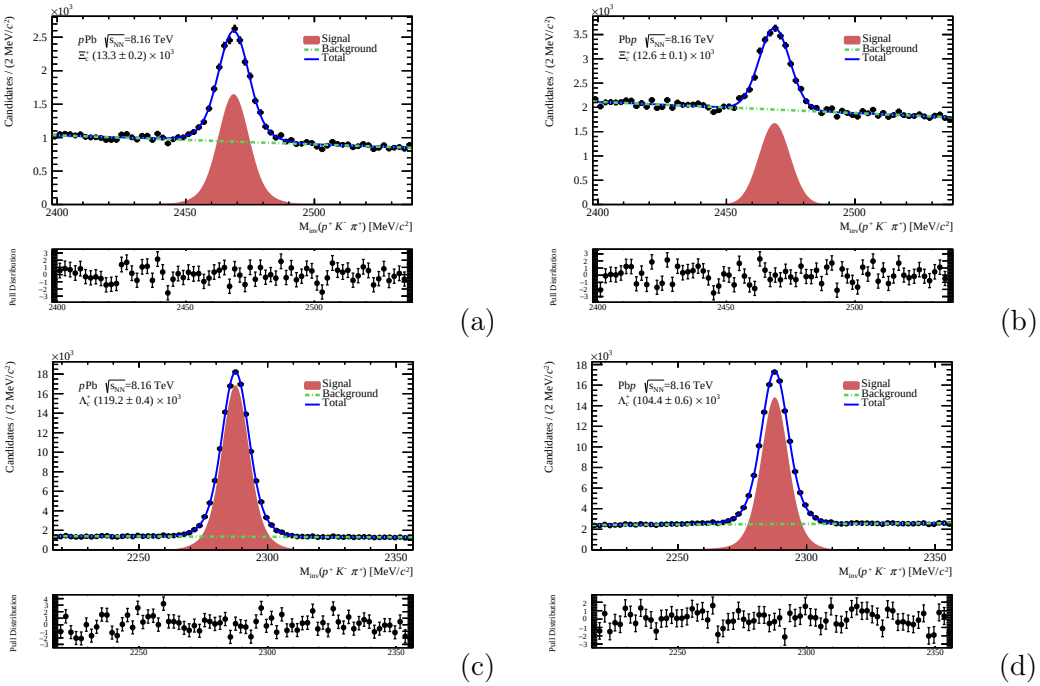

FIGURE 6.2: Invariant mass distribution fit. The solid blue line represents the total fit, which is composed of a first degree polynomial representing the background (green dashed line) and a CrystalBall function with a Guassian representing the Ξ_c^+ signal candidates (red shaded area).
a) Ξ_c^+ candidates in forward data, b) Ξ_c^+ candidates in backward data, c) Λ_c^+ candidates in forward data, d) Λ_c^+ candidates in backward data.

The number of background events is extracted using the sPlot [124] technique, which allows the disentanglement of signal from background contributions based on the fit of a discriminating variable. The sPlot method assigns a statistical weight to each event, representing the probability to be a "signal type" or a "background type" event. There are about 13.3k (12.6k) Ξ_c^+ and 119.2k (104.4k) Λ_c^+ candidates in the forward (backward) sample after background subtraction in total. Such fit was performed in each p_T and rapidity bin (See Appendix B for details).

6.4 Background cross-check

Since there might be correlations between the observables, to verify the quality of the sPlot technique signal extraction, the $log_{10}(\chi^2_{IP})$ (10 based logarithm) distribution of background events obtained with this technique was compared with the same distribution of events retrieved using the side-band technique, as shown in Fig. 6.3. On the distribution of selected background one can see that the two methods give consistent results. We use the sPlot technique as nominal procedure to evaluate the background and the sideband method to evaluate the systematic uncertainty associated with this procedure.

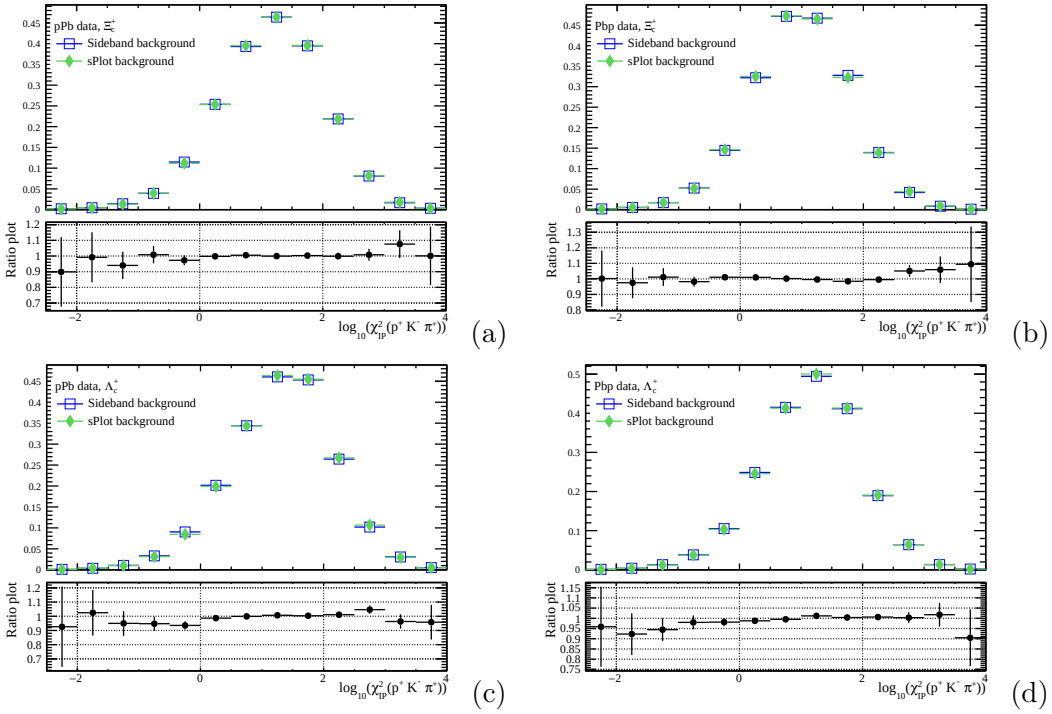

FIGURE 6.3: Background cross-check. The blue squares represents the sideband background and the green diamonds represents the sPlot background. Below is the ratio plot of two methods.
a) Forward background in Ξ_c^+ fit, b) backward background in Ξ_c^+ fit, c) Forward background in Λ_c^+ fit, d) backward background in Λ_c^+ fit.

6.5 Prompt signal determination

The extracted signal contains promptly produced baryons and non-prompt signal from b decay. In order to extract prompt events only, the $log_{10}(\chi^2_{IP})$ distribution is used. This method was developed in previous analyses [63]. Fig. 6.4 shows the t_z vs $log_{10}(\chi^2_{IP})$ bidimensional distribution for Λ_c^+ candidates from the forward data sample. The pseudo-proper decay time t_z is defined as

$$t_z = \frac{(z_{VD} - z_{PV}) M_{\Xi_c^+(\Lambda_c^+)}}{p_z}, \tag{6.4}$$

where z_{VD} and z_{PV} are the decay and collision coordinates at z-axis, $M_{\Xi_c^+(\Lambda_c^+)}$ is the mass of Ξ_c^+ (Λ_c^+) and p_z is the longitudinal momentum.

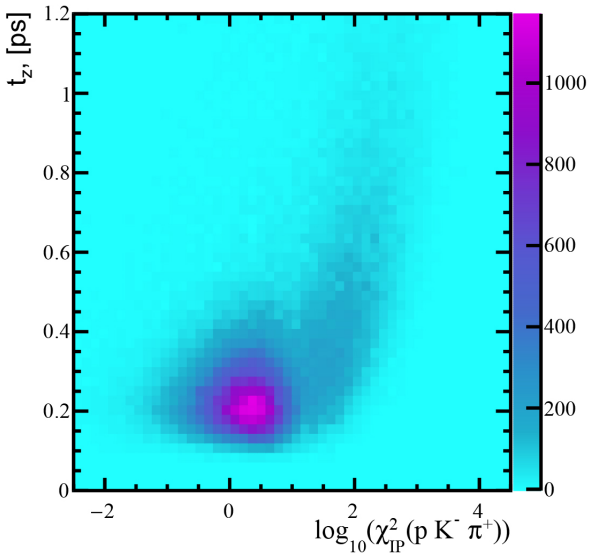

FIGURE 6.4: t_z vs $log_{10}(\chi^2_{IP})$.

In this figure, the cluster of events around zero on the x-axis corresponds to the promptly produced Λ_c^+ baryons, while the tail between $log_{10}(\chi^2_{IP}) = 1$ and 3 are from b-decayed baryons.

The prompt signal was extracted by fitting the two peaks of the $log_{10}(\chi^2_{IP})$ distribution, shown on Fig. 6.5. This method was previously developed in [125, 126, 63]. The fit consists of two components, fitted using the Bukin function defined as $f_{Bukin}(x; \mu, \sigma, \xi, \rho_L, \rho_R) =$

$$= \begin{cases} \exp\left(-\ln 2 \left[\frac{\ln\left(1+2\xi\sqrt{\xi^2+1}\frac{x-\mu}{\sigma\sqrt{2\ln 2}}\right)}{\ln\left(1+2\xi^2-2\xi\sqrt{\xi^2+1}\right)} \right]^2 \right) & x_L < x < x_R, \\ \exp\left(\frac{\xi\sqrt{\xi^2+1}(x-x_L)\sqrt{2\ln 2}}{\sigma\left(\sqrt{\xi^2+1}-\xi\right)^2 \ln\left(\sqrt{\xi^2+1}+\xi\right)} - \rho_L\left(\frac{x-x_L}{\mu-x_L}\right)^2 - \ln 2 \right) & x < x_L, \\ \exp\left(-\frac{\xi\sqrt{\xi^2+1}(x-x_R)\sqrt{2\ln 2}}{\sigma\left(\sqrt{\xi^2+1}+\xi\right)^2 \ln\left(\sqrt{\xi^2+1}+\xi\right)} - \rho_R\left(\frac{x-x_R}{\mu-x_R}\right)^2 - \ln 2 \right) & x > x_R, \end{cases} \tag{6.5}$$

where

$$x_{L,R} = \mu + \sigma\sqrt{2\ln 2}\left(\frac{\xi}{\sqrt{\xi^2+1}} \pm 1\right). \tag{6.6}$$

The prompt and non-prompt signals are each described by a Bukin function using the RooFit package [127], with the asymmetry parameters taken from the fit on the MC distribution and the mean value and variance are left free to vary. The sPlot technique is applied after the fit to extract the promptly produced $\Xi_c^+(\Lambda_c^+)$ candidates. The extracted events from the whole data samples are later used to correct the MC samples.

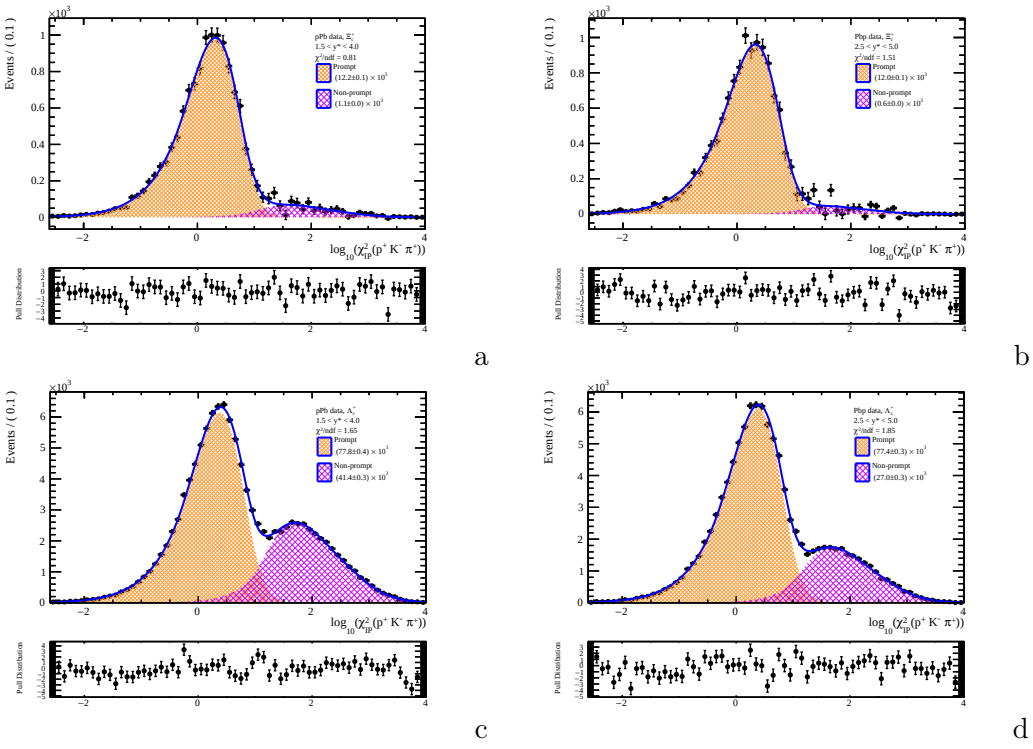

FIGURE 6.5: Fit of $log_{10}(\chi^2_{IP})$ distribution. The solid blue line represents the total fit, which is composed of a Bukin function representing the prompt signal (orange shaded area) and a another Bukin function representing the non-prompt signal (purple shaded area).
a) Ξ_c^+ candidates in forward data, b) Ξ_c^+ candidates in backward data, c) Λ_c^+ candidates in forward data, d) Λ_c^+ candidates in backward data.

In order to obtain the number of events in p_T and rapidity bins, the $log_{10}(\chi^2_{IP})$ distribution fit was performed in each bin (Appendix C). The prompt signal yields in p_T and rapidity bins are shown on Fig. 6.6.

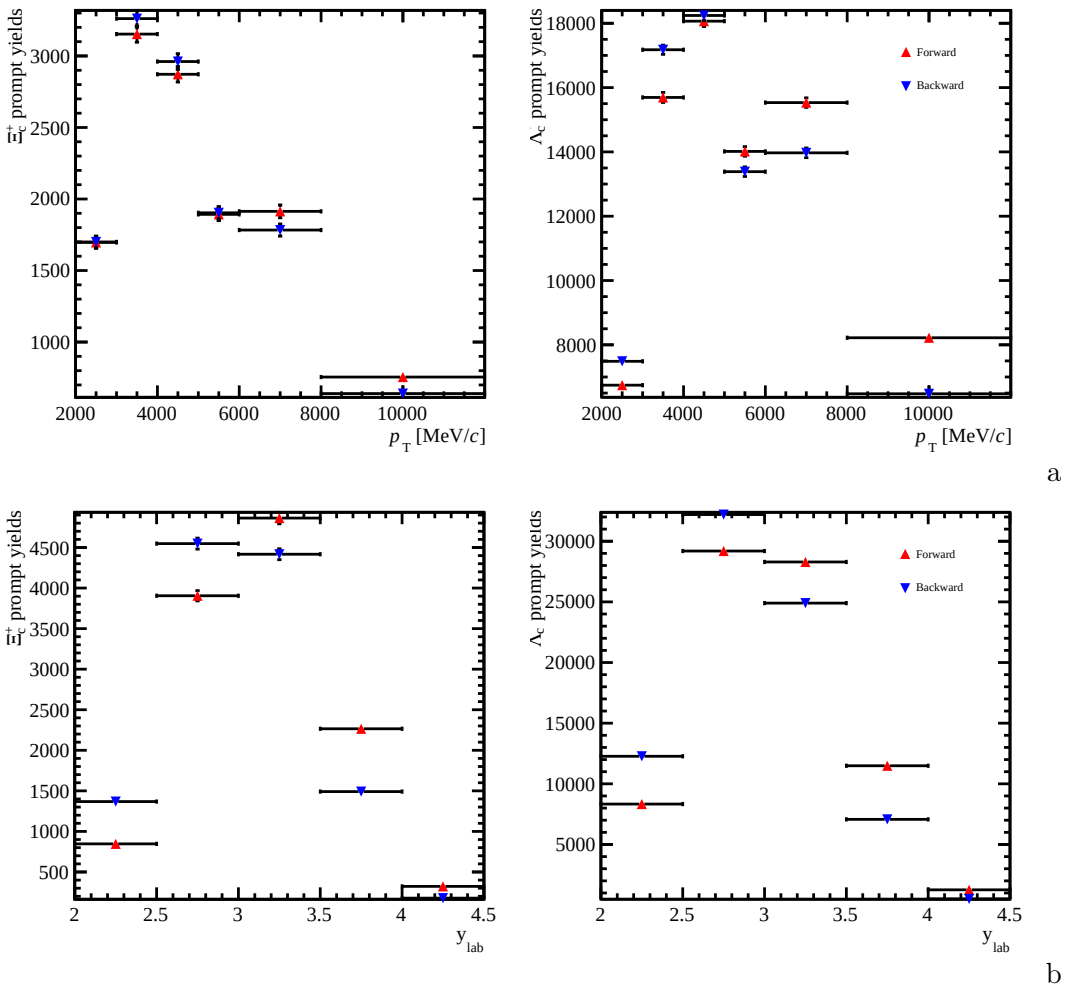

FIGURE 6.6: The prompt signal yields in p_T (top) and y_{lab} (bottom) bins.

The obtained number of promptly produced candidates in p_T and rapidity bins for forward and backward data samples are shown in Tables 6.4 and 6.5.

TABLE 6.4: The obtained number of promptly produced candidates in p_{T} bins for the forward and backward data samples.

Forward		
$p_{\mathrm{T}}/(\,\mathrm{GeV}/c)$	$N^{\Xi_c^+}$	$N^{\Lambda_c^+}$
(2.0, 3.0)	1696.5 ± 41.7	6745.6 ± 88.7
(3.0, 4.0)	3152.9 ± 57.0	15693.6 ± 155.9
(4.0, 5.0)	2872.0 ± 54.5	18065.0 ± 166.0
(5.0, 6.0)	1892.7 ± 44.1	14015.0 ± 149.6
(6.0, 8.0)	1913.7 ± 45.1	15533.1 ± 148.1
(8.0, 12.0)	755.3 ± 27.7	8220.0 ± 116.5
Backward		
$p_{\mathrm{T}}/(\,\mathrm{GeV}/c)$	$N^{\Xi_c^+}$	$N^{\Lambda_c^+}$
(2.0, 3.0)	1699.8 ± 41.7	7487.6 ± 91.2
(3.0, 4.0)	3261.1 ± 57.7	17176.7 ± 143.6
(4.0, 5.0)	2961.1 ± 55.4	18242.4 ± 159.1
(5.0, 6.0)	1903.5 ± 44.2	13385.2 ± 149.1
(6.0, 8.0)	1783.0 ± 42.7	13970.8 ± 150.9
(8.0, 12.0)	639.8 ± 26.0	6477.9 ± 109.2

TABLE 6.5: The obtained number of promptly produced candidates in rapidity bins for the forward and backward data samples.

Forward		
y^*	$N^{\Xi_c^+}$	$N^{\Lambda_c^+}$
(1.5, 2.0)	846.6 ± 29.5	8330.8 ± 94.2
(2.0, 2.5)	3905.0 ± 63.3	29192.4 ± 179.9
(2.5, 3.0)	4862.7 ± 71.0	28290.9 ± 223.5
(3.0, 3.5)	2265.3 ± 48.6	11488.7 ± 129.0
(3.5, 4.0)	322.5 ± 19.0	1260.8 ± 46.5
Backward		
y^*	$N^{\Xi_c^+}$	$N^{\Lambda_c^+}$
(-5.0, -4.5)	177.7 ± 13.6	511.2 ± 26.6
(-4.5, -4.0)	1491.0 ± 39.6	7070.4 ± 97.8
(-4.0, -3.5)	4416.9 ± 67.5	24898.0 ± 190.1
(-3.5, -3.0)	4547.8 ± 68.1	32198.2 ± 186.8
(-3.0, -2.5)	1368.0 ± 37.3	12270.5 ± 113.9

Chapter 7

Efficiencies

The obtained number of signal candidates of the Ξ_c^+ (Λ_c^+) baryon suffers from inefficiencies associated with the geometrical acceptance of the detector, track reconstruction, particle identification and offline selections. It is necessary to evaluate these inefficiencies in order to obtain the "true" number of produced signal in given regions of p_T and rapidity. Thus, the total efficiency of the procedure to identify the number of candidates consists of several components, *e.g.* the geometrical acceptance ε_{acc}, the trigger efficiency $\varepsilon_{trg/sel}$, the reconstruction and selection efficiency $\varepsilon_{sel/rec}$ and the particle identification (PID) efficiency ε_{PID}; it can be written as

$$\epsilon_{tot} = \varepsilon_{acc} \times \varepsilon_{trg/sel} \times \varepsilon_{sel/rec} \times \varepsilon_{PID}. \tag{7.1}$$

The methods to evaluate each efficiency component are described in the following.

7.1 Geometrical acceptance

The geometrical acceptance, ε_{acc}, is the efficiency of the selection applied on the children of the decaying particle to fall within the LHCb detector acceptance, defined by an angle of $10< \theta <400$ mrad. Such efficiency takes into account Ξ_c^+ (Λ_c^+) candidates in the LHCb acceptance which weren't reconstructed as one or more of their children didn't fall within the LHCb detector acceptance. Since this requirement is applied to the signal MC sample which is then used for the selection, ε_{acc} is evaluated using a generator-only sample without reconstruction applied, where this requirement is waived. Thus, ε_{acc} is defined as

$$\varepsilon_{acc} \equiv \frac{\Xi_c^+ \ (\Lambda_c^+) \text{ and its children} \in [10, 400]\,\text{mrad}}{\Xi_c^+ \ (\Lambda_c^+) \in [10, 400]\,\text{mrad}}. \tag{7.2}$$

In Fig. 7.1, the measured acceptance efficiency is shown for Ξ_c^+ (purple) and Λ_c^+ (blue) as a function of p_T in forward (a) and backward (b) and as a function of $|y^*|$ in forward (c) and backward (d). The values of ε_{acc} in different bins are reported in Tables 7.1 and 7.2.

As the acceptance efficiency is a geometrical value, it is not expected to depend on the multiplicity of the corresponding collision, therefore no corrections of the generator level MC is needed.

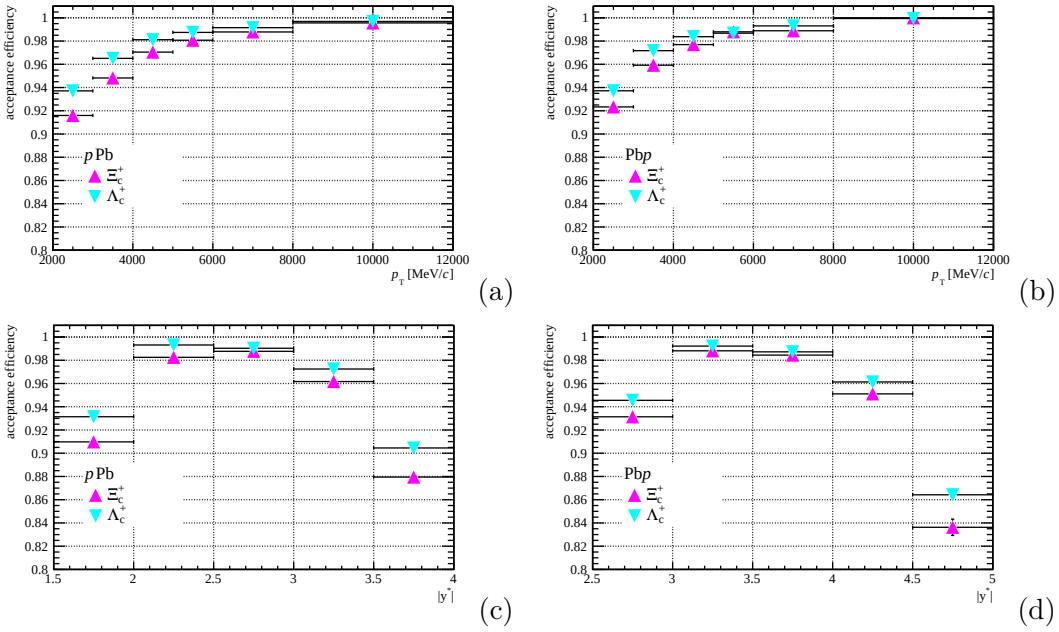

FIGURE 7.1: Acceptance efficiency for Ξ_c^+ (purple) and Λ_c^+ (blue) as a function of p_T of the baryon in forward (a) and backward (b) and as a function of $|y^*|$ in forward (c) and backward (d).

TABLE 7.1: Acceptance efficiency for Ξ_c^+ and Λ_c^+ in p_T bins for forward and backward data samples. The uncertainties are statistical only.

Forward		
$p_T/(\,\mathrm{GeV}/c)$	$\varepsilon_{\mathrm{acc}}{}^{\Xi_c^+}$ (%)	$\varepsilon_{\mathrm{acc}}{}^{\Lambda_c^+}$ (%)
(2.0, 3.0)	91.60 ± 0.20	93.71 ± 0.11
(3.0, 4.0)	94.82 ± 0.19	96.51 ± 0.11
(4.0, 5.0)	97.05 ± 0.19	98.11 ± 0.11
(5.0, 6.0)	98.07 ± 0.20	98.74 ± 0.11
(6.0, 8.0)	98.78 ± 0.17	99.15 ± 0.10
(8.0, 12.0)	99.56 ± 0.14	99.68 ± 0.09
Backward		
$p_T/(\,\mathrm{GeV}/c)$	$\varepsilon_{\mathrm{acc}}{}^{\Xi_c^+}$ (%)	$\varepsilon_{\mathrm{acc}}{}^{\Lambda_c^+}$ (%)
(2.0, 3.0)	92.33 ± 0.24	93.72 ± 0.13
(3.0, 4.0)	95.92 ± 0.23	97.17 ± 0.12
(4.0, 5.0)	97.69 ± 0.24	98.37 ± 0.13
(5.0, 6.0)	98.79 ± 0.25	98.68 ± 0.16
(6.0, 8.0)	98.88 ± 0.26	99.30 ± 0.13
(8.0, 12.0)	100.00 ± 0.13	99.94 ± 0.07

7.2 Reconstruction and selection efficiency

The efficiency of the reconstruction and selection $\varepsilon_{\mathrm{sel/rec}}$ is the efficiency of reconstructing the signal particle and that this particle survives the selection criteria described

TABLE 7.2: Acceptance efficiency for Ξ_c^+ and Λ_c^+ in rapidity bins for forward and backward data samples.

Forward		
y^*	$\varepsilon_{\text{acc}}{}^{\Xi_c^+}$ (%)	$\varepsilon_{\text{acc}}{}^{\Lambda_c^+}$ (%)
(1.5, 2.0)	90.98 ± 0.25	93.14 ± 0.15
(2.0, 2.5)	98.25 ± 0.12	99.31 ± 0.05
(2.5, 3.0)	98.77 ± 0.11	99.03 ± 0.06
(3.0, 3.5)	96.17 ± 0.20	97.25 ± 0.12
(3.5, 4.0)	87.95 ± 0.39	90.45 ± 0.24
Backward		
y^*	$\varepsilon_{\text{acc}}{}^{\Xi_c^+}$ (%)	$\varepsilon_{\text{acc}}{}^{\Lambda_c^+}$ (%)
(-5.0, -4.5)	83.63 ± 0.70	86.42 ± 0.39
(-4.5, -4.0)	95.11 ± 0.33	96.13 ± 0.18
(-4.0, -3.5)	98.44 ± 0.16	98.72 ± 0.09
(-3.5, -3.0)	98.81 ± 0.13	99.22 ± 0.06
(-3.0, -2.5)	93.13 ± 0.28	94.55 ± 0.15

in Tables 6.1 and 6.3 (excluding PID selections). The first part of the efficiency is the efficiency of reconstructing a track with the LHCb tracking procedure and can be affected by the different multiplicities found in the forward and backward configurations. Since the reconstruction algorithm is tuned to be efficient in pp collisions at low multiplicity, the reconstruction efficiency tends to decrease in proton-lead collisions as the charged particles multiplicity in the event increases with the detector occupancy. To correct for this effect we use the simulation. An example of the comparison of multiplicities in data and MC is shown in Fig. 7.2 where the distributions of the number of VELO clusters ($nVeloClusters$) is plotted. We can observe that the $nVeloClusters$ distributions in data are more similar for forward and backward data (left) than in Monte Carlo (right).

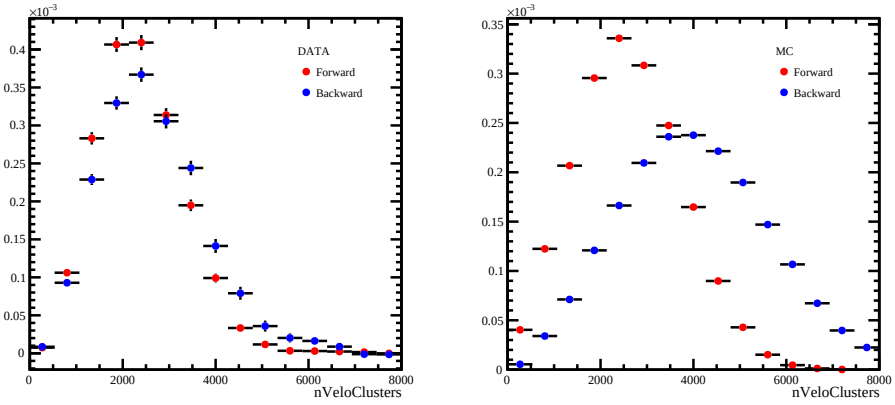

FIGURE 7.2: Distributions of $nVeloClusters$ in Ξ_c^+ signal data (left) and MC (right). We can observe that the $nVeloClusters$ distributions are quite similar for forward and backward in data and not in Monte Carlo.

$\varepsilon_{\text{sel/rec}}$ was studied by means of MC samples described in Sec. 4.4 with a full simulation of the LHCb detector. However simulated MC events don't reproduce the data perfectly since:

- The true shapes of p_{T} and rapidity of the signal are unknown;
- There are no intermediate states of Ξ_{c}^{+} (Λ_{c}^{+}) decay (*e.g.* $\Xi_{\text{c}}^{+} \to p^{+}K^{*}(892)$) included in the MC;
- The particle multiplicity is not well reproduced;
- The tracking efficiency is overestimated in the simulation compared to data.

Therefore, the MC samples need to be corrected to account for all these effects.

7.2.1 MC reweighting

The reconstruction/tracking efficiency has been studied by reweighting the MC distributions of p_{T}, y^{*}, $nVeloClusters$ and invariant mass of $p^{+}K^{-}$ and $K^{-}\pi^{+}$ with the same distributions obtained using prompt $\Xi_{\text{c}}^{+}(\Lambda_{\text{c}}^{+})$ signal from data. The Ξ_{c}^{+} (Λ_{c}^{+}) signal distributions are unfolded from data using the sPlot [124] technique and the weights are determined as the ratio of the distributions in data over that in simulation. The distributions of data signal, MC and reweighted MC are shown in Fig. 7.3, 7.4 for the Ξ_{c}^{+} samples and in Fig. 7.5, 7.6 for the Λ_{c}^{+} samples. The Dalitz plot distributions for data and MC are shown on Fig. 7.7, 7.8, 7.9, 7.10. One can find that after the reweighting procedure the MC reproduces well the kinematic of the Ξ_{c}^{+} (Λ_{c}^{+}) decay.

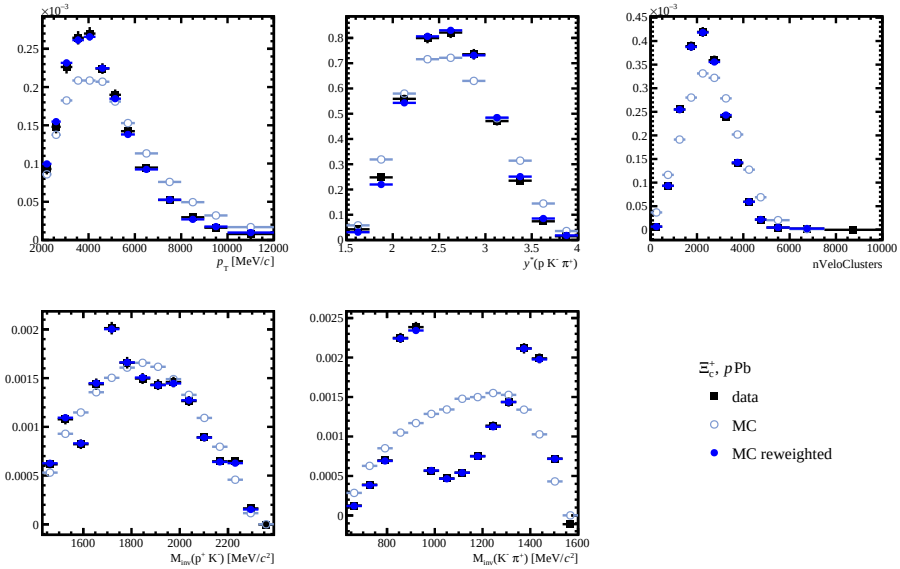

FIGURE 7.3: Normalised distributions of p_{T} (top-left), rapidity (top-middle), nVeloClusters (top-right), $M_{inv}(p^{+}K^{-})$ (bottom-left) and $M_{inv}(K^{-}\pi^{+})$ (bottom-middle) obtained in the Ξ_{c}^{+} signal data (black dots) and MC (empty circles). Reweighted MC (blue circles) is used for the evaluation of the reconstruction and selection efficiency.

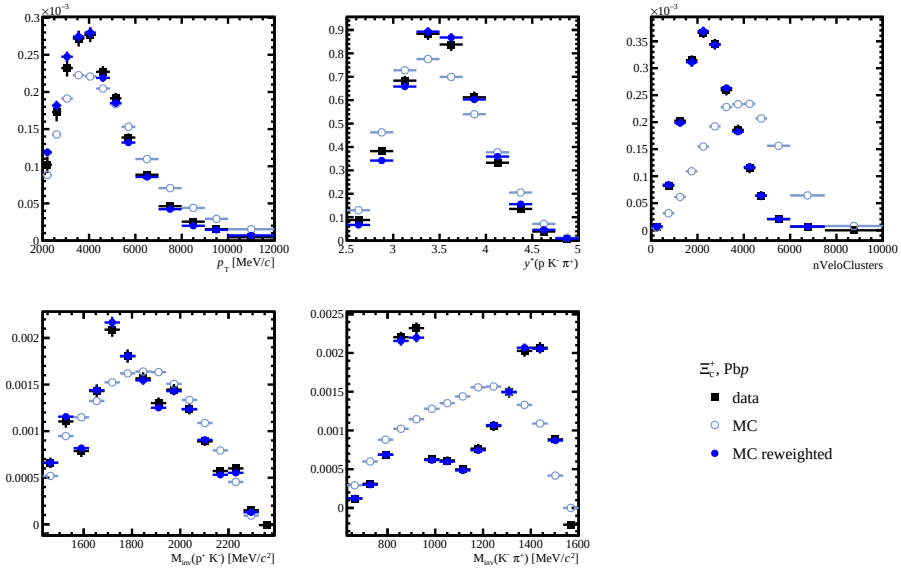

FIGURE 7.4: Normalised distributions of p_{T} (top-left), rapidity (top-middle), nVeloClusters (top-right), $M_{inv}(p^+K^-)$ (bottom-left) and $M_{inv}(K^-\pi^+)$ (bottom-middle) obtained in the Ξ_c^+ signal data (black dots) and MC (empty circles). Reweighted MC (blue circles) is used for the evaluation of the reconstruction and selection efficiency.

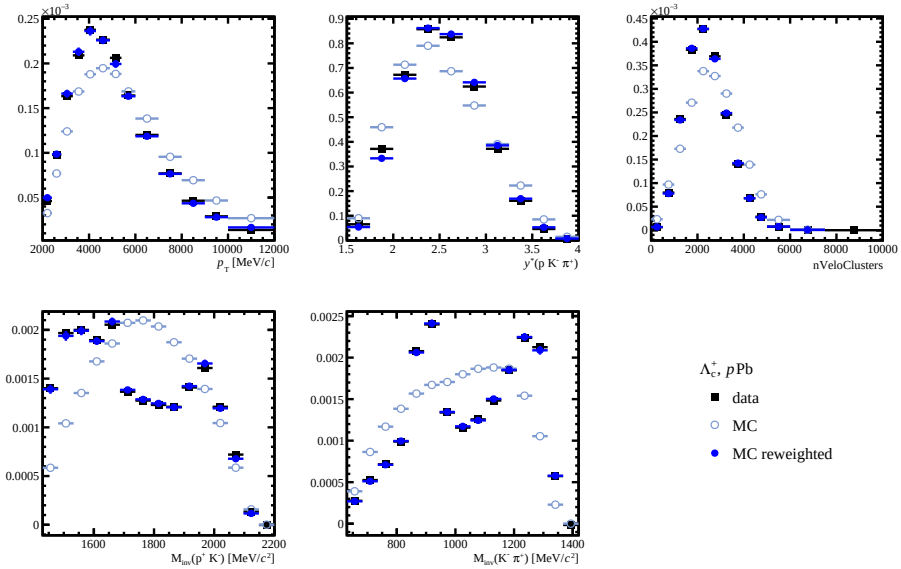

FIGURE 7.5: Normalised distributions of p_{T} (top-left), rapidity (top-middle), nVeloClusters (top-right), $M_{inv}(p^+K^-)$ (bottom-left) and $M_{inv}(K^-\pi^+)$ (bottom-middle) obtained in the Λ_c^+ signal data (black dots) and MC (empty circles). Reweighted MC (blue circles) is used for the evaluation of the reconstruction and selection efficiency.

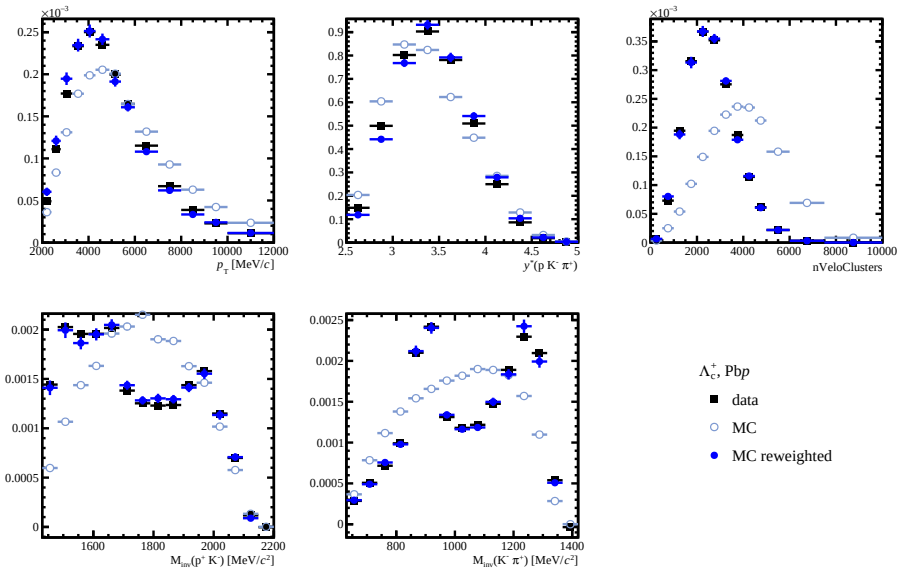

FIGURE 7.6: Normalised distributions of p_T (top-left), rapidity (top-middle), nVeloClusters (top-right), $M_{inv}(p^+K^-)$ (bottom-left) and $M_{inv}(K^-\pi^+)$ (bottom-middle) obtained in the Λ_c^+ signal data (black dots) and MC (empty circles). Reweighted MC (blue circles) is used for the evaluation of the reconstruction and selection efficiency.

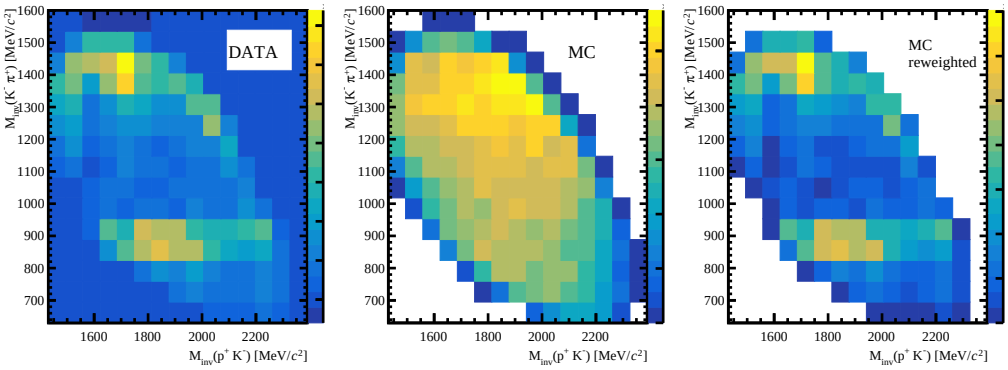

FIGURE 7.7: Dalitz plot distribution of $\Xi_c^+ \to p^+K^-\pi^+$ decay in forward data (left), MC (middle) and reweighted MC (right).

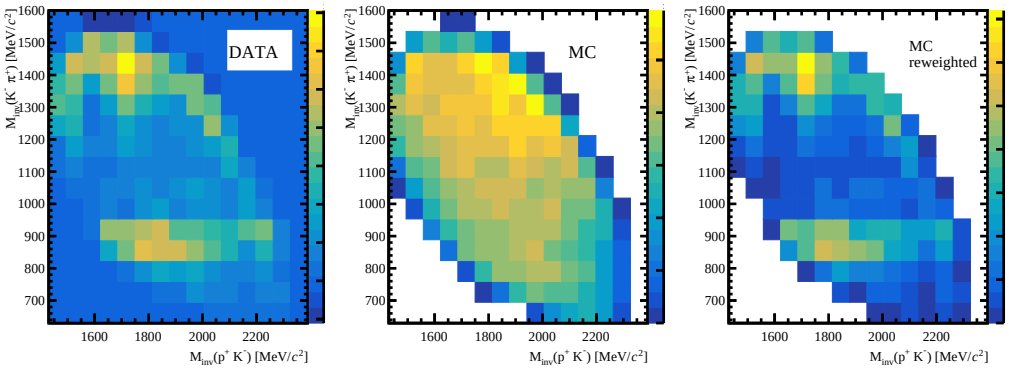

FIGURE 7.8: Dalitz plot distribution of $\Xi_c^+ \to p^+K^-\pi^+$ decay in backward data (left), MC (middle) and reweighted MC (right).

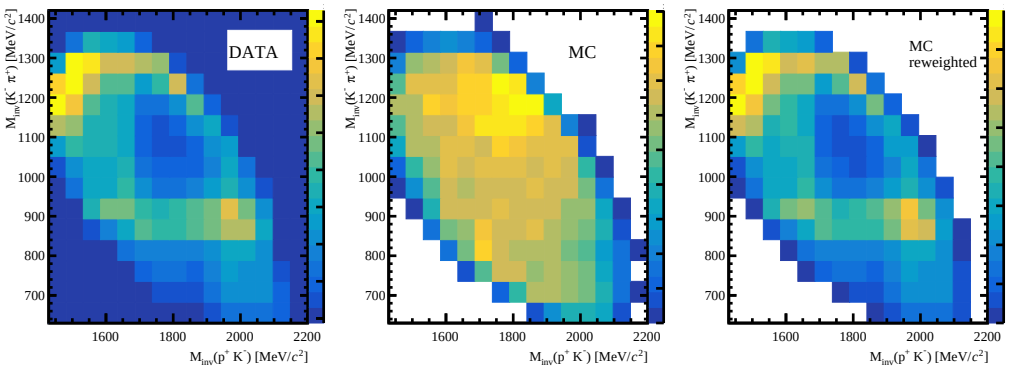

FIGURE 7.9: Dalitz plot distribution of $\Lambda_c^+ \to p^+K^-\pi^+$ decay in forward data (left), MC (middle) and reweighted MC (right).

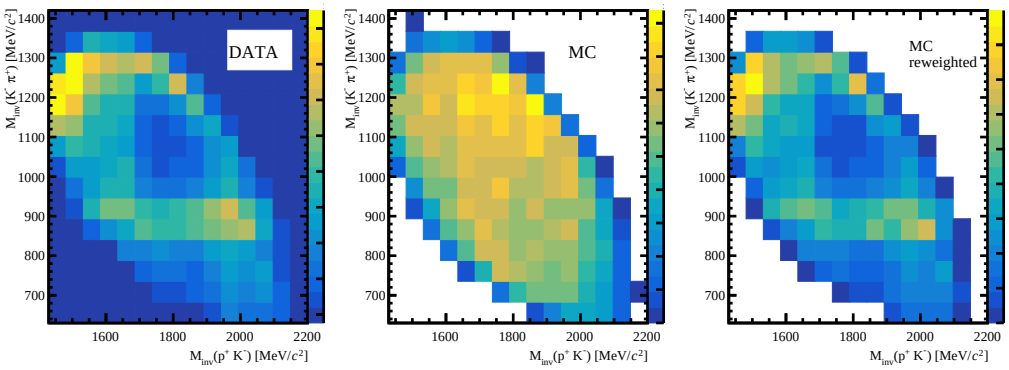

FIGURE 7.10: Dalitz plot distribution of $\Lambda_c^+ \to p^+K^-\pi^+$ decay in backward data (left), MC (middle) and reweighted MC (right).

7.2.2 Tracking corrections

The tracking efficiency for data and simulation is different. This efficiency is given as a function of momentum and pseudo-rapidity (Fig. 7.11), studied in b-hadron production

at $\sqrt{s} = 8$ TeV in pPb collisions [128]. The calibration is performed using a tag-and-probe method [1] with detached J/ψ decays constructed in the Turbo stream in both data and simulation. For hadrons the correlated uncertainties are evaluated as 1.1% for kaons, 1.4% for pions and 2.0% for protons.

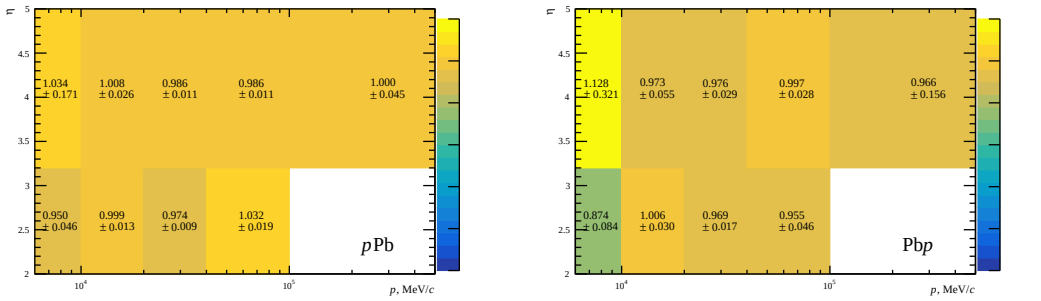

(a) (b)

FIGURE 7.11: The tracking efficiency table from tracking calibration of $\sqrt{s} = 8.16$ TeV b-hadron production analysis in the forward (a) and backward (b) configurations [128].

Combining all the ingredients together, the efficiency $\varepsilon_{\text{sel/rec}}$ is thus defined as

$$\varepsilon_{\text{sel/rec}} \equiv \frac{\sum_i \Xi_c^+(\Lambda_c^+) \text{ reconstructed and selected} \times w_i^{RW} \times w_i^{tr}}{\sum_i \Xi_c^+(\Lambda_c^+) \text{ and its children} \in [10, 400]\,\text{mrad} \times w_i^{RW} \times w_i^{tr}}, \tag{7.3}$$

where w_i^{RW} is the weight obtained in Sec. 7.2.1 for the i-th event and w_i^{tr} is the tracking correction for the i-th event, which is calculated as a product of corrections from Fig. 7.11 for a proton, a kaon and a pion $w_i^{tr} = w_i(p_{p^+}, \eta_{p^+}) \times w_i(p_{K^-}, \eta_{K^-}) \times w_i(p_{\pi^+}, \eta_{\pi^+})$. The measured $\varepsilon_{\text{sel/rec}}$ is shown in Fig. 7.12 as a function of p_{T} and y^*, and numerical values in percentile can be found in Tables 7.3 and 7.4. Due to the difference of Ξ_c^+ and Λ_c^+ mass, the same combinatorial cuts on their decay kinematic in the Turbo selection remove almost 10 times more signal events. Therefore, the $\varepsilon_{\text{sel/rec}}$ is higher for the Ξ_c^+ baryon.

[1] The tag-and-probe method is an experimental procedure that allows to measure a process' efficiency directly from data. The procedure provides an unbiased sample of *probe* objects that can be then used to measure the efficiency of a particular selection criteria.

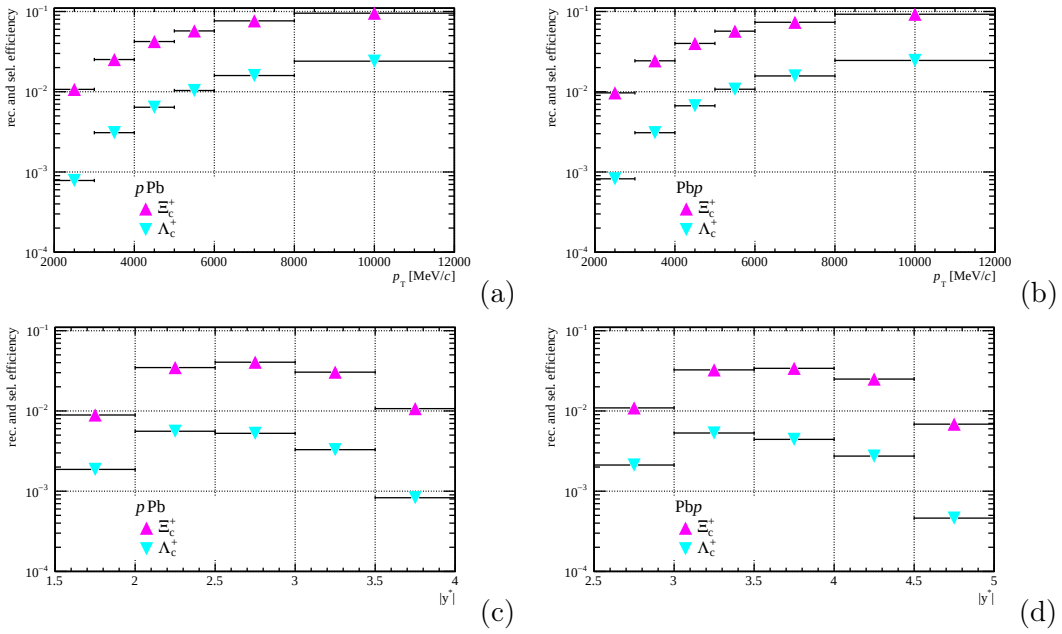

FIGURE 7.12: Reconstruction and selection efficiency for Ξ_c^+ (purple) and Λ_c^+ (blue) as a function of p_T in forward (a) and backward (b) and as a function of $|y^*|$ in forward (c) and backward (d).

TABLE 7.3: Reconstruction and selection efficiency for Ξ_c^+ and Λ_c^+ in p_T bins for forward and backward data samples.

Forward		
$p_T/(\,\mathrm{GeV}/c)$	$\varepsilon_{\mathrm{acc}}{}^{\Xi_c^+}$ (%)	$\varepsilon_{\mathrm{acc}}{}^{\Lambda_c^+}$ (%)
(2.0, 3.0)	1.070 ± 0.003	0.078 ± 0.000
(3.0, 4.0)	2.520 ± 0.005	0.309 ± 0.001
(4.0, 5.0)	4.224 ± 0.009	0.641 ± 0.001
(5.0, 6.0)	5.728 ± 0.013	1.036 ± 0.002
(6.0, 8.0)	7.646 ± 0.018	1.592 ± 0.002
(8.0, 12.0)	9.526 ± 0.026	2.404 ± 0.003
backward		
$p_T/(\,\mathrm{GeV}/c)$	$\varepsilon_{\mathrm{acc}}{}^{\Xi_c^+}$ (%)	$\varepsilon_{\mathrm{acc}}{}^{\Lambda_c^+}$ (%)
(2.0, 3.0)	0.968 ± 0.006	0.082 ± 0.001
(3.0, 4.0)	2.430 ± 0.011	0.309 ± 0.001
(4.0, 5.0)	4.000 ± 0.016	0.668 ± 0.002
(5.0, 6.0)	5.687 ± 0.025	1.075 ± 0.003
(6.0, 8.0)	7.340 ± 0.031	1.574 ± 0.004
(8.0, 12.0)	9.247 ± 0.086	2.454 ± 0.008

7.3 PID efficiency

The PID efficiency is the efficiency of the particle identification criteria applied in the DLL variable applied during the selection which is specific for each particle. This

TABLE 7.4: Reconstruction and selection efficiency for Ξ_c^+ and Λ_c^+ in rapidity bins for forward and backward data samples.

Forward		
y^*	$\varepsilon_{\rm acc}{}^{\Xi_c^+}$ (%)	$\varepsilon_{\rm acc}{}^{\Lambda_c^+}$ (%)
(1.5, 2.0)	0.891 ± 0.003	0.187 ± 0.000
(2.0, 2.5)	3.473 ± 0.006	0.559 ± 0.001
(2.5, 3.0)	4.052 ± 0.007	0.526 ± 0.001
(3.0, 3.5)	3.045 ± 0.007	0.329 ± 0.001
(3.5, 4.0)	1.069 ± 0.006	0.083 ± 0.000
Backward		
y^*	$\varepsilon_{\rm acc}{}^{\Xi_c^+}$ (%)	$\varepsilon_{\rm acc}{}^{\Lambda_c^+}$ (%)
(-5.0, -4.5)	0.685 ± 0.011	0.046 ± 0.001
(-4.5, -4.0)	2.497 ± 0.013	0.274 ± 0.001
(-4.0, -3.5)	3.399 ± 0.012	0.442 ± 0.001
(-3.5, -3.0)	3.250 ± 0.011	0.531 ± 0.001
(-3.0, -2.5)	1.092 ± 0.005	0.212 ± 0.001

efficiency is studied using the `PIDCalib2` package, which is based on [129] with dedicated PID calibration samples as a function of momentum, rapidity and nSPDHits[2], $\epsilon_{h^\pm} = \epsilon_{h^\pm}(p_{h^\pm}, \eta_{h^\pm}, \text{nSPDHits}_{h^\pm})$, for each proton, kaon and pion particle, differently in the forward and backward samples. These samples provide efficiencies for a single track to be identified with given PID selections criteria. The efficiency was calculated as convolution with $\Xi_c^+(\Lambda_c^+)$ decay kinematic distributions obtained from MC and reweighted by data, as described in Sec. 7.2. The PID efficiency was measured by the equation

$$\varepsilon_{\rm PID}{}^{\Xi_c^+(\Lambda_c^+)} = \frac{\sum_i \epsilon_{p^+} \cdot \epsilon_{K^-} \cdot \epsilon_{\pi^+} \times w_i^{RW}}{\sum_i w_i^{RW}}, \tag{7.4}$$

where $\epsilon_{h^\pm}$ is the single track PID efficiency and w_i^{RW} is the reweighting correction. The PID efficiency as a function of $p_{\rm T}$ and rapidity is shown in Fig. 7.13, and numerical values in percentile can be found in Tables 7.5 and 7.6.

7.4 Trigger efficiency

The trigger efficiency $\varepsilon_{\rm trg/sel}$ is the efficiency of the trigger selection. It is evaluated with simulation and it is defined as $\varepsilon_{\rm trg/sel} = \frac{A}{B}$, where B is the number of events which survived reconstruction and selection, and A is the subset of B where the event also fired at least one of the trigger lines defined in Sec. 6.2.2. The trigger efficiency is shown in Fig. 7.14 as a function of $p_{\rm T}$ and rapidity, and numerical values in percentile can be found in Tables 7.5 and 7.6.

[2]Number of hits in the SPD calorimeter

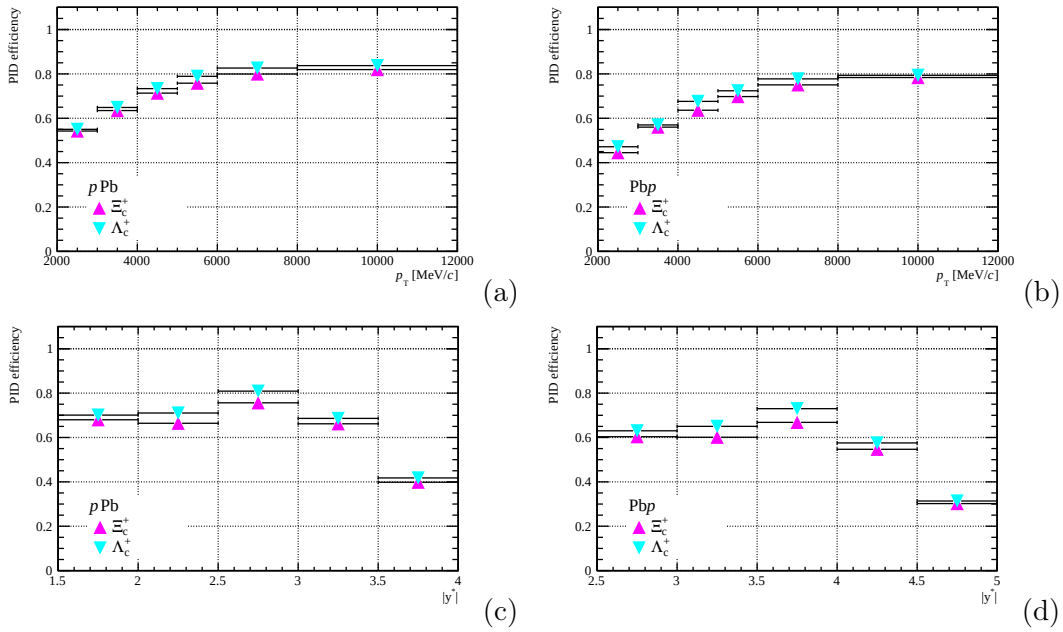

FIGURE 7.13: PID efficiency for Ξ_c^+ (purple) and Λ_c^+ (blue) as a function of p_T in forward (a) and backward (b) and as a function of $|y^*|$ in forward (c) and backward (d).

TABLE 7.5: PID efficiency for Ξ_c^+ and Λ_c^+ in p_T bins for forward and backward data samples.

Forward		
$p_T/(\,\mathrm{GeV}/c)$	$\varepsilon_{\mathrm{PID}}{}^{\Xi_c^+}$ (%)	$\varepsilon_{\mathrm{PID}}{}^{\Lambda_c^+}$ (%)
(2.0, 3.0)	54.25 ± 0.23	55.02 ± 0.26
(3.0, 4.0)	63.49 ± 0.20	64.87 ± 0.17
(4.0, 5.0)	71.33 ± 0.22	73.36 ± 0.16
(5.0, 6.0)	75.82 ± 0.24	78.91 ± 0.18
(6.0, 8.0)	79.95 ± 0.27	82.64 ± 0.15
(8.0, 12.0)	81.95 ± 0.30	83.73 ± 0.17
Backward		
$p_T/(\,\mathrm{GeV}/c)$	$\varepsilon_{\mathrm{PID}}{}^{\Xi_c^+}$ (%)	$\varepsilon_{\mathrm{PID}}{}^{\Lambda_c^+}$ (%)
(2.0, 3.0)	44.49 ± 0.43	47.17 ± 0.53
(3.0, 4.0)	56.01 ± 0.38	56.99 ± 0.35
(4.0, 5.0)	63.63 ± 0.39	67.61 ± 0.35
(5.0, 6.0)	69.79 ± 0.45	72.39 ± 0.34
(6.0, 8.0)	75.05 ± 0.46	77.76 ± 0.31
(8.0, 12.0)	78.37 ± 1.12	79.38 ± 0.36

TABLE 7.6: PID efficiency for Ξ_c^+ and Λ_c^+ in rapidity bins for forward and backward data samples.

Forward		
y^*	$\varepsilon_{\mathrm{PID}}{}^{\Xi_c^+}$ (%)	$\varepsilon_{\mathrm{PID}}{}^{\Lambda_c^+}$ (%)
(1.5, 2.0)	67.99 ± 0.40	70.09 ± 0.17
(2.0, 2.5)	66.41 ± 0.16	71.03 ± 0.11
(2.5, 3.0)	75.63 ± 0.17	80.89 ± 0.14
(3.0, 3.5)	66.18 ± 0.23	68.61 ± 0.18
(3.5, 4.0)	39.83 ± 0.34	41.78 ± 0.31
Backward		
y^*	$\varepsilon_{\mathrm{PID}}{}^{\Xi_c^+}$ (%)	$\varepsilon_{\mathrm{PID}}{}^{\Lambda_c^+}$ (%)
(-5.0, -4.5)	30.21 ± 0.82	31.37 ± 0.98
(-4.5, -4.0)	54.68 ± 0.46	57.55 ± 0.39
(-4.0, -3.5)	66.81 ± 0.34	72.99 ± 0.33
(-3.5, -3.0)	60.11 ± 0.31	65.02 ± 0.24
(-3.0, -2.5)	60.35 ± 0.41	63.02 ± 0.28

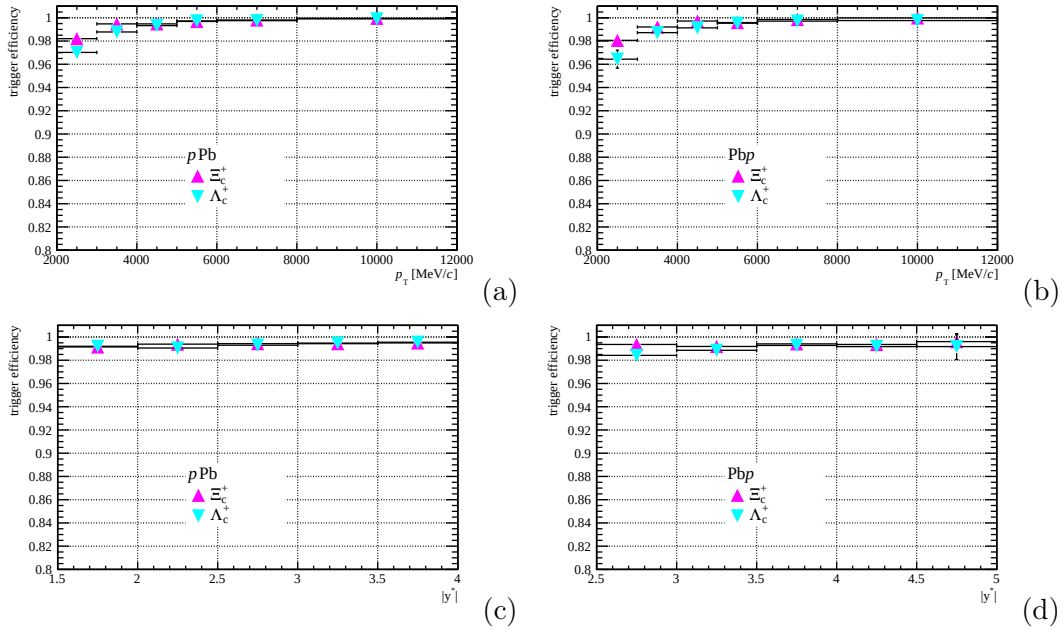

FIGURE 7.14: Trigger efficiency for Ξ_c^+ (purple) and Λ_c^+ (blue) as a function of p_{T} in forward (a) and backward (b) and as a function of $|y^*|$ in forward (c) and backward (d).

TABLE 7.7: Trigger efficiency for Ξ_c^+ and Λ_c^+ in p_T bins for forward and backward data samples.

Forward		
$p_T/(\,\mathrm{GeV}/c)$	$\varepsilon_{\mathrm{trg/sel}}{}^{\Xi_c^+}$ (%)	$\varepsilon_{\mathrm{trg/sel}}{}^{\Lambda_c^+}$ (%)
(2.0, 3.0)	98.20 ± 0.45	97.02 ± 0.43
(3.0, 4.0)	99.48 ± 0.41	98.78 ± 0.18
(4.0, 5.0)	99.48 ± 0.41	99.33 ± 0.12
(5.0, 6.0)	99.68 ± 0.41	99.73 ± 0.08
(6.0, 8.0)	99.81 ± 0.40	99.75 ± 0.07
(8.0, 12.0)	99.95 ± 0.40	99.90 ± 0.05
Backward		
$p_T/(\,\mathrm{GeV}/c)$	$\varepsilon_{\mathrm{trg/sel}}{}^{\Xi_c^+}$ (%)	$\varepsilon_{\mathrm{trg/sel}}{}^{\Lambda_c^+}$ (%)
(2.0, 3.0)	98.06 ± 0.51	96.44 ± 0.77
(3.0, 4.0)	99.21 ± 0.43	98.72 ± 0.48
(4.0, 5.0)	99.72 ± 0.41	99.13 ± 0.45
(5.0, 6.0)	99.59 ± 0.42	99.53 ± 0.43
(6.0, 8.0)	99.86 ± 0.41	99.71 ± 0.42
(8.0, 12.0)	99.99 ± 0.41	99.76 ± 0.42

TABLE 7.8: Trigger efficiency for Ξ_c^+ and Λ_c^+ in rapidity bins for forward and backward data samples.

Forward		
y^*	$\varepsilon_{\mathrm{trg/sel}}{}^{\Xi_c^+}$ (%)	$\varepsilon_{\mathrm{trg/sel}}{}^{\Lambda_c^+}$ (%)
(1.5, 2.0)	99.14 ± 0.44	99.20 ± 0.43
(2.0, 2.5)	99.39 ± 0.41	99.05 ± 0.41
(2.5, 3.0)	99.43 ± 0.41	99.29 ± 0.41
(3.0, 3.5)	99.43 ± 0.41	99.48 ± 0.42
(3.5, 4.0)	99.49 ± 0.44	99.56 ± 0.49
Backward		
y^*	$\varepsilon_{\mathrm{trg/sel}}{}^{\Xi_c^+}$ (%)	$\varepsilon_{\mathrm{trg/sel}}{}^{\Lambda_c^+}$ (%)
(-5.0, -4.5)	99.60 ± 0.58	99.18 ± 1.11
(-4.5, -4.0)	99.36 ± 0.44	99.17 ± 0.49
(-4.0, -3.5)	99.41 ± 0.42	99.27 ± 0.43
(-3.5, -3.0)	99.19 ± 0.42	98.85 ± 0.43
(-3.0, -2.5)	99.36 ± 0.44	98.42 ± 0.49

Chapter 8

Systematic uncertainties

There are several sources of uncertainties, which arise from the limitations of the methods we use and can affect the final result. In this chapter the evaluation of the systematic uncertainties that affect the measurement of the observables defined in Sec. 5 is addressed. The uncertainty associated with the signal candidates' extraction from the invariant mass and the $log_{10}(\chi^2_{IP})$ fit is described in Sec. 8.1 and Sec. 8.2, respectively. The systematic uncertainties coming from the efficiencies are described in Sec. 8.3.

8.1 Background estimate

The systematic uncertainty on the invariant mass fit is evaluated by varying the method used to evaluate the number of background events from the sPlot method to the sideband subtraction as explained in Sec. 6.3. The difference between the values found in these two ways is used as systematic uncertainty on the method. The relative systematic uncertainties on the invariant mass fit are presented on Fig. 8.1. The average systematic uncertainty is around ∼4.7% for the Ξ_c^+ invariant mass fit and ∼1.8% for the Λ_c^+ invariant mass fit.

8.2 Signal estimate

The systematic uncertainty on the signal determination is evaluated by varying the function used in the fit, which is nominally performed with a Bukin function. To evaluate the systematic, the fit is repeated using a Gaussian function for the non-promptly produced fraction of $\Xi_c^+(\Lambda_c^+)$ keeping the Bukin function for the prompt part and the number of signal events estimated again. The difference between this number and the nominal value is taken as systematic uncertainty on the signal. The relative systematic uncertainties on the signal are presented on Fig. 8.2. It can be noticed that the uncertainties on Λ_c^+ signal shows significant bin-to-bin correlation. Therefore, these uncertainties are taken as correlated in the analysis. The corresponding uncertainties amount to 4.8% and 2.8% in the forward and backward samples in p_{T} bins and 3.1% in the backward sample in $|y^*|$ bins on the Λ_c^+ signal. The average uncertainty on the Ξ_c^+ signal determination is around ∼1.1%.

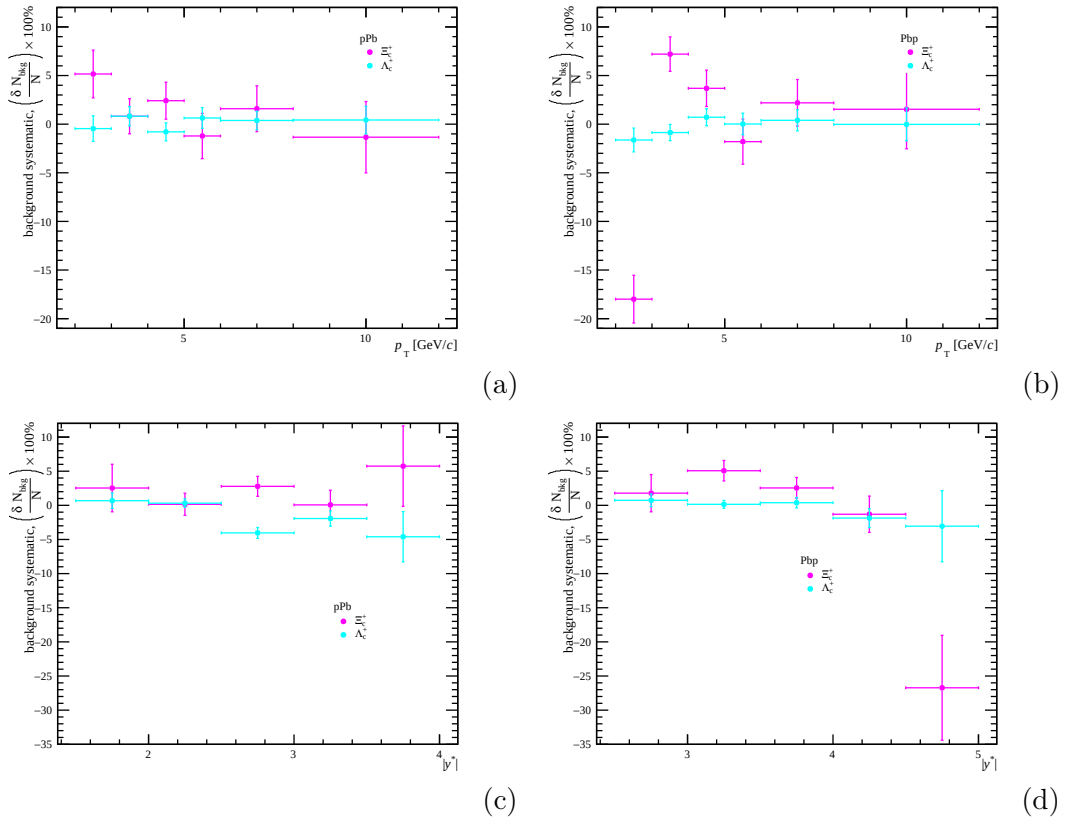

FIGURE 8.1: Relative systematic uncertainties on Ξ_c^+ (purple) and Λ_c^+ (blue) invariant mass fit as a function of p_T in forward (a) and backward (b) and as a function of $|y^*|$ in forward (c) and backward (d) data samples.

8.3 Efficiencies

The systematic uncertainty on the several components of the total efficiency are discussed in the following.

8.3.1 Acceptance

Since the acceptance has been evaluated using a privately generated sample with only generator information with limited statistics, the statistical uncertainty on the sample is taken as systematic uncertainty on ε_{acc}, which amounts to around $\sim$0.2%.

8.3.2 Reconstruction and selection efficiencies

The uncertainty on $\varepsilon_{\text{sel/rec}}$ has been evaluated by varying the reweighting procedure. The efficiency was calculated with weights, obtained from p_T, rapidity, $nVeloClusters$, $M_{\text{inv}}(p^+K^-)$, $M_{\text{inv}}(K^-\pi^+)$ and only from p_T, rapidity, $nVeloClusters$. The difference between the efficiencies found in these two ways combined with the statistical uncertainty on the MC sample and the uncertainty propagated from the weights is used as systematic uncertainty on $\varepsilon_{\text{sel/rec}}$. Another source of systematic uncertainty

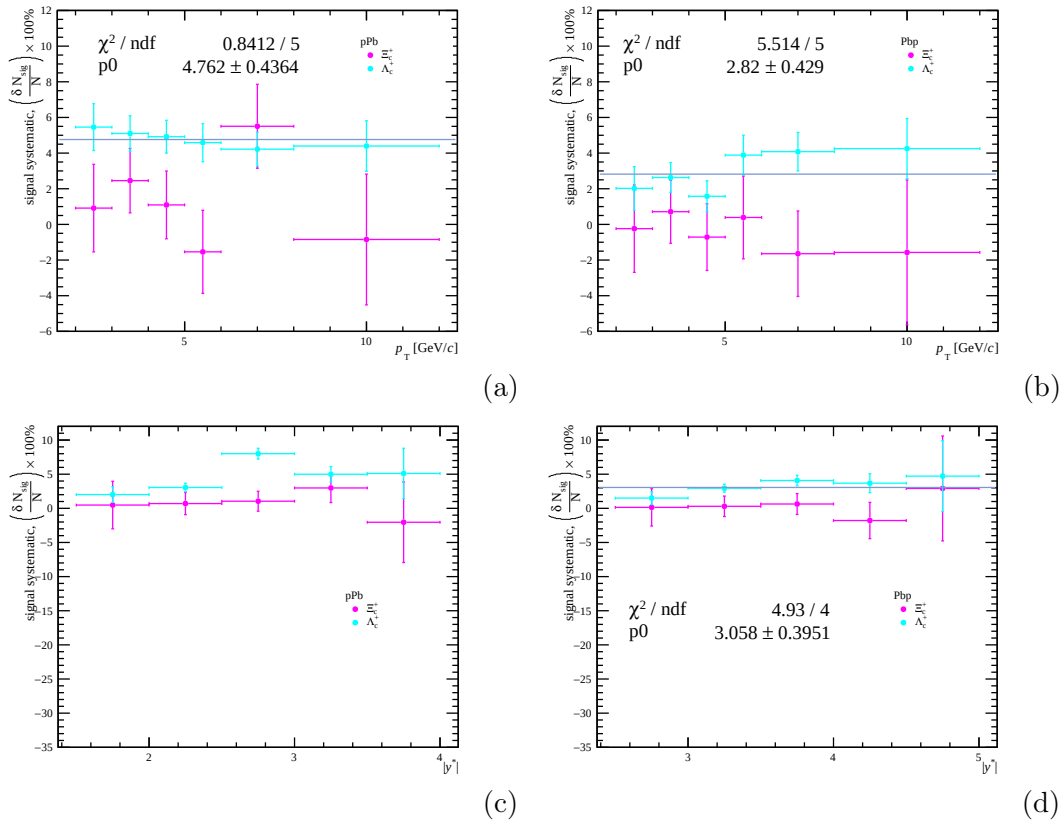

FIGURE 8.2: Relative systematic uncertainties on Ξ_c^+ (purple) and Λ_c^+ (blue) signal as a function of p_T in forward (a) and backward (b) and as a function of $|y^*|$ in forward (c) and backward (d) data samples. Blue line denotes the fit of the uncertainties on Λ_c^+ signal.

on $\varepsilon_{\text{sel/rec}}$ is originated from the tracking corrections. Since we apply the tracking corrections to both, Ξ_c^+ and Λ_c^+ simulation, we expect that some uncertainties might cancel out in the ratio. Thus, the uncertainty on the ratio was calculated by varying the tracking correction uncertainty up and down of one sigma, as in the formula

$$\delta R = \frac{R(w + \Delta w) - R(w - \Delta w)}{R(w)}, \tag{8.1}$$

where $R(w)$ is the ratio of $\frac{\varepsilon_{\text{sel/rec}}{}^{\Lambda_c^+}(w)}{\varepsilon_{\text{sel/rec}}{}^{\Xi_c^+}(w)}$ and w is the tracking correction from Fig. 7.11. δR in p_T and rapidity bins is presented on Fig. 8.3.

8.3.3 PID efficiencies

The systematic uncertainty on ε_{PID} consist of uncertainties evaluated by varying the reweighing procedure, likewise in 8.3.2, and the uncertainties propagated from the PIDCalib tables due to its finite size. Since we use the same PID tables for both Ξ_c^+ and Λ_c^+ simulation, we expect that some uncertainties might cancel out in the ratio. Thus, the uncertainty on the ratio was calculated by the formula 8.1. The uncertainty on the ratio is shown on Fig. 8.4.

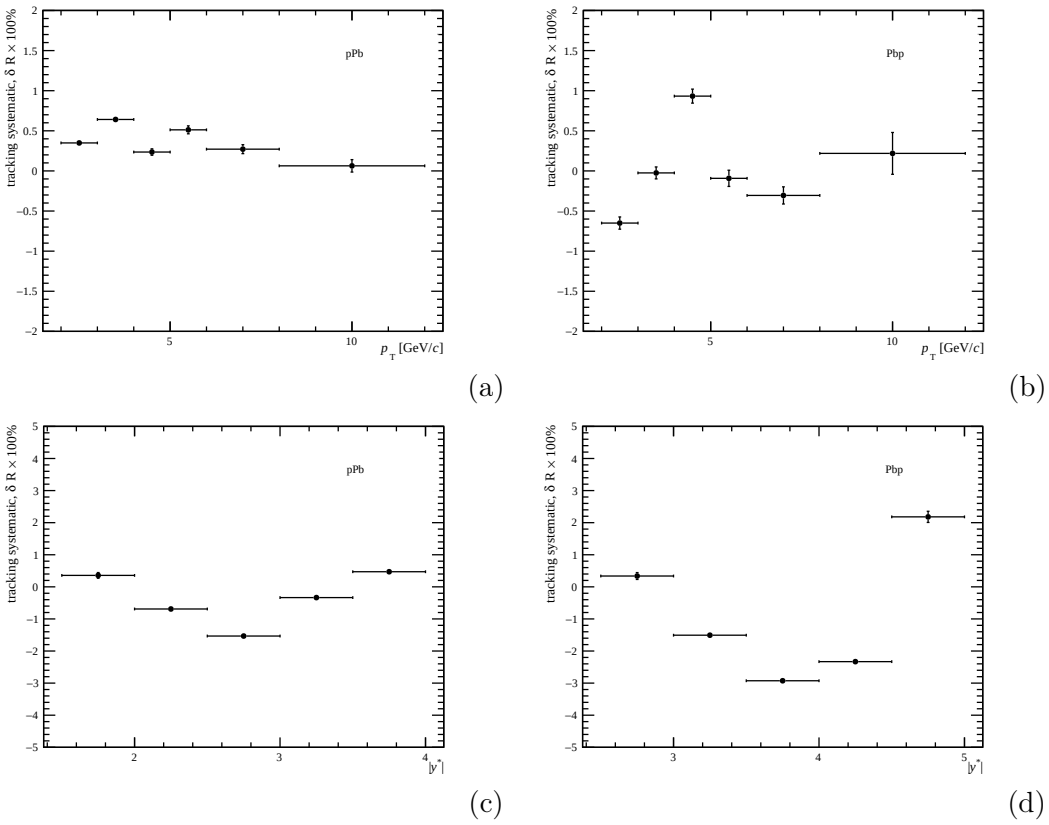

FIGURE 8.3: Relative systematic uncertainties on the Ξ_c^+/Λ_c^+ ratio from tracking corrections as a function of p_T in the forward (a) and backward (b) and as a function of $|y^*|$ in forward (c) and backward (d) data samples.

8.3.4 Trigger efficiencies

The systematic uncertainty on $\varepsilon_{\text{trg/sel}}$ was evaluated by varying the reweighing procedure, as was done in Sec. 8.3.2. The $\varepsilon_{\text{trg/sel}}$ also includes the systematic uncertainty coming from the difference of trigger efficiency in data and MC, which is 0.4%.

8.4 Branching ratio uncertainty

The largest uncertainty comes from the branching ratio (BR) uncertainty of Ξ_c^+ decay. In our measurement we used $\mathcal{B}(\Xi_c^+ \to p^+K^-\pi^+) = [0.62 \pm 0.30]\%$ taken from the PDG [68], which is a combination of two measurements made by Belle [120] and LHCb [121].

8.5 Summary

The summary of the systematic uncertainties on the Ξ_c^+ (Λ_c^+) cross section can be found in Tables 8.1, 8.2, and 8.5. The summary of systematic uncertainties on the Ξ_c^+/Λ_c^+ ratio can be found in Tables 8.3, 8.4.

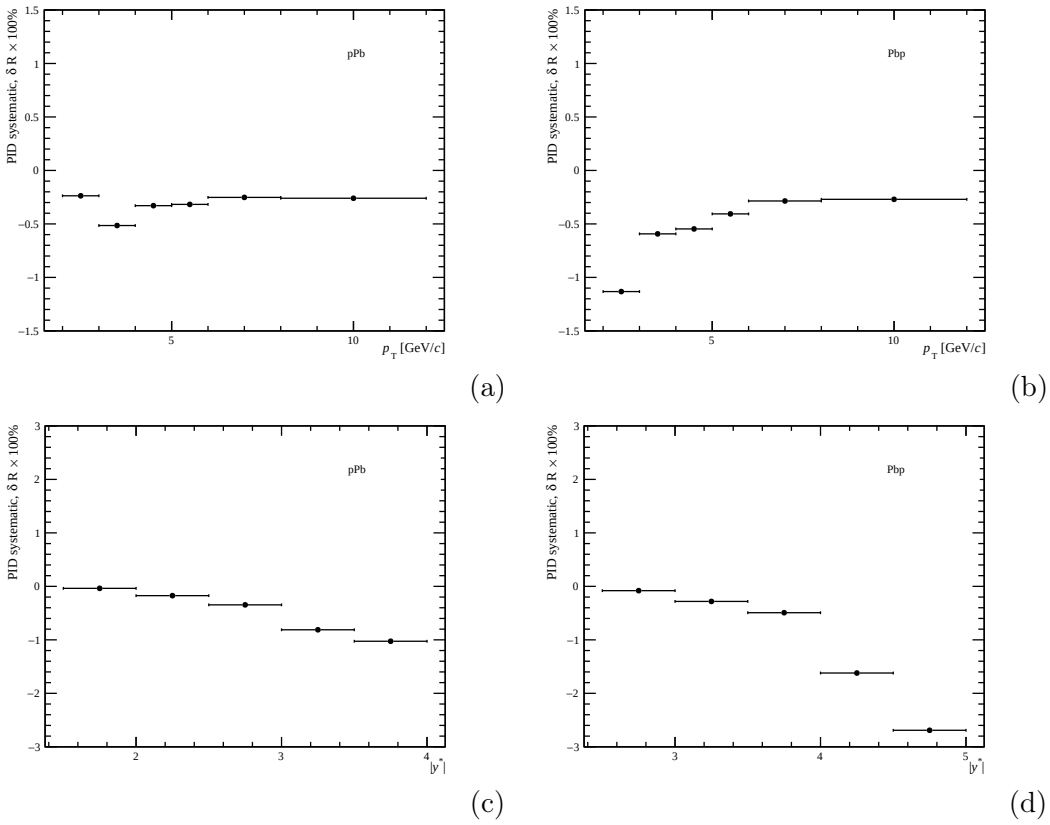

FIGURE 8.4: Relative systematic uncertainties on the Ξ_c^+/Λ_c^+ ratio from PIDCalib table as a function of p_T in forward (a) and backward (b) and as a function of $|y^*|$ in forward (c) and backward (d) data samples.

TABLE 8.1: Summary of systematic uncertainties on Ξ_c^+ and Λ_c^+ in p_T bins in the forward and backward samples.

	Ξ_c^+		Λ_c^+	
	Forward	Backward	Forward	Backward
Signal	0.1-2.2%	0.2-2.3%	-	-
Background	1.3-5.7%	0.5-18.0%	0.1-1.0%	0.1-0.8%
ε_{acc}	0.1-0.2%	0.1-0.3%	0.1-0.2%	0.1-0.2%
$\varepsilon_{\text{sel/rec}}$	1.1-3.5%	1.3-4.8%	3.6-7.3%	2.7-5.5%
ε_{PID}	0.3-0.7%	0.6-1.4%	0.2-0.6%	0.5-1.1%
$\varepsilon_{\text{trg/sel}}$	0.4-0.5%	0.4-0.5%	0.1-0.6%	0.4-0.8%
Total	2.0-6.3%	2.9-18.0%	3.6-7.3%	2.8-5.6%

TABLE 8.2: Summary of systematic uncertainties on Ξ_c^+ and Λ_c^+ in y^* bins in the forward and backward samples.

	Ξ_c^+		Λ_c^+	
	Forward	Backward	Forward	Backward
Signal	0.2-3.0%	0.2-3.6%	2.0-5.9%	-
Background	0.1-5.7%	1.7-27.4%	0.1-4.6%	0.7-17.7%
ε_{acc}	0.1-0.4%	0.1-0.8%	0.1-0.3%	0.1-0.5%
$\varepsilon_{\text{sel/rec}}$	0.7-2.8%	1.5-4.2%	3.4-6.8%	1.2-14.4%
ε_{PID}	0.4-1.5%	0.5-3.0%	0.2-2.3%	0.4-3.8%
$\varepsilon_{\text{trg/sel}}$	0.4-0.5%	0.4-0.6%	0.4-0.5%	0.4-1.2%
Total	1.6-6.4%	2.7-27.8%	4.1-9.9%	1.8-17.9%

TABLE 8.3: Summary of systematic uncertainties on Ξ_c^+/Λ_c^+ ratio in p_{T} bins.

	Forward	Backward
Signal	0.0-2.2%	0.2-2.3%
Background	1.4-5.7%	0.7-18.0%
ε_{acc}	0.1-0.2%	0.2-0.3%
$\varepsilon_{\text{sel/rec}}$	3.9-7.4%	4.6-5.6%
ε_{PID}	0.4-0.9%	0.8-1.5%
$\varepsilon_{\text{trg/sel}}$	0.4-0.7%	0.6-1.0%
Total	4.8-9.0%	4.8-19.0%

TABLE 8.4: Summary of systematic uncertainties on Ξ_c^+/Λ_c^+ ratio in y^* bins.

	Forward	Backward
Signal	2.1-6.0%	0.2-3.6%
Background	1.1-7.3%	1.8-27.4%
ε_{acc}	0.1-0.5%	0.1-1.0%
$\varepsilon_{\text{sel/rec}}$	3.5-6.9%	1.9-14.5%
ε_{PID}	0.5-2.7%	0.8-4.8%
$\varepsilon_{\text{trg/sel}}$	0.6-0.7%	0.6-1.3%
Total	5.1-11.8%	3.3-31.7%

TABLE 8.5: Summary of correlated uncertainties.

	Forward	Backward
Luminosity	2.6%	2.5%
Signal	4.8%	2.8-3.1%
Tracking	5.5%	
$\mathcal{B}(\Xi_c^+ \to p^+K^-\pi^+)$	48.4%	
$\mathcal{B}(\Lambda_c^+ \to p^+K^-\pi^+)$	5.1%	

Chapter 9

Results

Putting together all the ingredients described in the previous sections, we measure the double differential cross section of Ξ_c^+ and Λ_c^+, the production ratio of Ξ_c^+ to Λ_c^+, the production ratio of Ξ_c^+ to D^0, using the cross section measurement of D^0 in pPb at $\sqrt{s_{\rm NN}}$ = 8.16 TeV [122], and the forward-backward asymmetry of Ξ_c^+. The measurements are described in the following section.

9.1 Cross-section

We present the differential cross-sections, as defined in Eq. 5.1, of prompt Ξ_c^+ and Λ_c^+ production in pPb collisions at $\sqrt{s_{\rm NN}} = 8.16\,\text{TeV}$ measured in this analysis in Fig 9.1. On the plot (a) the cross-sections are plotted as a function of $p_{\rm T}$ integrated over y^* in the regions $1.5 < y^* < 4.0$ (for forward data) and $-5.0 < y^* < -2.5$ (for backward data). One can notice that both Ξ_c^+ and Λ_c^+ cross sections, decrease exponentially with $p_{\rm T}$. Likewise, on the plot (b) the cross-sections are plotted as a function of $|y^*|$ integrated over $p_{\rm T}$ between 2.0 and 12.0 GeV/c. It has decreasing trend all over the $|y^*|$ range. The error bars represent the statistical uncertainties, the black squares are the systematic uncertainties uncorrelated between bins and the shaded areas are the correlated uncertainties. The grey bands correspond to the uncertainties uncorrelated between bins. The corresponding numerical values of prompt Ξ_c^+ differential cross-sections can be found in Table 9.1 and 9.2.

Since the largest uncertainty is coming from the branching ratio (BR) of the $\Xi_c^+ \to \pi pK$ decay, we also present the measurements of the double differential cross section multiplied by the branching ratio in Fig. 9.2. The coloured curves are the theoretical predictions based on the work of Hua-Sheng Shao *et al.* [130, 131, 132] using the HELAC-Onia method [133, 134]. The predictions are given using three different factorisation scales in order to study the factorisation uncertainty as outlined in [48]. The data seem to prefer the predictions with $\mu_0 * 0.5$, although they overall sit at its lowest edge basically everywhere.

The total cross section is achieved by summing over all bins. For the forward and backward regions, the total cross sections are

$$\sigma_{p\mathrm{Pb}}(2 < p_{\mathrm{T}} < 12\,\mathrm{GeV}/c, 1.5 < y^* < 4.0) = 9.69 \pm 0.12^{stat} \pm 0.26^{sys} \pm 4.72^{corr}\mathrm{mb},$$
$$\sigma_{\mathrm{Pb}p}(2 < p_{\mathrm{T}} < 12\,\mathrm{GeV}/c, -5.0 < y^* < -2.5) = 8.10 \pm 0.11^{stat} \pm 0.72^{sys} \pm 3.95^{corr}\mathrm{mb}.$$

The first uncertainty is statistical, the second is the uncorrelated between bins systematic uncertainty and the third is the correlated uncertainty.

TABLE 9.1: One-dimensional cross-sections $\mathrm{d}\sigma/\mathrm{d}p_{\mathrm{T}}$ for prompt Ξ_{c}^{+} baryon as a function of p_{T} integrated over $1.5 < y^* < 4.0$ (forward) and $-5.0 < y^* < -2.5$ (backward). The first uncertainty is statistical, the second is the uncorrelated between bins systematic uncertainty and the third is the correlated uncertainty.

Forward		Backward	
$p_{\mathrm{T}}/(\,\mathrm{GeV}/c)$	$(\mathrm{d}\sigma/\mathrm{d}p_{\mathrm{T}})/(\mathrm{mb}/\,\mathrm{GeV}/c)$	$p_{\mathrm{T}}/(\,\mathrm{GeV}/c)$	$(\mathrm{d}\sigma/\mathrm{d}p_{\mathrm{T}})/(\mathrm{mb}/\,\mathrm{GeV}/c)$
(2.0, 3.0)	4.304 ± 0.106 ± 0.285 ± 2.083	(2.0, 3.0)	3.948 ± 0.097 ± 0.724 ± 1.910
(3.0, 4.0)	2.768 ± 0.050 ± 0.142 ± 1.339	(3.0, 4.0)	2.241 ± 0.040 ± 0.185 ± 1.084
(4.0, 5.0)	1.308 ± 0.025 ± 0.067 ± 0.633	(4.0, 5.0)	1.055 ± 0.020 ± 0.059 ± 0.510
(5.0, 6.0)	0.591 ± 0.014 ± 0.033 ± 0.286	(5.0, 6.0)	0.430 ± 0.010 ± 0.026 ± 0.208
(6.0, 8.0)	0.210 ± 0.005 ± 0.015 ± 0.102	(6.0, 8.0)	0.145 ± 0.003 ± 0.007 ± 0.070
(8.0, 12.0)	0.032 ± 0.001 ± 0.001 ± 0.016	(8.0, 12.0)	0.020 ± 0.001 ± 0.001 ± 0.010

TABLE 9.2: One-dimensional cross-sections $\mathrm{d}\sigma/\mathrm{d}y^*$ for prompt Ξ_{c}^{+} baryon as a function of y^* in forward and backward rapidity region, integrated over p_{T} in the range 2.0-12.0 GeV/c. The first uncertainty is statistical, the second is the uncorrelated between bins systematic uncertainty and the third is the correlated uncertainty.

Forward		Backward	
y^*	$(\mathrm{d}\sigma/\mathrm{d}y^*)/\mathrm{mb}$	y^*	$(\mathrm{d}\sigma/\mathrm{d}y^*)/\mathrm{mb}$
(1.5, 2.0)	4.107 ± 0.143 ± 0.206 ± 1.987	(-5.0, -4.5)	1.909 ± 0.147 ± 0.525 ± 0.924
(2.0, 2.5)	4.594 ± 0.075 ± 0.185 ± 2.223	(-4.5, -4.0)	2.020 ± 0.054 ± 0.118 ± 0.977
(2.5, 3.0)	4.281 ± 0.062 ± 0.239 ± 2.072	(-4.0, -3.5)	3.452 ± 0.053 ± 0.158 ± 1.670
(3.0, 3.5)	3.115 ± 0.067 ± 0.164 ± 1.507	(-3.5, -3.0)	4.135 ± 0.062 ± 0.259 ± 2.001
(3.5, 4.0)	2.293 ± 0.135 ± 0.178 ± 1.109	(-3.0, -2.5)	4.314 ± 0.118 ± 0.181 ± 2.088

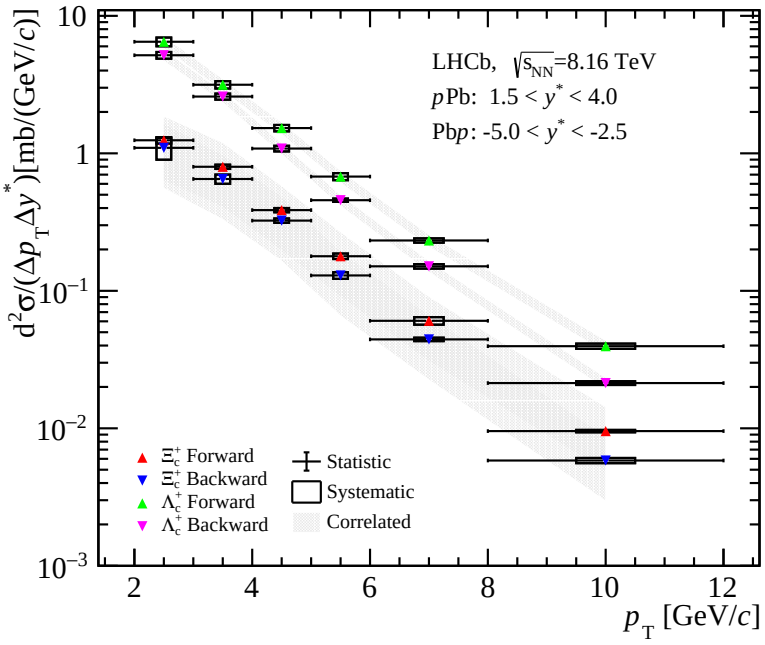

(a)

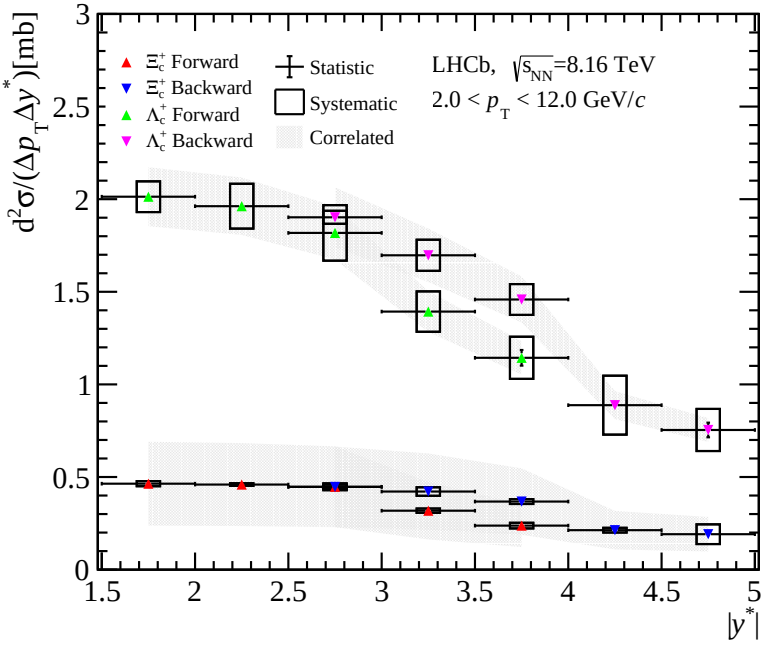

(b)

FIGURE 9.1: Double-differential cross-section of prompt Ξ_c^+ and Λ_c^+ baryons in pPb collisions as a function of (a) p_T and (b) y^* in the forward and backward collision samples. The error bars represent the statistical uncertainties, the black squares are the systematic uncertainties uncorrelated between bins and the shaded areas is the correlated uncertainty.

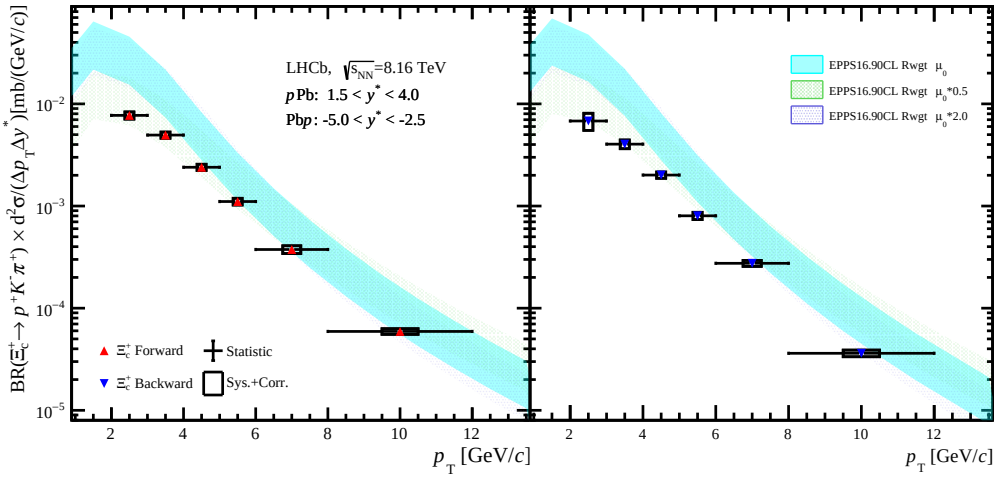

(a)

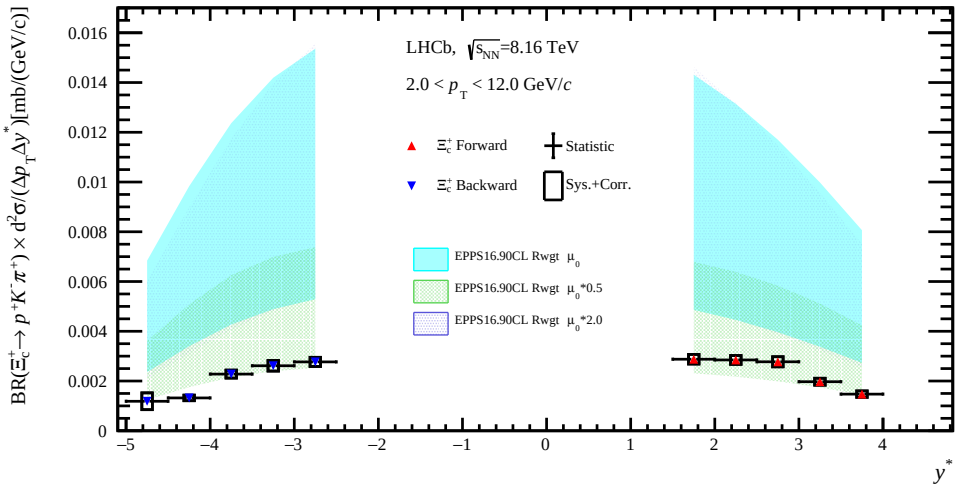

(b)

FIGURE 9.2: Double-differential cross-section multiplied by branching ratio of prompt Ξ_c^+ baryon in pPb collisions as a function of (a) p_T and (b) y^* in the forward and backward collision samples. The error bars represent the statistical uncertainties, black squares are the systematic uncertainties uncorrelated between bins and the shaded areas is the correlated uncertainty.

9.2 Ξ_c^+/Λ_c^+ ratio

The ratio of the cross-sections of Ξ_c^+ to Λ_c^+ was calculated through the Eq. 5.2 and has been measured in bins of transverse momentum of the baryon in the range 2.0-12.0 GeV/c, separately for the forward $1.5 < y^* < 4.0$ and the backward -5.0 $< y^* <$ -2.5 rapidity range, as shown in Fig. 9.3. The error bars represent the statistical uncertainties while the squares denote the systematic uncertainty. The shaded area is the correlated uncertainty. The ratio is roughly constant as a function of p_T around the value of 0.3, similarly for forward and backward in the region of p_T larger than about 4 GeV/c, while it seems to slightly decrease with p_T in the lower p_T region. The theoretical predictions are given using three different factorisation scales in order to study the factorisation uncertainty as outlined in [48]. Their uncertainties are negligible and not seen on the plot. The data seem to prefer the predictions with $\mu_0 * 0.5$, although they are systematically lower than the theory in the whole range. The same ratio has been measured as a function of rapidity integrated over p_T in the range 2-12 GeV/c, in bins of 0.5 in rapidity in the ranges $1.5 < y^* < 4.0$ for the forward and -5.0 $< y^* <$ -2.5 for the backward. The result is shown in Fig. 9.4. Again the prediction marked as $\mu_0 * 0.5$ seems to better reproduce the data, although slightly underestimating them everywhere. The numerical values of $R_{\Xi_c^+/\Lambda_c^+}$ can be found in Table 9.3 and 9.4. Likewise, the ratio has been measured as a function of $nVeloClusters$. As shown in Fig. 9.5, the ratio is rather constant as a function of multiplicity.

The differential ratio of Ξ_c^+/Λ_c^+ multiplied by branching ratio is shown in fig. 9.6 as a function of p_T (a) and y^* (b).

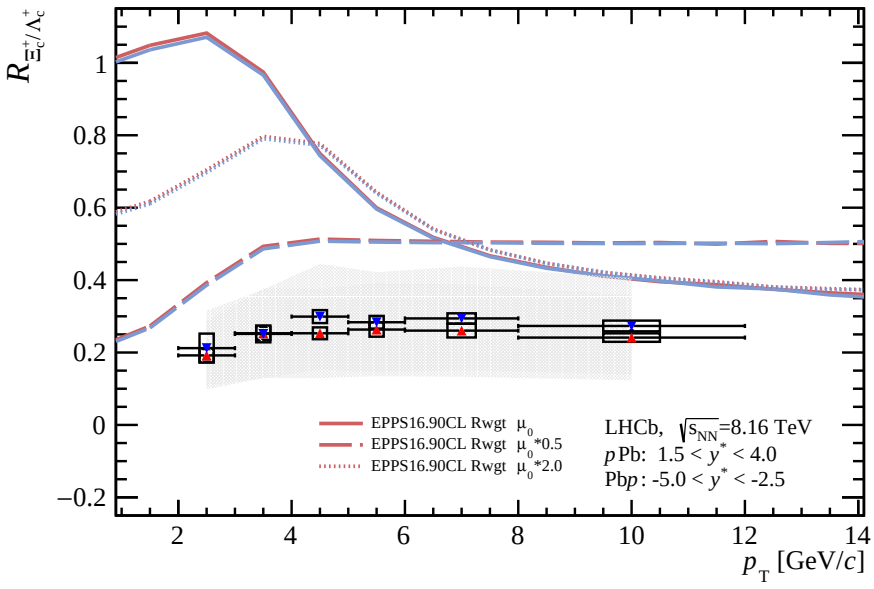

FIGURE 9.3: The production ratio of Ξ_c^+ to Λ_c^+ in Forward (red triangles) and Backward (blue triangles) data samples as a function of p_T. The error bars represent the statistical uncertainties while the squares denote the systematic uncertainty. The shaded area is correlated uncertainty. The theoretical predictions uncertainties are negligible and not visible on the plot.

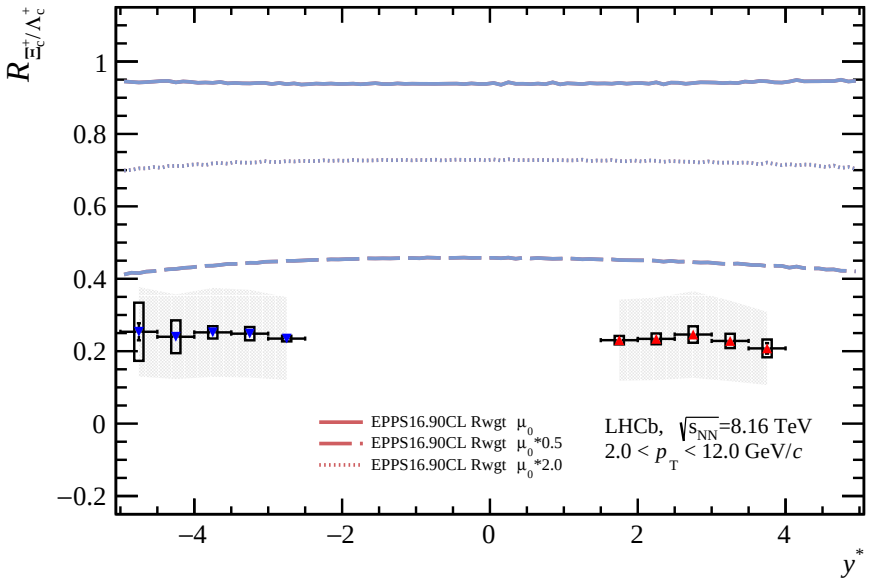

FIGURE 9.4: The production ratio of Ξ_c^+ to Λ_c^+ in Forward (red triangles) and Backward (blue triangles) data samples as a function of y^*. The error bars represent the statistical uncertainties while the squares denote the systematic uncertainty. The shaded area is the correlated uncertainty. The theoretical predictions uncertainties are negligible and not visible on the plot.

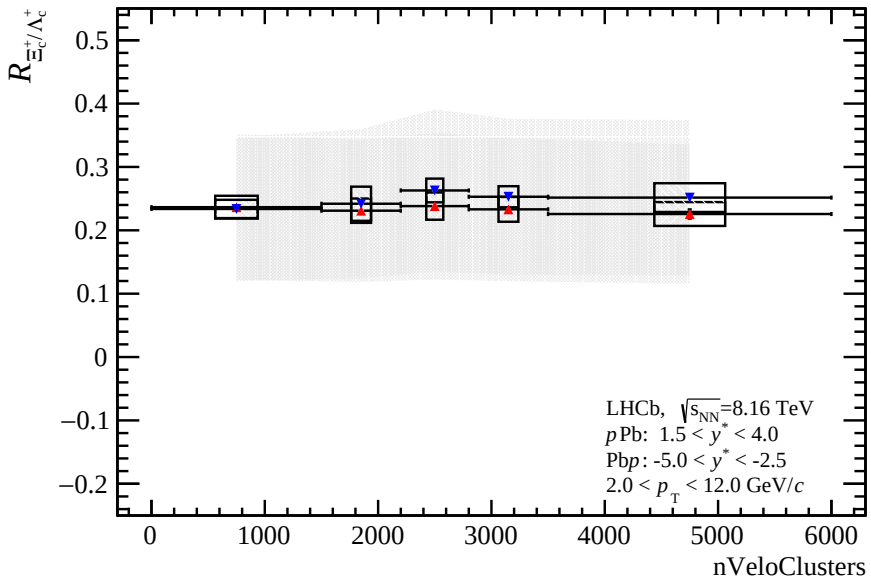

FIGURE 9.5: The production ratio of Ξ_c^+ to Λ_c^+ in Forward (red triangles) and Backward (blue triangles) data samples as a function of nVeloClusters. The error bars represent the statistical uncertainties while the squares denote the systematic uncertainty. The shaded area is correlated uncertainty.

TABLE 9.3: The production ratio of prompt Ξ_c^+ to Λ_c^+ as a function of p_T integrated over $1.5 < y^* < 4.0$ (forward) and $-5.0 < y^* < -2.5$ (backward). The first uncertainty is statistical, the second is the uncorrelated between bins systematic uncertainty and the third is the correlated uncertainty.

Forward		Backward	
$p_T/(\,\mathrm{GeV}/c)$	$R_{\Xi_c^+/\Lambda_c^+}$	$p_T/(\,\mathrm{GeV}/c)$	$R_{\Xi_c^+/\Lambda_c^+}$
(2.0, 3.0)	0.191 ± 0.005 ± 0.021 ± 0.093	(2.0, 3.0)	0.215 ± 0.006 ± 0.041 ± 0.105
(3.0, 4.0)	0.258 ± 0.005 ± 0.023 ± 0.125	(3.0, 4.0)	0.257 ± 0.005 ± 0.025 ± 0.125
(4.0, 5.0)	0.254 ± 0.005 ± 0.021 ± 0.123	(4.0, 5.0)	0.297 ± 0.006 ± 0.021 ± 0.145
(5.0, 6.0)	0.259 ± 0.007 ± 0.022 ± 0.126	(5.0, 6.0)	0.286 ± 0.007 ± 0.021 ± 0.139
(6.0, 8.0)	0.269 ± 0.007 ± 0.022 ± 0.131	(6.0, 8.0)	0.292 ± 0.008 ± 0.021 ± 0.142
(8.0, 12.0)	0.240 ± 0.009 ± 0.017 ± 0.117	(8.0, 12.0)	0.275 ± 0.012 ± 0.021 ± 0.134

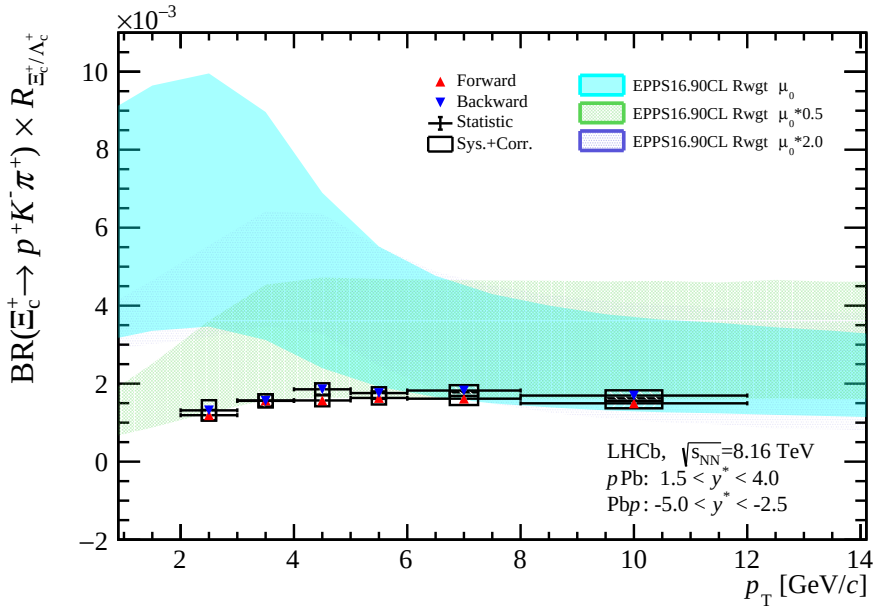

(a)

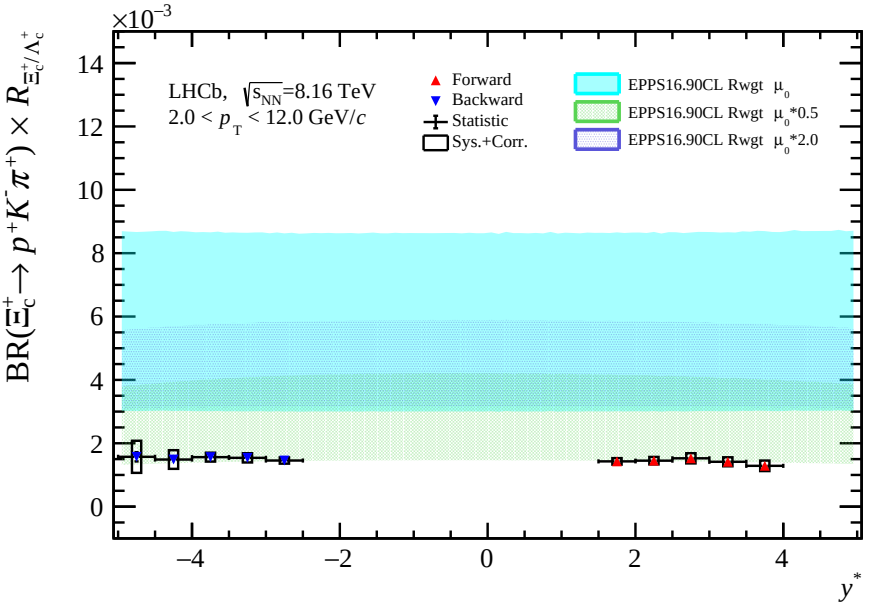

(b)

FIGURE 9.6: The production ratio of Ξ_c^+ to Λ_c^+ multiplied by branching ratio in Forward (red triangles) and Backward (blue triangles) data samples as a function of p_T (a) and y^* (b). The error bars represent the statistical uncertainties while the squares indicate the systematic uncertainty.

TABLE 9.4: The production ratio of prompt Ξ_c^+ to Λ_c^+ as a function of y^* in forward and backward rapidity region, integrated over p_T in the range 2.0-12.0 GeV/c. The first uncertainty is statistical, the second is the uncorrelated between bins systematic uncertainty and the third is the correlated uncertainty.

Forward		Backward	
y^*	$R_{\Xi_c^+/\Lambda_c^+}$	y^*	$R_{\Xi_c^+/\Lambda_c^+}$
(1.5, 2.0)	0.228 ± 0.008 ± 0.013 ± 0.111	(-5.0, -4.5)	0.271 ± 0.025 ± 0.088 ± 0.132
(2.0, 2.5)	0.235 ± 0.004 ± 0.015 ± 0.114	(-4.5, -4.0)	0.250 ± 0.007 ± 0.018 ± 0.122
(2.5, 3.0)	0.242 ± 0.004 ± 0.028 ± 0.118	(-4.0, -3.5)	0.256 ± 0.004 ± 0.020 ± 0.124
(3.0, 3.5)	0.226 ± 0.005 ± 0.020 ± 0.110	(-3.5, -3.0)	0.254 ± 0.004 ± 0.020 ± 0.123
(3.5, 4.0)	0.217 ± 0.015 ± 0.027 ± 0.105	(-3.0, -2.5)	0.255 ± 0.007 ± 0.011 ± 0.124

9.3 Ξ_c^+/D^0 ratio

Since LHCb has already measured the D^0 cross-section in pPb collisions at $\sqrt{s_{\rm NN}} = 8.16\,\text{TeV}$ [122], we are able to compute the cross section ratio, as defined in Eq. 5.3. On Fig.9.8 $R_{\Xi_c^+/D^0}$ is shown (a) as a function of $p_{\rm T}$ integrated over y^* in regions $1.5 < y^* < 4.0$ (forward data) and $-5.0 < y^* < -2.5$ (backward data) and (b) as a function of y^* integrated over $p_{\rm T}$ in the region 2.0-12.0 GeV/c. The result is compared to theoretical calculations using different factorisation scales [48]. As in sec. 9.2, the data exhibit an overall underestimation of the theoretical predictions. The numerical values of $R_{\Xi_c^+/D^0}$ can be found in Table 9.5 and 9.6.

The differential ratio of Ξ_c^+/D^0 multiplied by branching ratio is shown in fig. 9.7 as a function of $p_{\rm T}$ (a) and y^* (b).

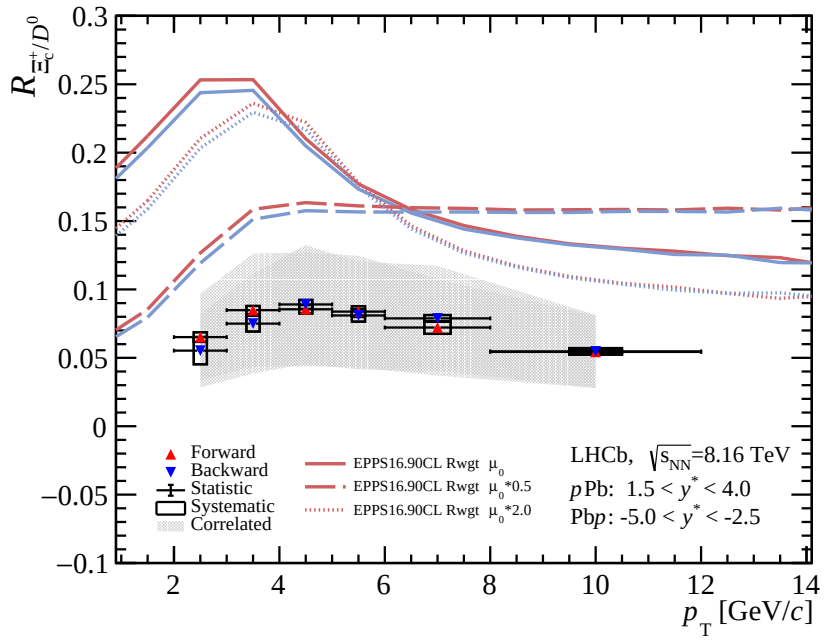

(a)

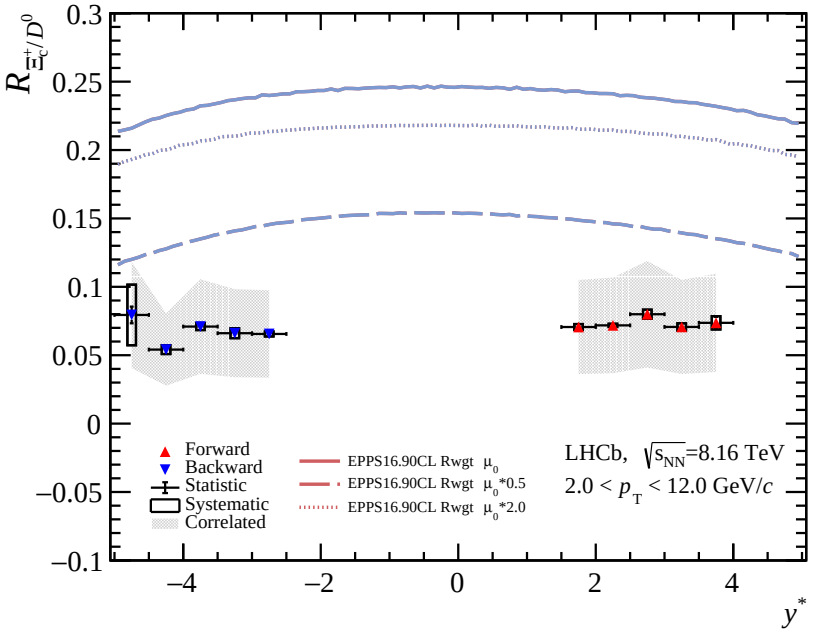

(b)

FIGURE 9.7: The production ratio of Ξ_c^+ to D^0 multiplied by branching ratio in Forward (red triangles) and Backward (blue triangles) data samples as a function of p_T (a) and y^* (b). The error bars represent the statistical uncertainties while the squares denote the systematic uncertainty. The shaded area is the correlated uncertainty. The theoretical predictions uncertainties are negligible and not visible on the plot.

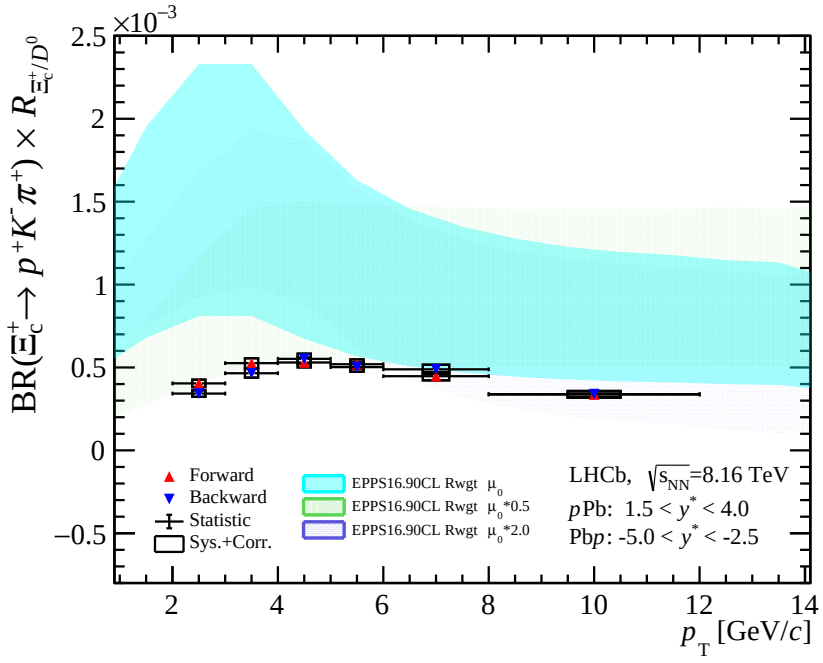

(a)

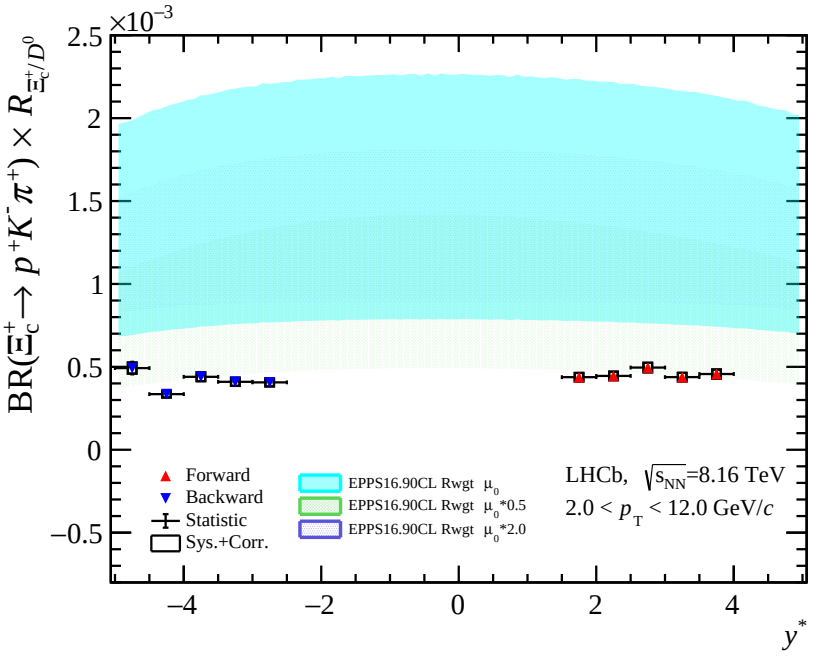

(b)

FIGURE 9.8: The production ratio of Ξ_c^+ to D^0 multiplied by branching ratio in Forward (red triangles) and Backward (blue triangles) data samples as a function of p_T (a) and y^* (b). The error bars represent the statistical uncertainties while the squares denote the systematic uncertainty.

9.4 Forward-backward asymmetry

The forward-backward ratio R_{FB}, defined by the Eq. 5.4 has been measured as a function of p_T and y^* and the results are shown in Fig. 9.9. The ratio is roughly

TABLE 9.5: The production ratio of prompt Ξ_c^+ to D^0 as a function of p_T integrated over $1.5 < y^* < 4.0$ (forward) and $-5.0 < y^* < -2.5$ (backward). The first uncertainty is statistical, the second is the uncorrelated between bins systematic uncertainty and the third is the correlated uncertainty.

Forward		Backward	
$p_T/(\text{GeV}/c)$	$R_{\Xi_c^+/D^0}$	$p_T/(\text{GeV}/c)$	$R_{\Xi_c^+/D^0}$
(2.0, 3.0)	0.064 ± 0.002 ± 0.007 ± 0.031	(2.0, 3.0)	0.057 ± 0.001 ± 0.021 ± 0.028
(3.0, 4.0)	0.084 ± 0.002 ± 0.007 ± 0.041	(3.0, 4.0)	0.074 ± 0.001 ± 0.012 ± 0.036
(4.0, 5.0)	0.083 ± 0.002 ± 0.007 ± 0.040	(4.0, 5.0)	0.083 ± 0.002 ± 0.009 ± 0.040
(5.0, 6.0)	0.079 ± 0.002 ± 0.008 ± 0.039	(5.0, 6.0)	0.077 ± 0.002 ± 0.009 ± 0.038
(6.0, 8.0)	0.072 ± 0.002 ± 0.010 ± 0.035	(6.0, 8.0)	0.073 ± 0.002 ± 0.008 ± 0.036
(8.0, 12.0)	0.052 ± 0.002 ± 0.015 ± 0.025	(8.0, 12.0)	0.053 ± 0.002 ± 0.015 ± 0.026

TABLE 9.6: The production ratio of prompt Ξ_c^+ to D^0 as a function of y^* in forward and backward rapidity region, integrated over p_T in the range 2.0-12.0 GeV/c. The first uncertainty is statistical, the second is the uncorrelated between bins systematic uncertainty and the third is the correlated uncertainty.

Forward		Backward	
y^*	$R_{\Xi_c^+/D^0}$	y^*	$R_{\Xi_c^+/D^0}$
(1.5, 2.0)	0.065 ± 0.002 ± 0.003 ± 0.032	(-5.0, -4.5)	0.065 ± 0.002 ± 0.003 ± 0.032
(2.0, 2.5)	0.075 ± 0.001 ± 0.003 ± 0.036	(-4.5, -4.0)	0.067 ± 0.001 ± 0.004 ± 0.032
(2.5, 3.0)	0.079 ± 0.001 ± 0.004 ± 0.038	(-4.0, -3.5)	0.068 ± 0.001 ± 0.003 ± 0.033
(3.0, 3.5)	0.071 ± 0.002 ± 0.004 ± 0.034	(-3.5, -3.0)	0.052 ± 0.001 ± 0.003 ± 0.025
(3.5, 4.0)	0.071 ± 0.004 ± 0.006 ± 0.035	(-3.0, -2.5)	0.079 ± 0.006 ± 0.022 ± 0.038

constant with p_T and exhibits a slight dependence on y* especially in the region of low rapidity. The results are compared with the theoretical predictions described in Sec. 9.2 and they are overall in good agreement in the central rapidity region with some tension on the edges where also the uncertainty is larger. The numerical values of R_{FB} can be found in Table 9.7 and 9.8.

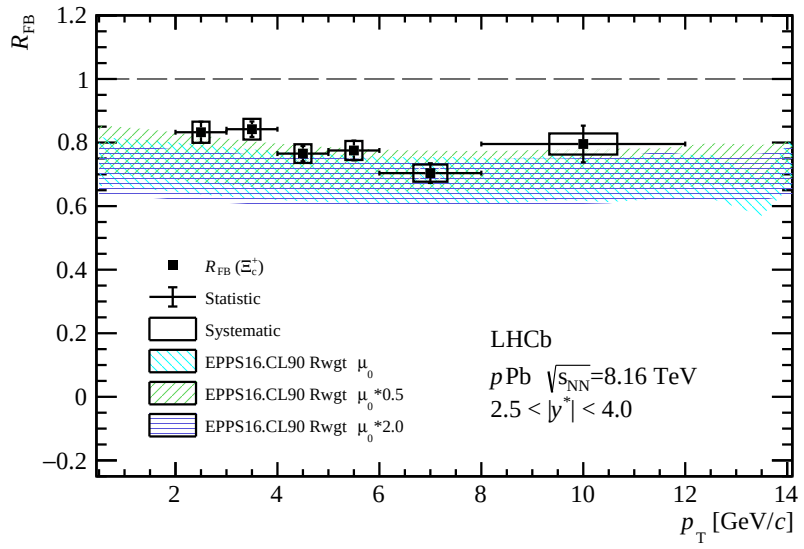

(a)

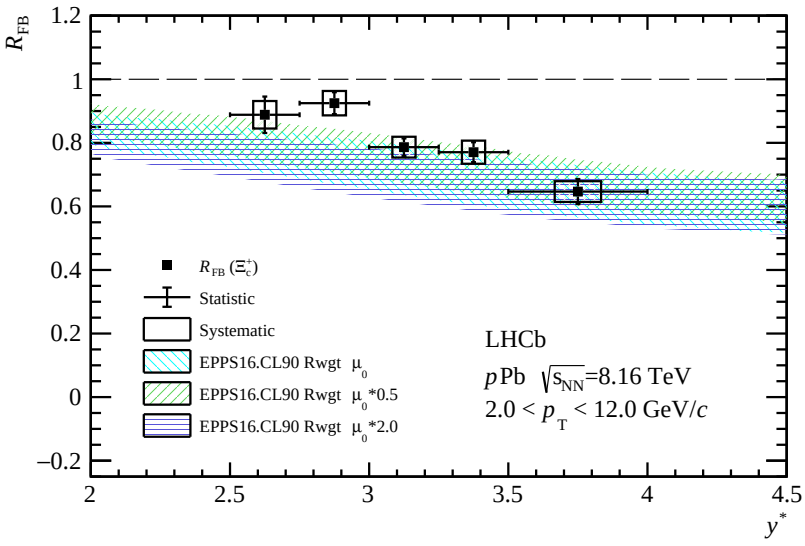

(b)

FIGURE 9.9: The forward-backward ratio of Ξ_c^+ production as a function of p_T (a) and y^* (b). The error bars represent the statistical uncertainties while the squares denote the systematic uncertainty.

TABLE 9.7: The forward-backward ratio of Ξ_c^+ production as a function of p_T, integrated over $2.5 < |y^*| < 4.0$. The first uncertainty is statistical, the second is the combination of systematic and correlated uncertainties.

$p_T/(\,\mathrm{GeV}/c)$	R_{FB}
(2.0, 3.0)	$0.798 \pm 0.032 \pm 0.041$
(3.0, 4.0)	$0.828 \pm 0.024 \pm 0.041$
(4.0, 5.0)	$0.763 \pm 0.024 \pm 0.038$
(5.0, 6.0)	$0.771 \pm 0.031 \pm 0.040$
(6.0, 8.0)	$0.705 \pm 0.031 \pm 0.037$
(8.0, 12.0)	$0.788 \pm 0.057 \pm 0.048$

TABLE 9.8: The forward-backward ratio of Ξ_c^+ production as a function of y^*, integrated over p_T in the range 2.0-12.0 GeV/c. The first uncertainty is statistical, the second is the combination of systematic and correlated uncertainties.

y^*	R_{FB}
(2.5, 2.8)	0.931 ± 0.060 ± 0.064
(2.8, 3.0)	0.954 ± 0.035 ± 0.051
(3.0, 3.2)	0.771 ± 0.027 ± 0.041
(3.2, 3.5)	0.768 ± 0.031 ± 0.045
(3.5, 4.0)	0.664 ± 0.040 ± 0.042

Chapter 10

Conclusions

The study of Ξ_c production has been performed in pPb collisions at $\sqrt{s} = 8.16\,\text{TeV}$ as a function of p_T and rapidity of the baryon in the $2.0 < p_\text{T} < 12.0$ transverse momentum region and in the $1.5 < y^* < 4.0$ and $-5.0 < y^* < -2.5$ rapidity regions. We presented the measurements of the Ξ_c^+ and Λ_c^+ cross sections, the production ratios of $\Xi_\text{c}^+/\Lambda_\text{c}^+$ and Ξ_c^+/D^0 and the forward-backward asymmetry for Ξ_c^+ production. The results have been compared with recent theoretical predictions and have found to be in reasonable agreement in particular with one choice of factorisation scale. It is also of particular interest for the charm hadronisation studies, as our ratio measurements are the most precise and the first ever in pPb collisions. This measurement can be a strong asset for the studies of the hadronisation universality in different collision systems and can provide an aid to constrain different theories. The Ξ_c^+ to Λ_c^+ ratio result can be fed back to theorists as input for more precise calculation on the process. Given that Ξ_c^+ baryon contains s quark, our results could be a strong indication of strangeness enhancement in small systems. More precise confirmations will come from the data to be collected in the upcoming Run 3, and from a possible measurement of the same quantity in pp collisions.

Appendix A

List of runs

The list of runs used in the analysis is shown in Tabels A.1 and A.2.

Run Numbers
186555, 186557, 186558, 186564, 186565, 186583, 186584, 186585, 186587, 186588, 186590, 186601, 186602, 186603, 186604, 186608, 186609, 186610, 186611, 186612, 186613, 186614, 186615, 186616, 186626, 186628, 186629, 186631, 186632, 186633, 186634, 186635, 186636, 186637, 186638, 186639, 186647, 186650, 186651, 186652, 186653, 186654, 186655, 186656, 186670, 186673, 186718, 186721, 186722, 186723, 186724, 186725, 186726, 186727, 186735, 186737, 186739, 186740, 186741, 186744, 186745, 186746, 186782, 186783, 186785, 186798, 186799, 186802, 186806, 186807, 186818, 186819, 186823, 186824, 186876, 186879, 186884, 186890, 186896, 186903, 186907, 186914, 186915, 186920

TABLE A.1: The list of runs with pPb configuration used in the analysis.

Run Numbers
186989, 186990, 186991, 187002, 187005, 187007, 187015, 187018, 187019, 187020, 187021, 187023, 187025, 187026, 187038, 187040, 187042, 187043, 187044, 187045, 187047, 187048, 187049, 187050, 187051, 187058, 187061, 187062, 187063, 187064, 187065, 187074, 187078, 187080, 187082, 187083, 187084, 187085, 187086, 187106, 187109, 187110, 187111, 187112, 187113, 187115, 187123, 187124, 187127, 187128, 187129, 187178, 187182, 187183, 187184, 187198, 187199, 187202, 187203, 187204, 187229, 187230, 187232, 187233, 187234, 187244, 187247, 187248, 187249, 187250, 187251, 187252, 187253, 187254, 187255, 187266, 187282, 187283, 187289, 187290, 187291, 187292, 187325, 187328, 187329, 187330, 187331, 187332, 187333, 187334, 187335, 187336, 187337, 187339, 187340, 187348, 187349, 187350, 187351, 187355, 187357, 187358, 187372, 187375, 187376, 187377, 187378, 187380, 187381, 187389, 187392, 187393, 187394, 187395, 187406, 187409, 187410

TABLE A.2: The list of runs with Pbp configuration used in the analysis.

Appendix B

Invariant mass distribution fit in each p_{T} and rapidity bin

In this section we report the invariant mass distribution fits used in each p_{T} and rapidity bins to obtain the signal events.

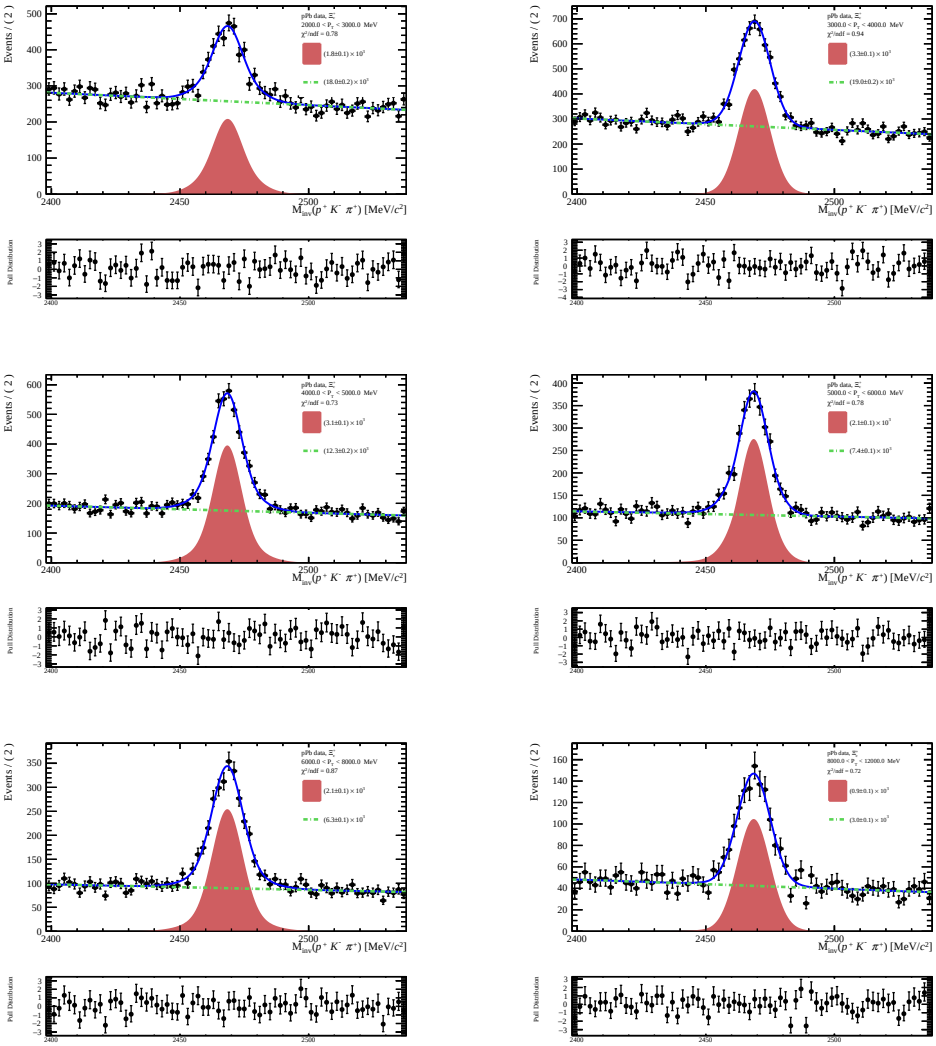

FIGURE B.1: Invariant mass distribution fit in each p_{T} bin. The solid blue line represents the total fit, which is composed of a first degree polynomial representing the background (green dashed line) and a CrystalBall function with a Guassian representing the Ξ_{c}^{+} signal candidates from pPb data (red shaded area).

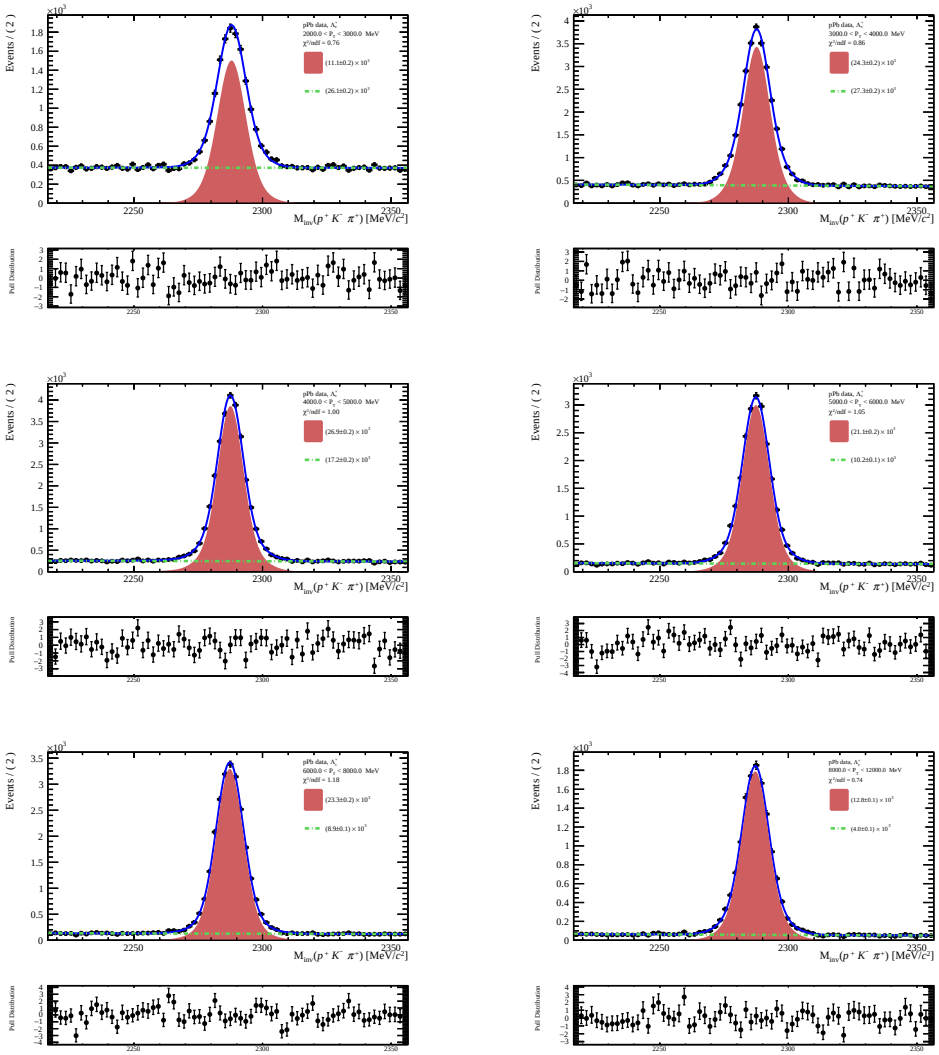

FIGURE B.2: Invariant mass distribution fit in each p_{T} bin. The solid blue line represents the total fit, which is composed of a first degree polynomial representing the background (green dashed line) and a CrystalBall function with a Guassian representing the Λ_{c}^{+} signal candidates from pPb data (red shaded area).

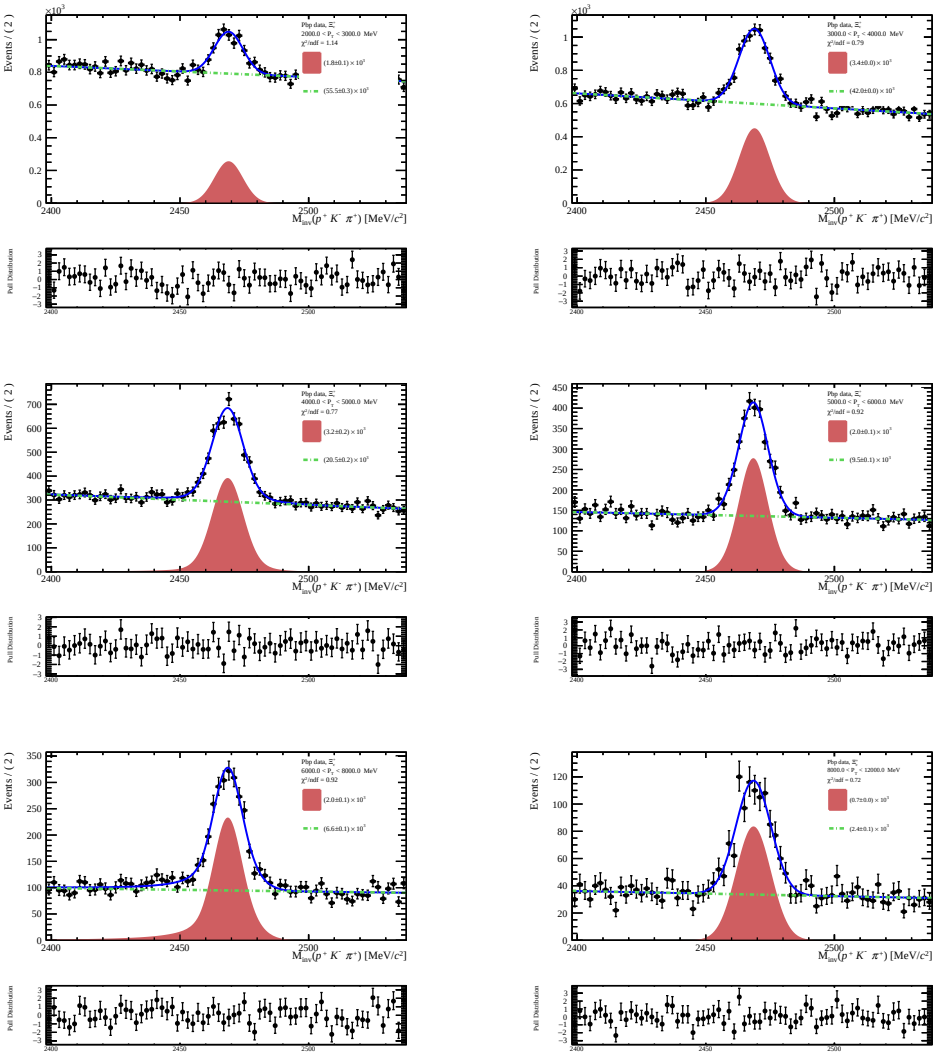

FIGURE B.3: Invariant mass distribution fit in each p_{T} bin. The solid blue line represents the total fit, which is composed of a first degree polynomial representing the background (green dashed line) and a CrystalBall function with a Guassian representing the Ξ_{c}^{+} signal candidates from Pbp data (red shaded area).

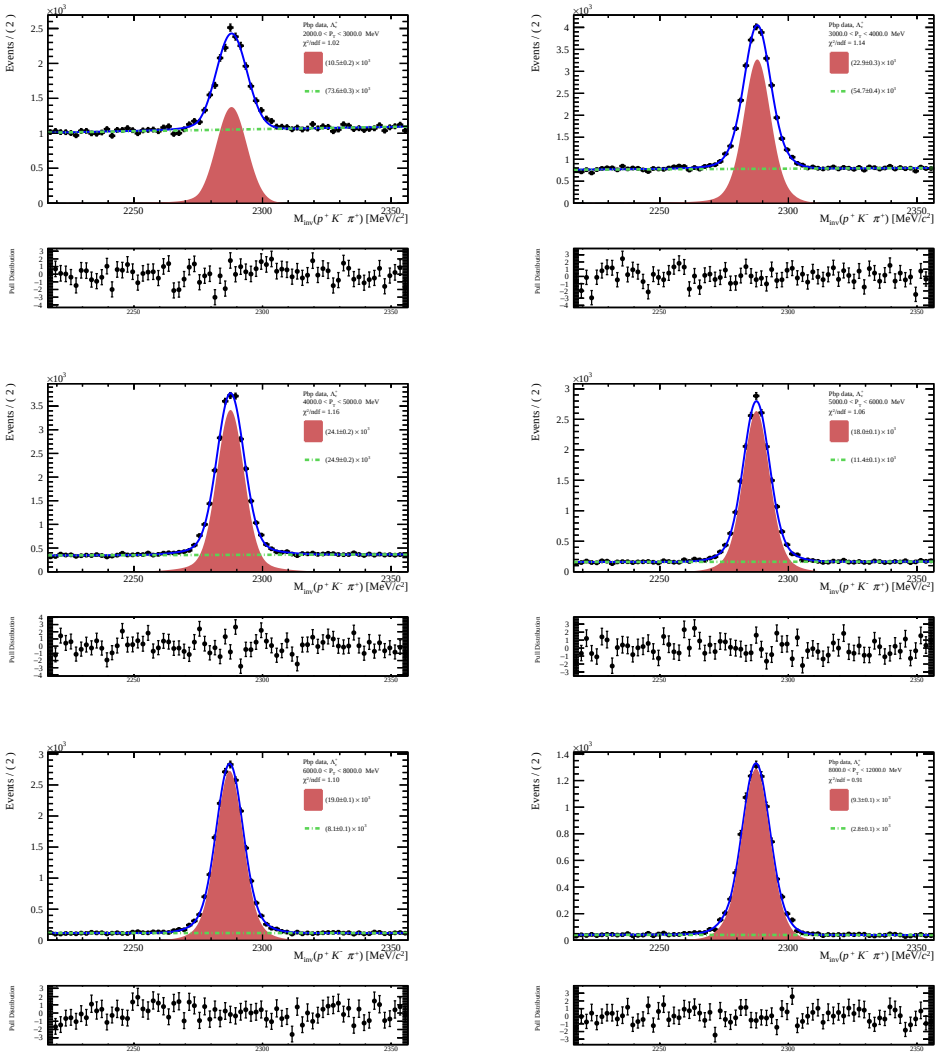

FIGURE B.4: Invariant mass distribution fit in each p_{T} bin. The solid blue line represents the total fit, which is composed of a first degree polynomial representing the background (green dashed line) and a CrystalBall function with a Guassian representing the Λ_{c}^{+} signal candidates from Pbp data (red shaded area).

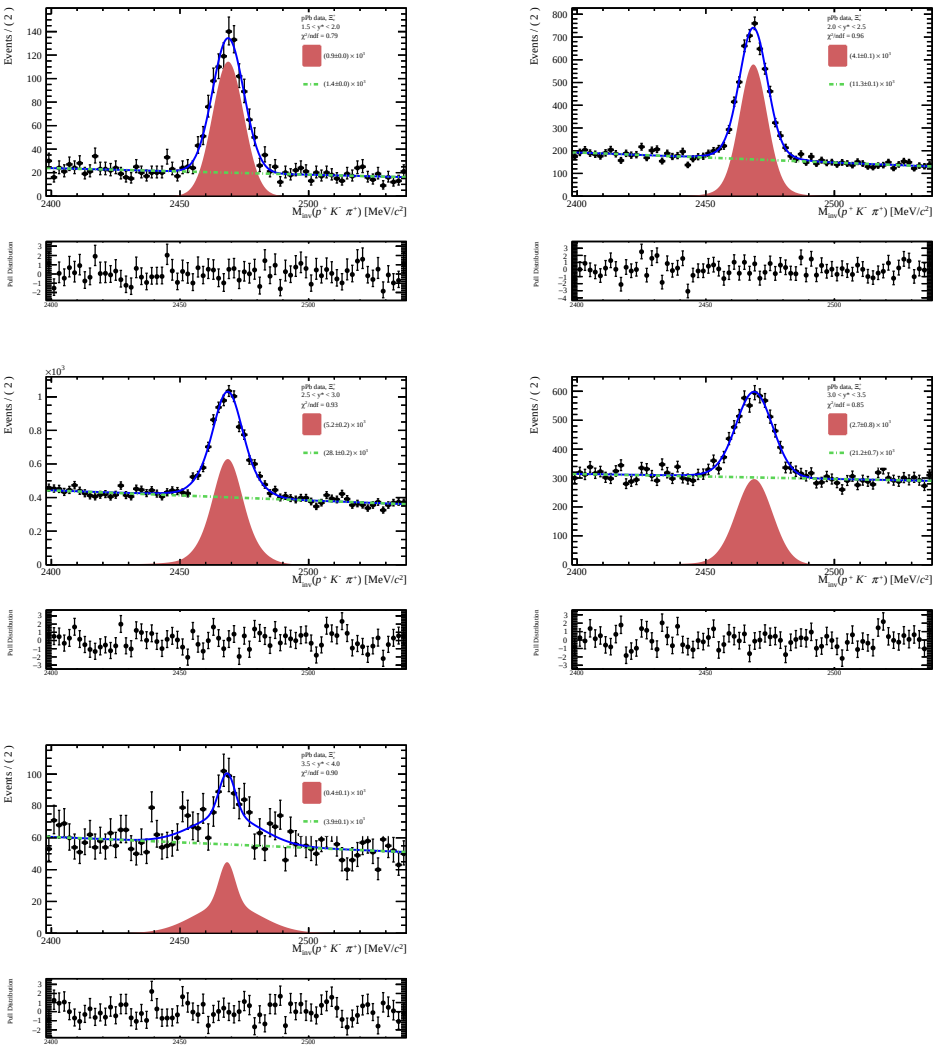

FIGURE B.5: Invariant mass distribution fit in each y^* bin. The solid blue line represents the total fit, which is composed of a first degree polynomial representing the background (green dashed line) and a CrystalBall function with a Guassian representing the Ξ_c^+ signal candidates from pPb data (red shaded area).

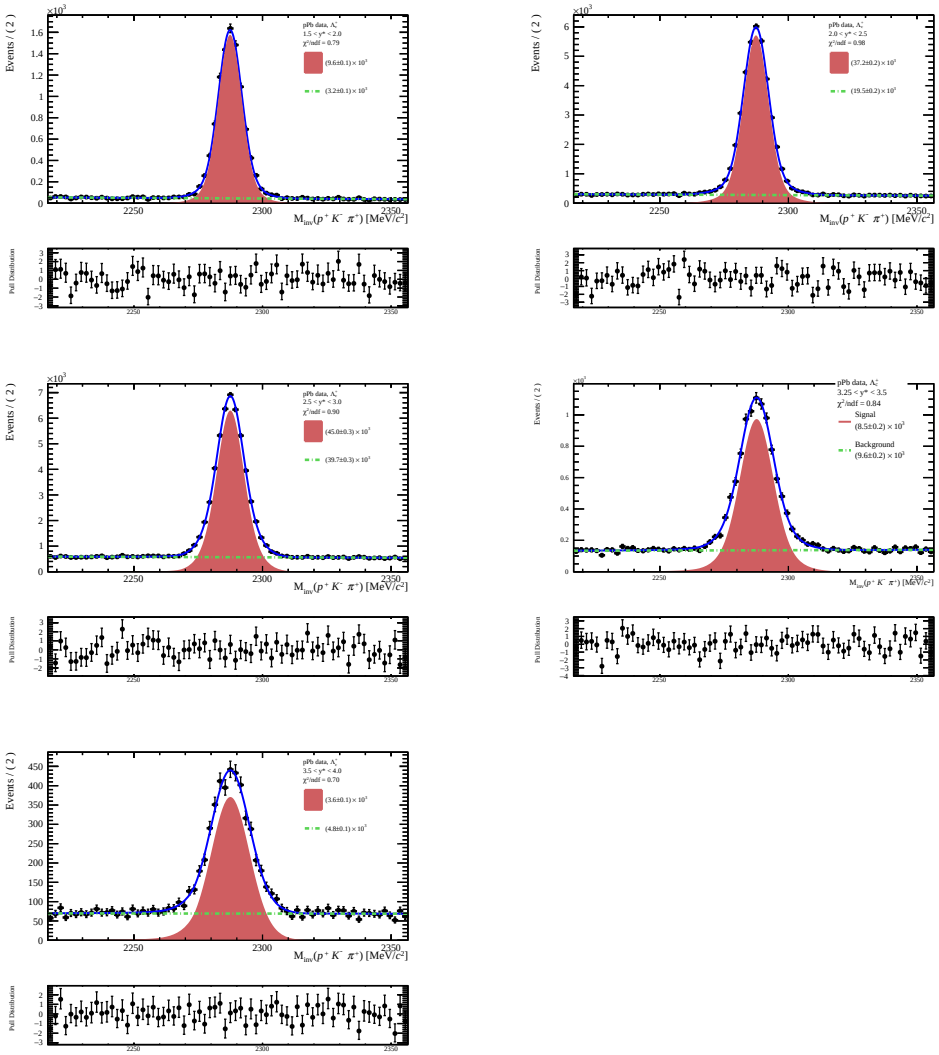

FIGURE B.6: Invariant mass distribution fit in each y^* bin. The solid blue line represents the total fit, which is composed of a first degree polynomial representing the background (green dashed line) and a CrystalBall function with a Guassian representing the Λ_c^+ signal candidates from pPb data (red shaded area).

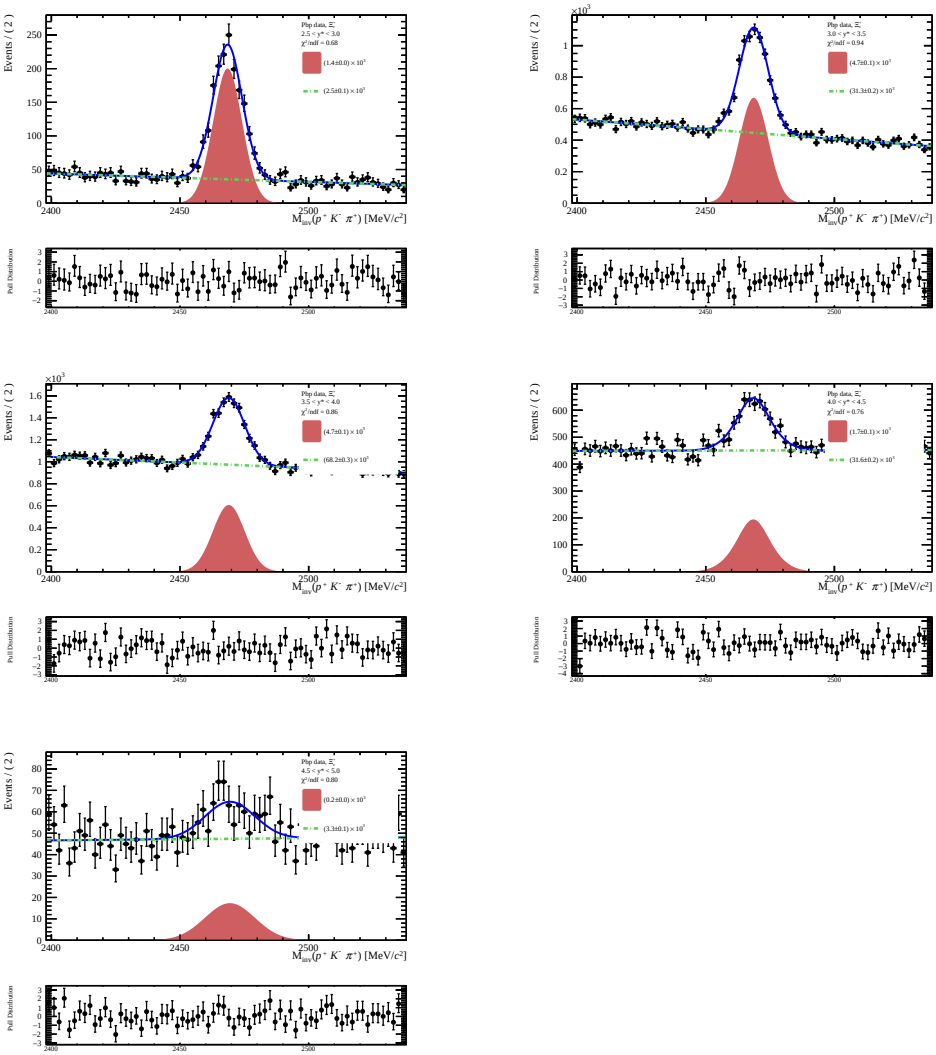

FIGURE B.7: Invariant mass distribution fit in each y^* bin. The solid blue line represents the total fit, which is composed of a first degree polynomial representing the background (green dashed line) and a CrystalBall function with a Guassian representing the Ξ_{c}^{+} signal candidates from Pbp data (red shaded area).

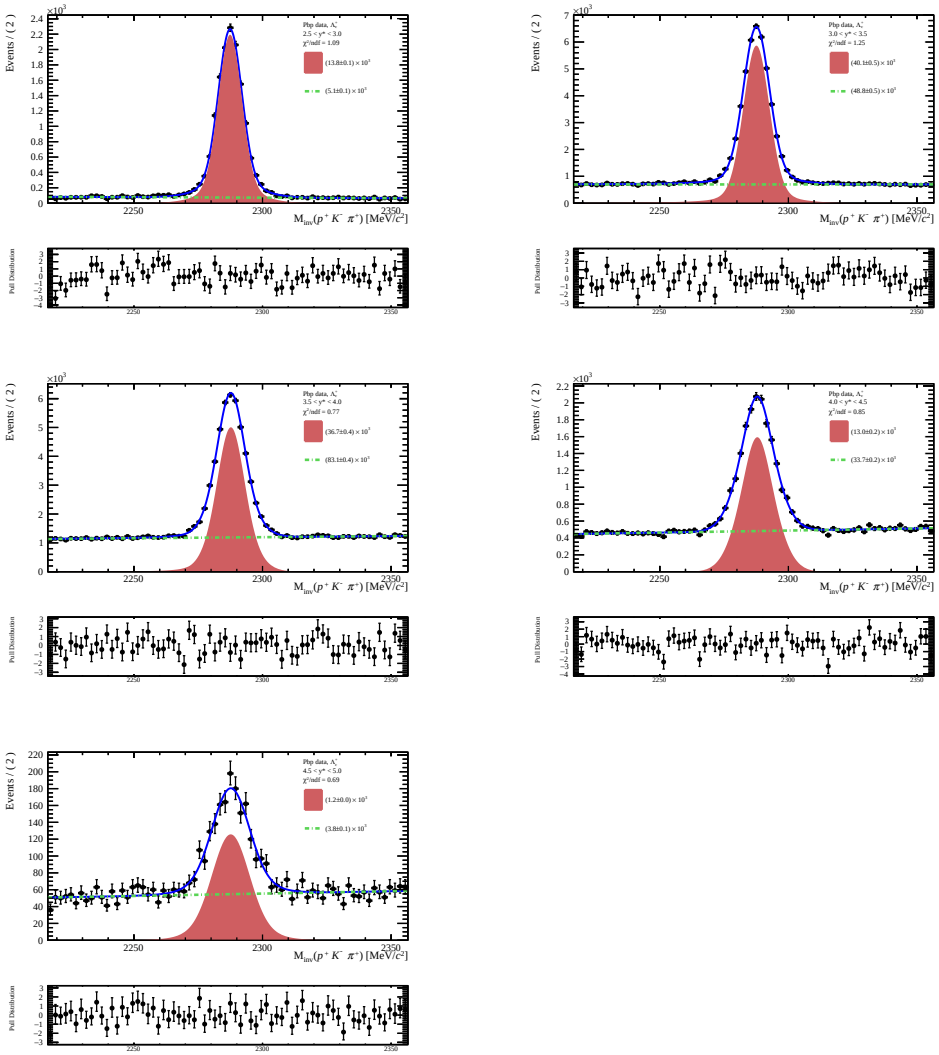

FIGURE B.8: Invariant mass distribution fit in each y^* bin. The solid blue line represents the total fit, which is composed of a first degree polynomial representing the background (green dashed line) and a CrystalBall function with a Guassian representing the Λ_{c}^{+} signal candidates from Pbp data (red shaded area).

Appendix C

$log_{10}(\chi^2_{IP})$ distribution fit in each p_{T} and rapidity bin

In this section we report the $log_{10}(\chi^2_{IP})$ distribution fits used in each p_{T} and rapidity bins to obtain the promptly produced events.

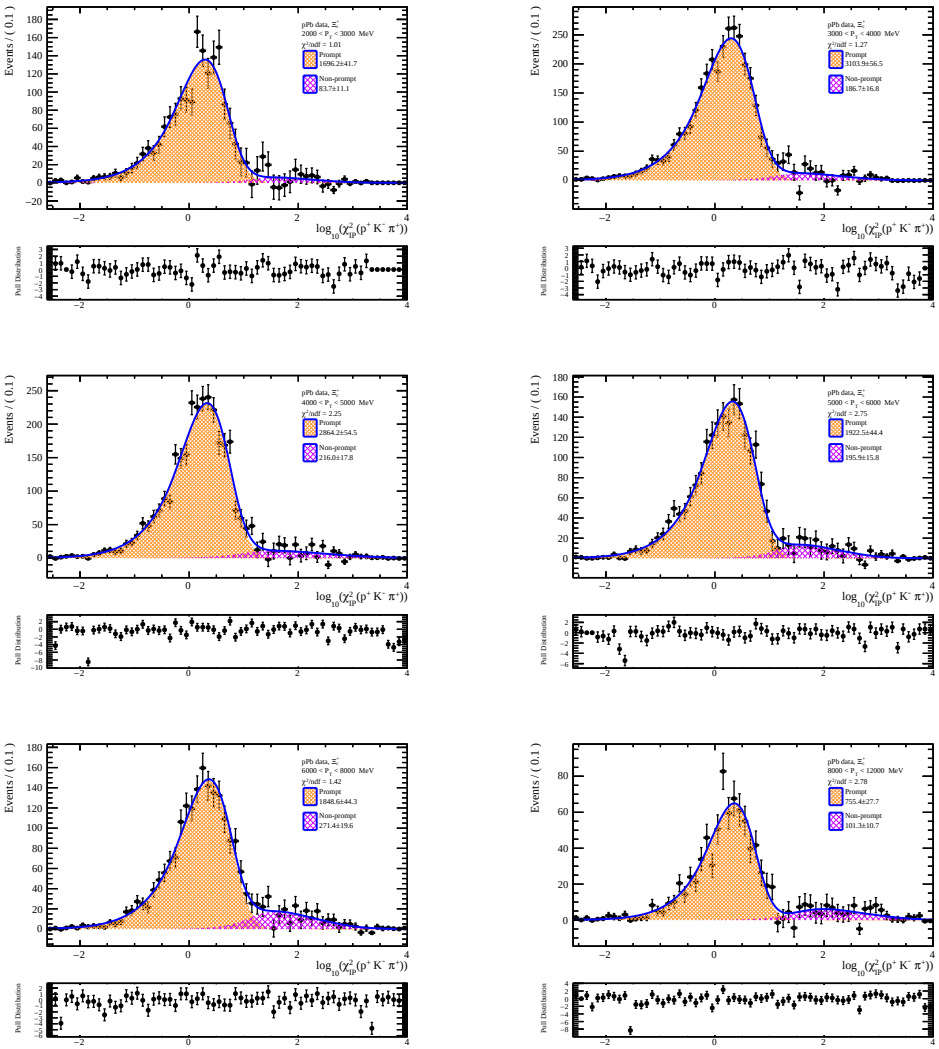

FIGURE C.1: $log_{10}(\chi^2_{IP})$ distribution fit in each p_{T} bin for Ξ_{c}^{+} from pPb data. The solid blue line represents the total fit, which is composed of a Bukin function representing the prompt signal (orange shaded area) and a another Bukin function representing the non-prompt signal (purple shaded area).

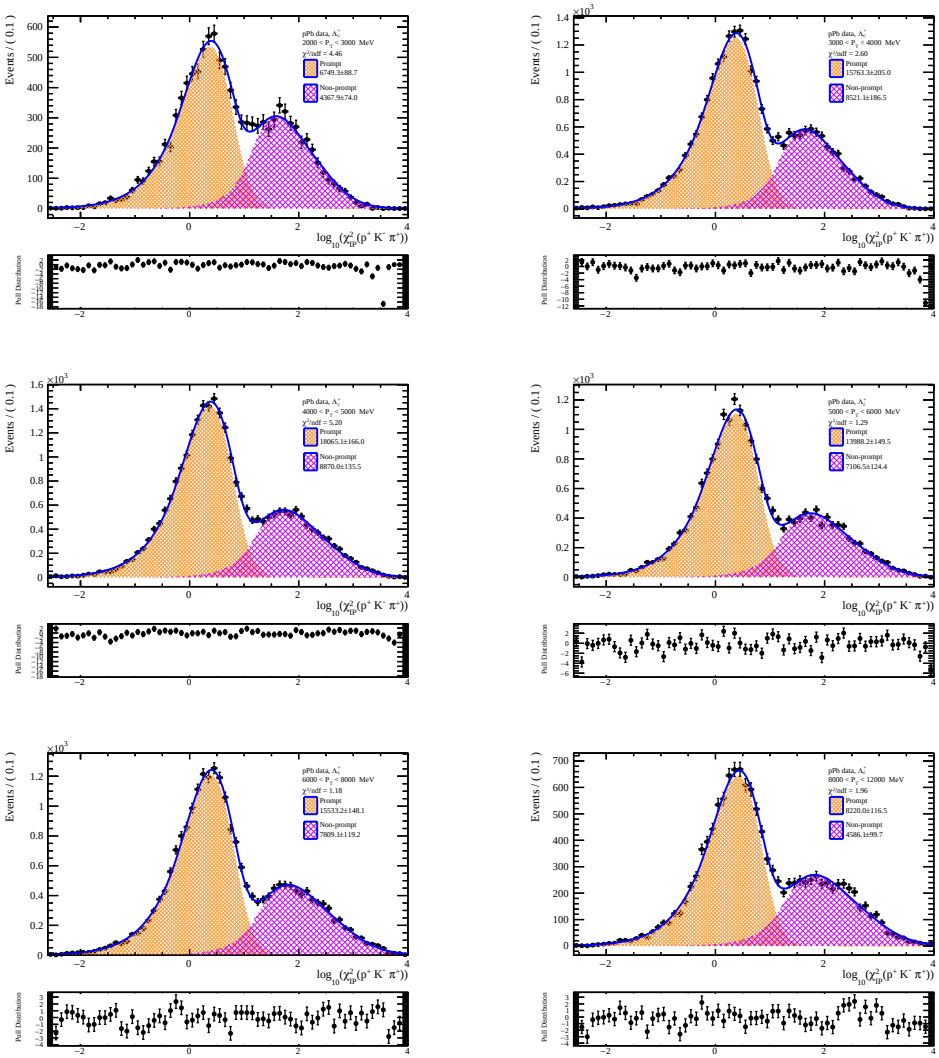

FIGURE C.2: $log_{10}(\chi^2_{IP})$ distribution fit in each p_{T} bin for Λ_{c}^{+} from pPb data. The solid blue line represents the total fit, which is composed of a Bukin function representing the prompt signal (orange shaded area) and a another Bukin function representing the non-prompt signal (purple shaded area).

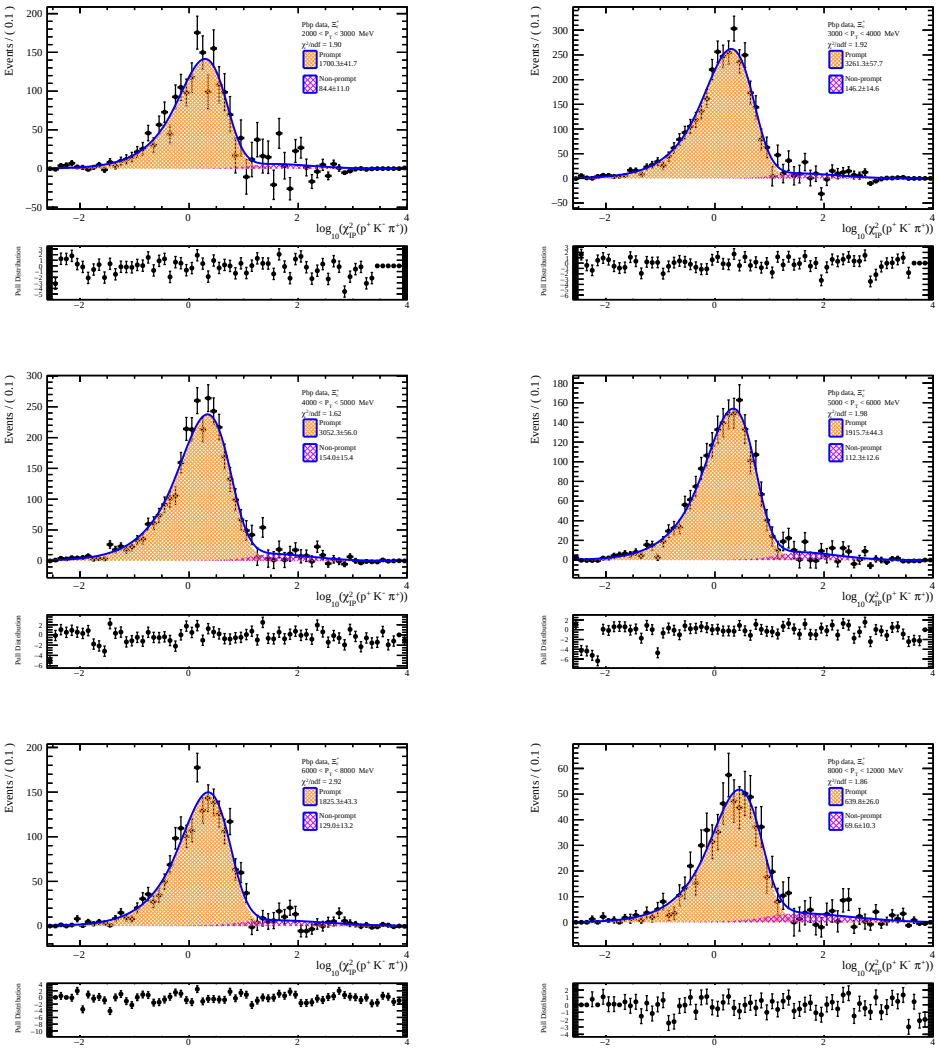

FIGURE C.3: $log_{10}(\chi^2_{IP})$ distribution fit in each p_{T} bin for Ξ_{c}^{+} from Pbp data. The solid blue line represents the total fit, which is composed of a Bukin function representing the prompt signal (orange shaded area) and a another Bukin function representing the non-prompt signal (purple shaded area).

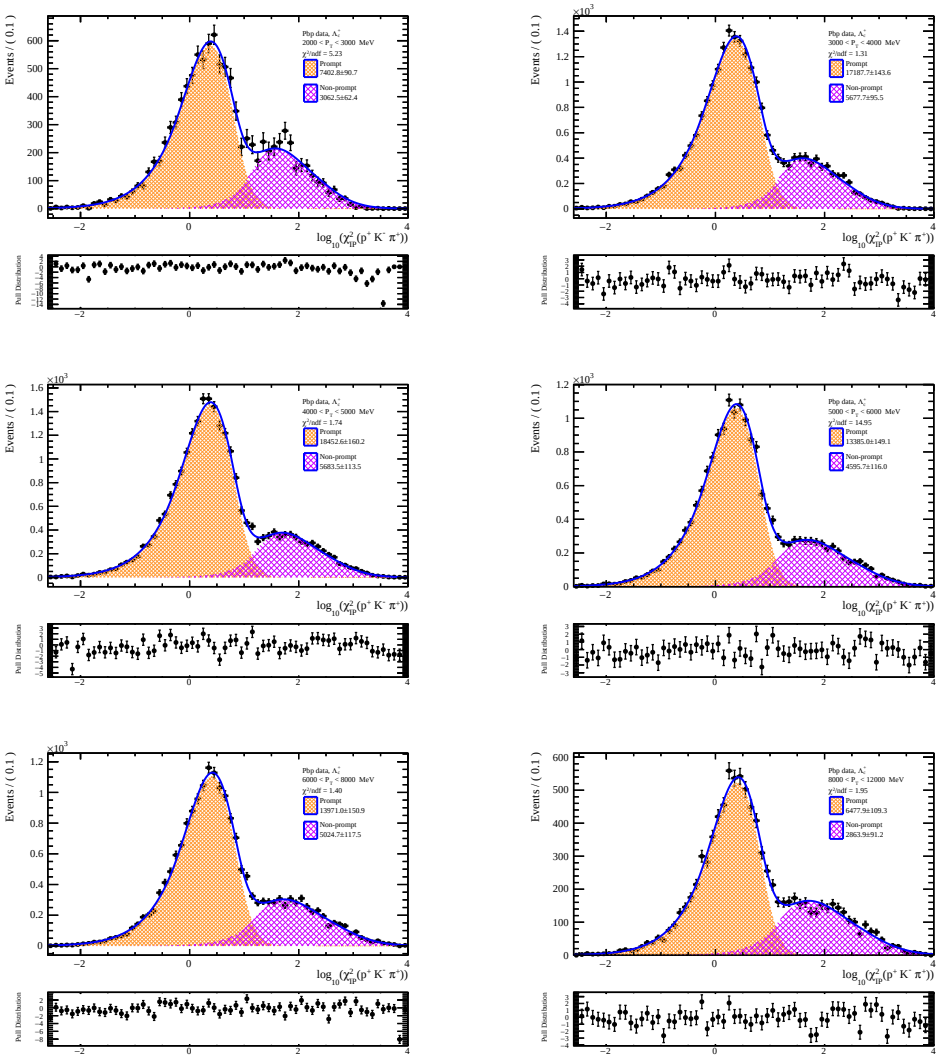

FIGURE C.4: $log_{10}(\chi^2_{IP})$ distribution fit in each p_{T} bin for Λ_c^+ from Pbp data. The solid blue line represents the total fit, which is composed of a Bukin function representing the prompt signal (orange shaded area) and a another Bukin function representing the non-prompt signal (purple shaded area).

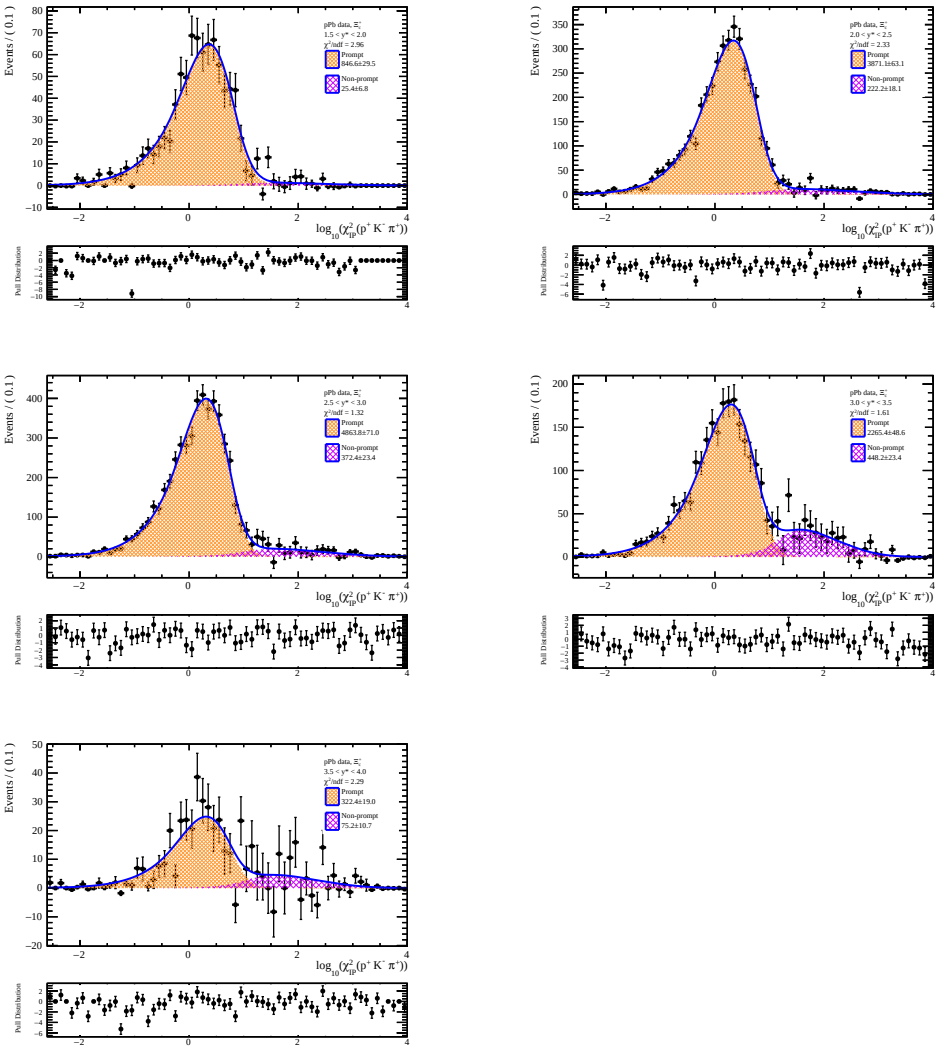

FIGURE C.5: $log_{10}(\chi^2_{IP})$ distribution fit in each y^* bin for Ξ_c^+ from pPb data. The solid blue line represents the total fit, which is composed of a Bukin function representing the prompt signal (orange shaded area) and a another Bukin function representing the non-prompt signal (purple shaded area).

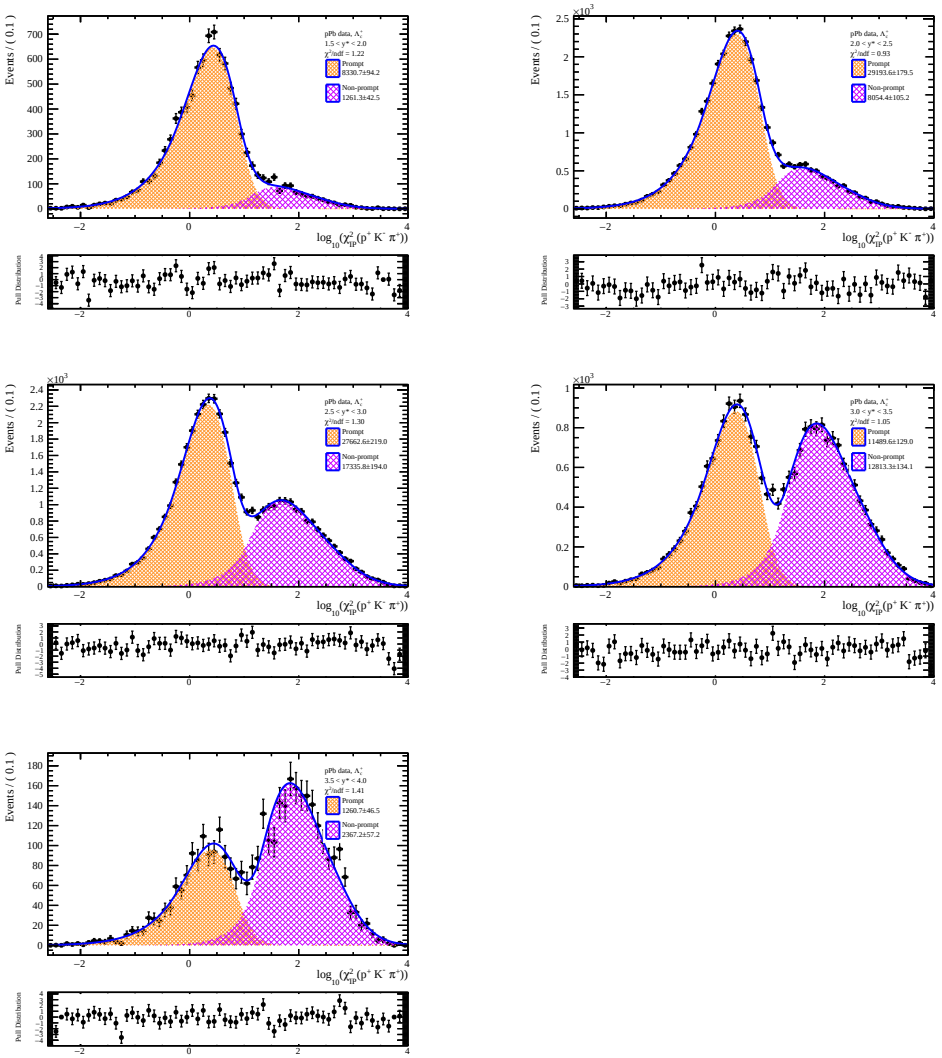

FIGURE C.6: $log_{10}(\chi^2_{IP})$ distribution fit in each y^* bin for Λ_c^+ from pPb data. The solid blue line represents the total fit, which is composed of a Bukin function representing the prompt signal (orange shaded area) and a another Bukin function representing the non-prompt signal (purple shaded area).

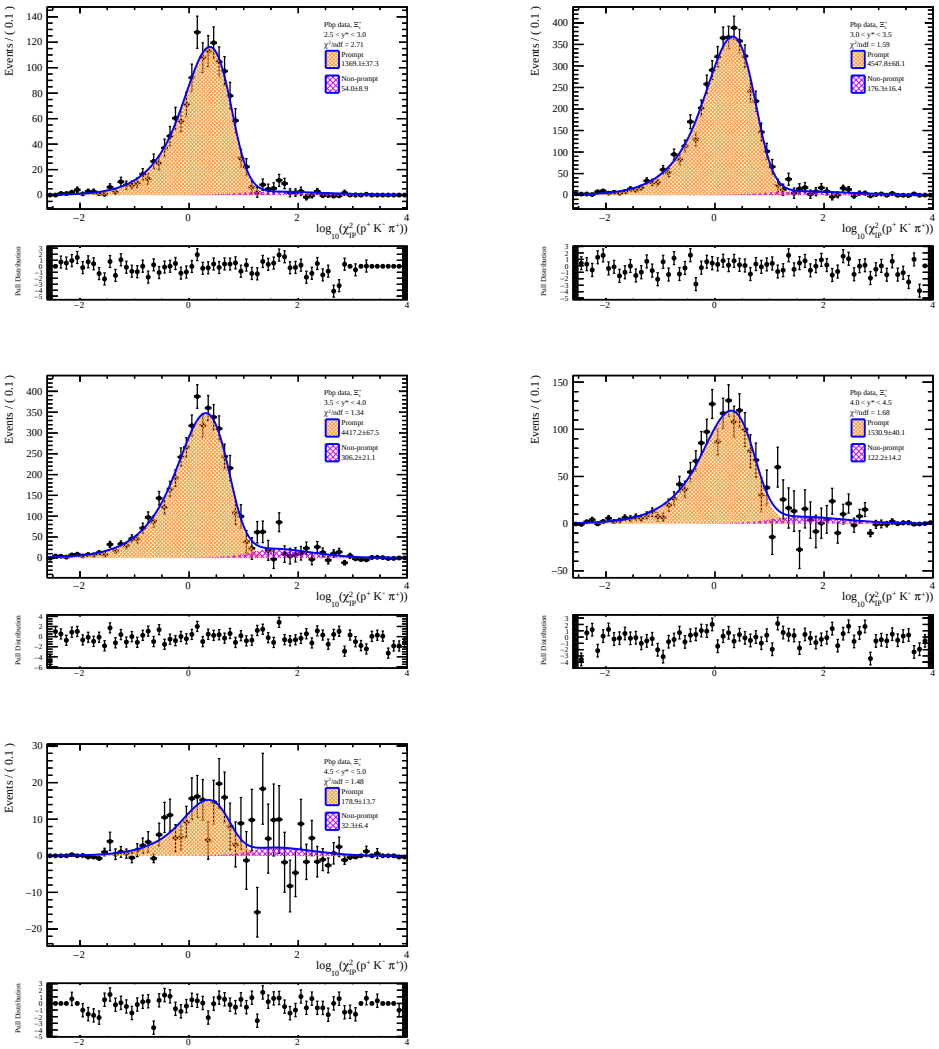

FIGURE C.7: $log_{10}(\chi^2_{IP})$ distribution fit in each y^* bin for Ξ_c^+ from Pbp data. The solid blue line represents the total fit, which is composed of a Bukin function representing the prompt signal (orange shaded area) and a another Bukin function representing the non-prompt signal (purple shaded area).

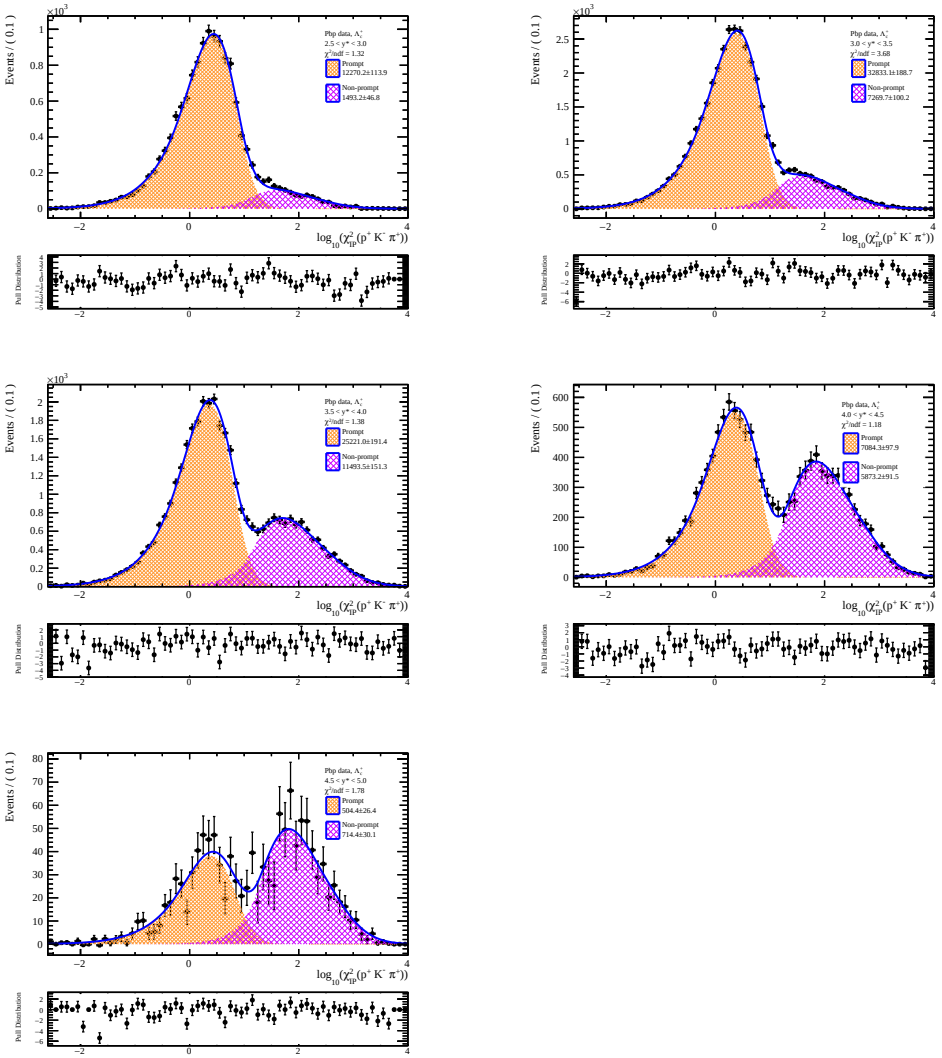

FIGURE C.8: $log_{10}(\chi^2_{IP})$ distribution fit in each y^* bin for Λ_c^+ from Pbp data. The solid blue line represents the total fit, which is composed of a Bukin function representing the prompt signal (orange shaded area) and a another Bukin function representing the non-prompt signal (purple shaded area).

Bibliography

[1] Wit Busza, Krishna Rajagopal, and Wilke van der Schee. "Heavy Ion Collisions: The Big Picture, and the Big Questions". In: *Ann. Rev. Nucl. Part. Sci.* 68 (2018), pp. 339–376. DOI: 10.1146/annurev-nucl-101917-020852. arXiv: 1802.04801 [hep-ph] (page 1).

[2] Robert Grajcarek. "Measurement of heavy-flavor production in Pb—Pb collisions at the LHC with ALICE". In: *Journal of Physics: Conference Series* 420 (Mar. 2013), p. 012032. ISSN: 1742-6596. DOI: 10.1088/1742-6596/420/1/012032. URL: http://dx.doi.org/10.1088/1742-6596/420/1/012032 (page 1).

[3] Raghunath Sahoo. "Possible Formation of QGP-droplets in Proton-Proton Collisions at the CERN Large Hadron Collider". In: *AAPPS Bull.* 29.4 (2019), pp. 16–21. DOI: 10.22661/AAPPSBL.2019.29.4.16. arXiv: 1908.10566 [nucl-ex] (pages 1, 16, 32).

[4] Néstor Armesto. "Nuclear shadowing". In: *Journal of Physics G: Nuclear and Particle Physics* 32.11 (2006), R367–R393. ISSN: 1361-6471. DOI: 10.1088/0954-3899/32/11/r01. URL: http://dx.doi.org/10.1088/0954-3899/32/11/R01 (page 2).

[5] Tianyu Dai et al. *Parton energy loss in a hard-soft factorized approach*. 2021. arXiv: 2012.03441 [hep-ph] (page 2).

[6] Matthew Wysocki. "Measurements of cold nuclear matter effects on J/ψ in the PHENIX experiment via deuteron–gold collisions". In: *Journal of Physics G: Nuclear and Particle Physics* 35.10 (2008), p. 104069. ISSN: 1361-6471. DOI: 10.1088/0954-3899/35/10/104069 (page 2).

[7] Johann Rafelski. "Strangeness production in the quark gluon plasma". In: *Nuclear Physics A* 418 (1984), pp. 215–235. ISSN: 0375-9474. DOI: https://doi.org/10.1016/0375-9474(84)90551-7. URL: https://www.sciencedirect.com/science/article/pii/0375947484905517 (page 2).

[8] Johann Rafelski. "Extreme States of Nuclear Matter - 1980". In: (1981). Ed. by Johann Rafelski, pp. 282–324 (page 2).

[9] P. Koch and Johann Rafelski. "Time Evolution of Strange Particle Densities in Hot Hadronic Matter". In: *Nucl. Phys. A* 444 (1985), pp. 678–691. DOI: 10.1016/0375-9474(85)90112-5 (page 2).

[10] P. Koch, Berndt Muller, and Johann Rafelski. "Strangeness in Relativistic Heavy Ion Collisions". In: *Phys. Rept.* 142 (1986), pp. 167–262. DOI: 10.1016/0370-1573(86)90096-7 (page 2).

[11] J. Adam et al. "Enhanced production of multi-strange hadrons in high-multiplicity proton–proton collisions". In: *Nature Physics* 13.6 (2017), 535–539. ISSN: 1745-2481. DOI: 10.1038/nphys4111. URL: http://dx.doi.org/10.1038/nphys4111 (page 2).

[12] Thomas A. Trainor. "QGP droplet formation in small asymmetric collision systems". In: *EPJ Web of Conferences* 235 (2020). Ed. by I. Vitev et al., p. 02006. DOI: 10.1051/epjconf/202023502006. URL: https://doi.org/10.1051%2Fepjconf%2F202023502006 (page 2).

[13] Ian Hinchliffe and Aneesh Manohar. "The QCD Coupling Constant". In: *Annual Review of Nuclear and Particle Science* 50.1 (2000), pp. 643–678. DOI: 10.1146/annurev.nucl.50.1.643 (page 8).

[14] M. Tanabashi et al. "Review of particle physics". In: *Phys. Rev.* D98 (2018), p. 030001. DOI: 10.1103/PhysRevD.98.030001 (page 9).

[15] Manuel Lorenz. "Geladene Kaonen Produktion in Ar+KCI Reaktionen bei 1.756 AGeV". IMPORT aus dem GDS: https://www.gsi.de/documents/DOC-2008-Aug-24.html; Universität Frankfurt/M., Diplomarbeit, 2008. Dipl. Darmstadt: Universität Frankfurt/M., 2008, 87 p. URL: https://repository.gsi.de/record/55278 (page 11).

[16] J. D. Bjorken. "Highly relativistic nucleus-nucleus collisions: The central rapidity region". In: *Phys. Rev. D* 27 (1 1983), pp. 140–151. DOI: 10.1103/PhysRevD.27.140. URL: https://link.aps.org/doi/10.1103/PhysRevD.27.140 (page 11).

[17] RaghunathSahoo. "Possible Formation of QGP-droplets in Proton- Proton Collisions at the CERN Large Hadron Collider". In: *AAPPS Bulletin* 29.4 (Aug. 2019), pp. 16–20 (page 12).

[18] Maria Elena Tejeda-Yeomans. *Heavy-ion physics: freedom to do hot, dense, exciting QCD*. 2020. DOI: 10.48550/ARXIV.2004.13812. URL: https://arxiv.org/abs/2004.13812 (page 12).

[19] Alberica Toia. "Participants and spectators at the heavy-ion fireball, How ALICE finds out how much of a heavy ion takes part in a collision." In: *CERN courier* (Apr. 2013). URL: cerncourier.com/a/participants-and-spectators-at-the-heavy-ion-fireball/ (page 13).

[20] Constantin Loizides, Jason Kamin, and David d'Enterria. "Improved Monte Carlo Glauber predictions at present and future nuclear colliders". In: *Phys. Rev. C* 97.5 (2018). [Erratum: Phys.Rev.C 99, 019901 (2019)], p. 054910. DOI: 10.1103/PhysRevC.97.054910. arXiv: 1710.07098 [nucl-ex] (page 13).

[21] Michael L. Miller et al. "Glauber Modeling in High-Energy Nuclear Collisions". In: *Annual Review of Nuclear and Particle Science* 57.1 (2007), pp. 205–243. DOI: 10.1146/annurev.nucl.57.090506.123020. eprint: https://doi.org/10.1146/annurev.nucl.57.090506.123020. URL: https://doi.org/10.1146/annurev.nucl.57.090506.123020 (page 14).

[22] F. Antinori et al. "Enhancement of hyperon production at central rapidity in 158-A-GeV/c Pb-Pb collisions". In: *J. Phys. G* 32 (2006), pp. 427–442. DOI: 10.1088/0954-3899/32/4/003. arXiv: nucl-ex/0601021 (page 15).

[23] Ajay Kumar Dash. "Multiplicity dependence of strangeness and hadronic resonance production in pp and p-Pb collisions with ALICE at the LHC". In: *Nuclear Physics A* 982 (2019). The 27th International Conference on Ultrarelativistic Nucleus-Nucleus Collisions: Quark Matter 2018, pp. 467–470. ISSN: 0375-9474. DOI: https://doi.org/10.1016/j.nuclphysa.2018.11.011. URL: https://www.sciencedirect.com/science/article/pii/S037594741830397X (page 15).

[24] "Corrigendum to "Multi-strange baryon production at mid-rapidity in Pb–Pb collisions at sNN=2.76 TeV" [Phys. Lett. B 728 (2014) 216-227]". In: *Physics Letters B* 734 (2014), pp. 409–410. ISSN: 0370-2693. DOI: https://doi.org/10.1016/j.physletb.2014.05.052. URL: https://www.sciencedirect.com/science/article/pii/S0370269314003621 (page 15).

[25] Serguei Chatrchyan et al. "Observation of Sequential Upsilon Suppression in PbPb Collisions". In: *Phys. Rev. Lett.* 109 (2012). [Erratum: Phys.Rev.Lett. 120, 199903 (2018)], p. 222301. DOI: 10.1103/PhysRevLett.109.222301. arXiv: 1208.2826 [nucl-ex] (page 15).

[26] Gabriele Gaetano Fronzé. Υ *production in p-Pb and Pb-Pb collisions with ALICE at the LHC*. Ed. by Guang-You Qin et al. 2017. DOI: 10.1016/j.nuclphysbps.2017.05.092. arXiv: 1612.06691 [hep-ex] (page 15).

[27] L. Adamczyk et al. "Upsilon production in U+U collisions at 193 GeV with the STAR experiment". In: *Physical Review C* 94.6 (2016). DOI: 10.1103/physrevc.94.064904. URL: https://doi.org/10.1103%2Fphysrevc.94.064904 (page 15).

[28] Pavol Štefko. "Study of jet quenching in heavy ion collisions at LHC using ATLAS detector". In: *18th Conference of Czech and Slovak Physicists*. 2015, pp. 93–95 (page 15).

[29] J. Adams et al. "Evidence from d + Au measurements for final state suppression of high p(T) hadrons in Au+Au collisions at RHIC". In: *Phys. Rev. Lett.* 91 (2003), p. 072304. DOI: 10.1103/PhysRevLett.91.072304. arXiv: nucl-ex/0306024 (page 15).

[30] Shanshan Cao and Xin-Nian Wang. "Jet quenching and medium response in high-energy heavy-ion collisions: a review". In: *Rept. Prog. Phys.* 84.2 (2021), p. 024301. DOI: 10.1088/1361-6633/abc22b. arXiv: 2002.04028 [hep-ph] (page 15).

[31] R. Vogt. "Cold Nuclear Matter Effects on Open and Hidden Heavy Flavor Production at the LHC". In: *7th International Workshop on Charm Physics*. Aug. 2015. arXiv: 1508.01286 [hep-ph] (page 16).

[32] Jiaxing Zhao et al. *Heavy flavors under extreme conditions in high energy nuclear collisions*. 2020. DOI: 10.48550/ARXIV.2005.08277. URL: https://arxiv.org/abs/2005.08277 (page 17).

[33] Rafał Maciuła and Antoni Szczurek. "Intrinsic charm in the nucleon and charm production at large rapidities in collinear, hybrid and kT-factorization approaches". In: *Journal of High Energy Physics* 2020.10 (2020). DOI: 10.1007/jhep10(2020)135. URL: https://doi.org/10.1007%2Fjhep10%282020%29135 (page 17).

[34] A. D. Martin et al. "Parton distributions for the LHC". In: *The European Physical Journal C* 63.2 (2009), pp. 189–285. DOI: 10.1140/epjc/s10052-009-1072-5. URL: https://doi.org/10.1140%2Fepjc%2Fs10052-009-1072-5 (page 18).

[35] Rafał Maciuła and Antoni Szczurek. "Consistent treatment of charm production in higher-orders at tree-level within kT factorization approach". In: *Physical Review D* 100.5 (2019). DOI: 10.1103/physrevd.100.054001. URL: https://doi.org/10.1103%2Fphysrevd.100.054001 (page 19).

[36] K.J Eskola, H Paukkunen, and C.A Salgado. "EPS09 — A new generation of NLO and LO nuclear parton distribution functions". In: *Journal of High Energy Physics* 2009.04 (2009), pp. 065–065. DOI: 10.1088/1126-6708/2009/04/065. URL: https://doi.org/10.1088%2F1126-6708%2F2009%2F04%2F065 (pages 19, 21).

[37] Koichi Saito and Toshihiro Uchiyama. "Effect of the Fermi Motion on Nuclear Structure Functions and the Emc Effect". In: *Z. Phys. A* 322 (1985), p. 299. DOI: 10.1007/BF01411895 (page 20).

[38] J. Seely et al. "New Measurements of the European Muon Collaboration Effect in Very Light Nuclei". In: *Phys. Rev. Lett.* 103 (20 2009), p. 202301. DOI: 10.1103/PhysRevLett.103.202301. URL: https://link.aps.org/doi/10.1103/PhysRevLett.103.202301 (page 20).

[39] Stanley J. Brodsky and Hung Jung Lu. "Shadowing and antishadowing of nuclear structure functions". In: *Phys. Rev. Lett.* 64 (12 1990), pp. 1342–1345. DOI: 10.1103/PhysRevLett.64.1342. URL: https://link.aps.org/doi/10.1103/PhysRevLett.64.1342 (page 20).

[40] Hannu Paukkunen. *Global analysis of nuclear parton distribution functions at leading and next-to-leading order perturbative QCD*. 2009. DOI: 10.48550/ARXIV.0906.2529. URL: https://arxiv.org/abs/0906.2529 (page 20).

[41] Dmitri Kharzeev and Kirill Tuchin. "Signatures of the color glass condensate in J/ψ production off nuclear targets". In: *Nucl. Phys. A* 770 (2006), pp. 40–56. DOI: 10.1016/j.nuclphysa.2006.01.017. arXiv: hep-ph/0510358 (page 20).

[42] J. W. Cronin et al. "Production of hadrons at large transverse momentum at 200, 300, and 400 GeV". In: *Phys. Rev. D* 11 (11 1975), pp. 3105–3123. DOI: 10.1103/PhysRevD.11.3105. URL: https://link.aps.org/doi/10.1103/PhysRevD.11.3105 (page 20).

[43] F. Arleo and V.-N. Tram. "A systematic study of J/ψ suppression in cold nuclear matter". In: *The European Physical Journal C* 55.3 (2008), pp. 449–461. DOI: 10.1140/epjc/s10052-008-0604-8. URL: https://doi.org/10.1140%2Fepjc%2Fs10052-008-0604-8 (page 21).

[44] K.J. Eskola, V.J. Kolhinen, and C.A. Salgado. "The scale dependent nuclear effects in parton distributions for practical applications". In: *The European Physical Journal C* 9.1 (1999), pp. 61–68. DOI: 10.1007/s100529900005. URL: https://doi.org/10.1007%2Fs100529900005 (page 21).

[45] Daniel de Florian et al. "Global analysis of nuclear parton distributions". In: *Phys. Rev. D* 85 (7 2012), p. 074028. DOI: 10.1103/PhysRevD.85.074028. URL: https://link.aps.org/doi/10.1103/PhysRevD.85.074028 (page 21).

[46] . "nCTEQ15: Global analysis of nuclear parton distributions with uncertainties in the CTEQ framework". In: *Phys. Rev. D* 93 (8 2016), p. 085037. DOI: 10.1103/PhysRevD.93.085037. URL: https://link.aps.org/doi/10.1103/PhysRevD.93.085037 (page 21).

[47] Kari J. Eskola et al. "EPPS16: nuclear parton distributions with LHC data". In: *The European Physical Journal C* 77.3 (8 2017), p. 085037. DOI: 10.1140/epjc/s10052-017-4725-9. URL: https://doi.org/10.1140%2Fepjc%2Fs10052-017-4725-9 (page 21).

[48] Aleksander Kusina et al. "Gluon Shadowing in Heavy-Flavor Production at the LHC". In: *Phys. Rev. Lett.* 121.5 (8 2018), p. 052004. DOI: 10.1103/PhysRevLett.121.052004. arXiv: 1712.07024 [hep-ph]. URL: https://link.aps.org/doi/10.1103/PhysRevD.93.085037 (pages 21, 22, 93, 97, 102).

[49] O Embré us, A Stahl, and T Fülöp. "Effect of bremsstrahlung radiation emission on fast electrons in plasmas". In: *New Journal of Physics* 18.9 (8 2016), p. 093023. DOI: 10.1088/1367-2630/18/9/093023. URL: https://doi.org/10.1088%2F1367-2630%2F18%2F9%2F093023 (page 22).

[50] F. Caporale et al. "Balitsky-Fadin-Kuraev-Lipatov Predictions for Inclusive Three Jet Production at the LHC". In: *Phys. Rev. Lett.* 116 (1 2016), p. 012001. DOI: 10.1103/PhysRevLett.116.012001. URL: https://link.aps.org/doi/10.1103/PhysRevLett.116.012001 (page 22).

[51] Cyrille Marquet. "Open questions in QCD at high parton density". In: *Nuclear Physics A* 904-905 (8 2013), pp. 294c–301c. DOI: 10.1016/j.nuclphysa.2013.01.075. URL: https://doi.org/10.1016%2Fj.nuclphysa.2013.01.075 (page 23).

[52] François Arleo, Greg Jackson, and Stéphane Peigné. "Impact of fully coherent energy loss on heavy meson production in pA collisions". In: *Journal of High Energy Physics* 2022.1 (8 2022), p. 085037. DOI: 10.1007/jhep01(2022)164. URL: https://doi.org/10.1007%2Fjhep01%282022%29164 (page 23).

[53] M J Tannenbaum. "How do quarks and gluons lose energy in the QGP?" In: *Journal of Physics: Conference Series* 589 (8 2015), p. 012019. DOI: 10.1088/1742-6596/589/1/012019. URL: https://doi.org/10.1088%2F1742-6596%2F589%2F1%2F012019 (page 24).

[54] S. S. Adler et al. "High-p_T charged hadron suppression in Au + Au collisions at $\sqrt{s_{NN}} = 200$ GeV". In: *Phys. Rev. C* 69 (3 2004), p. 034910. DOI: 10.1103/PhysRevC.69.034910. URL: https://link.aps.org/doi/10.1103/PhysRevC.69.034910 (page 25).

[55] Takao Sakaguchi and PHENIX collaboration. *Overview of latest results from PHENIX*. 2019. DOI: 10.48550/ARXIV.1901.01951. URL: https://arxiv.org/abs/1901.01951 (page 25).

[56] Roel Aaij et al. "Measurement of the Nuclear Modification Factor and Prompt Charged Particle Production in $p-Pb$ and pp Collisions at $\sqrt{s_{NN}}$=5 TeV". In: *Phys. Rev. Lett.* 128.14 (8 2022), p. 142004. DOI: 10.1103/PhysRevLett.128.142004. arXiv: 2108.13115 [hep-ex]. URL: https://link.aps.org/doi/10.1103/PhysRevD.93.085037 (page 25).

[57] Sayipjamal Dulat et al. "New parton distribution functions from a global analysis of quantum chromodynamics". In: *Phys. Rev. D* 93 (3 2016), p. 033006. DOI: 10.1103/PhysRevD.93.033006. URL: https://link.aps.org/doi/10.1103/PhysRevD.93.033006 (page 26).

[58] Daniel de Florian, Rodolfo Sassot, and Marco Stratmann. "Global analysis of fragmentation functions for pions and kaons and their uncertainties". In: *Phys. Rev. D* 75 (11 2007), p. 114010. DOI: 10.1103/PhysRevD.75.114010. URL: https://link.aps.org/doi/10.1103/PhysRevD.75.114010 (page 26).

[59] T. Lappi and H. Mäntysaari. "Single inclusive particle production at high energy from HERA data to proton-nucleus collisions". In: *Phys. Rev. D* 88 (11 2013), p. 114020. DOI: 10.1103/PhysRevD.88.114020. URL: https://link.aps.org/doi/10.1103/PhysRevD.88.114020 (page 26).

[60] Né stor Armesto. "Nuclear shadowing". In: *Journal of Physics G: Nuclear and Particle Physics* 32.11 (8 2006), R367–R393. DOI: 10.1088/0954-3899/32/11/r01. URL: https://doi.org/10.1088%2F0954-3899%2F32%2F11%2Fr01 (page 26).

[61] . "Study of prompt D^0 meson production in pPb at $\sqrt{s_{\rm NN}} = 8.16$ TeV at LHCb". In: *Phys. Rev. D* 93 (8 Nov. 2019), p. 085037. DOI: 10.1103/PhysRevD.93.085037. URL: https://link.aps.org/doi/10.1103/PhysRevD.93.085037 (page 26).

[62] R. Aaij et al. "Prompt and nonprompt J/ψ production and nuclear modification in pPb collisions at $\sqrt{s_{\rm NN}} = 8.16$ TeV". In: *Phys. Lett. B* 774 (8 Nov. 2017), pp. 159–178. DOI: 10.1016/j.physletb.2017.09.058. arXiv: 1706.07122 [hep-ex]. URL: https://link.aps.org/doi/10.1103/PhysRevD.93.085037 (page 26).

[63] Roel Aaij et al. "Prompt Λ_c^+ production in pPb collisions at $\sqrt{s_{NN}} = 5.02$ TeV". In: *JHEP* 02 (8 Nov. 2019), p. 102. DOI: 10.1007/JHEP02(2019)102. arXiv: 1809.01404 [hep-ex]. URL: https://link.aps.org/doi/10.1103/PhysRevD.93.085037 (pages 26, 69).

[64] Roel Aaij et al. "Study of Υ production in pPb collisions at $\sqrt{s_{NN}} = 8.16$ TeV". In: *JHEP* 11 (8 Nov. 2018). [Erratum: JHEP 02, 093 (2020)], p. 194. DOI: 10.1007/JHEP11(2018)194. arXiv: 1810.07655 [hep-ex]. URL: https://link.aps.org/doi/10.1103/PhysRevD.93.085037 (page 26).

[65] François Arleo, Greg Jackson, and Stéphane Peigné. "Impact of fully coherent energy loss on heavy meson production in pA collisions". In: *JHEP* 01 (8 Nov. 2022), p. 164. DOI: 10.1007/JHEP01(2022)164. arXiv: 2107.05871 [hep-ph]. URL: https://link.aps.org/doi/10.1103/PhysRevD.93.085037 (page 26).

[66] R. L. Workman and Others. "Review of Particle Physics". In: *PTEP* 2022 (8 Nov. 2022), p. 083C01. DOI: 10.1093/ptep/ptac097. URL: https://link.aps.org/doi/10.1103/PhysRevD.93.085037 (pages 27, 28, 60).

[67] H. J. Burckhart. "CHARM SEARCH WITH A HYPERON BEAM." In: vol. 93. American Physical Society, Nov. 1986, p. 085037. DOI: 10.1103/PhysRevD.93.085037. URL: https://link.aps.org/doi/10.1103/PhysRevD.93.085037 (page 27).

[68] P.A. Zyla et al. "Review of Particle Physics". In: *PTEP* 2020.8 (8 Nov. 2020). and 2021 update, p. 083C01. DOI: 10.1093/ptep/ptaa104. URL: https://link.aps.org/doi/10.1103/PhysRevD.93.085037 (pages 27, 60, 90).

[69] Y. B. Li et al. "First measurements of absolute branching fractions of the Ξ_c^+ baryon at Belle". In: *Phys. Rev. D* 100.3 (8 Nov. 2019), p. 031101. DOI: 10.1103/PhysRevD.100.031101. arXiv: 1904.12093 [hep-ex]. URL: https://link.aps.org/doi/10.1103/PhysRevD.93.085037 (page 27).

[70] Roel Aaij et al. "First branching fraction measurement of the suppressed decay $\Xi_c^0 \to \pi^- \Lambda_c^+$". In: *Phys. Rev. D* 102.7 (8 Nov. 2020), p. 071101. DOI: 10.1103/PhysRevD.102.071101. arXiv: 2007.12096 [hep-ex]. URL: https://link.aps.org/doi/10.1103/PhysRevD.93.085037 (page 27).

[71] J. C. Anjos et al. "Charm Photoproduction Results from E691: The Tagged Photon Spectrometer Collaboration". In: *23rd Rencontres de Moriond: Current Issues in Hadron Physics*. Vol. 93. American Physical Society, Nov. 1988, pp. 463–471. DOI: 10.1103/PhysRevD.93.085037. URL: https://link.aps.org/doi/10.1103/PhysRevD.93.085037 (page 27).

[72] V. Chabaud. "Recent results on Xi(c)+ and Lambda(c)+ baryons from the NA32 experiment." In: *Nucl. Phys. B Proc. Suppl.* 13 (8 Nov. 1990). Ed. by Paul Singer and Gad Eilam, pp. 244–246. DOI: 10.1016/0920-5632(90)90064-2. URL: https://link.aps.org/doi/10.1103/PhysRevD.93.085037 (page 27).

[73] Bernard Aubert et al. "A Study of anti-B —> Xi(c) anti-Lambda-(c) and anti-B —> anti-Lambda+(c) anti-Lambda-(c) anti-K decays at BABAR". In: *Phys. Rev. D* 77 (8 Nov. 2008), p. 031101. DOI: 10.1103/PhysRevD.77.031101. arXiv: 0710.5775 [hep-ex]. URL: https://link.aps.org/doi/10.1103/PhysRevD.93.085037 (page 27).

[74] R. Aaji et al. "Measurement of b hadron production fractions in 7 TeV pp collisions". In: *Phys. Rev. D* 85 (3 Nov. 2012), p. 032008. DOI: 10.1103/PhysRevD.85.032008. URL: https://link.aps.org/doi/10.1103/PhysRevD.85.032008 (page 29).

[75] Albert M Sirunyan et al. "Production of Λ_c^+ baryons in proton-proton and lead-lead collisions at $\sqrt{s_{\mathrm{NN}}} = 5.02$ TeV". In: *Phys. Lett. B* 803 (8 Nov. 2020), p. 135328. DOI: 10.1016/j.physletb.2020.135328. arXiv: 1906.03322 [hep-ex]. URL: https://link.aps.org/doi/10.1103/PhysRevD.93.085037 (page 29).

[76] Shreyasi Acharya et al. "Λ_c^+ Production and Baryon-to-Meson Ratios in pp and p-Pb Collisions at $\sqrt{s_{NN}}$=5.02 TeV at the LHC". In: *Phys. Rev. Lett.* 127.20 (8 Nov. 2021), p. 202301. DOI: 10.1103/PhysRevLett.127.202301. arXiv: 2011.06078 [nucl-ex]. URL: https://link.aps.org/doi/10.1103/PhysRevD.93.085037 (page 29).

[77] Shreyasi Acharya et al. "Measurement of Prompt D^0, Λ_c^+, and $\Sigma_c^{0,++}(2455)$ Production in Proton–Proton Collisions at $\sqrt{s} = 13$ TeV". In: *Phys. Rev. Lett.* 128.1 (8 Nov. 2022), p. 012001. DOI: 10.1103/PhysRevLett.128.012001. arXiv: 2106.08278 [hep-ex]. URL: https://link.aps.org/doi/10.1103/PhysRevD.93.085037 (page 29).

[78] Jianhui Zhu. "Hadronization studies at the LHC with ALICE". In: *PoS* ICHEP2020 (8 Nov. 2021), p. 524. DOI: 10.22323/1.390.0524. arXiv: 2104.11309

[hep-ex]. URL: https://link.aps.org/doi/10.1103/PhysRevD.93.085037 (pages 29, 30).

[79] B. A. Kniehl et al. "Collinear subtractions in hadroproduction of heavy quarks". In: *Eur. Phys. J. C* 41 (8 Nov. 2005), pp. 199–212. DOI: 10.1140/epjc/s2005-02200-7. arXiv: hep-ph/0502194. URL: https://link.aps.org/doi/10.1103/PhysRevD.93.085037 (page 29).

[80] B. A. Kniehl et al. "Inclusive Charmed-Meson Production at the CERN LHC". In: *Eur. Phys. J. C* 72 (8 Nov. 2012), p. 2082. DOI: 10.1140/epjc/s10052-012-2082-2. arXiv: 1202.0439 [hep-ph]. URL: https://link.aps.org/doi/10.1103/PhysRevD.93.085037 (page 29).

[81] Jesper R. Christiansen and Peter Z. Skands. "String Formation Beyond Leading Colour". In: *JHEP* 08 (8 Nov. 2015), p. 003. DOI: 10.1007/JHEP08(2015)003. arXiv: 1505.01681 [hep-ph]. URL: https://link.aps.org/doi/10.1103/PhysRevD.93.085037 (page 30).

[82] Jesper R. Christiansen. "Colour Reconnection - Models and Tests". In: *PoS* EPS-HEP2015 (8 Nov. 2015), p. 443. DOI: 10.22323/1.234.0443. arXiv: 1510.04859 [hep-ph]. URL: https://link.aps.org/doi/10.1103/PhysRevD.93.085037 (page 30).

[83] Pengyao Cui, Zhongbao Yin, and Liang Zheng. "Strange particle production in jets and underlying events in pp collisions at $\sqrt{s} = 7$ TeV with PYTHIA8 generator". In: *Eur. Phys. J. A* 58.3 (8 Nov. 2022), p. 53. DOI: 10.1140/epja/s10050-022-00709-7. arXiv: 2203.13416 [hep-ph]. URL: https://link.aps.org/doi/10.1103/PhysRevD.93.085037 (page 31).

[84] Vincenzo Minissale, Salvatore Plumari, and Vincenzo Greco. "Charm hadrons in pp collisions at LHC energy within a coalescence plus fragmentation approach". In: *Phys. Lett. B* 821 (8 Nov. 2021), p. 136622. DOI: 10.1016/j.physletb.2021.136622. arXiv: 2012.12001 [hep-ph]. URL: https://link.aps.org/doi/10.1103/PhysRevD.93.085037 (pages 30, 32, 33).

[85] Salvatore Plumari et al. "Charmed Hadrons from Coalescence plus Fragmentation in relativistic nucleus-nucleus collisions at RHIC and LHC". In: *Eur. Phys. J. C* 78.4 (8 Nov. 2018), p. 348. DOI: 10.1140/epjc/s10052-018-5828-7. arXiv: 1712.00730 [hep-ph]. URL: https://link.aps.org/doi/10.1103/PhysRevD.93.085037 (page 31).

[86] Jaroslav Adam et al. "Enhanced production of multi-strange hadrons in high-multiplicity proton-proton collisions". In: *Nature Phys.* 13 (8 Nov. 2017), pp. 535–539. DOI: 10.1038/nphys4111. arXiv: 1606.07424 [nucl-ex]. URL: https://link.aps.org/doi/10.1103/PhysRevD.93.085037 (pages 32, 34).

[87] Emilie Maurice. "Fixed-target physics at LHCb". In: *5th Large Hadron Collider Physics Conference*. Vol. 93. American Physical Society, Aug. 2017, p. 085037. DOI: 10.1103/PhysRevD.93.085037. arXiv: 1708.05184 [hep-ex]. URL: https://link.aps.org/doi/10.1103/PhysRevD.93.085037 (page 35).

[88] Esma Mobs. "The CERN accelerator complex. Complexe des accélérateurs du CERN". In: *Phys. Rev. D* 93 (8 Nov. 2016). General Photo, p. 085037. DOI: 10.1103/PhysRevD.93.085037. URL: https://cds.cern.ch/record/2197559 (page 36).

[89] R. Bailey and Paul Collier. *Standard Filling Schemes for Various LHC Operation Modes*. fr. Institution: CERN-LHC-Project-Note-323 Number: LHC-PROJECT-NOTE-323. Sept. 2003. DOI: 10.1103/PhysRevD.93.085037. URL: https://cds.cern.ch/record/691782 (page 36).

[90] Torbjorn Sjostrand, Stephen Mrenna, and Peter Z. Skands. "A Brief Introduction to PYTHIA 8.1". In: *Comput. Phys. Commun.* 178 (8 Nov. 2008), pp. 852–867. DOI: 10.1016/j.cpc.2008.01.036. arXiv: 0710.3820 [hep-ph]. URL: https://link.aps.org/doi/10.1103/PhysRevD.93.085037 (pages 38, 57).

[91] I. Belyaev et al. "The history of LHCb". In: *Eur. Phys. J. H* 46.1 (8 Nov. 2021), p. 3. DOI: 10.1140/epjh/s13129-021-00002-z. arXiv: 2101.05331 [physics.hist-ph]. URL: https://link.aps.org/doi/10.1103/PhysRevD.93.085037 (page 38).

[92] . *Performance of the LHCb RICH detector at the LHC*. Nov. 2019. DOI: 10.1103/PhysRevD.93.085037. URL: https://arxiv.org/abs/1211.6759v2 (page 45).

[93] A. Arefev et al. "Beam test results of the LHCb electromagnetic calorimeter". In: *Phys. Rev. D* 93 (8 Apr. 2008), p. 085037. DOI: 10.1103/PhysRevD.93.085037. URL: http://cds.cern.ch/record/1103500 (page 45).

[94] Albert Bursche et al. "Physics opportunities with the fixed-target program of the LHCb experiment using an unpolarized gas target". In: *Phys. Rev. D* 93 (8 Nov. 2018), p. 085037. DOI: 10.1103/PhysRevD.93.085037. URL: https://arxiv.org/abs/1211.6759v2 (page 46).

[95] Renato Quagliani. "Novel real-time alignment and calibration of LHCb detector for Run II and tracking for the upgrade." In: *Journal of Physics: Conference Series* 762 (8 Oct. 2016), p. 012046. DOI: 10.1088/1742-6596/762/1/012046. URL: https://arxiv.org/abs/1211.6759v2 (page 48).

[96] Denis Derkach, Mikhail Hushchyn, and Nikita Kazeev. "Machine Learning based Global Particle Identification Algorithms at the LHCb Experiment". In: *EPJ Web of Conferences* 214 (8 Jan. 2019), p. 06011. DOI: 10.1051/epjconf/201921406011. URL: https://arxiv.org/abs/1211.6759v2 (page 51).

[97] R. Calabrese et al. "Performance of the LHCb RICH detectors during LHC Run 2". In: *JINST* 17.07 (8 Nov. 2022), P07013. DOI: 10.1088/1748-0221/17/07/P07013. arXiv: 2205.13400 [physics.ins-det]. URL: https://arxiv.org/abs/1211.6759v2 (page 52).

[98] Denis Derkach, Mikhail Hushchyn, and Nikita Kazeev. "Machine Learning based Global Particle Identification Algorithms at the LHCb Experiment". en. In: *EPJ Web of Conferences* 214 (8 Nov. 2019). Publisher: EDP Sciences, p. 06011. ISSN: 2100-014X. DOI: 10.1051/epjconf/201921406011. URL: https://www.epj-conferences.org/articles/epjconf/abs/2019/19/epjconf_chep2018_06011/epjconf_chep2018_06011.html (page 52).

[99] G. Barrand et al. "GAUDI - A software architecture and framework for building HEP data processing applications". en. In: *Comput.Phys.Commun.* 140 (8 Dec. 2001), pp. 45–55. DOI: 10.1016/S0010-4655(01)00254-5. URL: https://inspirehep.net/literature/568472 (page 52).

[100] . *The GAUSS Project*. Nov. 2019. DOI: 10.1103/PhysRevD.93.085037. URL: http://lhcbdoc.web.cern.ch/lhcbdoc/gauss/ (page 53).

[101] . *The BOOLE Project*. Nov. 2019. DOI: 10.1103/PhysRevD.93.085037. URL: http://lhcbdoc.web.cern.ch/lhcbdoc/boole/ (pages 53, 54).

[102] . *The BRUNEL Project*. Nov. 2019. DOI: 10.1103/PhysRevD.93.085037. URL: http://lhcbdoc.web.cern.ch/lhcbdoc/brunel/ (page 53).

[103] . *The DAVINCI Project*. Nov. 2019. DOI: 10.1103/PhysRevD.93.085037. URL: http://lhcbdoc.web.cern.ch/lhcbdoc/davinci/ (page 53).

[104] . *The LHCb data flow — LHCb Starterkit Lessons documentation*. Nov. 2019. DOI: 10.1103/PhysRevD.93.085037. URL: https://lhcb.github.io/starterkit-lessons/first-analysis-steps/dataflow.html (page 53).

[105] Torbjörn Sjöstrand, Stephen Mrenna, and Peter Skands. "A brief introduction to PYTHIA 8.1". en. In: *Computer Physics Communications* 178.11 (8 June 2008), pp. 852–867. ISSN: 0010-4655. DOI: 10.1016/j.cpc.2008.01.036. URL: http://www.sciencedirect.com/science/article/pii/S0010465508000441 (visited on 07/22/2020) (page 54).

[106] T. Pierog et al. "EPOS LHC: Test of collective hadronization with data measured at the CERN Large Hadron Collider". In: *Physical Review C* 92.3 (8 Sept. 2015). Publisher: American Physical Society, p. 034906. DOI: 10.1103/PhysRevC.92.034906. URL: https://link.aps.org/doi/10.1103/PhysRevC.92.034906 (visited on 07/22/2020) (page 54).

[107] David J. Lange. "The EvtGen particle decay simulation package". en. In: *Nuclear Instruments and Methods in Physics Research Section A: Accelerators, Spectrometers, Detectors and Associated Equipment*. BEAUTY2000, Proceedings of the 7th Int. Conf. on B-Physics at Hadron Machines 462.1 (8 Apr. 2001), pp. 152–155. ISSN: 0168-9002. DOI: 10.1016/S0168-9002(01)00089-4. URL:

http://www.sciencedirect.com/science/article/pii/S0168900201000894 (visited on 07/22/2020) (page 54).

[108] Agostinelli. "Geant4—a simulation toolkit". en. In: *Nuclear Instruments and Methods in Physics Research Section A: Accelerators, Spectrometers, Detectors and Associated Equipment* 506.3 (8 July 2003), pp. 250–303. ISSN: 0168-9002. DOI: 10.1016/S0168-9002(03)01368-8. URL: http://www.sciencedirect.com/science/article/pii/S0168900203013688 (page 54).

[109] Roel Aaij et al. "Precision luminosity measurements at LHCb". In: *JINST* 9.12 (8 Nov. 2014), P12005. DOI: 10.1088/1748-0221/9/12/P12005. arXiv: 1410.0149 [hep-ex]. URL: https://lhcb.github.io/starterkit-lessons/first-analysis-steps/dataflow.html (page 55).

[110] Vladislav Balagura. "Notes on van der Meer Scan for Absolute Luminosity Measurement". In: *Nucl. Instrum. Meth. A* 654 (8 Nov. 2011), pp. 634–638. DOI: 10.1016/j.nima.2011.06.007. arXiv: 1103.1129 [physics.ins-det]. URL: https://lhcb.github.io/starterkit-lessons/first-analysis-steps/dataflow.html (page 55).

[111] Massimiliano Ferro-Luzzi. "Proposal for an absolute luminosity determination in colliding beam experiments using vertex detection of beam–gas interactions". In: *Nuclear Instruments and Methods in Physics Research Section A: Accelerators, Spectrometers, Detectors and Associated Equipment* 553.3 (8 Nov. 2005), pp. 388–399. ISSN: 0168-9002. DOI: https://doi.org/10.1016/j.nima.2005.07.010. URL: https://www.sciencedirect.com/science/article/pii/S0168900205014130 (page 55).

[112] Georges Aad et al. "Improved luminosity determination in pp collisions at sqrt(s) = 7 TeV using the ATLAS detector at the LHC". In: *Eur. Phys. J. C* 73.8 (8 Nov. 2013), p. 2518. DOI: 10.1140/epjc/s10052-013-2518-3. arXiv: 1302.4393 [hep-ex]. URL: https://lhcb.github.io/starterkit-lessons/first-analysis-steps/dataflow.html (page 55).

[113] . "CMS Luminosity Based on Pixel Cluster Counting - Summer 2013 Update". In: *Phys. Rev. D* 93 (8 Nov. 2013), p. 085037. DOI: 10.1103/PhysRevD.93.085037. URL: https://lhcb.github.io/starterkit-lessons/first-analysis-steps/dataflow.html (page 56).

[114] Betty Bezverkhny Abelev et al. "Measurement of visible cross sections in proton-lead collisions at $\sqrt{s_{\mathrm{NN}}}$ = 5.02 TeV in van der Meer scans with the ALICE detector". In: *JINST* 9.11 (8 Nov. 2014), P11003. DOI: 10.1088/1748-0221/9/11/P11003. arXiv: 1405.1849 [nucl-ex]. URL: https://lhcb.github.io/starterkit-lessons/first-analysis-steps/dataflow.html (page 56).

[115] S. van der Meer. "Calibration of the Effective Beam Height in the ISR". In: *Phys. Rev. D* 93 (8 June 1968), p. 085037. DOI: 10.1103/PhysRevD.93.085037.

URL: https://lhcb.github.io/starterkit-lessons/first-analysis-steps/dataflow.html (page 56).

[116] Sean Benson et al. "The LHCb Turbo Stream". In: *Journal of Physics: Conference Series* 664.8 (8 Nov. 2015), p. 082004. DOI: 10.1088/1742-6596/664/8/082004. URL: https://doi.org/10.1088/1742-6596/664/8/082004 (pages 56, 57).

[117] T. Pierog et al. "EPOS LHC: Test of collective hadronization with data measured at the CERN Large Hadron Collider". In: *Phys. Rev.* C92.3 (8 Nov. 2015), p. 034906. DOI: 10.1103/PhysRevC.92.034906. arXiv: 1306.0121 [hep-ph]. URL: https://lhcb.github.io/starterkit-lessons/first-analysis-steps/dataflow.html (page 57).

[118] D. J. Lange. "The EvtGen particle decay simulation package". In: *Nucl. Instrum. Meth. A* 462 (8 Nov. 2001). Ed. by S. Erhan, P. Schlein, and Y. Rozen, pp. 152–155. DOI: 10.1016/S0168-9002(01)00089-4. URL: https://lhcb.github.io/starterkit-lessons/first-analysis-steps/dataflow.html (page 57).

[119] S. Agostinelli et al. "GEANT4–a simulation toolkit". In: *Nucl. Instrum. Meth. A* 506 (8 Nov. 2003), pp. 250–303. DOI: 10.1016/S0168-9002(03)01368-8. URL: https://lhcb.github.io/starterkit-lessons/first-analysis-steps/dataflow.html (page 57).

[120] C.P.Shen Belle Collaboration: Y.B.Li. "First measurements of absolute branching fractions of the Ξ_c^+ baryon at Belle". In: *Physical Review D* 100.3 (8 Nov. 2019), p. 085037. DOI: 10.1103/physrevd.100.031101. URL: https://doi.org/10.1103%2Fphysrevd.100.031101 (pages 60, 90).

[121] R. Aaij et al. "First branching fraction measurement of the suppressed decay $\Xi_c^0 \to \pi^-\Lambda_c^+$". In: *Physical Review D* 102.7 (8 Nov. 2020), p. 085037. DOI: 10.1103/physrevd.102.071101. URL: https://doi.org/10.1103%2Fphysrevd.102.071101 (pages 60, 90).

[122] LHCb collaboration. *Measurement of the prompt D^0 nuclear modification factor in pPb collisions at $\sqrt{s_{\rm NN}} = 8.16$ TeV*. Nov. 2022. DOI: 10.1103/PhysRevD.93.085037. arXiv: 2205.03936 [nucl-ex]. URL: https://lhcb.github.io/starterkit-lessons/first-analysis-steps/dataflow.html (pages 60, 93, 102).

[123] Sean Benson et al. "The LHCb Turbo Stream". In: *J. Phys. Conf. Ser.* 664.8 (8 Nov. 2015), p. 082004. DOI: 10.1088/1742-6596/664/8/082004. URL: https://lhcb.github.io/starterkit-lessons/first-analysis-steps/dataflow.html (page 64).

[124] M. Pivk and F.R. Le Diberder. ": A statistical tool to unfold data distributions". In: *Nuclear Instruments and Methods in Physics Research Section A: Accelerators, Spectrometers, Detectors and Associated Equipment* 555.1-2 (8 Nov. 2005), pp. 356–369. DOI: 10.1016/j.nima.2005.08.106. URL: https://doi.org/10.1016%2Fj.nima.2005.08.106 (pages 68, 76).

[125] R Aaij et al. "Prompt charm production in pp collisions at sqrt(s)=7 TeV". In: *Nucl. Phys. B* 871 (8 Nov. 2013), pp. 1–20. DOI: 10.1016/j.nuclphysb.2013.02.010. arXiv: 1302.2864 [hep-ex]. URL: https://lhcb.github.io/starterkit-lessons/first-analysis-steps/dataflow.html (page 69).

[126] Roel Aaij et al. "Study of prompt D^0 meson production in pPb collisions at $\sqrt{s_{NN}} = 5$ TeV". In: *JHEP* 10 (8 Nov. 2017), p. 090. DOI: 10.1007/JHEP10(2017)090. arXiv: 1707.02750 [hep-ex]. URL: https://lhcb.github.io/starterkit-lessons/first-analysis-steps/dataflow.html (page 69).

[127] Wouter Verkerke and David Kirkby. *The RooFit toolkit for data modeling*. Nov. 2003. DOI: 10.1103/PhysRevD.93.085037. arXiv: physics/0306116 [physics.data-an]. URL: https://lhcb.github.io/starterkit-lessons/first-analysis-steps/dataflow.html (page 70).

[128] R. Aaij et al. "Measurement of B^+, B^0 and Λ_b^0 production in pPb collisions at $\sqrt{s}_{NN}$=8.16 TeV". In: *Physical Review D* 99.5 (8 Nov. 2019), p. 085037. DOI: 10.1103/physrevd.99.052011. URL: https://doi.org/10.1103%2Fphysrevd.99.052011 (page 80).

[129] Lucio Anderlini et al. "The PIDCalib package". In: *Phys. Rev. D* 93 (8 Nov. 2016), p. 085037. DOI: 10.1103/PhysRevD.93.085037. URL: https://lhcb.github.io/starterkit-lessons/first-analysis-steps/dataflow.html (page 82).

[130] Jean-Philippe Lansberg and Hua-Sheng Shao. "Towards an automated tool to evaluate the impact of the nuclear modification of the gluon density on quarkonium, D and B meson production in proton–nucleus collisions". In: *Eur. Phys. J.* C77.1 (8 Nov. 2017), p. 1. DOI: 10.1140/epjc/s10052-016-4575-x. arXiv: 1610.05382 [hep-ph]. URL: https://lhcb.github.io/starterkit-lessons/first-analysis-steps/dataflow.html (page 93).

[131] Aleksander Kusina et al. "Gluon shadowing and antishadowing in heavy-flavor production at the LHC". In: *Phys. Rev. D* 93 (8 Nov. 2017), p. 085037. DOI: 10.1103/PhysRevD.93.085037. arXiv: 1712.07024 [hep-ph]. URL: https://lhcb.github.io/starterkit-lessons/first-analysis-steps/dataflow.html (page 93).

[132] Aleksander Kusina et al. "Reweighted nuclear PDFs using heavy-flavor production data at the LHC". In: *Phys. Rev. D* 104.1 (8 Nov. 2021), p. 014010. DOI: 10.1103/PhysRevD.104.014010. arXiv: 2012.11462 [hep-ph]. URL:

https://lhcb.github.io/starterkit-lessons/first-analysis-steps/dataflow.html (page 93).

[133] Hua-Sheng Shao. "HELAC-Onia: An automatic matrix element generator for heavy quarkonium physics". In: *Comput. Phys. Commun.* 184 (8 Nov. 2013), pp. 2562–2570. DOI: 10.1016/j.cpc.2013.05.023. arXiv: 1212.5293 [hep-ph]. URL: https://lhcb.github.io/starterkit-lessons/first-analysis-steps/dataflow.html (page 93).

[134] Hua-Sheng Shao. "HELAC-Onia 2.0: An upgraded matrix-element and event generator for heavy quarkonium physics". In: *Comput. Phys. Commun.* 198 (8 Nov. 2016), pp. 238–259. DOI: 10.1016/j.cpc.2015.09.011. arXiv: 1507.03435 [hep-ph]. URL: https://lhcb.github.io/starterkit-lessons/first-analysis-steps/dataflow.html (page 93).

List of Figures

List of Tables